Double Pionic Fusion to ^{4}He

Kinematically Complete Measurements over the Energy Region of the ABC Effect

Dissertation
der Mathematisch-Naturwissenschaftlichen Fakultät
der Eberhard Karls Universität Tübingen
zur Erlangung des Grades eines
Doktors der Naturwissenschaften
(Dr.rer.nat.)

vorgelegt von
Annette Pricking
aus Köln

Tübingen
2010

Tag der mündlichen Prüfung:	7. Februar 2011
Dekan:	Prof. Dr. Wolfgang Rosenstiel
1. Berichterstatter:	Prof. Dr. Heinz Clement
2. Berichterstatter:	Prof. Dr. Frank Hinterberger
3. Berichterstatter:	Prof. Dr. Hans Ströher

Zusammenfassung

Die doppelt-pionische Fusion leichter Kerne wird kurz oberhalb der Energieschwelle vom sogenannten ABC-Effekt dominiert, einer riesigen Überhöhung an der Massenschwelle im Spektrum der invarianten Masse des Pionpaars. Bis heute, 50 Jahre nach seiner Entdeckung, gibt es keine zufriedenstellende Erklärung für dieses Phänomen. Ein Grund dafür ist, dass in den früheren Messungen nur das schwere Ejektil gemessen und nicht alle kinematischen Variablen ermittelt werden konnten. Deshalb wurden mit dem WASA Detektor exklusive, kinematisch vollständige Messungen der Zwei-Pion-Produktion unternommmen.

Diese Arbeit widmet sich der Fusion zu ^{4}He. Bei neun Strahlenergien über den gesamten Bereich des ABC-Effekts wurde die Reaktion dd $\rightarrow$ ^{4}He$\pi^0\pi^0$ gemessen. Damit wird zum erstem Mal die Energieabhängigkeit des ABC-Effekts in exklusiven Messungen untersucht. Zur Durchführung der Experimente wurden neue Detektorkomponenten für den WASA Detektor benötigt, deren Entwicklung und Aufbau ebenfalls Teil dieser Arbeit sind.

Die Ergebnissse eröffnen einen völlig neuen Zugang zum ABC-Effekt. Die zusätzlichen Informationen durch die Messung aller kinematischen Variablen erweisen sich als essentiell für das Verständnis des Phänomens. So können die konventionellen Modelle, die anhand der inklusiven Daten entwickelt wurden, die neuen Ergebnisse nicht repoduzieren.
Die Daten weisen die Überhöhung bei kleinen invarianten $\pi\pi$-Massen als einen sehr hohen und schmalen Peak aus, der mit einer starken Energieabhängigkeit des totalen Wirkungsquerschnitts einhergeht. Der Vergleich mit den neuesten Ergebnissen in der Basisreaktion des ABC-Effekts, $pn \rightarrow d\pi\pi$, untermauert die Vermutung, dass sowohl der Fusion zu d als auch der Fusion zu ^{4}He derselbe Prozess zugrunde liegt.
Die Resultate weisen darauf hin, dass der ABC-Effekt von einer Resonanz in $pn-$ und $\Delta\Delta$-Systemen getragen wird, die stark genug ist, auch im nuklearen Medium zu bestehen. Tatsächlich beschreibt das neu entwickelte ABC-Resonanz-Modell die Daten in beiden Reaktion mit bemerkenswerter Genauigkeit.

Abstract

The double-pionic fusion to light nuclei slightly above the threshold is governed by the so-called ABC effect, a huge enhancement in the invariant mass spectrum of the pion pair at low masses. Now 50 years have passed since its discovery, but still this phenomenon is lacking a satisfying explanation.
One reason is that all the early experiments were inclusive, measuring only the heavy ejectile. Thus not all kinematic variables could be obtained. For this reason exclusive, kinematically complete measurements of the double-pion production were performed with the WASA detector.

This work is about the fusion to ^{4}He. At nine beam energies over the whole energy region of the ABC effect the $dd \to {}^4\mathrm{He}\pi^0\pi^0$ reaction was measured. For the first time the energy dependence of the ABC effect was investigated in exclusive measurements. For these experiments new detector components for the WASA detector system were developed, which was also part of this thesis.

The results open a completely new view on the ABC effect. Apparently the additional information gained by the measurement of all kinematic variables is essential for the understanding of the phenomenon. Previous models developed at hand of inclusive measurements cannot reproduce the new results.
The data identify the enhancement at low $\pi\pi$ invariant masses as a very strong and narrow peak accompanied with a strong energy dependence of the total cross section. A comparison with the recent results in the basic reaction of the ABC effect, $pn \to d\pi\pi$, confirms the assumption that both reactions, the fusion to deuteron and the fusion to ^{4}He, are goverend by the same underlying process.
The results indicate that the ABC effect is driven by a resonance in the pn and $\Delta\Delta$ systems, which is strong enough to survive in a nuclear medium. And in fact the recently developed ABC resonance model describes both reactions with amazing accuracy.

Contents

1 Introduction **1**
1.1 History of the ABC Effect 2

2 Experimental Setup: WASA-at-COSY **7**
2.1 The COSY Storage Ring 7
2.2 The Pellet Target System PTS 9
2.3 The WASA Detector 9
2.3.1 Coordinate System 10
2.3.2 The Forward Detector 11
2.3.3 The Central Detector 15
2.3.4 Plastic Scintillator Barrel PS 16
2.3.5 Superconducting Solenoid 16
2.3.6 Scintillating Electromagnetic Calorimeter SE 16
2.4 Data Acquisition DAQ 18
2.4.1 Signal Handling 18

3 Upgrade of the WASA Forward Detector **20**
3.1 The new Forward Window Counter FWC 20
3.1.1 The old FWC 20
3.1.2 Design Considerations for the new FWC 21
3.1.3 Scintillator 23
3.1.4 Photomultipliers 25
3.1.5 Lightguides 27
3.1.6 Preparation and Installation of the new FWC 31
3.1.7 Performance of the new FWC 37
3.2 The new FVH 42
3.2.1 The old FVH 42
3.2.2 Design Considerations for the New FVH 42
3.2.3 Scintillators 44
3.2.4 Photomultipliers 45
3.2.5 Lightguides 46
3.2.6 Installation of the new FVH 46

4 Analysis Tools **50**
4.1 RootSorter . . . 50
4.2 Forward Track Reconstruction . . . 51
4.3 Central Detector Track Reconstruction . . . 55
4.4 Event Tree . . . 55
4.5 Calibration . . . 56
4.6 Magnetic Field Correction for Forward Tracks . . . 57
4.7 Particle Identification . . . 58
4.7.1 Forward Detector . . . 58
4.7.2 Central Detector . . . 59
4.8 Kinetic Energy Reconstruction . . . 60
4.9 WASA Monte Carlo WMC . . . 61
4.10 Event Generation . . . 62

5 Analysis **64**
5.1 The Reaction dd $\rightarrow {}^4\mathrm{He}\pi^0\pi^0$ . . . 64
5.1.1 Kinematics . . . 65
5.2 Experiment . . . 66
5.3 Preselection . . . 68
5.4 Selection of dd $\rightarrow {}^4\mathrm{He}\pi^0\pi^0$ . . . 69
5.4.1 Forward Detector: ^{4}He Selection . . . 69
5.4.2 Central Detector: $\pi^0\pi^0$ Selection . . . 73
5.4.3 Kinematic Fit . . . 75
5.4.4 Efficiency and Acceptance Corrections . . . 83
5.5 Selection of $dd \rightarrow {}^3\mathrm{He}n$ Events . . . 84

6 Results **90**
6.1 Theoretical Models . . . 90
6.1.1 The GFW Model for $dd \rightarrow {}^4\mathrm{He}\pi\pi$ . . . 90
6.1.2 The ABC Resonance Model . . . 91
6.2 Invariant Mass Distribution . . . 100
6.2.1 Comparison to CELSIUS-WASA Results at 1.029 GeV . . . 101
6.3 Angular Distributions . . . 102
6.4 Energy Dependence of the Differential Cross Sections . . . 104
6.4.1 $M_{\pi^0\pi^0}$ and $M_{^4\mathrm{He}\pi^0}$ Distributions . . . 104
6.4.2 Dalitz Plot $M_{^4\mathrm{He}\pi^0_1}$ versus $M_{^4\mathrm{He}\pi^0_2}$ . . . 105
6.4.3 Angular Distributions . . . 109
6.5 Absolute Normalization . . . 113
6.5.1 Error Estimation . . . 114
6.5.2 Total Cross Section . . . 116

7 Summary **120**

8 Outlook **121**

9 Appendix **122**
9.1 List of Acronyms . . . 122
9.2 Kinematics of dd $\rightarrow {}^4\mathrm{He}\pi^0\pi^0$ . . . 123
9.3 Analysis of dd $\rightarrow {}^4\mathrm{He}\pi^0\pi^0$ . . . 124
9.4 Analysis of $dd \rightarrow {}^3\mathrm{He}n$ . . . 134
9.5 Differential Distributions with Phase Space Correction . . . 144
9.6 Total Cross Section of dd $\rightarrow {}^4\mathrm{He}\pi^0\pi^0$ as Function of the Probability Cut . . . 149
9.7 Total Cross Section of dd $\rightarrow {}^4\mathrm{He}\pi^0\pi^0$ as Function of the Run Number 151
9.8 Commissioning Beam Time: 1.0 and 1.2 GeV . . . 153
9.9 Technical Drawings for the new FWC . . . 157
9.10 Technical Drawings for the new FVH . . . 163

Bibliography **171**

1 *Introduction*

I'll tell you about the magic,
and it'll free your soul
But it's like trying to tell a stranger
'bout rock and roll

Do You Believe in Magic,
The Lovin' Spoonful [Seb65]

Currently the standard model of particle physics is the best way to describe the fundamental particles and their interactions. It is based on three fundamental interactions: the electromagnetic, the weak and the strong force. They are mediated between the basic constituents of matter, quarks and leptons, via gauge bosons. The electromagnetic force is carried by the photon, the weak force by Z^0 and $W^{\pm}$ bosons. These two interactions are unified in the electroweak interaction, described by the Glashow-Weinberg-Salam theory. The strong interaction is described by Quantum-Chromo-Dynamics (QCD), the corresponding mediator is the gluon.

The standard model describes many phenomena in particle physics amazingly well, predicted several particles which were actually found later, and many features could be verified by experiments. However the understanding of one puzzle only opens the view on the next one. Such things as neutrino masses, dark matter, dark energy and the simple fact that humans are alive and not annihilated with all that antimatter at the very beginning of the universe are still a kind of magic.

But even in the energy regime where the standard model is valid, nature left some challenges. At very high energies, above roughly 10 GeV center of mass energy, where quarks and gluons rather than nucleons are the ruling particles, the standard model describes nature amazingly well. Also at low energies, where the inner structure of the nucleons is not resolved, the world can be described reasonably. But in between, where more and more particles join the game and are needed to describe what's going on, where the strong coupling constant rises higher and higher, hindering a usual perturbative approach, nature appears still too complicated to calculate it. With effective theories like the Chiral Perturbation Theory (χPT) or new computation ideas like in the Lattice QCD, physicists have tried to understand nature, but often models are needed to at least get a glimpse of nature, which is maybe biased by the model inputs.

But whatever theory or model says, experimental data are needed to verify or falsify it. There are still many fields where the amount of experimental data is not sufficient to check the corresponding theories or models. And often it happens that somebody looks in more detail into a field which physicists think they understand, and it turns out that they actually do not. That way also the ABC effect was pulled back in the realm of mystery.

1.1 History of the ABC Effect

The story of the ABC effect started already 50 years ago with a 1960 paper of Alexander Abashian, Norman E. Booth and Kenneth M. Crowe [ABC60], whose initials later gave the reason for the name ABC effect. They performed an experiment with a single arm magnetic spectrometer in Berkeley with a proton beam and a deuteron gas target, looking at the reaction $pd \to {}^3\mathrm{He}X$. They measured at four beam energies (624 MeV, 648 MeV, 695 MeV and 743 MeV) at a single polar angle of 11.7°. That way they could reconstruct the mass of the system X only by measuring the momentum of the ^{3}He.
The resulting invariant mass spectrum of the system X exhibited just at the 2 pion threshold an unexpected enhancement. In all four energies the effect occurred at roughly the same position. Figure 1.1 shows the result for one energy. Three years

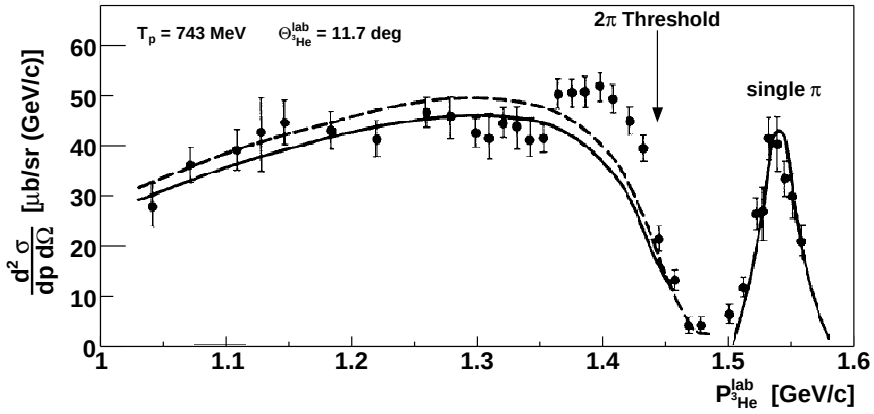

Figure 1.1: *Experimental result of the first publication about the ABC effect in the reaction $pd \to {}^3\mathrm{He}X$ [ABC60] . The solid and dashed lines correspond to phase space with different normalizations, the strong peak at the right is single pion production. The enhancement with respect to phase space around 1.4 GeV/c is the so called ABC effect.*

later a paper of the same authors was published, giving the result for one more energy, which showed qualitatively the same behavior.
In the following years, several other groups performed similar experiments:

Birmingham 1969 [Hal69] $pd \to d(p_{spec}) + X$

Saclay 1970 [Ban71] $dp \to d(p_{spec}) + X$ and $dp \to {}^3\mathrm{He} + X$

Saclay 1973 [Ban73] $dp \to {}^3\mathrm{He}X$ with X being electrically neutral

Saclay 1978 [Plo78] $np \to d + X$ with X being electrically neutral

Saclay 1976 [Ban76] $dd \to {}^4\mathrm{He} + X$ with X being electrically neutral

All these experiments measured the reaction in the same energy range, 150-400 MeV above the $\pi\pi$ threshold. They are all single-arm measurements detecting only the heavy recoil particle and reconstructing the invariant mass of system X via the missing mass of the heavy particle. Hence there was no way to distinguish between different channels like $\pi^+\pi^-$ and $\pi^0\pi^0$, 3π contributions or even other particles like the η meson.
In conclusion of all these experiments an enhancement at the $\pi\pi$ threshold is observed if the system X is electrically neutral and isoscalar and if the nucleons in the outgoing channel are fused. This enhancement was named the ABC effect. It appears in the $\pi\pi$ invariant mass spectrum as a bump at low invariant masses, starting just at threshold.

In the first ABC paper [ABC60], the authors proposed a strong $\pi\pi$ interaction or a new meson state as an explanation of the effect. But the deduced s-wave $\pi\pi$ scattering length of $a_s = 2.4$ fm was an order of magnitude larger than the results from other, non-fusion reactions. In the seventies the idea was born that the two participating nucleons of the basic reaction $pn \to \pi\pi$ are excited into their first excited state, the Δ resonance. The Δ resonance preferably decays into $N\pi$, the pions are emitted and the nucleons fuse to the deuteron. The Feynman diagram for this process is depicted in Fig.1.2.

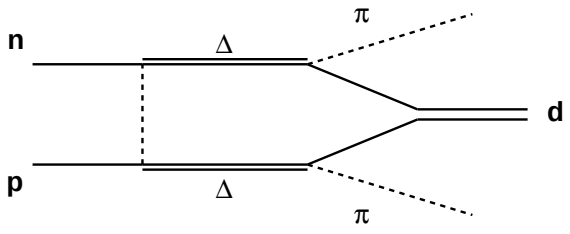

Figure 1.2: *Feynman diagram of the t-channel $\Delta\Delta$ model for the basic ABC reaction $pn \to d\pi\pi$.*

The energy range in which the ABC effect shows up just fits the energy of two Δ, and since in a three body system resonances in two subsystems (the two $d\pi$ systems) may be reflected in the other subsystem (the $\pi\pi$ system) as resonance-like structures[1], the double Δ idea might explain the experimental results.
Risser and Shuster calculated in 1973 [RS73] that in case of a bound nuclear system in the final state, the excitation of two Δ leads to two preferred configurations: either the pions fly in the same direction (low relative momentum of the two Δ) or back-to-back (high relative momentum). This would lead to an enhancement of low invariant masses in the parallel kinematics and high invariant masses in the

[1] In a three body system the invariant masses of the subsystems are constrained by $M_{12}^2 + M_{13}^2 + M_{23}^2 = const \propto S$.

back-to-back kinematics, as indeed observed in the Saclay experiments [Plo78]. At energies $\sqrt{s}$ below the $\Delta\Delta$ mass, the low-mass peak should be preferred, above the high-mass peak, and if $\sqrt{s} \approx 2M_\Delta$ both peaks should be equal.
Translated into the momentum of the heavy particle, one would see three bumps. The middle one corresponds to high invariant $\pi\pi$ masses, the two outer ones to low $\pi\pi$ masses with the heavy particle flying forward in the center of mass system (large momentum) or backward (small momentum). This behavior is seen in figure 1.3 which shows the experimental results for the momentum of the deuteron in the reaction $np \to d+X$ compared to $\Delta\Delta$ calculations. On top of the figure the scale for the missing mass of the deuteron (equivalent to the invariant mass of the two pions) is plotted. Note the nonlinear scale where left and right side appear compressed and the middle part with the high $\pi\pi$ masses stretched. The calculations describe the

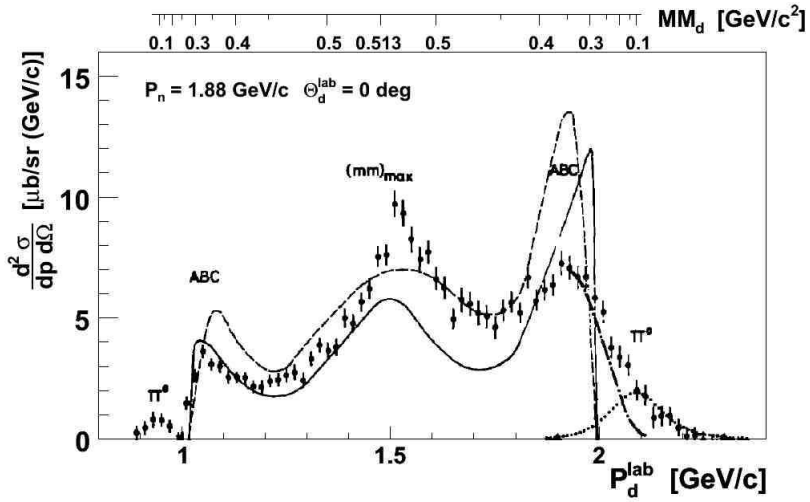

Figure 1.3: *Experimental result for the reaction $np \to dX$ (dots) compared to two different calculations of the t-channel $\Delta\Delta$ model [Plo78]. Displayed is the laboratory momentum of the deuteron. The translation to the missing mass of the deuteron is shown on top. Note the nonlinearity of the scale. Expressed in terms of the missing mass the two outer bumps would merge to one bump at low missing masses, while the middle one corresponds to high missing masses.*

data on a qualitative level, but the experiments performed were inclusive[2] ones, the production of $\pi\pi$ just an assumption on the basis of the missing mass of the heavy particle. In 1990 [PFW90] warned that also other particles might contaminate the spectrum, and that the bump at high invariant masses, the middle bump in the momentum spectrum respectively, could originate from 3π or η production. Two exclusive measurements were performed in 1999 and 2000 ([And00], [Bel99]), but

[2]Inclusive experiments measure only one of the outgoing particles, thus all possible channels, like eg. ^{4}He$\pi^0\pi^0$, ^{4}He$\pi^+\pi^-$, ^{4}He$\pi^+\pi^-\pi^0$ (^{4}He$\pi^+\pi^-\pi^0$ is forbidden due to isospin conservation) and ^{4}Heη, are included in the data and might be separated by the missing mass of the measured particle. In exclusive experiments at least as many ejectiles are measured as necessary to be kinematically complete.

the corresponding energies were below the ABC region, and in case of [And00] the statistics is low.
In that situation the CELSIUS-WASA collaboration at Uppsala started to measure the ABC effect for the first time in kinematically complete, exclusive measurements with high statistics. In March 2005 measurements on the fusion to ^{3}He in both the $\pi^0\pi^0$ and the $\pi^+\pi^-$ channel were performed ([Bas06]). And indeed the result was rather unexpected: The enhancement occurs only at low $\pi\pi$ masses, not at higher ones. Obviously the high-mass bump is not produced by $\pi\pi$ production as assumed in the last 40 years.
In 2004-2005 the basic ABC reaction was investigated, the fusion to deuteron, in the quasi-free reaction $pn(p_{spec}) \rightarrow d(p_{spec}) + \pi\pi$ ([Kha09]). Similarly a bump at low invariant masses and no bump at high invariant masses were seen. Furthermore the energy dependence of the total cross section was measured. Also here the result was very surprising: just in between already existing total cross section data for $pn \rightarrow d + \pi^+\pi^-$ [Abd80, Bar73], which can be related to $pn \rightarrow d + \pi^+\pi^-$ via isospin relations, a narrow peak appeared. After WASA moved to COSY the same reaction was measured in January 2008 with much higher statistics at five energies [Basc] and the same peak was seen, even more clearly with the better data (Fig. 1.4).

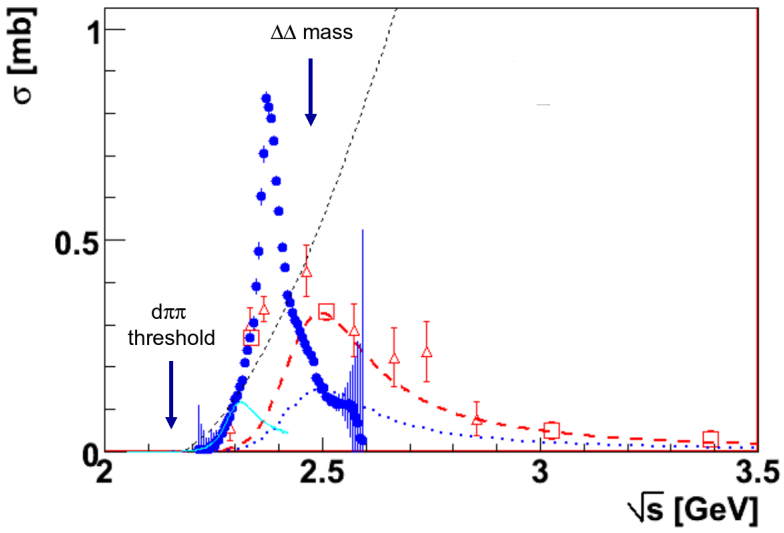

Figure 1.4: *Experimental result of the exclusive measurements of $pn(p_{spec}) \rightarrow d(p_{spec}) + \pi^0\pi^0$ with WASA-at-COSY [Basc]. Blue dots are data, red and blue lines indicate the contribution from the conventional $\Delta\Delta$ process, the black dashed line shows the energy dependence of the 3-body phase space. The red open symbols represent data for $pn \rightarrow d + \pi^+\pi^-$ [Abd80, Bar73]. Picture from M.Bashkanov [Basa]*

None of the currently accepted models can explain this behavior. In [Bas06] the idea was born that the two Δ resonances may be attracting each other, might even be bound together. That would suppress configurations where the relative momentum between both Δ is large, which corresponds to the high $\pi\pi$ masses, being exactly what is seen in the exclusive measurements. The resonance-like structure in the total

cross section of the *pn* data further supports the idea of a $\Delta\Delta$ bound state. If true, this could possibly be the first solid evidence for a dibaryonic resonance - a true 6-quark state in contrast to a molecule-like object such as the deuteron.
This so-called ABC-resonance model needs further profound theoretical and experimental investigations. Currently several groups are working on the interpretation of the available data, calculating different models. Recently the ANKE collaboration also measured some ABC-channels. Their analyses are not yet finalized, but the current status is very similar to the previous results by WASA: In $pd \to pd\pi\pi$ the invariant mass spectrum of the system $d\pi\pi$, which is equivalent to the total cross section of the fusion to $d\pi\pi$, shows the same resonance-like structure as in the direct measurements of $pn \to d\pi\pi$ [Aza10]. In the fusion to ^{3}He the invariant mass of the pions shows the same strong peak at low invariant masses, but no peak at high masses [Mie]. The ANKE results fit well to the ABC-resonance model, but of course also other explanations are investigated.
As usual more data are needed, especially in different channels. If the ABC-effect is due to a $\Delta\Delta$ resonance, it should show the same features in all channels. The fusion to d and ^{3}He was measured exclusively[3], still to be investigated is the fusion to ^{4}He, which is actually very well suited for the investigation of the ABC effect, because this occurs only if the $\pi\pi$-system is isoscalar, which is the only allowed channel in case of dd $\to {}^4\mathrm{He}\pi^0\pi^0$ due to isospin conservation. This reaction was also measured exclusively at CELSIUS-WASA in the very last experiment at CELSIUS before it was closed [Kel08]. Here also a strong peak at low invariant $\pi\pi$ masses was seen. But only at a single energy in the ABC regime (100 to 400 MeV above the $\pi\pi$ threshold) a total cross section was measured. Thus the energy dependence of the total cross section, which is especially interesting in the realm of the ABC-resonance idea, was still not known.
Therefore, at WASA-at-COSY the fusion to ^{4}He was measured exclusively at nine energies, all with sufficiently high statistics. The analysis and results of these measurements are presented in this thesis.

[3]The fusion to ^{3}He was measured only at one energy, hence also here more data are needed to learn about the energy dependence. These data are on the way and will be the topic of the PhD thesis of E.Perez del Rio.

2 *Experimental Setup: WASA-at-COSY*

You are so beautiful
To me ...

You Are So Beautiful, Joe Cocker
[FP74]

The **W**ide **A**ngle **S**hower **A**pparatus (WASA) is a detector designed to study the production and decay of light mesons in hadronic interactions. It can measure the neutral and the charged decay products and the recoil particles as well. A pellet target system was developed to provide a high target thickness and high luminosities. The data analyzed in this work were measured with the WASA detector [Ada04] at the COSY storage ring of the Forschungszentrum Jülich. But the first home and birthplace of the WASA detector was the CELSIUS storage ring in the Theodor Svedberg Laboratory in Uppsala, Sweden [Bar08]. When CELSIUS was shut down in 2005 WASA was moved to Jülich and installed at COSY. Since COSY can provide substantially higher beam energies than CELSIUS (up to 2.9 GeV for protons compared to 1.45 GeV), larger luminosities and a polarized beam, new experiments are possible [Ada04]. But the detector has to cope with the new situation. For this reason several sub-detectors were renewed and extended. Some of the extensions were part of this work and will be explained in detail in chapter 3. In this chapter the COSY accelerator and the detector components will be described briefly.
This thesis actually started with the dismantling of WASA in summer 2005. One year later, all components had arrived in Jülich and the installation at COSY took place. In August 2006 the detector was successfully commissioned at COSY and in April 2007 the first beam time aiming for new experimental results was performed.

2.1 The COSY Storage Ring

The **CO**oler **SY**nchrotron COSY is a storage ring with 184 m circumference, situated in and maintained by the Forschungszentrum Jülich. It can provide polarized and unpolarized protons and deuterons in a momentum range of 0.6 to 3.7 GeV/c [Mai97b, Mai97a]. Up to 10^{11} particles can be stored in the ring, resulting in typical luminosities of 10^{31} $\mathrm{cm}^{-2}\mathrm{s}^{-1}$ for internal experiments. In combination with the pellet target system (section 2.2) of WASA even luminosities of 10^{32} $\mathrm{cm}^{-2}\mathrm{s}^{-1}$ are feasible.
As Fig. 2.1 shows, COSY is shaped like a ring with two straight sections, which host the tools for cooling and monitoring and up to four internal experiments (one of them is WASA). The beam can also be extracted and delivered to external experiments.

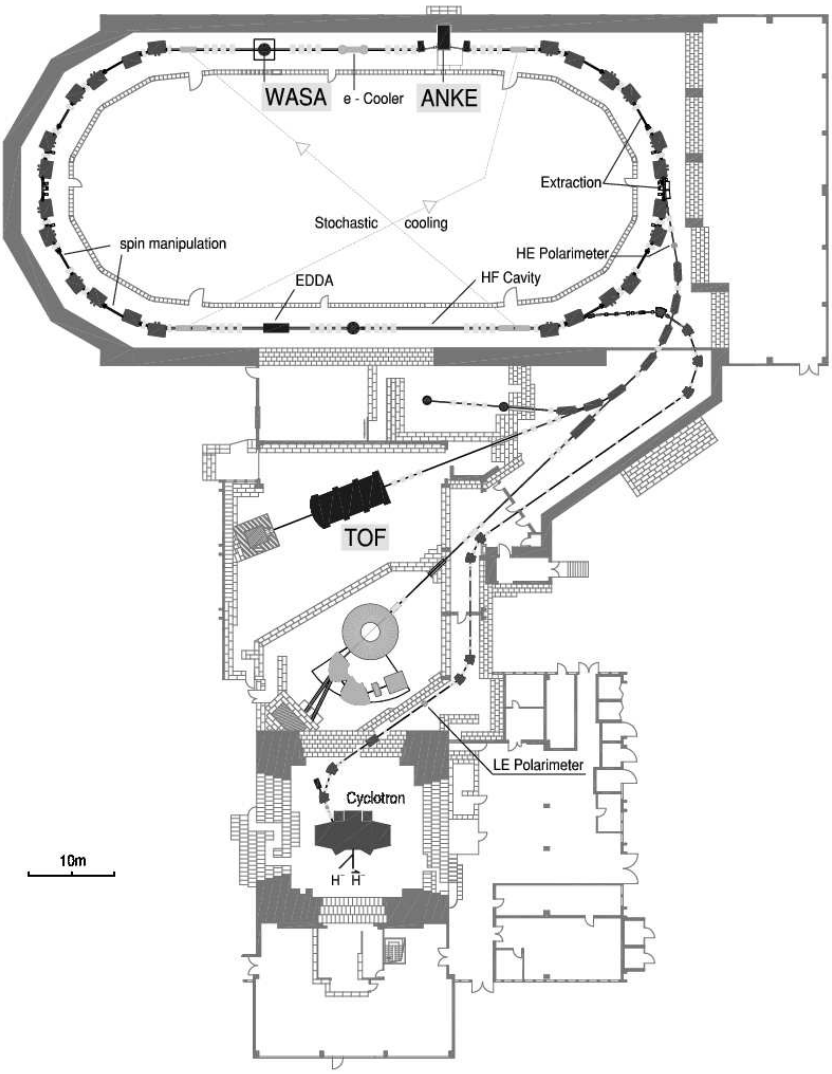

Figure 2.1: *Floor plan of the COSY ring [Mai97a].*

An isochronous cyclotron provides the protons and deuterons with an energy of up to 45 MeV. At injection energies the beam can be cooled by electron cooling and by stochastic cooling at higher energies [Pra00]. This yields a high momentum resolution of the beam of up to $\Delta p/p \approx 1 \cdot 10^{-4}$. Additionally a barrier bucket can be used to compensate for the mean energy loss due to beam target interactions [Geb09] (this had not yet been installed during the measurements described in this work). Typically the beam lifetime is in the order of a few minutes. In measurements without target lifetimes of the beam of more than 1 hour have been achieved.

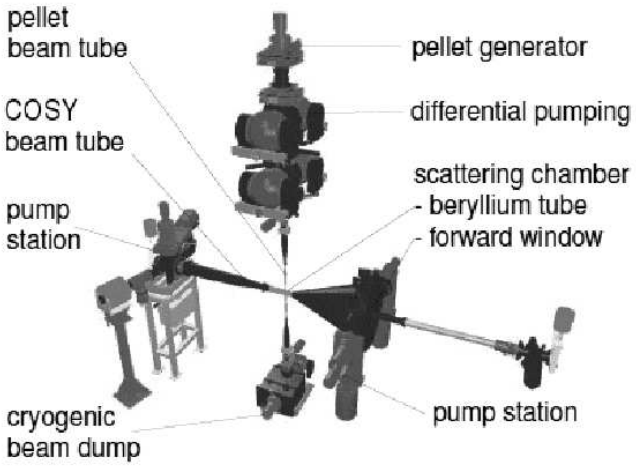

Figure 2.2: *Sketch of the WASA PTS [Tro95].*

2.2 The Pellet Target System PTS

The requirements for the physics program at WASA made the development of a pellet target necessary. It should have a very high density (10^{15} atoms/ cm^2), but still allow beam lifetimes in the order of a few minutes. The detector should cover a solid angle of almost 4π and contain a target without walls to hold the target. A pellet target can fulfill all these requirements.
The pellets are produced from hydrogen or deuterium gas[1] which is liquefied and pressed through a glass nozzle that vibrates and breaks the stream into equidistant droplets of equal size. In the droplet chamber the droplets freeze by evaporation to solid globes with a diameter of roughly 20-35 μm. Accelerated by a carrier gas to velocities of up to 100 m/s the pellets fall through the beam pipe with a frequency of several kHz (in 2008 the standard frequency for protons was 8 kHz, for deuterons 20 kHz [Ber08]).
To collimate the pellet beam, the pellets pass the skimmer, a 2 m long tube with 7 mm diameter. At the interaction point the pellet beam has a diameter of 2 - 4 mm. After passing through the beam, the pellets are collected in the pellet dump to prevent them from bouncing back in the beam pipe.
More information about the pellet target and its performance can be found in [Tro95, Ber08]

2.3 The WASA Detector

The WASA 4π detector system is divided into two main parts. The forward detector is designed to measure the charged, and to some extent the neutral emitted particles.

[1] In principle other target materials like nitrogen, argon, methane, alcohol, or water are also possible.

Pellet size	$\approx 35\,\mu$m
Pellet frequency	5-20 kHz
Pellet velocity	60-100 m/s
Pellet stream diameter	2-4 mm
Effective target thickness	$> 10^{15}$ atoms/ cm^2

Table 2.1: *Performance of the PTS*

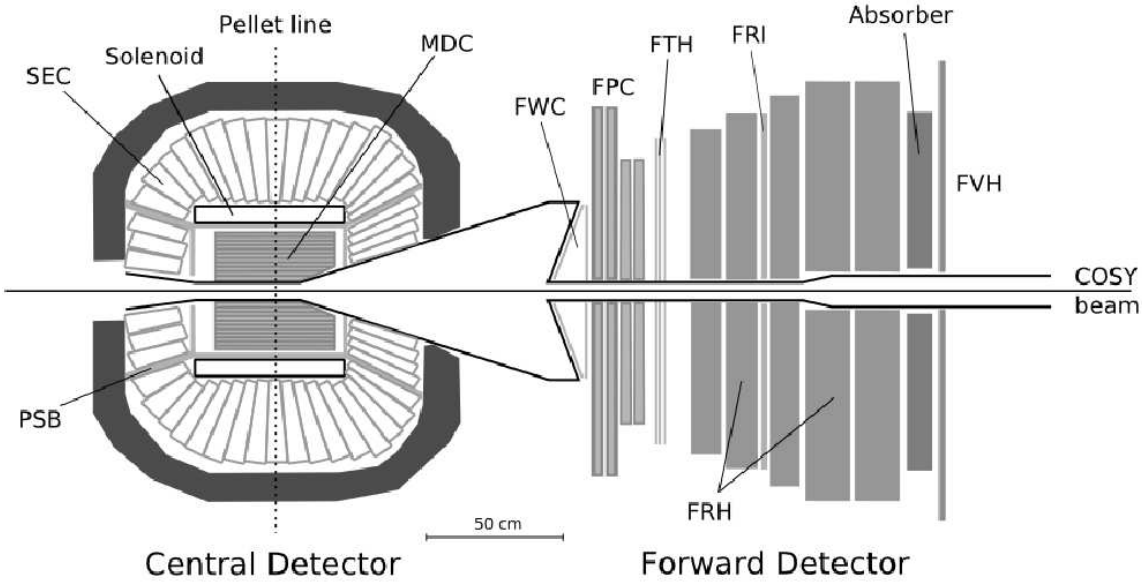

Figure 2.3: *Schematic view of the WASA detector [Red10]*

The central detector is well suited for the detection of charged and neutral mesons and their decay products. It incorporates a magnetic field and a drift chamber to follow very accurately the path of the particles to reconstruct their charge and momentum. Figure 2.3 shows a sketch of the whole WASA detector. In the following the detector components will be described.

2.3.1 Coordinate System

In the WASA frame the origin of the coordinate system is set to the interaction point and the Z-axis points along the beam axis. The X- axis points horizontally to the outside of the COSY ring, the Y-axis vertically upwards[2]. The polar angle θ is

[2]The detector elements of the forward circular detectors are usually numbered clockwise so that element 1 corresponds to y=0. That means the numbering is started with the horizontal elements at the outside of the COSY tunnel.

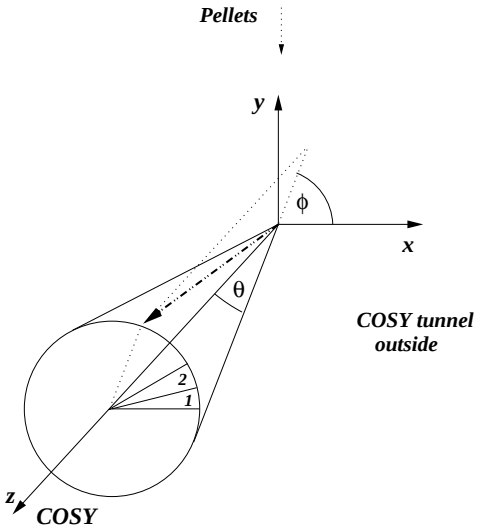

Figure 2.4: *Sketch of the WASA coordinate system*

measured from the Z-axis and the azimuthal angle ϕ is measured in the XY plane, starting from the X axis.

2.3.2 The Forward Detector

The Forward Detector covers a polar angular range of 3 to 18°, limited by the beam pipe and the vacuum chamber exit window. It is designed for precise reconstruction of the energy and the angles of charged particles. It consists of several layers of plastic scintillator, thin ones for the trigger system and the track reconstruction, and thick ones for the energy reconstruction. A proportional chamber provides good angular resolution.

Forward Window Counter FWC

The FWC is the very first detector just behind the vacuum chamber exit window. It is built out of two layers of thin plastic scintillator. The first layer is conical, the elements are tilted with respect to the vertical plane by 20°. The second layer is planar, see Fig. 2.5a.
This detector is very important for the first level trigger, especially for the detection of helium nuclei, and it is used for the particle identification in case the particle stops in front of the second FRH layer.
A part of this work was the design, manufacturing and installation of this detector, hence a detailed description can be found in chapter 3.1.

Forward Proportional Chamber FPC

The FPC [Cal96] is a straw tube tracker used for precise reconstruction of the track coordinates. It consists of four modules, each made of four planes with 122 straws.

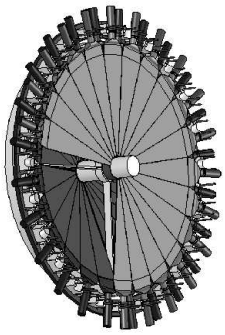

(a) *Forward Window Counter FWC.*

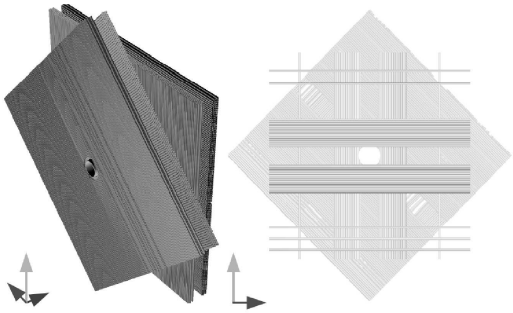

(b) *Forward Proportional Chamber FPC*

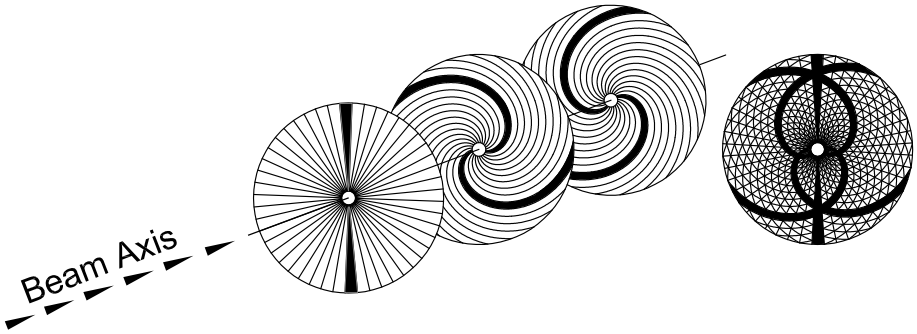

(c) *Forward Trigger Hodoscope FTH*

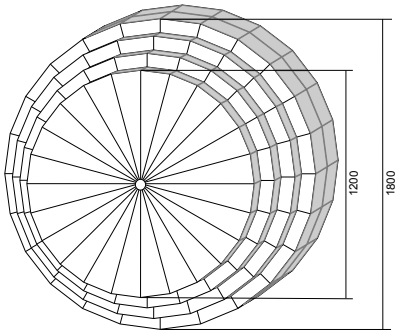

(d) *Sketch of Forward Range Hodoscope FRH, dimensions in mm*

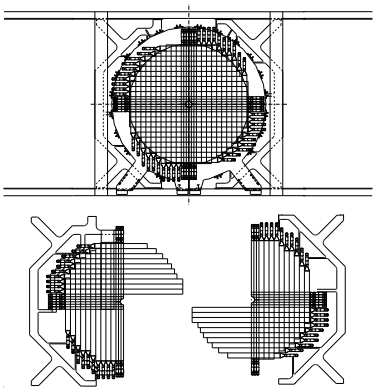

(e) *Forward Range Intermediate Hodoscope FRI*

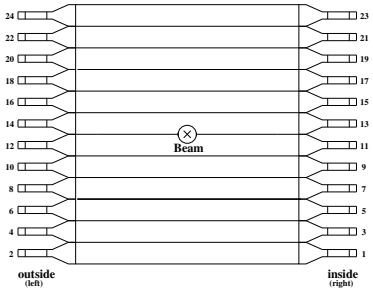

(f) *Old Forward Veto Hodoscope FVH*

Figure 2.5: *The sub-detectors of the WASA forward detector [Ada04]*

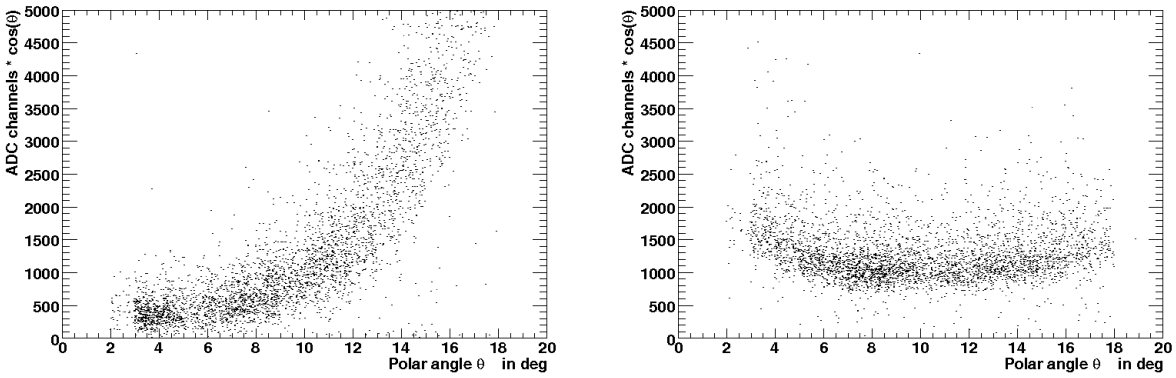

(a) *Nonuniformity of the old detector (2007)* **(b)** *Nonuniformity of the new detector (2008)*

Figure 2.6: *Light output as a function of the position (small θ angles correspond to positions far away from the PMT, large θ angles are close to the the PMT) for element 11 of layer 2 before and after renewal [Red10].*

The planes are shifted by a straw radius with respect to each other, so that there is no gap left. The straws are cylindrical drift tubes made of 26 μm thick aluminized mylar and a central sensing wire of 20 μm stainless steel stretched with a tension of 40 g. The drift gas is a mixture of 80% argon and 20% ethane.

The four modules are oriented in different directions as shown in Fig. 2.5b: going in the beam direction, the first and second modules are rotated by $+45°$ and $-45°$ with respect to the X-axis, while the third and fourth modules are aligned along X and Y. Figure 2.5b shows a front and side view of the detector.

Forward Trigger Hodoscope FTH

The next detector in the row is the FTH [Dah94], positioned 1.5 m away from the interaction point. It consists of three 5 mm thick plastic scintillator layers. The first layer in the beam direction has 48 elements shaped like cake pieces, the second and the third have 24 elements shaped like Archimedian spirals (see Fig. 2.5c). That way the polar and the azimuthal scattering angle can be measured with a constant angular resolution over the full area.

This detector is crucial for the offline track reconstruction, since a track is defined by having a pixel (hits in at least two layers) in the FTH. Because of the complicated shape of the spirals the light output is very nonuniform and the calibration is very complicated. This effect is even stronger due to aging effects in the detector material. For this reason the detector was rebuilt in summer 2008 with new material. Figure 2.6 shows the nonuniformity for one element of the second layer before and after the installation of the new detector. Unfortunately this update came after the data analyzed in this work were taken.

Forward Range Hodoscope FRH

The FRH consists of five layers of 11 cm (first three layers) and 15 cm (last two layers) thick plastic scintillator. Each layer is made of 24 elements, shaped like cake pieces which are installed in a way that they cover two elements of the first layer of the FTH. Figure 2.5d shows a sketch of the setup.

Particle	FRH1 reached	punched through FRH5
π	25 MeV	200 MeV
p	60 MeV	370 MeV
d	80 MeV	450 MeV
^{3}He	210 MeV	1000 MeV
^{4}He	250 MeV	1100 MeV

Table 2.2: *Energy range in which the particles are stopped in the FRH for various particles*

Its main purpose is the energy reconstruction. The setup with five layers offers the possibility to compare different $\Delta E_i - \Delta E_j\,, (i, j = 1 - 5)$ combinations, and allows the energy reconstruction even if the particle undergoes some nuclear interaction. The best energy resolution (roughly 3%) is achieved when the particles stop in the FRH. Table 2.2 shows the stopping power, the maximum kinetic energy at which the particle stops in the FD, for different particles. When WASA was installed at CELSIUS, only four 11 cm thick layers were used. In order to increase the stopping power to accommodate to the higher beam energies at COSY, two new, thicker layers were installed and the first old one was removed. The old second layer is now the first layer. The scintillator pieces are directly connected with optical grease to the photomultiplier tubes, without a lightguide. Because of that, the nonuniformity along ϕ is large for large θ angles. In the new setup at COSY the first (former second) layer was moved a few cm further upstream with respect to its original position at CELSIUS. That way the nonuniformity along ϕ is negligible, the first few cm of the scintillator at the photomultiplier practically work as a lightguide.

Forward Range Intermediate Hodoscope FRI

The FRI is built of two layers of 5 mm thick plastic scintillator. Each consists of 32 stripes of different lengths and widths. The two layers are rotated against each other by 90°, thus the overlap of both layers gives a X and Y position. It is situated between the second and third FRH layer. Figure 2.5e shows a sketch of this detector. More information can be found in [Pau06].
Its main purpose is the tracking of neutrons which are detected by the recoil protons they knock out in the first two FRH layers. Also the position and energy information

for charged particles is improved.
At the moment this detector is not taken into account in the track reconstruction and not used in the analysis.

Forward Veto Hodoscope FVH

The very last detector in the sequence is the FVH [Bro95]. It consists of 12 bars of 2 cm thick, 13.7 cm wide and 165 cm long plastic scintillator, which are read out on both sides (see Fig. 2.5f). It can be used for energy reconstruction of fast particles, but the main purpose is to identify particles which punched through the FRH on trigger level. Due to the double sided readout it is possible to deduce the position of the hit along the bar with an accuracy of roughly 5 cm (σ).
Because of the larger FRH at COSY, the distance to the interaction point increased compared to CELSIUS-WASA and the FVH does not cover anymore the desired angular range. Furthermore a detector far away from the interaction point with good timing became interesting for WASA because the new FWC has much better time resolution than the old one due to its simpler geometry. The combination of these two detectors can allow to use the time of flight as additional information to identify particles. This is of special interest for η' reactions where fast protons and pions fly into the forward detector.
Thus it was decided to build a new, additional layer. The design of the new detector was done in the scope of this thesis and is explained in detail in chapter 3.2.

2.3.3 The Central Detector

The central detector, surrounding the interaction point with different detector shells, is supposed to measure charged and neutral particles with good precision. The innermost part is a drift chamber (MDC) used to measure the particle tracks with high accuracy and especially their curvature due to the magnetic field, which is formed by a thin superconducting solenoid. Between the solenoid and the MDC a thin plastic scintillator (PSB) is used to discriminate between charged and neutral particles. The last sub-detector is made of 1017 crystals (SE), which measure the energy of neutral and charged particles.

Mini Drift Chamber MDC

The MDC [Jac04] is a cylindrical drift chamber consisting of 1738 drift tubes assembled in 17 layers. It covers the angular range from 24° to 159° in θ. Each tube is made of aluminized mylar, 25 μm thin, and a sensing wire of 20 μm stainless steel, stretched with a tension of 40 g. The radius of the tubes increases from 2 mm for the five innermost layers, 3 mm for the following six layers, to 4 mm for the last six layers. Nine layers are aligned along the beam axis while every second layer is skewed by an angle of $6° - 9°$ in respect to the beam axis, see Fig. 2.7b.

The MDC can measure the vertex position, polar and azimuthal angles at the vertex and the curvature of charged particles in the magnetic field, hence the sign of the charge can be deduced.

2.3.4 Plastic Scintillator Barrel PS

The PS [Jac04] is made of 8 mm thick plastic scintillator. It consists of three parts. The cylindrical central part (PSC) surrounds the superconducting solenoid. It is made of 50 bars, which are installed so that the elements overlap on each side by 6 mm with the neighboring elements. Where the pellet tube crosses the detector, the bars are cut in two halfs. For this reason 50 elements are used to form 48 ϕ sectors. The forward (PSF) and backward (PSB) parts close the barrel. Each of them is made of 48 cake piece shaped elements fitting to the 48 sectors of the PSC. The elements overlap at the edges to avoid gaps. The forward part is perpendicular to the beam axis while the backward part is conical, the elements inclined by 30°.
Lightguides are attached to the elements to transport the light to the photomultipliers outside the iron yoke. Figure 2.7d shows a sector of the PS with lightguides. In summer 2007 the elements of the central part were rebuilt because the efficiency of the old one was very low due to aging effects [Pod09].
On trigger level the PS is used for the definition of a charged particle in the central detector. Also in the offline analysis the energy deposited here is used for the identification of charged particles.

2.3.5 Superconducting Solenoid

The magnetic field is provided by the superconducting solenoid. With a thickness corresponding to 0.18 radiation lengths it can provide field strengths up to 1.3 T. It is cooled down to 4.5 K by liquid Helium. An iron yoke around the calorimeter confines the magnetic field, so that the photomultipliers for the SE and the PS are shielded from the magnetic field.

2.3.6 Scintillating Electromagnetic Calorimeter SE

The outermost part of the central detector is the SE [Koc04]. It consists of 1012 Na doped CsI crystals, which are arranged in 24 rings. They build three parts with differently sized crystals, as can be seen in Fig. 2.7e.
Each element is read out by a photomultiplier. The detector covers polar angles from 20° to 169°, corresponding to 96% of the full solid angle. Gaps are left for the pellet tube and the liquid helium supply of the solenoid.
The crystals have a length between 20 and 30 cm and correspond to $\sim$ 16 radiation lengths and $\sim$ 0.8 hadronic interaction lengths. Hence they can measure both charged particles and photons. They are used in the offline analysis for the energy reconstruction, but their response is fast enough that they can also be used on trigger level.

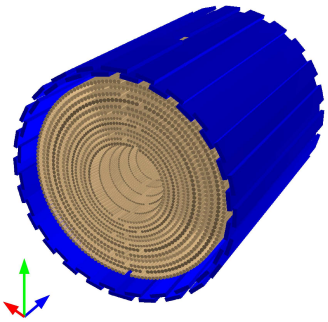

(a) *Sketch of the MDC*

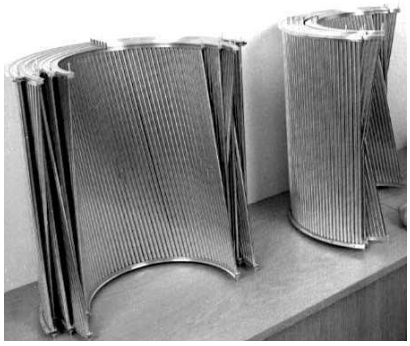

(b) *Photo of of the half-shells of the MDC*

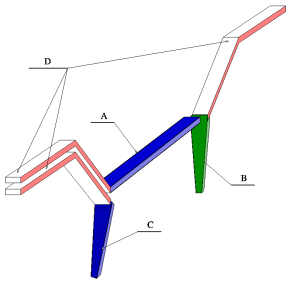

(c) *One sector of the Plastic Scintillator Barrel PS with connected lightguides*

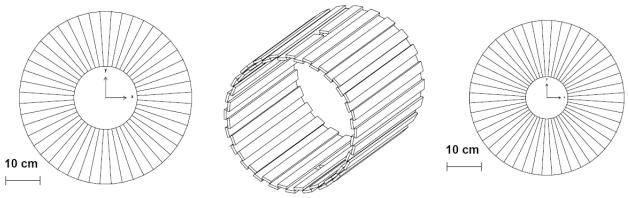

(d) *Forward (left), center (middle) and backward (right) part of the Plastic Scintillator Barrel PS*

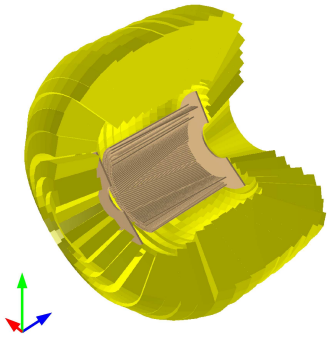

(e) *Sketch of the Scintillating Electromagnetic Calorimeter SE with a part of the MDC in the center.*

Figure 2.7: *The sub-detectors of the WASA central detector [Ada04]*

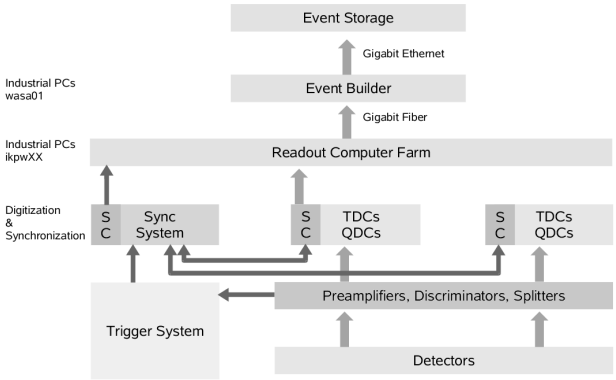

Figure 2.8: *Flowchart of the WASA DAQ System [Red10]*

2.4 Data Acquisition DAQ

The DAQ system was designed to stand the desired luminosities at WASA-at-COSY and reaches a dead-time of $\approx 20\mu s$. The limiting factor is the writing speed of the hard disc which allows $\approx 80\,\mathrm{MB/s}$. With a typical event size of 8 kB trigger rates of 10 kHz are manageable.
All signals are stored in a buffer and saved in the case that a trigger signal arrived. The synchronization is done in the ems (Experiment Message Specification) framework [Zwo94], which was developed at the Forschungszentrum Jülich and is used by several experiments at COSY.
Figure 2.8 shows a sketch of the DAQ system.

2.4.1 Signal Handling

The analog signals of the plastic scintillators are sent via a splitter box both to the Charge-To-Digital Converters (QDC) and the discriminators. If the signal reaches the threshold of the discriminator, a logical signal is sent to the Time-To-Digital Converters (TDC) and the trigger logic. In case of the new FWC actually two splitter boxes are used which feed two discriminators. That way it is possible to use high and low thresholds in the trigger at the same time .
The crystal signals are split with active splitters, which on the one hand provide the input for the QDCs and on the other hand form the analog sum of groups of crystals. In the forward part a group is built by 4×3 crystals, in the central part by 4×4 and in the backward part by 3×3 crystals. These group signals pass through dual threshold discriminators, which provide logic signals for the trigger.
The basic trigger conditions can be combined to form more complex triggers, like for example the so called matching trigger, which is the main trigger for the data analyzed in this work. It requires the alignment of hits in both FWC layers, the first FTH layer and the first FRH layer. Additional conditions like a veto in the third

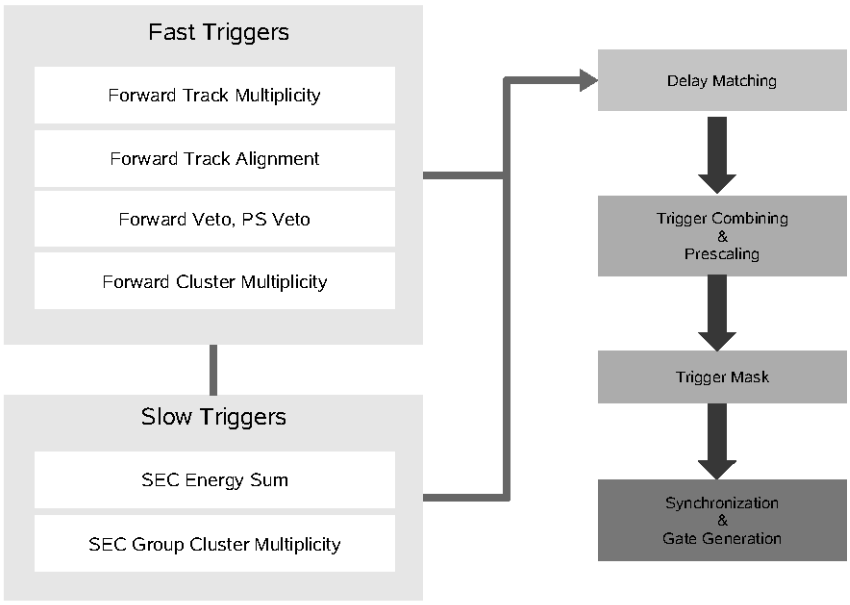

Figure 2.9: *Flowchart of the WASA Trigger System [Red10]*

FRH layer are added depending on the particular kinematics.
Figure 2.9 shows a schematic overview of the trigger system.
The detector signals are continously sampled by Flash-ADCs[3]. By FPGAs (Field Programmable Gate Arrays) not only the charge integral is extracted, but also the time by zero crossing detection. Furthermore double pulse detection and pedestal subtraction is included, and for debugging purpose the signal amplitude and the baseline can be obtained as well.

[3]Thus the QDCs actually are Flash-ADCs.

3 *Upgrade of the WASA Forward Detector*

Here comes the sun
here comes the sun, and I say
It's alright

Here comes the the Sun, The Beatles [Har69]

WASA's new host COSY has several advantages over the original accelerator CELSIUS. Apart from a smaller beam diameter and much better momentum resolution, the main advantages are the possibility for a polarized beam and a much higher beam energy [Ada04].
Consequently also the detector has to cope with the new situation. Especially the forward detector in its old design needs to be extended. The most important update was the installation of the fifth FRH layer to increase the stopping power of the FRH.
But in addition, two new detectors were installed at WASA: the old FWC was removed and a new two-layer detector was installed, and the FVH was extended by one more layer. The design, manufacturing and installation of these two detectors will be described in this chapter.

3.1 The new Forward Window Counter FWC

The FWC is the forward detector nearest to the interaction point. It is mainly used for the trigger, but also for particle identification of slow projectiles which stop early in the FRH.

3.1.1 The old FWC

The main purpose of the old detector was to get rid of particles which were scattered off the beam pipe flange. Such particles give a signal in the later layers of the FD, but no signals in the FWC, because it was placed just behind the forward scattering chamber exit window.
It was a conical layer, made of 12 elements of 5 mm thick plastic scintillator BC408 which were shaped like cake pieces. The elements were tilted with respect to the XY-plane by 18° to fit to the exit window. The readout was done with 2 inch photomultiplier tubes XP2020. Due to the installed vacuum pumps at the side, it was impossible to attach the lightguides and photomultipliers radially. All had to be placed on top or bottom of the detector. Due to a metal cross supporting the exit window, the elements were arranged in four quarters, leaving gaps for the cross.

Each quadrant had the same geometry, but the lightguides of the three elements in a quarter had very different and very complicated shapes as can be seen in Fig. 3.1. Consequently the light transportation was very different from element to element and also inside a single element. In other words, the non-uniformity was very large. More details about the old FWC can be found in [Mes99].

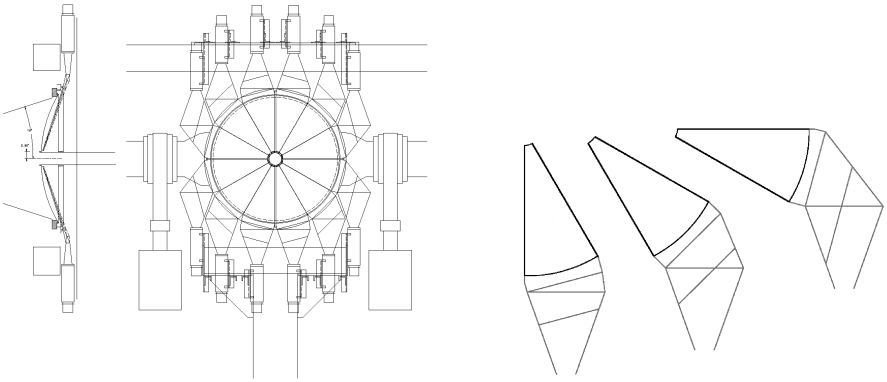

(a) *Sketch of the old FWC*

(b) *Geometry of the elements of one quarter.*

Figure 3.1: *The old FWC [Mes99].*

3.1.2 Design Considerations for the new FWC

Several reasons led to the decision to build a new FWC. The old detector was divided into only 12 elements, while the FRH has 24 and the FTH even 48 elements. Since the number of particles emitted in the forward direction is higher at higher beam energies due to the relativistic boost and higher total cross section, the multiplicity in the forward detectors increased compared to CELSIUS-WASA. Furthermore, the anticipated luminosities of $10^{32}\,\mathrm{cm}^{-2}\mathrm{s}^{-1}$ produce more background. A detector with the same granularity as the FTH would enhance the trigger efficiency, since the overlap of both detectors can be requested to reduce the amount of events originating from unphysical background. In addition, the detector can handle higher rates, since each element covers a smaller area.

Another reason was the bad uniformity of the old detector due to the complicated shape of the lightguides. A homogenous light output is important, not only for the trigger but also for the offline analysis. In case the particles stop in the first FRH layer, the energy resolution in FTH and FWC is crucial for the particle identification.

Both arguments play together: A higher granularity means a smaller element size. And that allows to use PMTs with a smaller diameter which are also shorter. With these considerations it is possible to construct the detector in a way that the PMTs are arranged radially despite the limited available space. Yet another advantage follows from this setup: the time resolution becomes much better with straight and short lightguides.

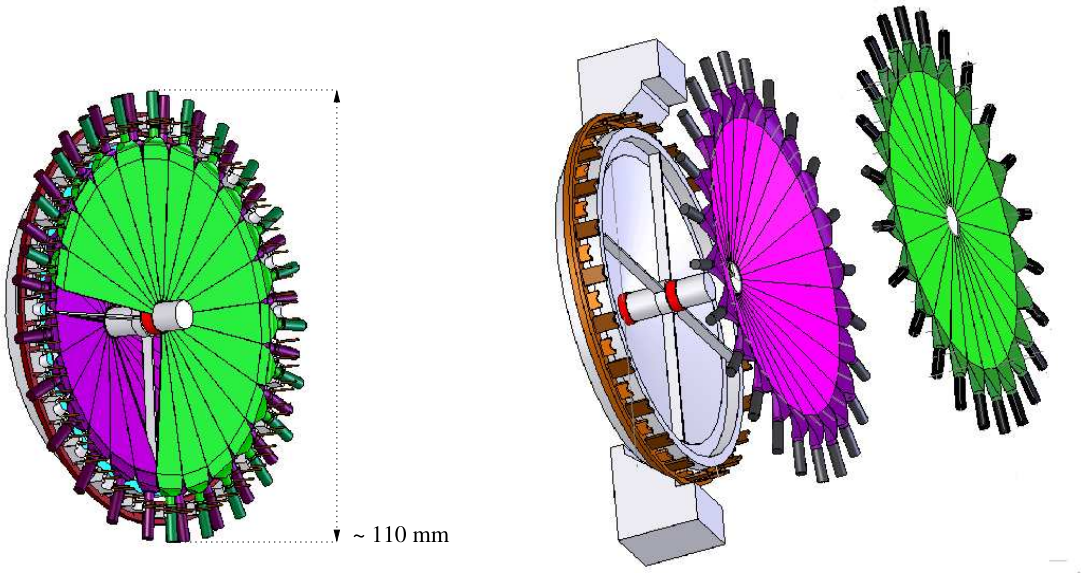

Figure 3.2: *Sketch of the new FWC. The right side shows the layers and the scattering window separated in an explosion view. The vacuum tubes and the ring of screws at the scattering window are adumbrated.*

Instead of one layer with 48 elements, two layers with 24 elements can be built, the second layer rotated by half the width of an element. The overlap of both detectors gives a granularity of 48 like the FTH. In this case the time resolution is improved even more, since the time of both layers can be combined to reduce the width of time distribution by a factor of $\sqrt{2}$. Also the gaps because of the metal cross are not necessary for the second layer, since it can be placed above it[1]. The first layer needs to be conical, tilted by 20° [2] with respect to the XY-plane to fit to the scattering window. The second layer is planar, which makes especially the lightguides easier to build. That way it is in principle possible to deduce the polar angle θ from the time difference between both layers, since the distance between them decreases with increasing θ. However, that was never tried, because for that purpose a very good time calibration would be required.

Fig. 3.2a shows a sketch of the two layers of the new FWC. One quarter of the second, upper layer is removed to make the first layer visible.

A crucial factor for the design was the very limited space available, not only at the sides, but also to the downstream front, where the next detector is located. Fig. 3.3 shows the relevant distances at the position of the new FWC. At the sides, the vacuum pumps leave only about 150 mm space measured from the end of the supporting cross. The scintillator element should cover a polar angle of 18°, which means the top resides about 15 mm before the end of the cross. Thus the space

[1]The second layer must be placed above the cross, since it is rotated by half an element, thus the cross would go right through the element.

[2]Here 20° were used, whereas the old FWC is tilted by 18°, because the geometry of the lightguides is different and this angle turned out to be best fitting to all spatial conditions.

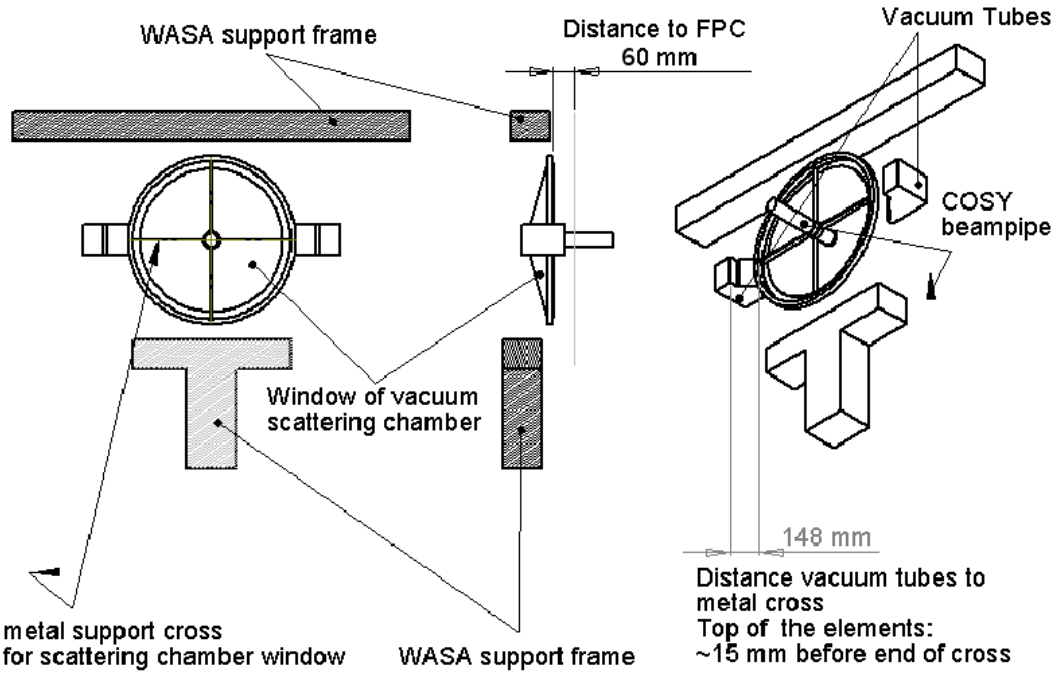

Figure 3.3: *Sketch of the constructions around the FWC. The WASA support frame is connected to the central detector and the platform above the WASA detector where the pellet target is situated. The vacuum tubes are sketched only roughly with the appropriate dimensions. The support frame does not intersect with the PMTs, but the ring where the detector is mounted finally just fits to the frame.*

available for the PMT and the lightguide is roughly 150 mm.
The front of the next detector downstream, the FPC, is situated 60 mm away from the supporting cross. Since the detector elements and the PMTs must be in front of the cross (looking towards the beam as in Fig. 3.4), only a few mm will be left between the two detectors.
For these reasons a very accurate design was necessary, making sure that the detector does not extend into the FPC or the pumps, still leaving enough tolerance to accommodate for the inaccuracies during the installation itself.
The detector should be as thin as possible, since even slow particles should not stop here, but in the later detectors designed for the energy reconstruction. On the other hand a thinner material also means less light output, thus a poorer energy resolution and a higher probability that the signal is as low as the noise. It was decided to use a thickness of 3 mm as the best compromise. With 6.2 mm effective thickness it is not much thicker than the old FWC with 5.3 mm.

3.1.3 Scintillator

Plastic scintillators are commonly used for particle detection. They consist of a solution of scintillating molecules in a polymerized solvent and can easily be fabricated

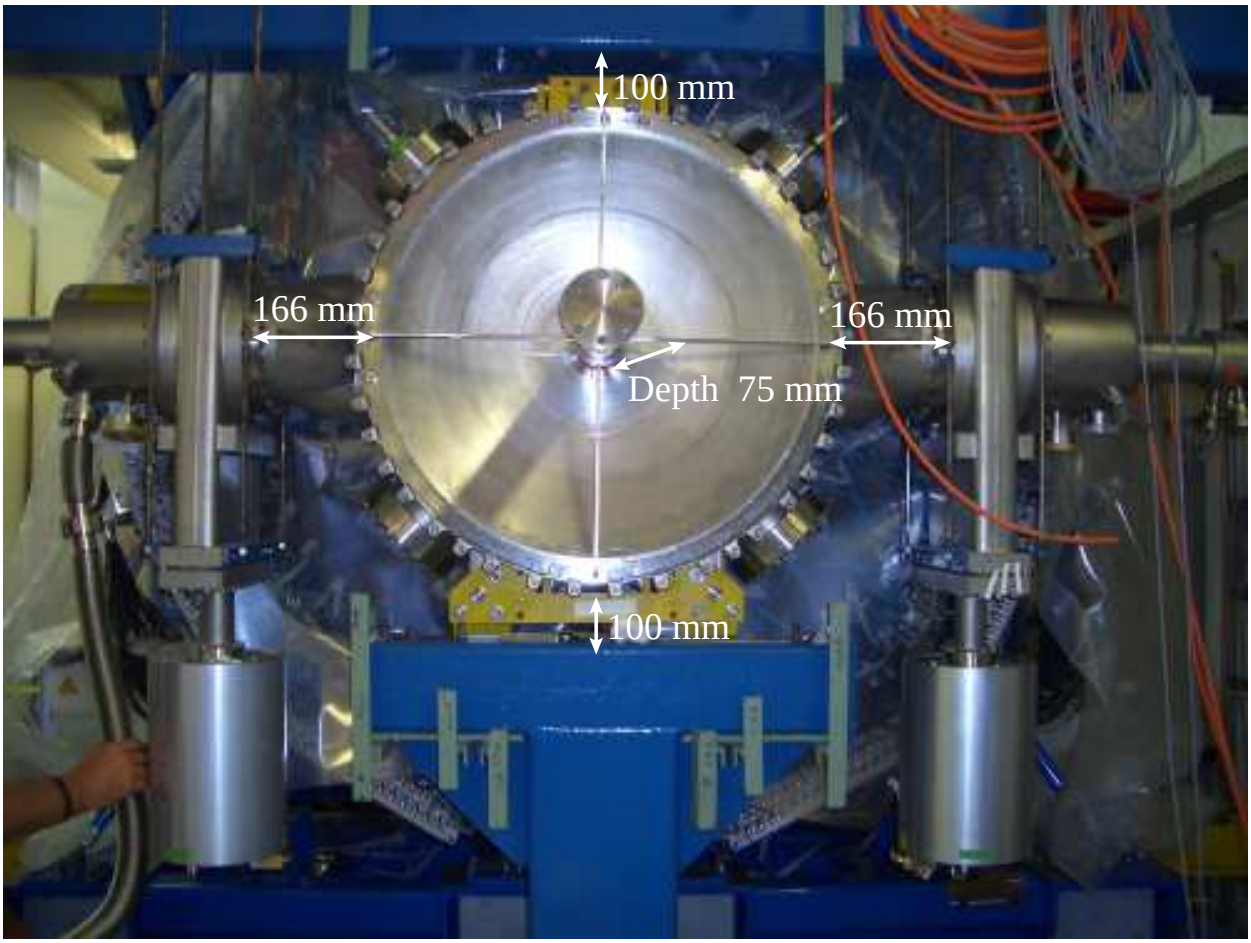

Figure 3.4: *Photo of the place where the FWC was installed later on.*

and machined to any desired shape. Ionizing particles produce a flash of light by excitation of atoms or molecules. A photomultiplier (or any other photon detector) attached to the scintillator converts the light into electronic signals. The decay time of plastic scintillators is relatively short (in the order of ns), which also makes them a suitable material for time measurements.

For the new FWC 3 mm thick BC408 from Bicron/Saint Gerbain was used. With a roughly 2.5 ns FWHM pulse width it has good timing properties and a long attenuation length of 210 cm. Fig. 3.5a shows the emission spectrum of the material and table 3.1 summarizes its properties [BIC].

The material was ordered in rectangular pieces and cut in the Tübingen workshop to the desired shape. The edges were polished with dry Micro Mesh MM polishing paper with granularities from 4000 particles/ cm^2 to 12000 particles/ cm^2. The elements are roughly 350 mm long and 100 mm wide. For the 8 elements in the conical layer which neighbor the metal cross, a 2.6 mm wide strip was cut parallel to the long leg of the triangle. The exact dimensions can be found in the Appendix 9.9.

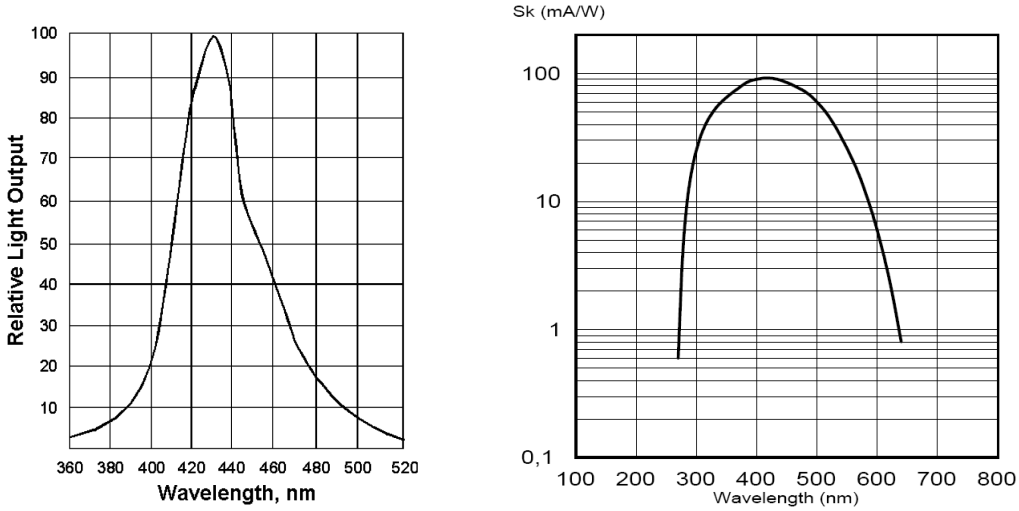

(a) *Plastic scintillator BC408 emission spectrum.*

(b) *PMT XP3112 absorption spectrum.*

Figure 3.5: *Emission spectra of the scintillator and the photomultiplier used for the FWC.[BIC, Phoa]*

Refractive Index	1.58
Light Output [% Anthracene]	68
Rise Time [ns]	0.7
Decay Time [ns]	1.8
Pulse Width, FWHM [ns]	2.2
Bulk Light Attenuation Length [cm]	380
Wavelength of Max. Emission [nm]	425

Table 3.1: *Properties of BC408 scintillator material [BIC]*

3.1.4 Photomultipliers

The light emitted by the scintillator is detected and converted to electrical signals by photomultipliers (PMTs). The incident photons hit the photocathode and produce electrons via the photo effect. The electrons are accelerated in an electric field to hit an electrode (so-called dynode) where each of them produces several secondary electrons. These electrons are accelerated to the next dynode, produce again secondary electrons and so on until they finally reach the anode and form an electric pulse.
The typical potential between two dynodes is in the order of 100 V. The voltage is supplied by voltage dividers, the PM bases, which consist of a chain of resistors to provide the desired voltages for each dynode.
To detect all of the produced light, the active area of the photomultipliers should be the same as or larger than the light output area of the scintillator. Both layers are

Refractive Index at 420 nm	1.48
Window material	Borosilicate glass
Photocathode	Bi-alkali
Active area (diameter)	21 mm
Multiplier structure	Circular cage
Spectral range	270-650 nm
Maximum sensitivity	420 nm
Gain slope (vs. supp. Volt, log/log)	6.8
Continuous anode current	0.2 mA
For a supply voltage of 1100 V:	
Linearity (2%) of anode current up to	30 mA
Gain	$2 \cdot 10^6$
Rise time	2 ns
Duration at half height	3.1 ns
Transit time	19 ns
Supply voltage	anode grounded (cathode at -HV)
typical	1000 V
maximal	1600 V

Table 3.2: *Properties of the PM assembly XP3112PB [Phoa]*

roughly 100 mm wide at the top and 3 mm thick, thus the output area is 300 mm^2, which can be covered by a 1 inch PMT (314 mm^2 for the XP3112).

Due to the limited space, the main request on the PMTs is their size. The used PMT XP1312 from Photonis has a length of 43.5 mm for the PMT itself and 78.5 mm for the whole assembly of the PMT and the base (VD1A1T/A) [3]. The base and the PMT are directly connected to each other to reduce the length of the setup by 5 mm compared to the version where both parts are separable. Fig. 3.6 shows a sketch of the PMT.

A mu-metal foil is glued around the assembly to protect the dynodes from magnetic fields. Since the magnetic field at the position of the FWC is low, this thin foil is sufficient.

Fig. 3.5b shows the sensitivity spectrum of the PMT, next to the emission spectrum of the scintillator. Table 3.2 summarizes the specifications of the photomultiplier.

[3] As a comparison: The widely used 2 inch PMT XP2020 has a total length of 300 mm with the base connected. The 1 inch PMT R3998-02 and XP2822 come to 60 mm without the base, which adds up another $\sim$ 40 mm.

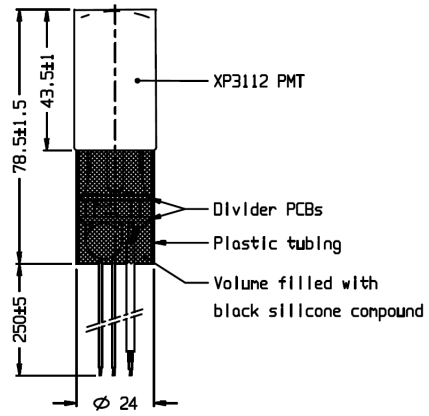

Figure 3.6: *Sketch of the PMT used for the FWC, the XP3112PB from Photonis [Phoa]*

3.1.5 Lightguides

Lightguides are used to transport the light from the rectangular output area of the scintillator to the circular active area of the PMT. The main requirements are an optimal light collection and a uniform response of the scintillator.

According to Liouville's theorem [Mar71] the cross section area should not become smaller on the way, otherwise light is lost: because of the incompressibility of light not more than the ratio $\frac{A_i}{A_o}$ of the incoming area A_i and the outgoing area A_o can be transported, even with perfect optical properties. In an adiabatic lightguide these conditions are met and the cross section area does not change over its length.

The vacuum tubes at the side are situated 166 mm away from the end of the scattering window (see Fig. 3.3) where also the top of the scintillator elements is placed. Hence the total length of PMT and lightguide must not exceed 160 mm to have enough space for the cables. With the PMT being 78 mm long, 80 mm are left for the lightguides. Over this length the cross section change from a 3×100 mm^2 rectangle to a circle with 20 mm diameter must be performed.

A common shape is the so called fish-tail as sketched in Fig. 3.7. This shape works well, if the changes of the cross section shape are slow ($\alpha \leq 24°$) and a parallel section of 10 to 20 mm at the connection to the scintillator is included [Tho83]. In case of such a short lightguide as necessary here, the light losses are quite large, even if the lightguide is adiabatic.

A so-called twisted lightguide is made of several strips of constant cross section which fit to the (usually rectangular) area at the scintillator and are bent separately to be combined on the PMT side to the desired (usually circular) shape. Many different geometries are possible, but the machinery is lengthy and complicated. However, both the uniformity of the scintillator response and the light transmission is much better than in case of a fishtail lightguide.

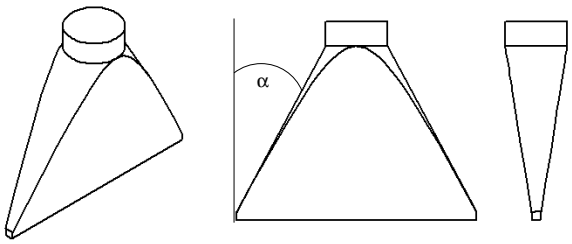

Figure 3.7: *Example sketch of a fishtail lightguide*

Comparison of different Lightguide Designs: Simulations

In order to decide about the lightguide design and understand the properties of different setups, the ray tracing simulation program GUIDEIT was used [Sim93]. Fishtail designs with different lengths were compared to each other in terms of light output and uniformity. Due to the limitations of the supported surfaces only an approximate simulation for the later used twisted lightguide design was possible: instead of seven strips with different widths three strips with the same width were used. Additionally in the simulation the middle strip is just straight, the two outer strips bent to overlap with the middle strip, whereas in reality all strips were bent to perform a turn by 90° and then deformed to overlap.
But already in the approximation the improvements against the simpler fishtail design are obvious. Fig. 3.8 shows the simulated light output as a function of the light source position in the detector element for a fishtail lightguide (left) and the approximated twisted lightguide (right). Here the quantum efficiency of the PMT is not taken into account. Not only the amount of light reaching the PMT is about a factor of two larger, but also the dependence on the position is much smoother in case of the twisted lightguide.
The 'best' light is the direct light from the source to the output area. Light which is emitted perpendicularly to this plane undergoes many reflections until it reaches the PMT, hence the light path is very long and light is absorbed easily. Thus the maximum light output is expected from the tip of the element, since here all light which is emitted parallel to the element is immediately reflected towards the outgoing area. On the other hand in the region just at the PMT the part of the light which is emitted parallel to the element but towards the tip has to travel a long way until it reaches a surface where it can be reflected towards the PMT. This focusing effect of the geometry of the detector element is clearly visible in the twisted design whereas the fishtail design shows a bump in the center of the scintillator.

Comparison of different Lightguide Designs: Measurements

To test the performance of different lightguide designs in reality, a fishtail lightguide with 100 mm length (thus a bit longer than allowed in the final design) and twisted lightguide with 80 mm length were connected with optical grease to a scintillator

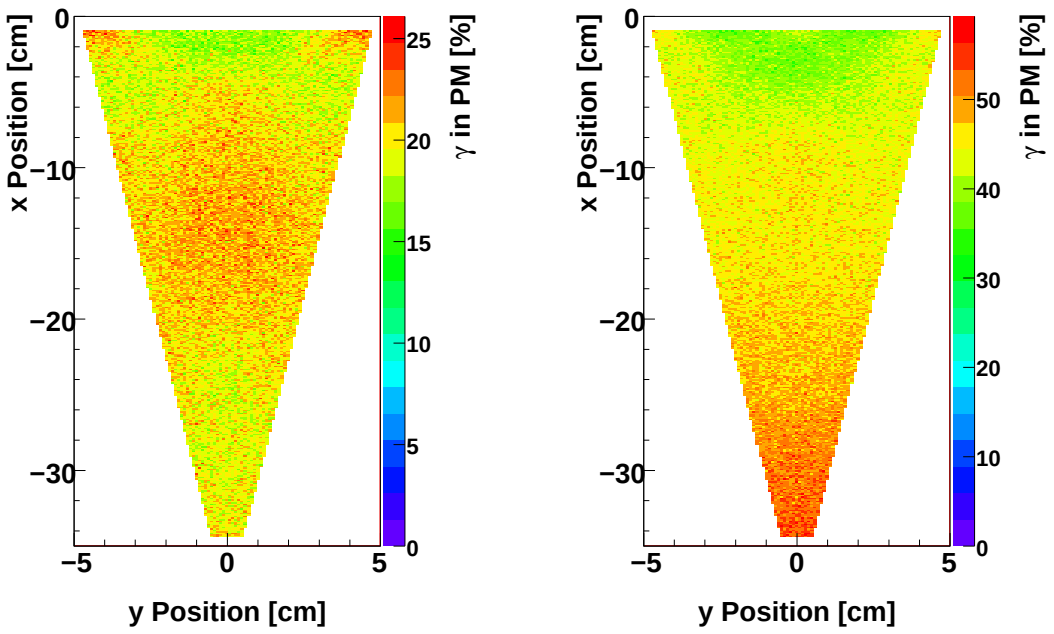

Figure 3.8: *Simulated light output of the detector element for a fishtail (left) and a twisted (right) lightguide. The x-axis points along the length of the element, towards the PMT (which would be connected on top of the plot) and the y-axis points along the width of the element. The focusing effect of the geometry is apparent in case of the twisted lightguide, whereas the fishtail lightguide shows a bump in the center. Note the different scales.*

module. A ^{90}Sr source was put on different positions of the scintillator to compare the light output in dependence of the source position. The readout was done with a digital oscilloscope which allowed to store each single pulse form and deduce all information about the time and the amplitude of the pulse later. The drawback of such a setup is that the data taking time is relatively long since the dead-time is much longer compared to a usual QDC module.

The typical spectrum shows the usual noise at low amplitudes, due to the electronics and small light leaks, and a signal peak at higher amplitudes, well separated from the noise. The signal is produced by the e^- from the β-decay of the ^{90}Sr. Fig. 3.9 shows the spectrum for the fishtail (dashed line) and the twisted lightguide (solid line) with the source situated at three different positions (from near the PMT to far away from the PMT) on the symmetry axis of the detector element.

The mean values of the signal peak are lower in amplitude in case of the fishtail lightguide compared to the twisted lightguide. This difference is increasing with increasing distance to the PMT: the output of the fishtail lightguide is decreasing a bit, whereas the output from the twisted lightguide increases with increasing distance, as predicted by the simulations.

Thus also the measurements show that the light output of the fishtail lightguide is

lower compared to the twisted lightguide. Since the scintillator is only 3 mm thick, and thus rather little light is produced, the quality of the lightguide is crucial. It was decided to construct a twisted lightguide, despite the huge efforts concerning the fabrication.

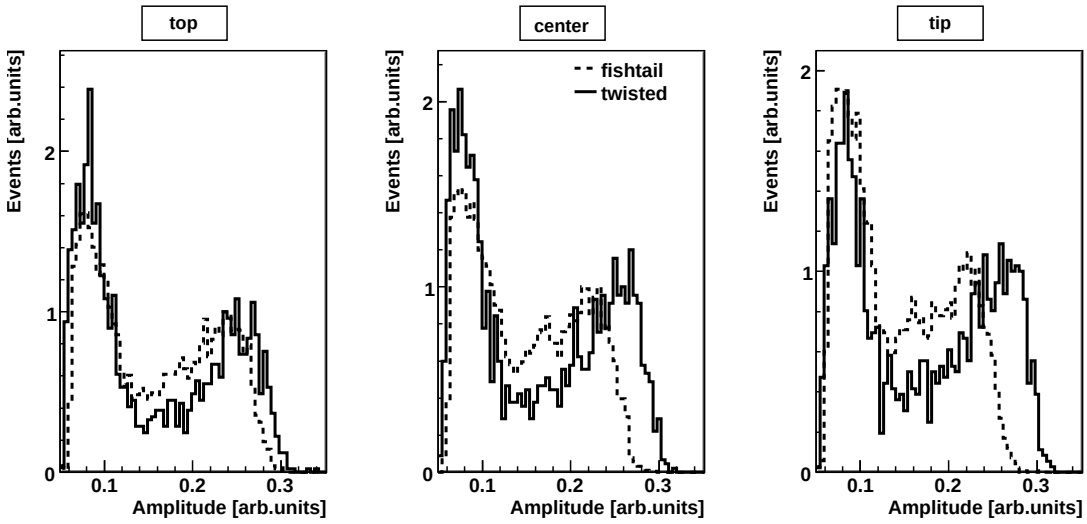

Figure 3.9: *Light output measurements for a 10 cm long fishtail lightguide (dashed line) and a twisted lightguide (solid line) as it was used in the final setup. A* ^{90}Sr *source was positioned on the symmetry axis of the element at the top (near the PMT), in the center and at the tip (far away from the PMT).*

Manufacturing of the Lightguides

The twisted lightguides were constructed of 6 strips with widths between 10.3 and 20.0 mm (see Fig. 3.10). They were made of 3 mm thick plexiglass PMMA gs222 from Roehm[4]. They were sawed, milled and wet polished at the sides with MicroMesh polishing paper. To lessen the tension in the material introduced by machining it, the pieces were heated up to $75-85^\circ$ C. This process is called 'tempering' and should be done within one week after each treatment, but since the polishing was done just after the milling, it was enough to do it only once.
Because the tolerances in the sizes of plexiglass are quite large[5], the widths of the '3 mm' material varies between 2.9 and 4.5 mm. The strips were sorted according to their width so that only strips with a similar width were combined to a lightguide. After the plexiglass was heated up to 165° C to deform it, each strip was twisted by 90° so that all strips together formed the 3 mm$\times$100 mm rectangle of the scintillator on one side and the circle-like shape on the other side. In case of the conical layer, they had to be bent by 20°. That way the PMTs from both layers were aligned in the same plane, perpendicular to the beam. A holding system was used to ensure all lightguides were constructed in the same way. Later they were tempered again before fixing them in the holding device and milling to the desired length (they were

[4]At least that was ordered, but since the two charges bought behave differently when heated up, the suspicion arises, that the Tübingen University Werkstoff Abteilung bought cheaper plexiglass from a different company.

[5]The usual tolerances specified by the selling companies for plexiglass or plastic scintillator material are $+/-(0,4+0,1\times thickness)$ mm.

much longer than necessary to handle them during the bending process).

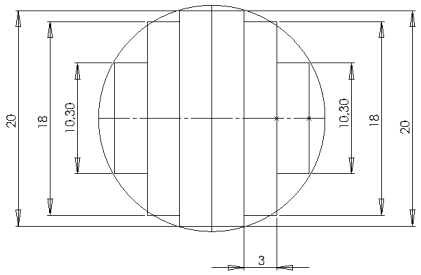

Figure 3.10: *Combination of strips for the twisted lightguide for the new FWC.*

During the heating process the plexiglass changes its shape a bit due to the memory effect of the production process. It is unavoidable that the strips become thicker and more narrow, and it is not possible to go back to the original sizes. For example, a 3 mm thick material will not be 3 mm after the deformation process, but rather 3.2 mm thick, and a 4.5 mm wide material will become e.g. 4.1 mm wide. These changes have to be taken into account when the material is cut.

After the lightguides were cut to the desired length, each single strip was wet-polished at the cut surface with MicroMesh polishing paper with granularities between 3600 and 12000 parts/ cm^2. They were tempered once more and glued together with Acrifix190 glue at the scintillator side. After the gluing the surface pointing to the scintillator had to be polished again, because the surface was usually not perfectly planar due to small mismatches in the gluing process. In the last step the lightguide was glued to the PMT and the holding ring with Devcon glue. Additionally, a glasfiber was glued in the holding ring, the head pointing towards the PMT, to connect the lightpulser system at WASA, which is used to monitor the gain drifts. Fig. 3.11 shows the lightguides before polishing and the final lightguide, glued to the PMT.

At the eight lightguides of the conical layer which were supposed to be glued to the elements at the cross, a 2.6 mm wide strip was cut off so that the width at the scintillator side was 2.6 mm smaller, like the scintillator elements. Hence these lightguides ware not symmetrical as all other lightguides. Of course the cut part at the side of these strips had to be polished, too.

The lightguide production was difficult (painful) and had to be done in a short time, which was only possible with the help of the whole group in Tübingen and big efforts from the workshop. Also the development of the handling was a challenging task the workshop managed perfectly, willing to learn from the Jülich workshop.

3.1.6 Preparation and Installation of the new FWC

The lightguides have to be glued to the scintillator elements. For this, holding devices were built where the lightguides could be fixed. The scintillator was fixed in the right height and pressed to it. For this gluing part Devcon glue was used. This glue does not dissolve the material, as does the Acrifix190. When heated up to 100° C it can be removed easily. If the gluing surface breaks, the glue will adhere only on the

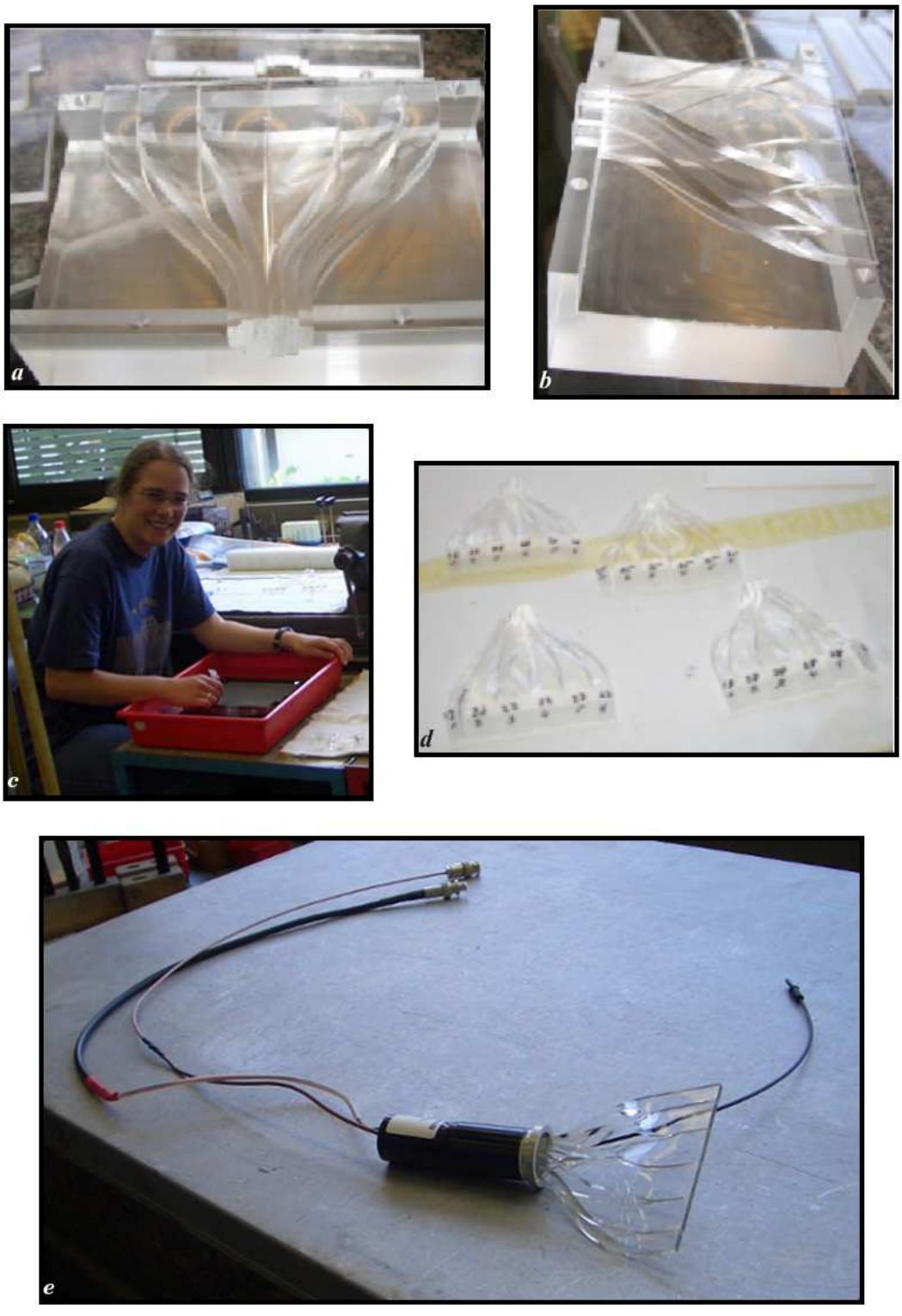

Figure 3.11: *Manufacturing of the lightguides: Photos a) and b) show a lightguide just after bending in the holding device used for positioning the strips after/during the bending. Photo c) shows the polishing of the each single strip with polishing paper in water, photo d) the not yet polished strips. After gluing and again polishing the rectangular surface the lightguide is glued in the ring to the PMT (e).*



(a) *Elements of the cone-like layer and the planar layer mounted next to each other.*

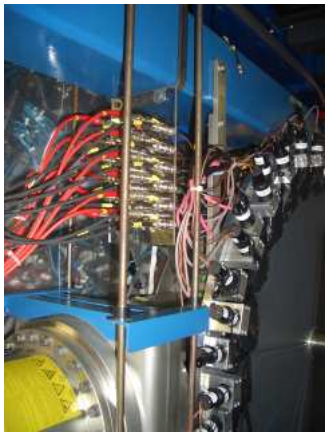

(b) *Patch-panel for the signal (black cables) and high voltage cables (red).*

Figure 3.12: *Detailed view on the positioning of the two layers and the cables.*

plexiglass of the lightguide, not on the scintillator[6]. That way the lightguide could simply be cleaned and glued again. The glue needed several hours to dry completely[7]. Although the gluing surface is quite small with the only 3 mm thick scintillator, it was very solid. Only one element broke during the transport to Jülich, which was recovered there.

All elements were wrapped in 15 μm thick aluminized Mylar foil, which was scrambled first to make sure that the reflection is diffuse. After that 50 μm thick black Tedlar foil keeps the element light tight. Black tape is used to make sure each border is covered. Special interest lies in the ring which is fixed with the clamp. Here several layers of tape are necessary to make it light tight. Fig. 3.13 illustrates the wrapping process.

The wrapped elements were transported to COSY and installed at WASA. Since the FWC is the very first detector in the FD row, all other detectors had to be de-installed to make the access possible. The outer supporting ring is fixed to the main support structure and each element is fixed with clamps to this ring. Each layer is fixed at the beam pipe by an aluminum ring with a rim to hold the elements in place. The cables are guided to four patch panels made of plexiglass[8] and connected to the long high voltage and signal cables (see Fig. 3.12b). Finally, a sheet of black Tedlar is tightened over the lightguides and the PMTs for additional light protection and to protect the next detector FPC from overhanging cables. Fig. 3.14 shows some steps during the installation at WASA. The last picture shows the final detector as it is installed now in Jülich. It is sometimes called the 'Black Sun of Tübingen', an association which is apparent, looking at the final installation.

[6]This is related to the different molecular structure of scintillator and plexiglass. In view of the big similarities that was surprising.

[7]In the very first tests it was resting for only 2 hours but this gluing surface was not solid.

[8]The patch panels must not be made of metal to make sure all PMTs are electrically insulated.

The elements are numbered according to the usual WASA rules: looking in beam direction, the first element above the horizontal axis on the left half (towards the outside of the COSY tunnel) is assigned as number 1 and the following elements are numbered clockwise. The ϕ angle associated to the middle of the first element is 7.5° in case of the first, conical, layer, and 0° in case of the second, planar, layer. In contrast to most other detectors the FWC signals are connected to two discriminators, to allow two different thresholds. The TDC is connected to the low threshold, which is not changed, whereas the high threshold can be adapted via software for each experiment. The trigger on the FWC which requires a high threshold turned out to be very helpful to trigger on ^{3}He or ^{4}He. On the other hand the additional low threshold allows timing information also in case of low deposited energies, where the high discriminator threshold would not be reached and thus no TDC signal would be measured.

1st Layer	tip z-position	1008 mm
	tilting angle	20°
	radius at tip (projected)	39 mm
	radius at top (projected)	372 mm
2nd Layer	z-position	1156 mm
	radius at tip	39 mm
	radius at top	377 mm
Scintillator material		BC408
Scintillator thickness		3 mm
Mylar thickness		15 μm
Tedlar thickness		50 μm

Table 3.3: *Dimensions of the new FWC. The z-position is measured from the center of the scintillator. The radius denotes the radius of the scintillator element measured from the center of the beam pipe.*

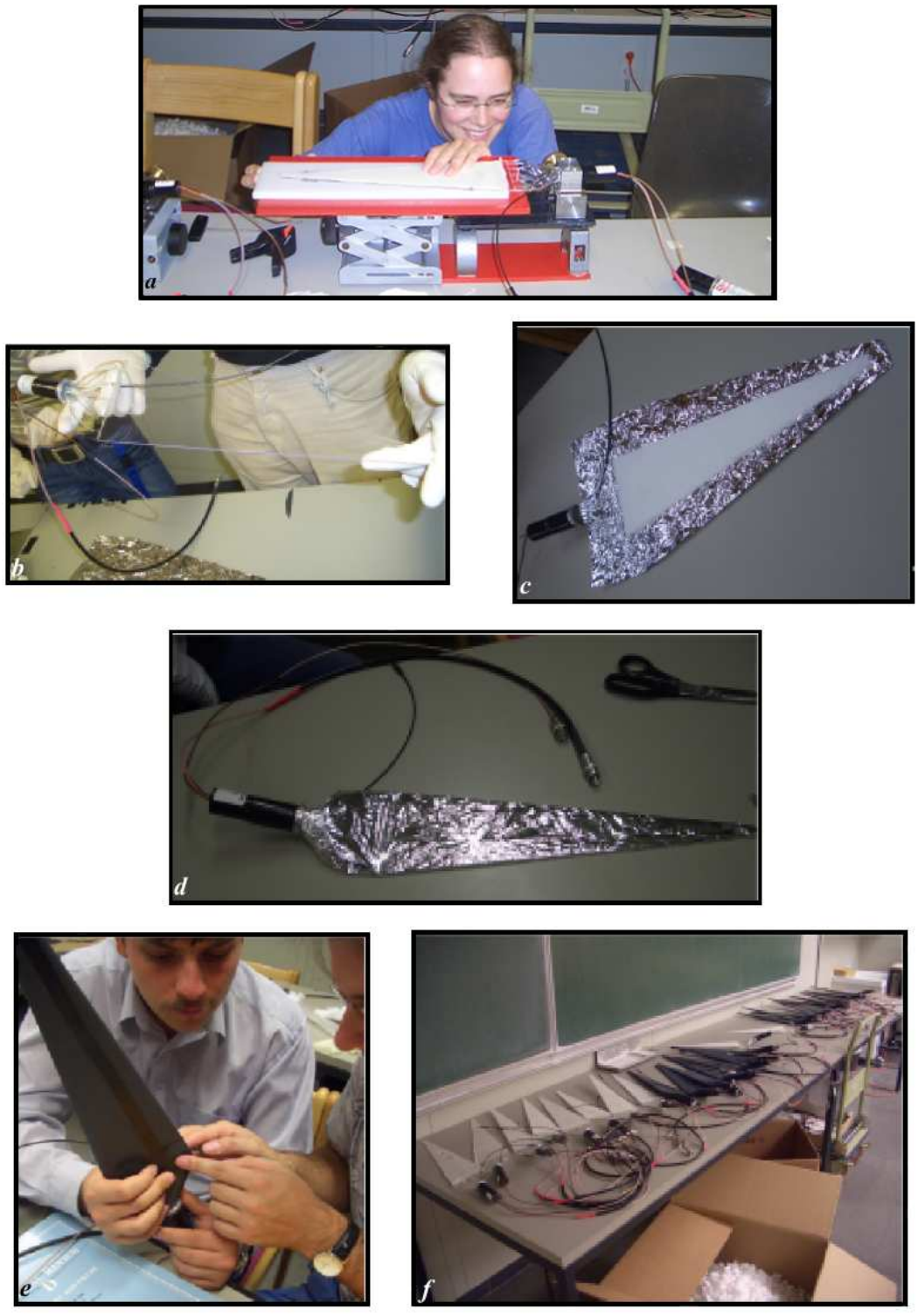

Figure 3.13: *After the lightguides are glued to the PMT's, they are glued to the scintillator (photo a) shows an element of the bent layer, photo b) shows a glued element of the planar layer) and wrapped in Mylar (c,d) and Tedlar (e). Photo f) shows the glued elements. Some are already wrapped both in Mylar and Tedlar, some are not yet wrapped and the protection paper still covers the scintillator.*

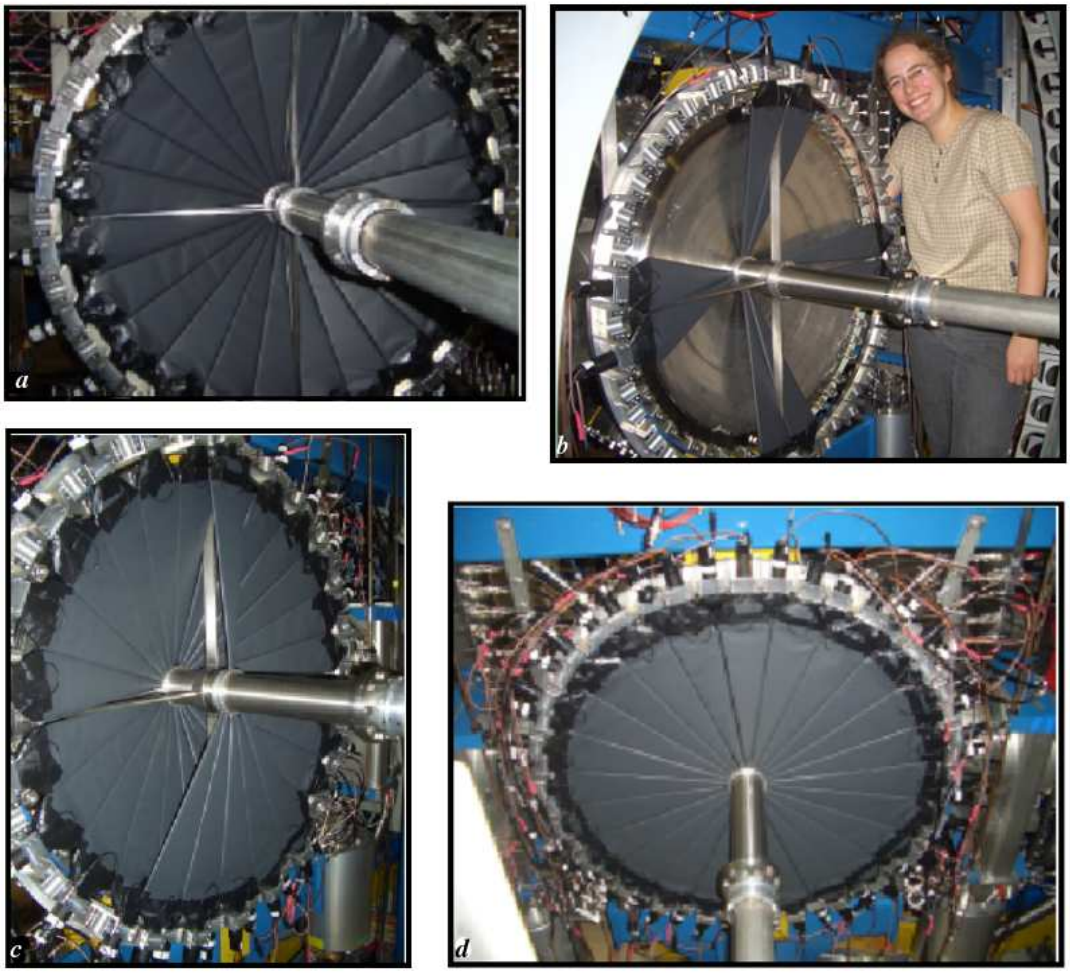

Figure 3.14: *Installation of the FWC at WASA: Photo a) the fully mounted conical layer, photo b) shows the elements of the conical layer at the cross. Photo c)shows the fully mounted conical layer with some elements of the planar layer mounted already and photo d) shows the fully mounted planar layer (the conical layer is inside, not visible anymore).*

3.1.7 Performance of the new FWC

Nonuniformity

The uniformity of the light output was one of the crucial arguments for building a new FWC. Due to the geometry of the element and the lightguide the light output, and thus the QDC value of a signal, depends on the position of the light source. Usually the dependence in ϕ, i.e along the width of the element, is small[9], but the dependence in θ, i.e. along the length of the element can be large. Here not only the geometry of the setup is crucial, but also the aging effects in the material, i.e. absorption changes due to coloring or microcracks in the material.
The nonuniformity denotes the θ dependence of the QDC value for a constant energy deposition. In Fig. 3.15 the QDC value is plotted as a function of the scattering angle θ for a typical element of the FWC1, FWC2 and the FTH1. The different path length inside the scintillator due to the angle at which the particle penetrates the detector is considered by the factor $cos(\theta)$. The PMT is situated on the right side, at large θ values. Geometrically the FTH1 is similar to the FWC: it is also a thin (5 mm) plastic scintillator and built of wedges. Here the old FTH is used, which has been renewed in the meanwhile because of its bad light output due to aging effects.
To be sure that the produced light is the same for all θ angles, minimum ionizing particles are used, which deposit the same energy per path length (2 MeV/cm).

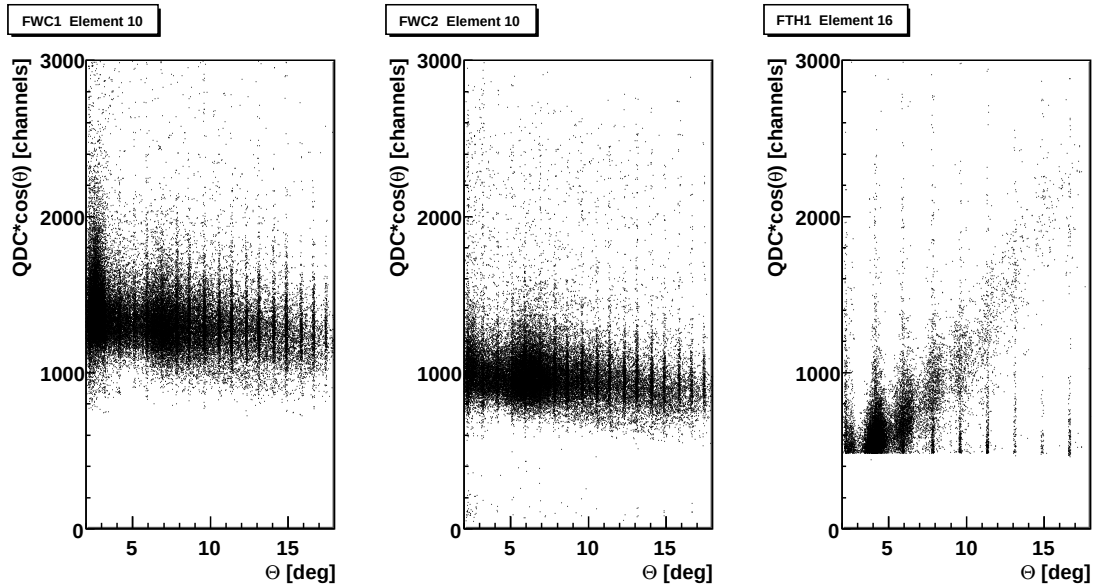

Figure 3.15: *QDC values of an element in the FWC1, the FWC2 and the FTH1 as a function of the polar scattering angle θ. Large θ values correspond to positions near the PMT.*

[9]If the lightguide is not asymmetric, as it was the case in the old FWC, and the parallel section at the scintillator is large enough.

In case of the FWC elements the light output decreases towards larger θ values, as expected by the simulations of a perfect detector due to the "focusing effect". (see Fig. 3.8b). In comparison in the FTH1 element the light output depends strongly on the θ angle, showing a very strong rise towards large θ angles and towards the PMT, respectively. In this element the threshold on the discriminator apparently was too high for small angles, which shows up in the cut at 500 QDC channels.
Fig. 3.16 shows the nonuniformity for all elements. Here each element is divided into five bins in θ and two bins in ϕ. The ADC distribution of each bin is fitted with a Gaussian, the mean value is normalized to the value at the tip of the element (same ϕ but $\theta = 0$). Thus a flat cylinder at a z-value of one would mean that all elements were very uniform, the light output independent of the θ angle. This is the case for the two FWC layers, where the deviations are not larger than 10%. In comparison, the FTH1 response is very different for each element. Some elements are relatively flat (note the different scale than in case of the FWC detectors), but others show a very strong θ dependence.
The work put in the light guides of the FWC to achieve a radial symmetric geometry pays off in the very good uniformity of the light output.

Efficiency

In order to estimate the efficiency of the FWC, the coincidence with the FTH is used. With n being the true (unknown) number of tracks and n_i the number of hits seen by detector i, the efficiency ϵ_i is defined as $n_i = \epsilon_i\, n$. The number of coincident tracks n_{ij} is given by the product of both efficiencies $n_{ij} = \epsilon_i\, \epsilon_j\, n$.
Thus if the number of coincident tracks is known and the number of tracks in detector j, the efficiency of detector i can be calculated by:

$$\epsilon_i = \frac{n_{ij}}{n_j} \tag{3.1}$$

Hence the ratio of tracks which have a hit in the FTH1 and those which have also a hit in one of the FWC layers gives the efficiency of the new FWC.
A problem is to make sure that the number of tracks is really the same for both detectors and that the efficiencies are independent[10]. For that reason the FTH is used, which is the next scintillator after the FWC in the FD sequence, thus all particles reaching the FTH must pass through the FWC as well. Furthermore the reconstruction of charged forward tracks is based on the FTH but does not depend on the FWC.
For the estimation a subset of the 1.05 GeV measurements was used. To get a clean data sample, single track events with a minimum biased trigger (at least one track in FRH1) are used.

[10] E.g. the number of tracks penetrating the very last detector FVH, 3 m away from the interaction point, is less than in case of the very first detector FWC, 1 m away from the interaction point, since many particles will be stopped in the detector layers in between.

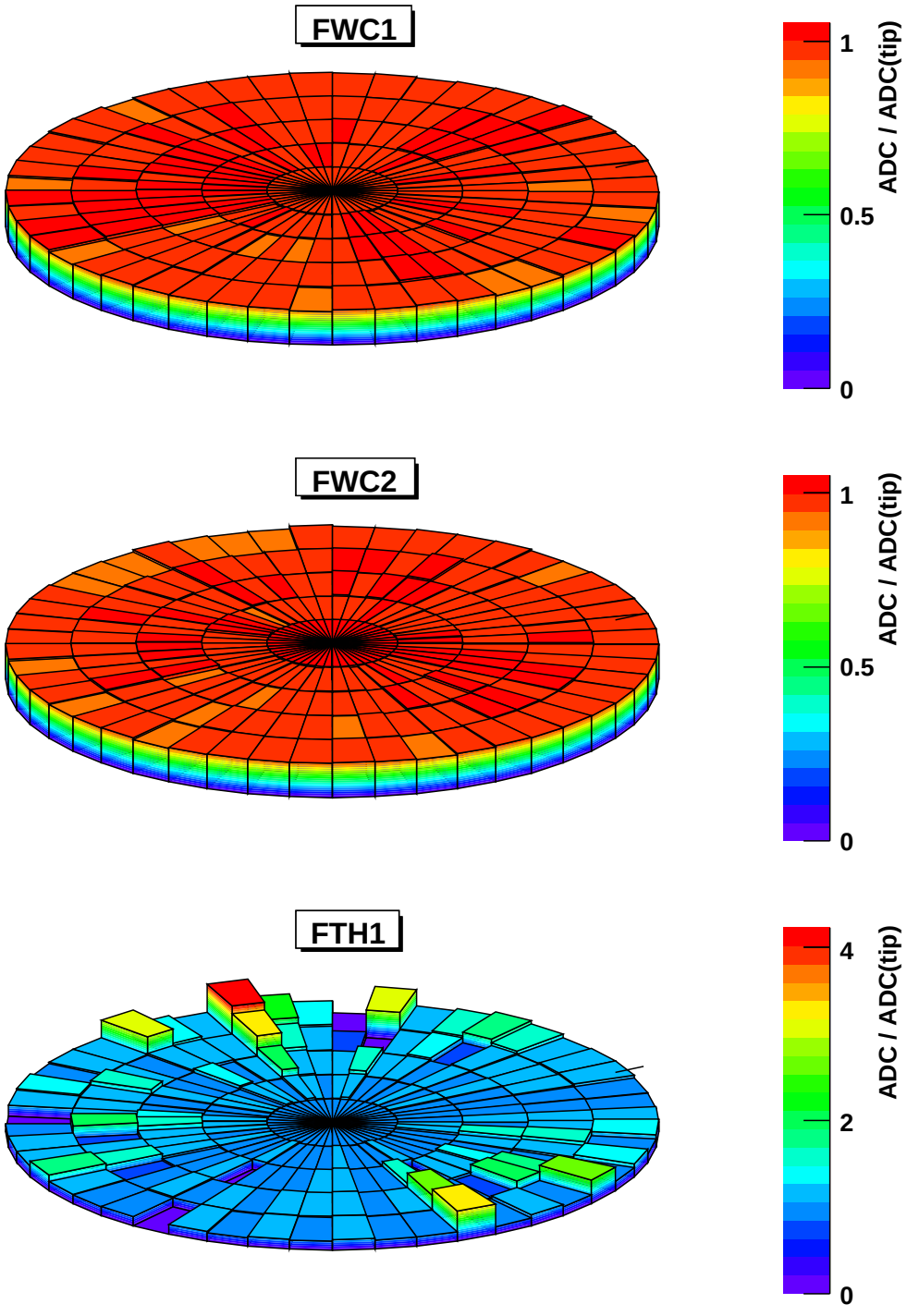

Figure 3.16: *Light output of the FWC1, the FWC2 and the FTH1 normalized to the tip (in the center). Each element is divided in five bins in θ and 2 bins in ϕ.*

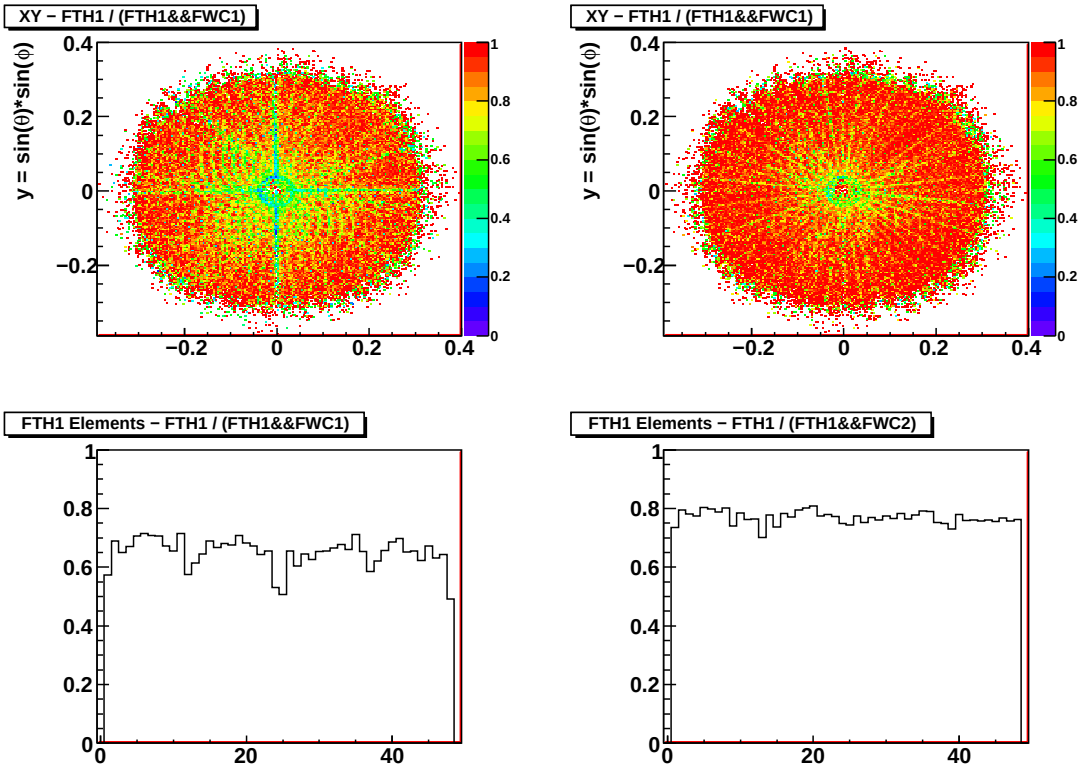

Figure 3.17: *Efficiency for the FWC1 (left) and the FWC2 (right). The upper row shows the efficiency as a function of x and y, the low as a function of the element number. In the FWC1 plots the efficiency drops due to the holes for the metal supporting cross are nicely visible.*

Fig. 3.17 shows the efficiency as function of x and y (upper row) and as function of the element number (lower row) On the left side for the first, conical layer (FWC1), on the right side for the second, planar layer (FWC2).

Both detectors show inefficiencies in the innermost and the outermost part. The former is probably due to the aluminum ring at the beampipe, the latter due to the fact that the FTH covers a bit more than the nominal 18° covered by the forward detector. The FWC just covers the 18° and not more to fit in the available space. However both the inner and the outer part are not useful tracks but lie outside the nominal angular range of the FD.

The spacial separation between single elements is seen as narrow dips in the efficiency. Unlike the FWC2, the FWC1 has holes for the metal cross from the vacuum window. This is nicely seen in the x-y-plot of the conical layer (FWC1, middle) and also in the dips in the element distribution at elements 48/1, 12/13, 24/25 and 36/37. The reason for the smaller efficiency in a wide area around the center in case of the FWC1 is probably that particles are scattered at the beam pipe or the aluminum ring to larger θ angle so that it is detected in the subsequent layers, but not the FWC since this is positioned just behind the scattering window. Thus requesting a

hit in the FWC1 would reject many of those particles, which was one of the reasons to built this detector.
Apart from these understood effects the efficiency distributions are rather flat with a value of about 0.7 for the FWC1 and 0.8 for the FWC2.

Time Resolution

In order to use the time of flight for the particle identification, the time resolution of the FWC must be good enough, that means in the order of $\sigma = 0.15 - 0.2$ ns. To achieve that, a very thorough time calibration is necessary, which will be done in connection with a systematic check of the time of flight measurements. Up to now, e.g., walk corrections are not yet included. Fig. 3.18 shows the time difference between the first and second layer for one detector element for ^{3}He and ^{4}He particles, which have a high energy deposit and should not be affected much by the walk effect. Since the first layer is conical and the second planar, the distance between the layers changes with θ, only the interval between 0.2 and 0.25 rad ($11 - 14$ °) in θ is used. The Gaussian fits for these two elements yield σ values of 0.16 ns and 0.17 ns, respectively.
Already without a time calibration elaborated towards the time of flight measurements, the time resolution is in the order of the desired resolution.

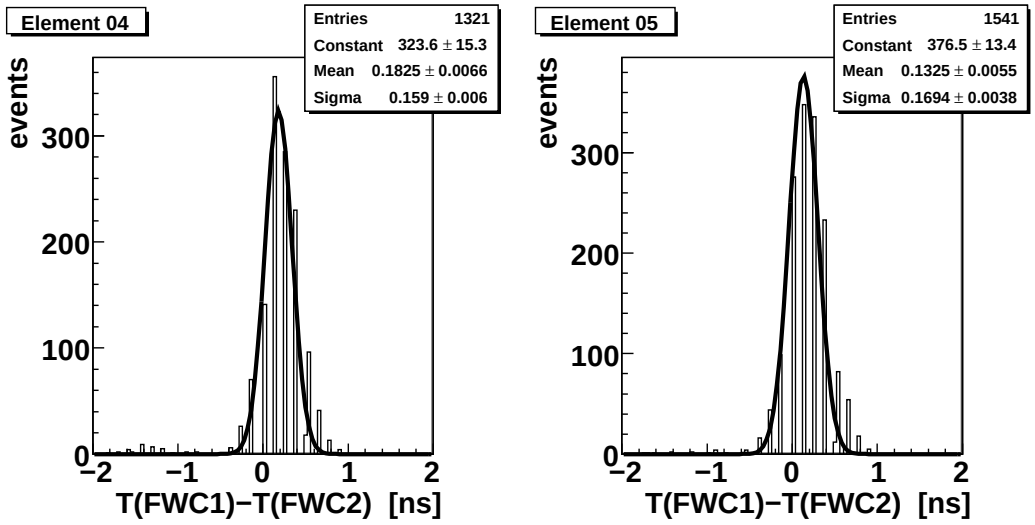

Figure 3.18: *Time differenct between FWC1 and FWC2 for element 3 (left) and element 19 (right).*

3.2 The new FVH

The FVH is the detector farest away from the interaction point. It is mainly used in the trigger to distinguish punched-through particles from those stopped in the FRH already on trigger level. For this purpose an iron absorber in front of the FVH can be used to increase the stopping power of the forward detector.

3.2.1 The old FVH

The old FVH is built of 12 plastic scintillator bars with a thickness of 20 mm, a width of 137 mm and a length of 1650 mm. The bars are placed horizontally so that they cover a quadratic area. A half-hole is cut in the two bars at the beampipe as can be seen in Fig. 3.19.

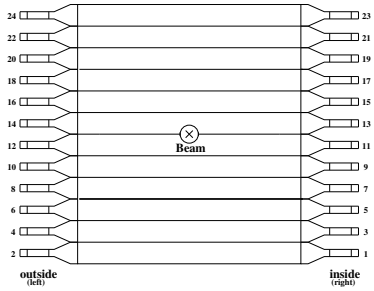

Figure 3.19: *Sketch of the old FVH*

The detector is placed at a distance of 2.9 m from the interaction point, which corresponds to a polar angle coverage of 15.8°. It does not cover 18° as all other detectors in the FD because it was originally designed to be placed nearer to the interaction point, covering the full angular range.
A doublesided readout allows to determine also the x-position of the hit by the time difference between both signals. In case of the two middle bars the signals are very different if they originate from the side of the PMT of the other side of the half hole (Fig. 3.20). To make sure that signals from both sides pass the discriminator threshold, which is the same for all elements, the supply voltage has to be so high that the lower of the two signals is as high as the signals of the other detectors. The calibration is more complicated in these cases, because the nonuniformity corrections must take care of the two different signals in the light output. Also the time calibration gets more complicated, which is a problem especially in view of using the time of flight for particle identification.

3.2.2 Design Considerations for the New FVH

The first argument for building a new last detector is the demand of covering the whole FD polar angle range. In order to fulfill that, the new FVH simply has to be large enough.

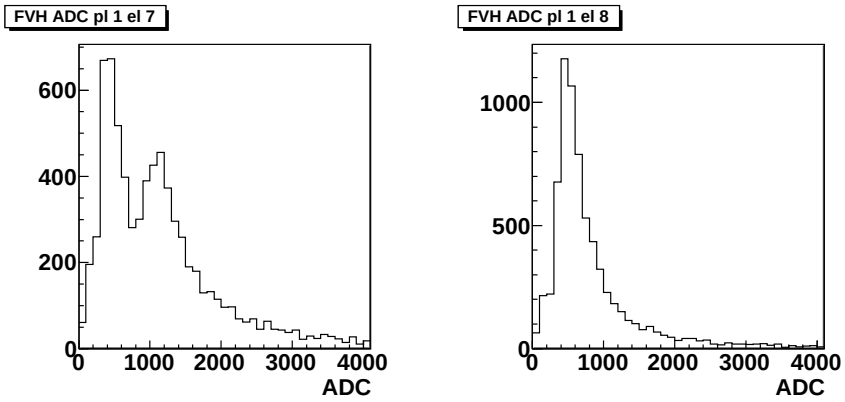

Figure 3.20: *ADC output for the old FVH for a bar with half hole (left) and without (right). The half-hole introduces a second peak. Light which has to pass the half-hole is suppressed compared to light which can travel directly to the PMT.*

A second argument arises from the new FWC: since the time resolution is significantly improved compared to the old version, one could use the time of flight (TOF) between the first and the last detector as additional information for the particle identification. Especially in experiments with high beam energies, when the energy resolution of the FRH becomes worse, the TOF improves the particle identification a lot. For this of course a good time resolution is needed and also a large distance between the start and the stop detectors.
Thus it was decided to place the detector as far away from the interaction point as possible. This position is defined by a COSY-quadrupole at roughly 4 m distance from the interaction point.
Again the detector is built of bars, because that allows a double sided readout, which improves the time resolution by a factor of $\sqrt{2}$. Instead of removing the old layer, one can just leave it where it is and add the new layer to the FD system. In the new layer, the bars are aligned vertically. Thus, together with the horizontal old FVH the x and y position can be extracted.
Since the performance of the half-hole bars in the old FVH is much worse than that of the other bars and thereby especially spoils the time resolution, a different solution was developed for the new detector: the bars at the beampipe are cut in two halves which are read out on both sides for a better time resolution. The readout at the beampipe is done with lightguides mounted perpendicular to the element. A mirrored prism reflects the light by 90° from the scintillator element to the lightguide. Details about this setup can be found in [Per09]. Two more bars are mounted horizontally behind the others, covering all other elements. Their signal can be used as a reference signal for the time calibration, which makes the calibration easier and better. These two bars are also read out perpendicular to the element, like the middle bars, because otherwise they would hinder the passing through the tunnel, which is not only inconvenient, but also not allowed by safety regulations (and somebody could hit the elements).

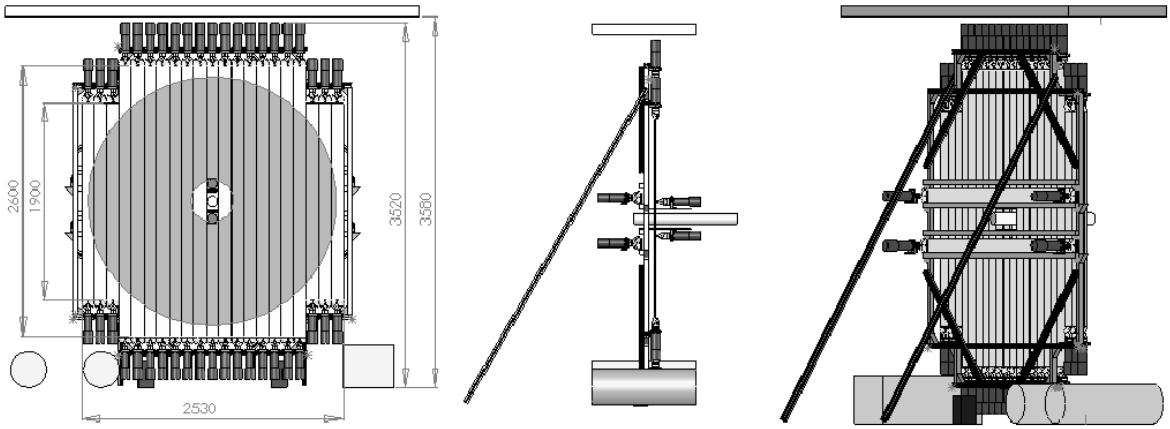

Figure 3.21: *Sketch of the new FVH. Left: looking onto the detector from the interaction poin. The red shaded area marks the acceptance range of the FD. Middle: The PMTs of the horizontal bars point in beam direction, the PMTs of the middle bars point towards the beam direction, because on the backside no space is available due to the quadrupole. Right: inclined view on the rear side, the two horizontal bars are visible.*

.

The height of the tunnel turned out to be a limiting factor as well. To be sure to cover the full 18°, the scintillator must have a length of 2600 mm, while the tunnel has a height of 3700 mm. Thus for the two pairs of lightguides and PMTs only 1100 mm are left. With a PMT length of approximately 300 mm only 20 cm are left for the lightguide. So again a twisted lightguide with better light propagation properties is preferred, although it is not as important as in the case of the FWC as the expected light output is much larger because of the thicker scintillator.
On the floor of the tunnel a tube and a cable tray from COSY hinder the detector. This disadvantage could be overcome by using smaller elements at the side of the detector, where the full length is anyway not needed because the corners are not covered by the 18° circle. So actually this design is better than the originally planned design with only full sized elements. Fig. 3.21 shows a CAD drawing of the detector and the indicated tubes on the floor. The shaded area shows the angular coverage of the FD.

3.2.3 Scintillators

The new FVH is made of 24 plastic scintillator EJ200 bars, each 20 mm thick and 120 mm wide. Fig. 3.22a shows the emission spectrum of the scintillator, its properties are summarized in table 3.4. The two middle bars are installed below and

above the beampipe and have a length of 1165 mm (below) and 1145 mm (above). The 14 bars next to the beampipe (7 to the left and 7 to the right) have a length of 2600 mm and the outer 6 bars (3 left, 3 right) have a length of 1900 mm. Two bars with a length of 2600 mm are mounted horizontally behind the others to give a reference signal for the time calibration.

The middle bars were cut and polished by the workshop in Jülich, the others were bought with polished surfaces[11].

All elements were glued and wrapped in Jülich[12]. Like the FWC the first cover is 15 μm thick aluminized mylar foil which was scrampled before wrapping, and the second, light tight cover is black tedlar foil.

Refractive Index	1.58
Light Output [% Anthracene]	64
Rise Time [ns]	0.9
Decay Time [ns]	2.1
Pulse Width, FWHM [ns]	2.5
Light Attenuation Length [cm]	400
Wavelength of Max. Emission [nm]	425

Table 3.4: *Properties of EJ200 scintillator material [ELJ]*

3.2.4 Photomultipliers

The main request to the PMTs is a good time resolution. The XP2020C is a PMT with a very good time performance. It is commonly used in experiments which need an accurate timing. Table 3.5 summarizes the properties of the PMT. Spare tubes from the TOF experiment in Jülich, together with an iron housing, could be used for the new FVH. To fulfill the requirements at WASA the cylindrical iron housing had to be cut and a new screw thread drilled, which was done by the workshop in Tübingen. Still the total size of the PMT with base and housing was roughly 30 cm, leaving only 15 cm for the lightguides. Hence cables could not be installed in the usual way, just parallel to the base, but with a T-shape connector perpendicular to the PMT for the signal cable, and with an additional 20 cm long cable for the high voltage respectively.

[11]The large surface was not polished since the usual process of machinery produces very good surfaces, which would get worse by polishing.

[12]Many FVH elements were glued by Dr. C. Pauly and Dr. F. Goldenbaum in Jülich. Thanks a lot.

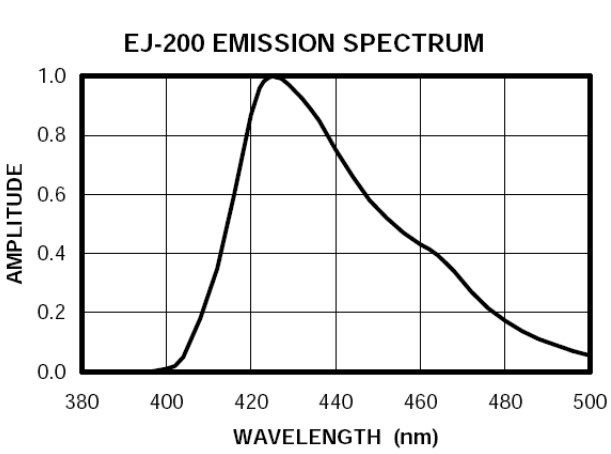

(a) *Plastic scintillator EJ200 emission spectrum*

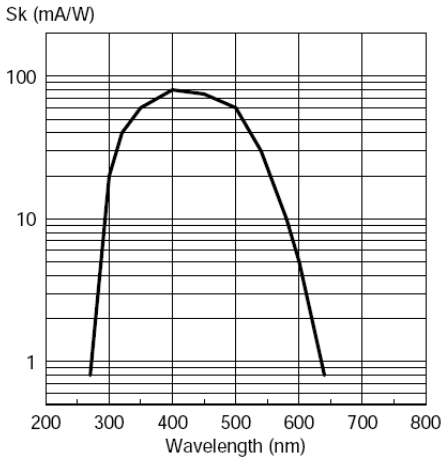

(b) *PMT XP2020 absorption spectrum*

Figure 3.22: *Emission spectra of the scintillator and the PMT for the new FVH.*

3.2.5 Lightguides

The lightguides are made of two 25 mm thick Roehm plexiglas strips with a width of 60 mm. They are twisted and smoothly cut in the central part to fit exactly to each other. The lightguides are a bit thicker than the scintillator element, because the size tolerances both for the scintillator and the plexiglas are quite big. With the bigger plexiglas no light is lost due to a smaller surface of the lightguide.
The plexiglas strips were cut with a diamond polishing tool, hence it was not necessary to polish them by hand[13]. Fig. 3.23 shows a photo of a lightguide. The two strips are not glued together, but pressed with two screws in a metal housing. However, they are glued to the detector element with Devcon glue and indirectly fixed to each other by the gluing surface at the scintillator.
The middle bars are installed perpendicularly to the element and coupled to it with an additional plexiglas prism with a mirror foil. The construction of the rectangular readout was done in the scope of the master thesis of E. Perez del Rio [Per09].

3.2.6 Installation of the new FVH

The holding structure for the detector is made of Bosch-Rexroth profiles with a 45×45 mm^2 basis [Rex]. The frame is built of these profiles and fixed to the COSY floor with two podests to install it in the correct height above the floor. Two long profiles at the sides are used for additional stabilization. As the system is very flexible, it is possible to move the holding devices along the profiles to any place.

[13]The diamond polisher was a very good investment. The first few lightguides were still polished by hand, which was very time consuming due to the large surface. Especially the curved surface between the strips was hard to polish in good quality without touching the area which already had a very good quality.

Refractive Index at 420 nm	1.48
Window material	Borosilicate glass
Photocathode	Bi-alkali
Multiplier structure	linear focused
Spectral range	290-650 nm
Maximum sensitivity	420 nm
Gain slope (vs. supp. Volt, log/log)	9
Anode dark current (typ)	10 nA
Continous anode current (max)	0.2 mA
For a supply voltage of 2000 V:	
Linearity (2%) of anode current up to	25 mA
Gain	$3 \cdot 10^7$
Rise time	1.6 ns
Duration at half height	3.7 ns
Transit time	28 ns

Table 3.5: *Properties of the PMT XP2020 [Phob]*

The elements are fixed to this frame at the lightguide-PMT connection. At that point the lightguide strips are fixed to each other in a cylindrical metal housing. Clamps fix the housing to the frame. In case of the lower part of the elements, a rim at the housing prevents the elements from falling down even if the clamp is not yet strongly fixed. First the lower part is fixed on the clamp so that the rim sits on it. Only then the upper part is fixed, making sure that no tension is included by pulling from both sides of the element.

The housing with the PMT is screwed to the metal lightguide holding when the scintillator-lightguide system is installed. That way the PMT can easily be connected and disconnected and the heavy iron housing is fixed not directly at the lightguide or scintillator, but at the holding system, which is fixed to the support structure. If the heavy cylinders were mounted at the ends during the installation, it would be very difficult to handle the elements without breaking them.

The installation took place in three steps: in April 2008, the frame and the first two elements were installed (with the lightguides polished by hand). In August 2008, all other elements with straight readout were installed (with diamond polished lightguides). The four bars with the rectangular readout were installed one year later, after the readout system was developed. Since WASA is an internal experiment, situated just at the COSY beampipe, access to the detector is only possible when no beamtime for any experiment is scheduled. In the last years, a long shutdown period of a few weeks was scheduled during summer and only a few days over the year.

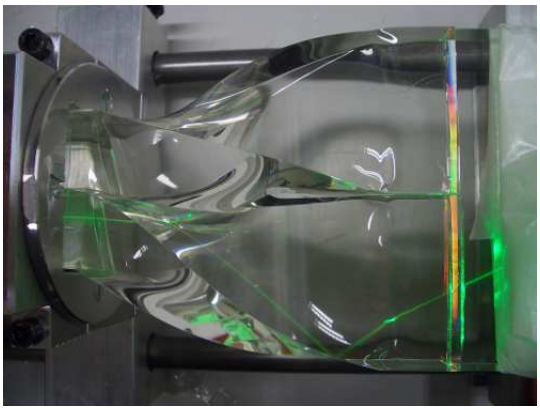

Figure 3.23: *Photo of one of the FVH lightguides after gluing. In the lower strip a green light ray from a laser pointer at the other side of the element is visible.*

Details about the first tests and the calibration of the new FVH can be found in [Per09].

z-position	3673 mm
Scintillator material	EL200
Scintillator thickness	20 mm
Mylar thickness	15 μm
Tedlar thickness	50 μm
Element lengths	2600 / 1900 / 1165 / 1145 mm

Table 3.6: *Dimensions of the new FVH. The z-position is measured from the center of the vertical scintillators.*



Figure 3.24: *Installation of the new FVH layer: First the element is put on the lower holding system, which holds the weight of the element (a). After that the upper part is attached (b, c) and both clamps are fixed. The exact position of the upper clamp is not fixed to allow tolerances in the length of the element. Photo d) shows the first two installed elements, photo e) the elements at the beam pipe. Photo f) shows the horizontal bar above the beam pipe. Photo g) shows the detector (without the beampipe bars) from the rear side, photo h) shows the right part of the detector (in beam direction) from the bottom.*

4 Analysis Tools

Get your motor runnin'
Head out on the highway
Lookin' for adventure
And whatever comes our way

Born to be wild, Steppenwolf [Bon68]

Detectors used in this work provide nothing else but electronic signals: the charge at a certain time, the integrated charge over a time interval and/or the time the signal has reached some threshold. To handle all these signals and come to an understanding what actually happened, one needs to go through several steps:

- Remove the electronic noise in the detector and find the real hits.
- Transform the electric signals into energy and time information.
- Combine the hits to tracks
- Identify the particle which produced the track.
- And if all this is known, there are several methods to improve the resolution of the detector and the understanding of what is going on.

The idea as well as the performance of the main parts will be explained in this chapter.

4.1 RootSorter

The basic analysis, online during data taking and offline when the data are taken and the specific reaction is analyzed, is done in the RootSorter framework [HHM03]. It is based on Root/C++ [CER] libraries and organized in modules which are loaded only if needed. A high level module automatically loads the low-level ones used in this particular part. Decoding tables, geometry information and calibration constants for each run period are stored in a central database. Via setup files or the command line the tables for a specific time or interest[1] are defined either by assigning the time or number of the run or directly by the filename. Also parameters for analysis modules are defined in setup files which can be changed without recompilation.
The first step is the decoding of detector information and the combination of the TDC and the ADC information to hits, which are stored in so-called HitBanks. At

[1] If the interest is in e.g. in ^{3}He nuclei, the calibration might be significantly improved if constants are used which were identified on Helium compared to constants identified on e.g. protons, because the energy deposit is so much different.

that point it can happen that more than one ADC and TDC pulse is assigned to one hit because in the allowed time window more than one signal arrived. These pieces of information allow to check the detector performance and settings like thresholds or timing, which is done at the beginning of a beam time. The final combination of the ADC and the TDC is done during the calibration process together with the conversion to energy in GeV and time in ns. Because the Monte Carlo simulations do not include a de-calibration, but return the result of a perfect detector, instead of the calibration a filter is applied for simulated data, which worsens the resolution so that it fits to the experiment. After that Monte Carlo and experimental data are processed in the same way.
Low level analyses, showing raw hit distributions for monitoring the experiment, and higher level parts which are needed by every user, like track finding and calibration, are provided in the framework. High level analyses specialized for a certain task are designed by the user himself.
When WASA moved from CELSIUS to COSY, it was decided to accommodate the RootSorter package, which was used for the ANKE experiment, for WASA-at-COSY. All detector specific routines, e.g. hit reconstruction, monitoring and track reconstruction, had to be implemented. Thus although the detector itself is already ten years old, the main software package is new and continously updated. The analysis presented in this work was performed with RootSorter Rev.3253 and compiled with ROOT 5.20.00.

4.2 Forward Track Reconstruction

Particles flying in the forward detector produce hits, and maybe clusters of hits, in the detector layers they pass. The track reconstruction combines hit and cluster information to determine the path of the particle. The resulting WTrack object stores, apart from the angles and the time of the track, all clusters which belong to the track. Via the cluster the hits are accessible, thus it is possible to go from the track level down to raw hits.
The track reconstruction for charged tracks works as follows:

A pixel in the FTH is the necessary and the only requirement to start a WTrack object. The geometry of the FTH is chosen in a way that a track passing through all three layers is determined not only in the azimuthal angle, as in the case of the other plastic scintillators in the forward detector, but also in the polar angle[2] (see section 2.3.2). A pixel in the FTH is determined, if overlapping hits[3] in at least two of the three FTH layers are found.

Ambiguities arise as soon as there are several tracks in one event. In this case the combination with the smallest time difference between the involved hits is

[2]This is valid under the basic assumption that a charged track in the FD originates directly from the interaction point.

[3]In the FTH no clusters are built, or rather only clusters containing just one hit.

chosen[4]. The average time of the FTH hits is used as the time of the track.

Hits in the wedged FD scintillators (the two layers of the FWC and the five FRH layers) are added to the track if the corresponding azimuthal angle ϕ fits to the angle of the track[5]. In this case, this hit starts a cluster, possible adjacent hits in the same layer are added to this cluster, which is then added to the track. The corresponding hits cannot be part of another track. Clusters are added independently of geometrical considerations, e.g. if a cluster in the fifth FRH layer is found which fits to the track, but clusters in the previous layers are not, it is still added to the track.

Hits in the FVH are added to the track if the corresponding x and y position fits the track and if the hit occurred inside a time window around the track time. Although the FVH is made out of long bars, it can provide not only a decent resolution in y (according to the 12 cm width of a bar), but also in the x direction. The time difference between the signals arriving on the left and on the right side of a bar corresponds directly to the position in x with a resolution of 30 cm as default[6]. If a hit in the FVH fits to the track, it starts a cluster, is added to the clusters of the track and can still be used in another track. The new layer of the FVH is not yet implemented, but the procedure is the same as that with the first layer. However, at the time the data presented in this thesis were taken, the new layer had not yet been installed. And even at 1400 MeV, the highest energy measured, the ^{3}He is stopped latest in the last FRH layer.

Angle correction with the FPC is achieved after all plastic scintillators have been checked. Since the FPC gives a much better resolution than the FTH, which is the plastic scintillator with the best resolution in ϕ and θ, the angles of the tracks are reviewed with the help of the FPC. For the routine used here, a direction as input is needed, hence it can only be called after the basic track reconstruction.

This track reconstruction procedure can be done with raw or calibrated hit banks. In the case of raw hits, energy thresholds and time cuts must be applied. In the case of calibrated hits, a basic calibration is done before the track reconstruction, but for a good calibration the polar angle θ is necessary, too. For this reason the calibration

[4]It might be possible to solve the ambiguity problem in a more satisfying way by using, already at this point, the hit information of the other layers. Especially the new FWC, which has the same granularity in ϕ as the FTH and is placed even before it, could be useful. But that has not yet been implemented.

[5]If the track angle is inside the ϕ interval covered by the hit element, which has a width of 15° in the case of the FWC and the FRH, or the neighboring element, the hit angle fits to the track angle.

[6]The FVH resolution in x is actually much better than 30 cm, in the order of 5 cm σ, but to achieve that a detailed time calibration is necessary. To be on the safe side the larger value is used as default.

routine is called again, during the track reconstruction with the θ reconstructed from the track. A new calibrated hit bank is filled and these hits are added to the track, not the original ones.
In principle the calibration could be done even better after the angles have been corrected with the FPC, but the difference in θ is small compared to the resolution achieved in the calibration, and that has not yet been implemented.
Figure 4.1 summarizes the track reconstruction for charged particles.

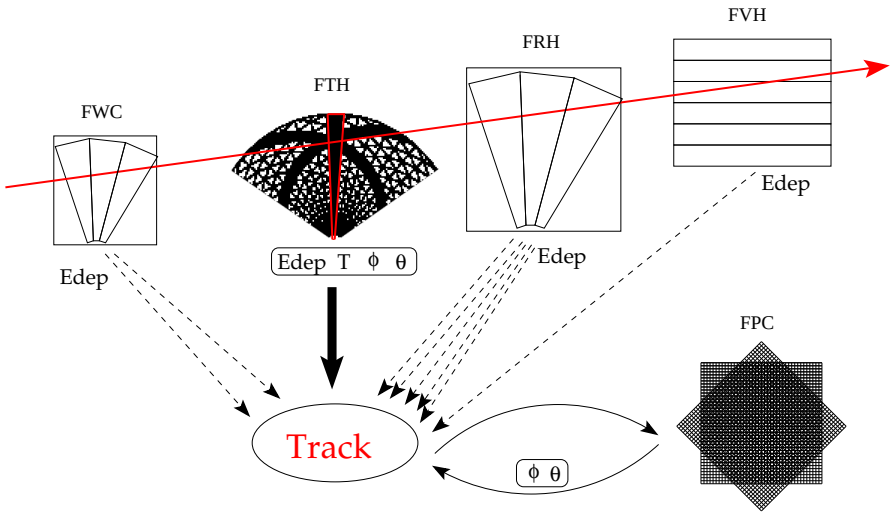

Figure 4.1: *The FD track reconstruction. A particle track flying into the FD can deposit energy in the two FWC, the three FTH, the five FRH layers and the first FVH layer (the new second one is not yet included). Time, θ and ϕ are determined by the FTH, the angles are later corrected using the FPC. The (calibrated) hits are added to the track, the sum of their deposited energies is the total deposited energy of the track.*

Neutral particles do not deposit energy in the plastic scintillator, unless they produce charged, ionizing particles. Hard photons can produce an electromagnetic shower in the thick detectors, the probability in case of the WASA is roughly 50% as is seen in Fig. 4.2. The probability for neutrons to knock out a proton off a nucleus is roughly 1% per cm of plastic scintillator. Hence it is improbable that in the very first layers (FWC and FTH with in sum less than 2.5 cm thickness) a neutral particle is detected.
For this reason the usual definition of a neutral track is the absence of hits in FWC and FTH, although the later layers show hits which can be combined to clusters and tracks. However, the combination of hits into tracks is much more complicated than that for charged tracks, because the tracks look different in size (electromagnetic showers extend over a larger ϕ and θ range than a single particle) and direction (knockout protons do not need to follow ϕ and θ because they generally move in a different direction than the initial neutron). Additionally, many hits will be simply noise, without any connection to a track. Since at the moment there is no interest in neutral particle detection in the FD, the reconstruction of neutral tracks has not

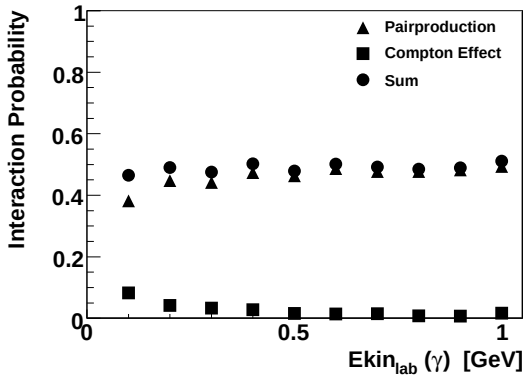

Figure 4.2: *Probability that a photon interacts with the FD material as a function of the photon energy. Squares denote Compton effect, triangles pair production (photo effect is negligible) and the circles present the sum of both effects.*

yet been fully implemented. All hits which are left over in the FRH after the track reconstruction, are stored as neutral tracks, without combining them to clusters. This information gives a measure of the background in an event and the quality of the track reconstruction, which might be used by the user.

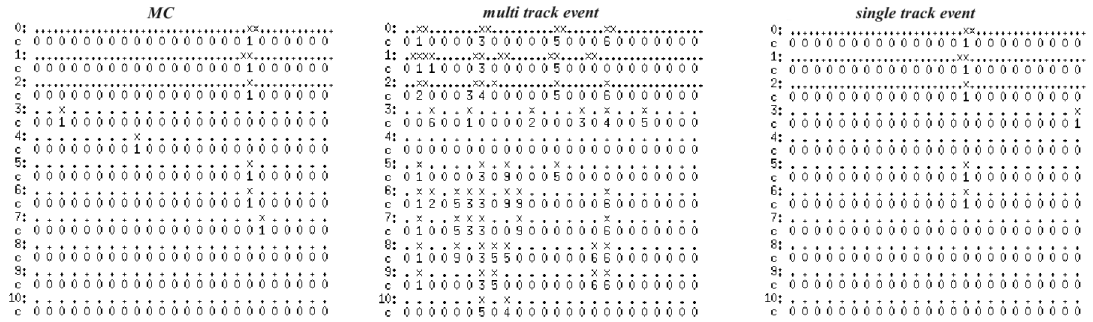

(a) *Monte Carlo Simulation of a single* ^{4}He *track in the FD*

(b) *Experimental data for 1.117 GeV. Selected "bad" event.*

(c) *Experimental data for 1.117 GeV. Selected event, maybe* ^{4}He.

Figure 4.3: *Simple event display for debugging purpose of the forward track finder. The numbers 0 to 10 denote the FD layers (without FRI and FVH2). The dots denote elements, ordered by element number, "x" means a hit in that element. In FWC and FRH one element corresponds to two FTH1 elements, to visualize the shift by half an element of the FWC2 in respect to FWC1, elements in FWC1 and FWC2 are marked with two dots. The lines with "c" at the beginning denote the track number the corresponding hit was added to.*

An example of the simple event display for debugging is shown in Fig. 4.3. This tool helps to understand the principle and the problems of the track finder. The Monte Carlo simulation shows a clear track reconstruction, all hits were found. Note that the element numbers of FTH2 (number 3), FTH3 (number 4) and FVH (number

10) do not correspond to ϕ position, as is the case with FWC, FTH1 and FRH. For experimental data, the situation can be much more complicated, because usually several hits which do not belong to a clear track are recorded and disturb the track reconstruction. Even if there were only clear tracks, but several of them, they could interfere with each other and complicate the track reconstruction.
Figure 4.3b shows a particularly complicated event measured in the experiment. It looks like at least four tracks passed through the FD. The track numbered with 6 in the display could be followed clearly and stops in the last FRH layer. The track numbered with 1 could also be followed, but somehow the hit in FTH1 is lost and put to some other track. Track number 3 seems to undergo some nuclear interaction and created larger clusters in the FRH. Track number 5 seems to stop in FRH1. The hits marked with 9 are defined as neutral tracks.
Figure 4.3c shows a particular good event, which might well be ^{4}He or ^{3}He since it stops in the second FRH layer (number 5). No hit was recorded in the FTH3 (number 4), which is one of the bent layers, which was renewed half a year after this beam time.

4.3 Central Detector Track Reconstruction

Particles flying into the central detector underly the magnetic field of the solenoid, thus charged particles are bent to circles. To follow the trajectory, the MDC is used (see [Jac04]). ϕ and θ angles at the origin, the momentum and the charge of the particles can be extracted.
The next step is the PSB, which is made of thin plastic scintillator stripes. Like the MDC this detector sees only charged particles. It is used both in the trigger and in the track reconstruction for the definition of a charged particle[7].
The last part of the central detector is the SE, which is made of 1012 crystals that detect charged and neutral particles. Very few neutrons reach the SE, hence all neutral tracks in the central detector are assumed to be photons.
All these detectors use very different ways to extract the needed information, thus there are three different "cluster finder" for the central detector. The track reconstruction combines all of them to tracks and stores them in a track bank. Details about the algorithm can be found in [Red10].

4.4 Event Tree

Many pieces of information stored in the raw data are needed only on a low level for the hit and track reconstruction. Once the tracks are known, it is possible to reduce the storage place for the data significantly if only several items of information about the tracks are stored. And more importantly, the data processing speed is increased

[7] A charged particle can also be defined differently, but this is the default way, used in this analysis.

a lot, because all the steps to reconstruct tracks, which are the parts consuming the largest amount of time, do not have to be repeated each time the analysis is redone with slightly different settings.

In this thesis, angles and deposited energies of each cluster in a track and some additional event information are retained in Root TTrees. The idea and the format are taken from M.Bashkanov [Basb]. After further processing, when the particles are identified, a new tree is filled with Lorentz vectors and several more data, which allows very easy histogram plotting.

If simulated data are processed, in addition a tree containing the Lorentz-vectors of the simulated tracks, which also can be extracted by RootSorter, is filled and stored in the same file. That way it is secured that the efficiency and acceptance corrections later on are achieved with the same simulated data.

4.5 Calibration

To come from raw data to deposited energies and times which can be compared to each other, a calibration is necessary.

For the time calibration, the TDC channels have to be related to the time in ns and shifted in a way so that $T = 0$ is the same for all detectors. The different rise times of signals with low and high amplitudes result in different TDC values although the signal actually arrived at the same time. This is the so called 'walk effect' and has to be corrected. Also the light propagation time has to be taken into account.

The most important effects for the energy calibration are the nonuniformity of the light collection, which depends on the geometry of the detector element, and the nonlinearity of the photomultiplier signal. The gain of a photomultiplier is in general not linear, at least not over the full range of amplitudes. Another problem is the so called quenching effect, which is described by Birk's Formula and implemented in the Monte Carlo. Thus it is implicitly taken into account, however for ^{4}He the parameters are not known, but just assumed to be similar to ^{3}He and even these parameters are not known precisely. The physical appearance of the material, like microcracks or coloring due to aging, also effects the performance. A detailed description of the calibration procedure can be found in [Bas06].

Unfortunately at the time the calibration was done the Monte Carlo simulation of the detector was not correct because the new FWC had not yet been included. Consequently the measured energy loss did not fit to the simulated one and a recalibration was necessary. But because the calibration was very good with respect to the separation of ^{3}He and ^{4}He, slight changes, described with a linear function, were enough to achieve a good calibration. For this task ROOT scripts were used, which offered an easy way to change the calibration values and check the resulting $\Delta E - \Delta E$ plots at once. Figure 4.4 shows a screen shot of the recalibration window for the case when the He stops in the second FRH layer. A comparison of the $\Delta E - \Delta E$ plots before and after recalibration can be seen in Fig. 4.5.

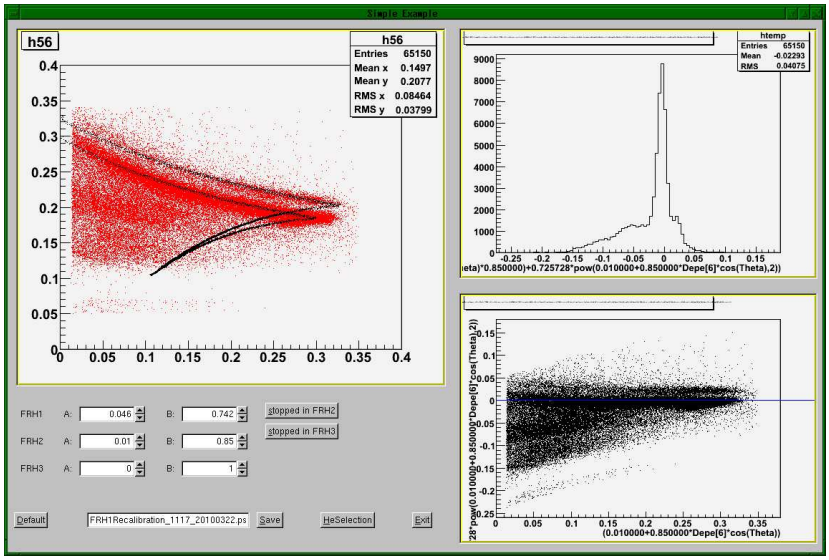

Figure 4.4: *Screen shot of the recalibration window for the case that the particle stops in the FRH2. The left picture shows the deposited energy in FRH1 versus the deposited energy in FRH2, the black lines are simulations for* ^{3}He *and* ^{4}He *(also passing through the FRH2), the red dots are experimental data. The right lower picture shows the deposited energies minus the simulation for* ^{3}He*. If all displayed events were* ^{3}He *a line at* $y = 0$ *would be seen. The projection of this plot to its y-axis is shown in the upper right picture.*

4.6 Magnetic Field Correction for Forward Tracks

Forward going charged particles fly partly through the magnetic field provided by the solenoid. Inside the field their paths follow a helix, outside they are straight lines. Assuming a homogeneous magnetic field, the formula for the correction angle ϕ' [8] is:

$$\phi' = \frac{0.3 \cdot l\, z\, B}{P \cdot cos\theta} \tag{4.1}$$

Here B is the magnetic field strength in Tesla, z is the particle charge in units of the electron charge, P the particle momentum in GeV, θ the polar scattering angle and l the distance the particle covers in the magnetic field in meter. This last parameter is known in principle, but it is better to fit it to the data to account for nonhomogenities of the magnetic field. In this analysis a value of 0.1352 m is used.

A detailed derivation of this formula can be found in [Bas06].

[8] Only the azimuthal angle is changed, the polar angle is not affected by the magnetic field.

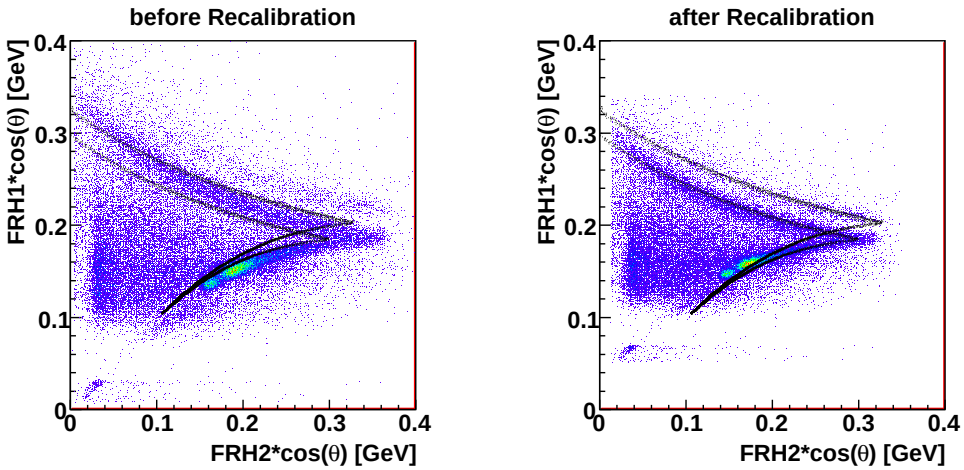

Figure 4.5: *Deposited energy in FRH1 versus deposited energy in FRH2. Black lines are Monte Carlo data for* ^{3}He *(lower line) and* ^{4}He *(upper line), the colored dots are experimental data. The left side is before recalibration, the right side afterwards. Note that only the "banana" of the tracks which are stopped in the FRH2 is of interest in this case, not the back bending part.*

4.7 Particle Identification

4.7.1 Forward Detector

Charged particle identification in the forward detector is achieved by the $\Delta E_i - \Delta E_j$ method, where i, j denote the ΔE-detector passed. The energy loss of a particle is described by the Bethe-Bloch-Formula and depends on its mass and charge. Hence the relation between the energy loss in one part of the detector and in another part depends on the particle type. Figure 4.6 shows a typical combination used in this analysis: the deposited energy in the FRH1 versus the FRH2 for simulated events, different colors denote different particles. The falling branches belong to energies where the particle stops in the FRH2, thus the deposited energy in the FRH2 rises with rising energy, while the deposited energy in the FRH1 decreases. If the particle is fast enough to punch through the FRH2, the energy deposited here decreases until the particle reaches the minimum ionizing point, where all particles, independently of their mass and charge, deposit roughly 2 MeV per cm. Obviously the best separation is achieved on the falling branch, where protons and deuterons are well separated, while ^{4}He and ^{3}He are very similar. At the energies which were measured for this thesis, both ^{4}He and ^{3}He are far away from the minimum ionizing point and are well separated from deuterons and protons.

In the case that the particle stops in the FRH1, the thin plastic scintillator layers, which have a much lower energy resolution than the thick ones, must be used for the particle identification. To increase the resolution here, the sum of the FWC1,

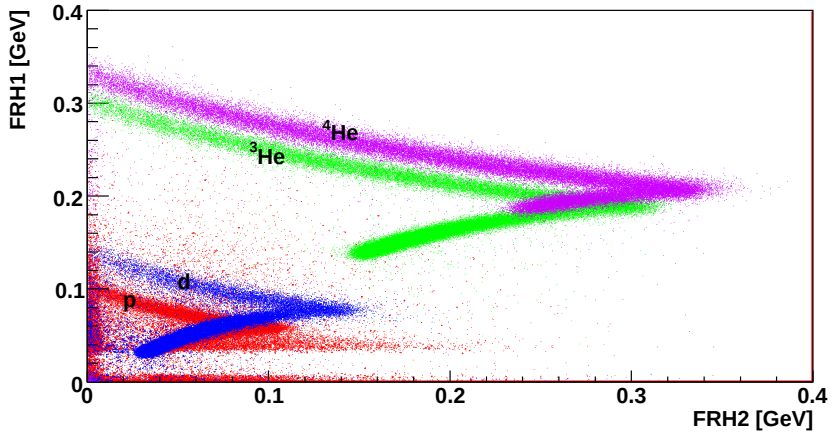

Figure 4.6: *Deposited energy in the FRH1 versus deposited energy in the FRH2 for simulated single events. Red points are protons, blue deuteron, green* ^{3}He *and violet* ^{4}He*. Here the Monte Carlo simulations of single tracks were used.*

FWC2, and FTH1 is used[9].

Due to different path lengths in the detector the deposited energy is different for different polar angles. To correct for that effect the deposited energy is multiplied by $cos\theta$ [10].

^{4}He and ^{3}He both are very well distinguished from the other particles, but the separation between them is not as clear. For the case that the particle stops in the FRH1 a separation with the $\Delta E_i - \Delta E_j$ method is only possible for a few elements. In the analysis the constraint to fulfill the kinematics of the reaction $dd \rightarrow {}^4He\pi^0\pi^0$ helped a lot to distinguish between ^{3}He and ^{4}He.

Neutral tracks in the forward detector are currently not considered. In principle photons and neutrons could be distinguished by the spread of the signals they produce. Photons initiate an electromagnetic shower, which affects several elements, while neutrons are detected by their recoil protons. Hence the tracks, the pulse shapes and the times of these secondaries should look very different.

4.7.2 Central Detector

All neutral particles in the CD are regarded as photons, because the probability of neutrons to arrive at and produce a signal in the SE is very low due to kinematics. Charged particles can be separated from each other by the relation between their momentum (measured in the MDC) and the deposited energy in the SE. The sign of their charge can be determined in the MDC via their curvature. Figure 4.7 shows a single event in the MDC.

[9] The FTH2 and FTH3 are not used, because the elements of these detectors have very large nonuniformities since the elements are shaped like Archimedian spirals.

[10] In case if the FWC, which is titled by 20° the deposited energy is multiplied by $cos(\theta + 20°)$.

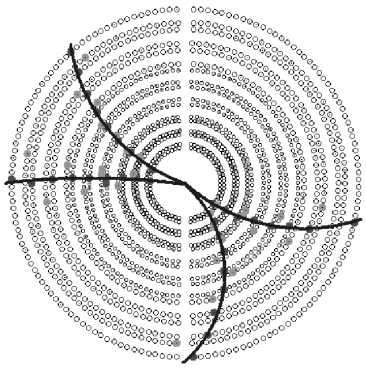

Figure 4.7: *Single event in the MDC. Four tracks are recognized (blue lines). The red dots denote hit tubes in the layers parallel to the beam pipe, the blue dots denote hit tubes in the skewed layers [Yur].*

4.8 Kinetic Energy Reconstruction

To reconstruct the kinetic energy for ^{4}He and ^{3}He, the deposited energies measured in the FD are compared to the simulated ones. Figure 4.8 shows the deposited energy versus the kinetic energy for simulated ^{4}He events without correction for the different path lengths at different angles. Above a kinetic energy of approximately 2 GeV the slope of the band is almost constant because the particles approach the minimum ionizing point even for the farthest detector, the FRH5. The kinetic energy reconstruction is no longer possible or has a very large error, respectively. In case of ^{4}He that does not matter, since the energies at COSY are anyway not that large, but for protons, deuterons and of course pions this problem arises at much earlier kinetic energies.

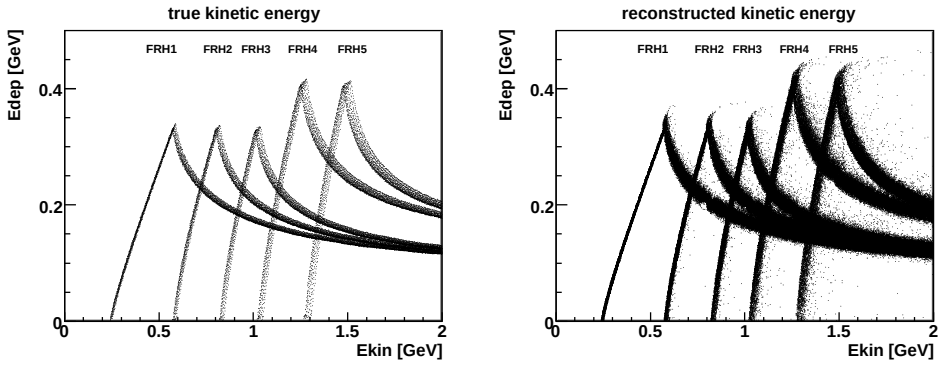

Figure 4.8: *Deposited energy versus kinetic energy without angle correction for simulated* ^{4}He *events. The different branches show the deposited energy in different FRH layers. On the left side the true simulated kinetic energy is plotted, on the right side the reconstructed. The maximum kinetic energy of the* ^{4}He *originating from* $\mathrm{dd} \rightarrow {}^4\mathrm{He}\pi^0\pi^0$ *is 1 GeV at the highest measured energy 1.4 GeV.*

As a basis for the comparison, single tracks in the forward detector at several kinetic energies were simulated. For each energy and θ bin the resulting deposited energy distribution was fitted with a Gaussian. Finally the fit parameters of this Gaussian were stored in ROOT TTrees. These trees were provided by C.Pauly [Pau].
For each energy in the θ bin next to the experimental value the sum of squares of the difference between the measured and the simulated deposited energy in each detector was calculated, weighted by the error of the Gaussian fit.

$$D = \sum_{detector} \left(\frac{E_i - E_i^{sim}}{\Delta E_i^{sim}}\right)^2 \tag{4.2}$$

The weighted mean value of the 5 best values for D was used as kinetic energy. Of course only detectors with a hit in both simulated and reconstructed data were considered.
The sum could be built of all detectors or only a subset, e.g. the thin layers at the beginning of the FD could be rejected, since their energy resolution is bad anyway. As the quenching effect, which changes the light to energy correlation in case of high energy deposit, is not perfectly well described for ^{4}He, the calibration for particles stopped in a detector could be worse (or better) than for particles punched through. In order to avoid mixing both versions one might use only the layer where the particle stopped, or only the other ones.
It turns out that in the cases regarded in this thesis the results for the different possibilities are actually very similar. Figure 4.9 shows the result in case all layers of the FD are used for a sample of simulated ^{4}He$\pi^0\pi^0$ data. The reconstruction is independent of the polar angle θ, but the energy dependence is strong. The spike in the uncertainty around a kinetic energy of roughly 0.75 GeV results from the transition from the second FRH layer to the third one. Here the FRI, which is not included in the track reconstruction is situated. The energy deposited here is not measured, hence the kinetic energy of particles stopping in these few cm cannot be reconstructed well.

4.9 WASA Monte Carlo WMC

In contrast to the analysis program, which was completely changed in connection with the relocation to COSY, the framework of the simulation program is still the old, well tested program designed for CELSIUS-WASA. The Monte Carlo program is written in FORTRAN and uses the GEANT3 library developed at CERN. The output is written in the ems format, like the experimental data. As input either an external event generator, providing a set of Lorentz-vectors from a certain reaction, or an internal event generator producing e.g. one single track in the FD, can be used.
All detector components, supporting structures and the magnetic field of the solenoid are simulated and can be controlled with parameter files. All reactions a particle can undergo on its way through the detector are simulated, including the quenching

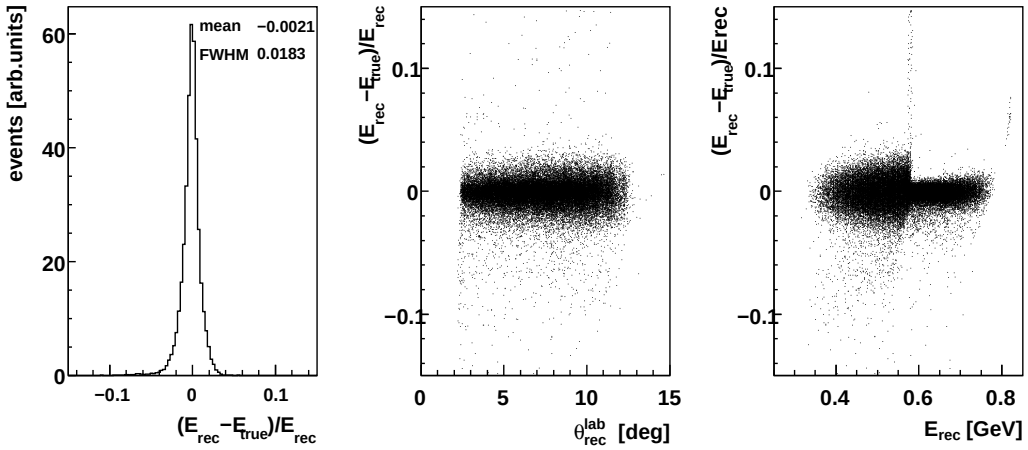

Figure 4.9: *Kinetic energy reconstruction of simulated events.The left plot shows the relative difference between the reconstructed and the true kinetic energy. The dependences on the θ angle and the reconstructed energy are plotted in the middle and on the right, respectively.*

effect. But effects like the light propagation, the response of the photomultipliers or electronic noise are not taken into account. To achieve the same resolution in the Monte Carlo simulations as in the experiment, smearing parameters are applied when the simulated data are processed by the analysis program.

4.10 Event Generation

For the event generation the ROOT library TGenPhaseSpace is used. A set of Lorentz-vectors for the particular n-body reaction is generated where each event gets a weight attributed so that the weighted distribution follows the phase space distribution. Thus the events are evenly distributed over all possible combinations, but weighted very differently. In all plots and calculations the weight must be taken into account. If a distribution different from phase space is requested, the weights are changed to fit the desired distribution.

Another approach is to reject events, while the probability to be rejected is calculated for each event. To find this probability, the given weight is compared to a random number between zero and the largest possible weight. The event is rejected if the random number is larger than the weight. In this method the events are not evenly distributed, but regions where in the first method the weight would be large are higher populated than regions with a small weight. All events generated in this second approach have the same weight, like the experimental data.

In order to obtain a distribution different from phase space the corresponding function is multiplied to the phase space weight and the result is compared to the random

number[11].
In this work the latter procedure was used. Since the statistics is not infinitely large, the maximum of the random number should be larger than the maximum weight. Here a value approximately twice as large was chosen.

[11] Of course the maximum of the random number is also changed so that it corresponds to the new largest weight.

5 *Analysis of the Reaction* $dd \to {}^4He\pi^0\pi^0$

A long and winding road
that leads to your door
will never disappear
I've seen that road before

The Beatles [Len69]

It is a long and winding road from the raw data stored on discs just after the experiment to the differential spectra and the total cross sections shown in a paper. In this chapter the turns, and sometimes turnarounds, of that road will be described. As a first step, Monte Carlo simulations give an understanding of the kinematics of the reaction and how it can be identified in the detector. This allows to set up a trigger for the experiment. A preselection of the data to get rid of events which obviously do not belong to the interesting reaction is necessary to reduce the amount of data to be processed substantially. What survives this first selection has to go through a more sophisticated analysis involving cuts on the track parameters and a kinematic fit to identify the ^{4}He-nuclei and the pions. Figure 5.1 visualizes the analysis chain. If not mentioned differently the plots shown in this chapter describe the analysis of the 1.117 GeV data. The steps for other energies are essentially the same, the according pictures can be found in the appendix.

5.1 The Reaction $dd \to {}^4He\pi^0\pi^0$

The isospin of the deuteron as well as of the ^{4}He is zero, the pion is an isospin triplet. Thus, due to isospin conservation, the two pions must be in an isospin $I = 0$ state. This is especially interesting with respect to the ABC effect, which, as noted in the introduction, only occurs in the $I = 0$ case, hence the reaction $dd \to {}^4He\pi^0\pi^0$ offers access to a clear situation. Also the background from single and triple π^0 production is not allowed by isospin conservation [1], only $\pi^+\pi^-\pi^0$ production is possible, but negligibly small compared to $\pi^0\pi^0$ production at the energies of interest here.
Since the separation between ^{4}He and ^{3}He is very difficult, this is also a source for background due to wrongly identified ^{4}He. ^{3}He could originate either from direct production ($dd \to {}^3He n\pi^0\pi^0$, $dd \to {}^3He n\pi^0\pi^0\pi^0$), or from ^{4}He breakup due to nuclear interactions.

[1] Charge symmetry breaking in the reaction $dd \to {}^4He\pi^0$ has been observed at IUCF [Ste03], and is investigated by the WASA experiment as well. However, the cross section is negligible compared to the double π^0 cross section.

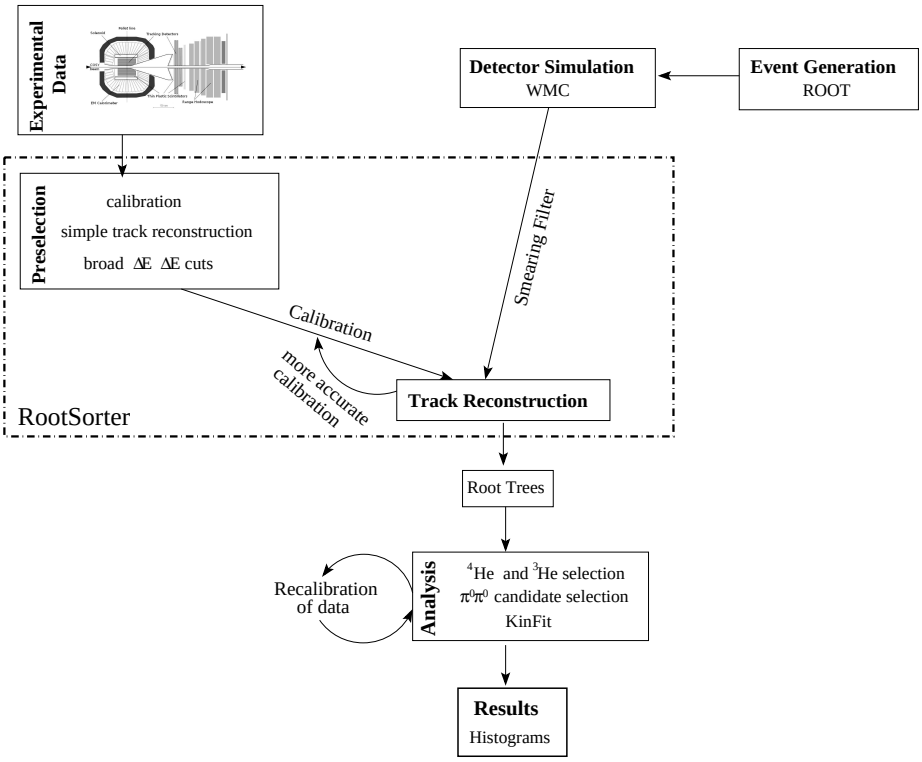

Figure 5.1: *Flow chart of the analysis chain for the reaction* dd → ^{4}He$\pi^0\pi^0$

5.1.1 Kinematics

The reaction dd → ^{4}He$\pi^0\pi^0$ was measured in an energy range from 800 MeV to 1400 MeV. At all energies the ^{4}He intrudes the FD, the largest polar angle θ is 15° for 1400 MeV. Figure 5.2a shows the laboratory scattering angle versus the kinetic energy of the ^{4}He. The lines mark the area which is covered by the forward detector. Only a fraction of the ^{4}He particles of about 10% is lost in the hole for the beam pipe below 3° polar angle.
This plot also gives a qualitative insight into other observables: points with the same invariant mass of the $\pi^0\pi^0$ system lie on ellipses around the center, with the innermost ellipse corresponding to the largest invariant mass. The center of mass scattering angle θ of the ^{4}He follows radial lines, the downward pointing lines correspond to large scattering angles (going backward in the center of mass system).

The main decay channel of π^0 is $\pi^0 \to \gamma\gamma$ with a lifetime of 10^{-16} s, which corresponds to a mean propagation distance of < 25 nm. That means a π^0 itself cannot be seen in the WASA detector, but only the two decay photons. Thus the signature of two π^0 are two pairs of photons, each pair having an invariant mass which fits to the pion mass. The central detector covers an angular range from 20° to 169° polar angle; outside this range photons cannot be detected, hence pions which emit a photon in this direction cannot be reconstructed and the event is rejected[2]. For

[2]Since all other particles are measured, the missing photon could in principle be reconstructed

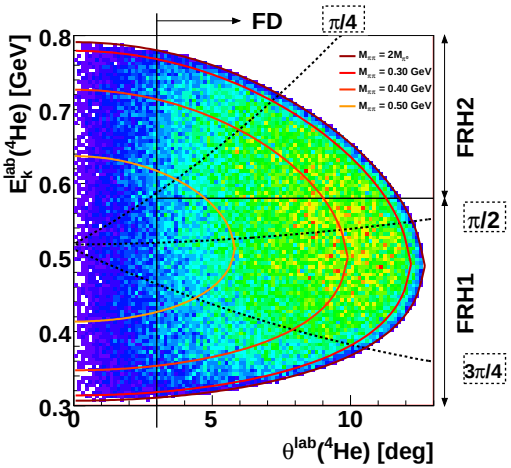

(a) *Particles below a polar angle of 3° fly in the beam pipe and cannot be detected by the FD.* ^{4}He *with a kinetic energy of 250 MeV reach the FRH1, above 580 MeV the FRH2. The ellipses indicate regions which correspond to the same invariant mass of the* $\pi^0\pi^0$ *system. The radial lines denote regions with the same center of mass polar angle* θ*.*

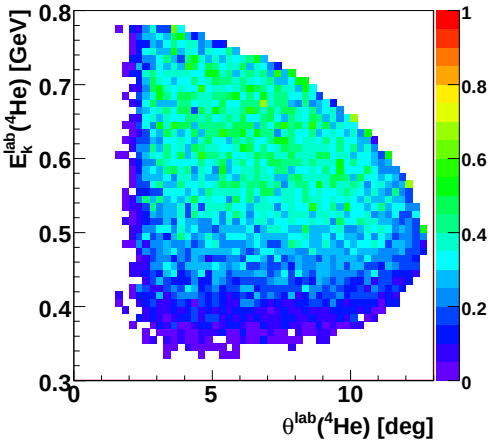

(b) *Efficiency and acceptance correction as function of* $E_{kin}^{lab}(^4\text{He})$ *and* $\theta^{lab}(^4\text{He})$*: reconstructed events divided by the input for the simulation. The drop towards small* ^{4}He *angles and low* ^{4}He *kinetic energies follows from the detection limitation for* γ *to* $20 - 169°$ *and for particles in the FD to* $3 - 18°$*.*

Figure 5.2: *Monte Carlo phase space simulation of the reaction* $\text{dd} \rightarrow {}^4\text{He}\pi^0\pi^0$ *for a beam energy of 1.117 GeV. The plots shows the kinetic energy of the* ^{4}He *in the laboratory system* E_{kin}^{lab} *versus its polar angle* θ^{lab}*.*

that reason the acceptance for pions going in the center of mass system in the forward direction (and the ^{4}He going backward respectively) is less than for the pions which are emitted backward[3]. This can be seen in Fig. 5.2b, which again shows the laboratory scattering angle versus the kinetic energy of the ^{4}He, but the ratio between the reconstructed and the simulated events. In the region with small ^{4}He laboratory angle and small kinetic energies a clear drop in the acceptance is seen. However, except for this part, the acceptance is rather flat and homogeneous with a value of roughly 0.5, thus the model dependence of the efficiency and acceptance corrections should be small above a ^{4}He laboratory kinetic energy of 450 MeV.

5.2 Experiment

In summer 2007 the new FWC and the renewed PS were installed and shortly after the installation two weeks beam time in September were dedicated to the commission

via energy and momentum conservation.

[3]In the laboratory system the particles are boosted in forward directions, e.g. a ^{4}He going backward in cms is going "less forward" (thus at a larger θ angle) in the laboratory system, but it is still detected in the FD.

of the new detectors and a test of the first deuteron pellets and deuteron beam at WASA-at-COSY. During these weeks it was possible to take data for the double pion production at 1.0 and 1.2 GeV. Later that year, in December, two weeks were dedicated to measure the same reaction at seven more energies between 0.8 and 1.4 GeV.
Both beam times ran very smoothly, the COSY-beam as well as the pellet target had no major problems[4]. The pellet target had to be heated up and cooled down again for 8 hours every 40 hours (roughly) [5]. The magnetic field of the solenoid was 1 T, the pellet frequency could not be measured, because the counting system was broken. All together 1730 files (1213 during the dedicated and 520 during the commissioning beam time) could be stored, each 20 GB large, corresponding to about 30 min data taking (depending on luminosity and trigger settings). Such a file is called a run and named by consecutive numbers. Table 5.1 presents the runs used for the analysis. The only trigger requirement was one track in the forward detector, based on the

energy/GeV	**No. runs**	**Main Trigger**	**No.** ^{4}He$\pi^0\pi^0$
0.8	342	fHedwr1 & Vfrhc1 (and fHedwr1)	26263
0.9	54	fHedwr1 & Vfrhc1	40208
	1	fHedwr1	63
1.0	143	fHedwr1	26398
1.05	69	fHedwr1 & Vfrhc1 (and fHedwr1)	33425
1.117	102	fHedwr1	11878
1.2	39	fHedwr1	2129
1.25	80	fHedwr1	11500
1.32	202	fHedwr1	41901
1.4	39	fHedwr1	7817

Table 5.1: *Run Summary: Number of runs which could be used, the main triggers for these runs and the number of* dd $\rightarrow$ ^{4}He$\pi^0\pi^0$ *events in the final differential distribution plots. "*hHedwr1*" denotes the standard trigger used, essentially one track in the forward detector. "*Vfrhc1*" means that additionally a veto on FRH3 was included.*

coincidence of one sector in the FWC1, FWC2, FTH1 and FRH1 ("fHedwr1"). The thresholds on the FWC layers and the FRH1 were adjusted for each energy to filter events with high energy deposit. That way a very efficient Helium selection was possible, allowing all channels with ^{4}He and ^{3}He. At some energies also a veto on

[4]Except some problems during the second half of the commissioning beam time, as turned out later (see Appendix 9.8).

[5]This problem was probably due to impurities in the system. In this case the small hole in the nozzle, which has to be passed by the pellets, is filled up and hinders the pellets to pass. The reason for the impurities can be a leak in the system, which can be very hard to identify if it is situated at an inaccessible place. Heating up the pellet system often helps, because the impurities liquidize and drain off.

the FRH3 was used ("Vfrhc1"), but in these cases an additional trigger without veto was set up (except for 0.9 GeV). It turned out that for some energies one of the thresholds actually cut the interesting data in a few detector elements. However these elements could be identified and excluded from the analysis.

5.3 Preselection

After the commissioning beam time in September an analysis chain was developed for a very fast and rough preselection to reduce the amount of data, and hence the time needed for the further processing. The preselection like the trigger required one track in the forward detector and did not put any condition on the central detector. However the forward detector track could now be identified as He, using a track finder based on pure geometry (in contrast to the usual track finder, which takes more time). Exactly one track which hits the FWC1, FWC2, FTH1, FTH2 and/or FTH3 and FRH1 was demanded plus a cut on the He band. The cut on exactly one track was quite strict. Since the statistics in all energies was large enough, the clear case was preferred. Figure 5.3 shows the energy deposited in the first FRH

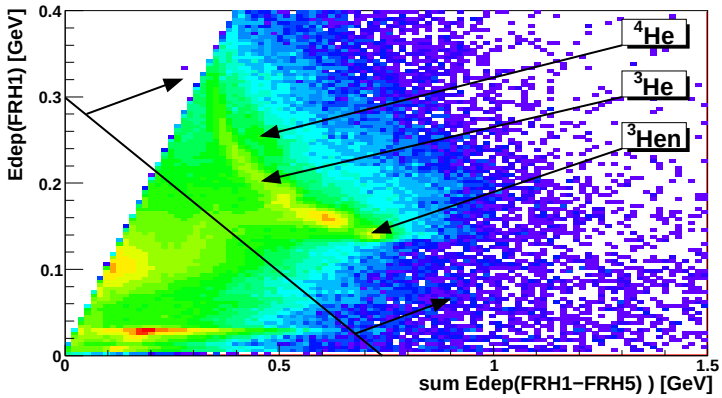

Figure 5.3: *Preselection: Deposited energy in the first layer of the FRH versus the sum of all FRH layers for tracks punching through the FRH1. Tracks are reconstructed using the preselection analysis. The line shows the cut used.*

versus the sum of all five FRH layers in a logarithmic scale for 1.05 GeV. The ^{3}He band in the middle of the picture is clearly seen. Since Helium deposits much more energy than deuterons or protons, it is very well separated. The fastest ^{3}He particles originate from the reaction $dd \rightarrow {}^3\mathrm{He}n$ and stop mainly in the fourth layer of the FRH. The kink arises from the FRI, which is situated between the second and third layer of the FRH, and not taken into account in the energy sum. Above the ^{3}He band the ^{4}He band is hardly visible (for an untrained eye), which does not extend as far as the ^{3}He because it is heavier and slower. At this beam energy it stops latest in the second FRH layer. The line shows the cut used in the preselection. All tracks on the right side of the line pass the preselection. Figure 5.4 shows the number of

events which pass the different cuts. After all cuts the amount of data is reduced by a factor of 10. Analyzing one run takes roughly 2 hours, all data could be processed in a few weeks.

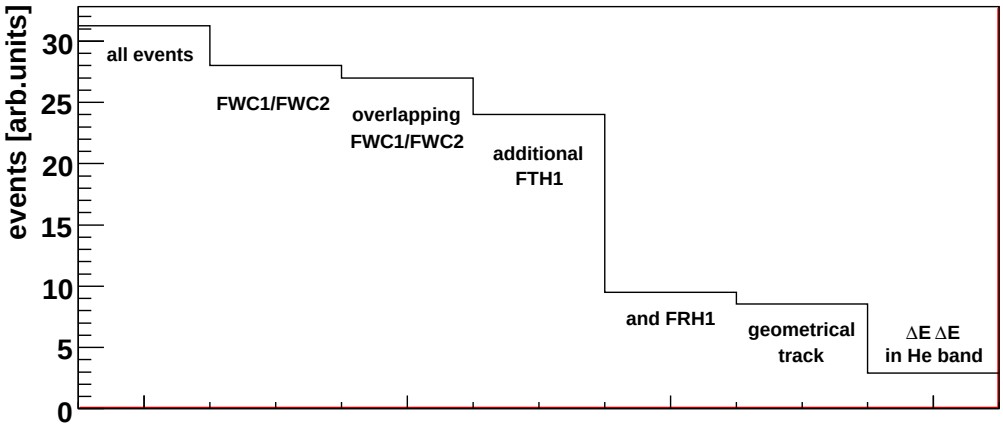

Figure 5.4: *Number of events which passed the different cuts of the preselection.*

5.4 Selection of dd → ^{4}He$\pi^0\pi^0$

After the preselection, the raw data are transformed into Root trees, which store all interesting information about the tracks (see section 4.4). All further processing is done with these trees. The analysis uses the whole Root-Sorter package, thus track reconstruction and calibration is much more sophisticated than the basic but fast version elaborated for the preselection.

5.4.1 Forward Detector: ^{4}He Selection

First, several basic cuts, which are listed in table 5.2, are applied, to have only good tracks with useful hits. With this data sample the recalibration and He selection is done. For 1.117 GeV the ^{4}He stops either in the first or in the second FRH layer. In the case that it stops in the FRH2 the interesting ΔE-ΔE plot is FRH1 versus FRH2. Figure 5.5b shows this plot for all tracks (a). The ^{3}He and ^{4}He "bananas" are seen among a large background. A part of the ^{3}He passes through the second layer and lies on the back bending band. Plot (b) in that Fig.5.5b shows the same plot with the basic cuts applied. Apart from the He only little background is left, which can be cut out easily. ^{3}He and ^{4}He are clearly separated.
The less populated band between 0.02 and 0.1 GeV in the FRH1 is due to the threshold used in the trigger: Only for hits which deposit more than ∼0.08 GeV a TDC signal is measured. With less accuracy the time can also be extracted from the ADC signal. This is done only if no TDC time can be assigned to the hit and if

Basic conditions		
for each event:		
number of charged forward tracks > 0		
number of neutral central tracks ≥ 3		
for each Forward Track (additionally)		
Edep(FWC1) >0	Edep(FWC1) < 0.04	
Edep(FWC2) >0	Edep(FWC2) < 0.04	
Edep(FTH1) >0	Edep(FTH1) < 0.04	
Edep(FRH1) >0	Edep(FRH1) < 0.4	
Edep(FRH1-FRH5) > 0	Edep(FRH1-FRH5) < 1.5	
Edep(FWC1) $> 0.003 \cdot$ Edep(FWC2)		
$\Theta > 1°$	$\Theta < 18°$	
for each Central Track (additionally)		
Edep(MDC)==0	Edep(PS)==0	
$\Theta > 0.3$	Ekin < 0.005	
Condition for Forward Track to ...		
stop in FRH1		
Edep(FRH2) $= 0$		
stop in FRH2		
Edep(FRH3) $= 0$		
Edep(FRH2) >0	Edep(FRH2) < 0.4	
stop in FRH3		
Edep(FRH4) $= 0$		
Edep(FRH2) >0	Edep(FRH2) < 0.4	
Edep(FRH3) >0	Edep(FRH3) < 0.4	

Table 5.2: *Basic cut conditions, Edep(X) denotes the deposited energy in detector layer X in GeV.*

the ADC is below some value, which is a parameter of the analysis. Here this value was set to 0.02 GeV.
In the case that the He already stops in the FRH1, the corresponding ΔE-ΔE plots are the FWC or the FTH versus FRH1. That means one axis is given by a thin detector (3 mm for the FWC, 5 mm for the FTH) and has a much lower resolution than the thick (11 cm) FRH. Consequently the separation between ^{4}He and ^{3}He is much worse and can only be done for a few detector elements. Figure 5.5a shows the sum of the first three layers (FWC1, FWC2, and FTH1), which yields a slightly better resolution, but still, a direct ^{4}He identification is not possible. Again the sparsely filled band in the FRH1 due to the threshold is obvious.
When the analysis was started, the first idea was to use the few elements which allow a separation. The statistics is large enough that such a cut would not cause severe problems. But with such a cut a part of the interesting events might be rejected

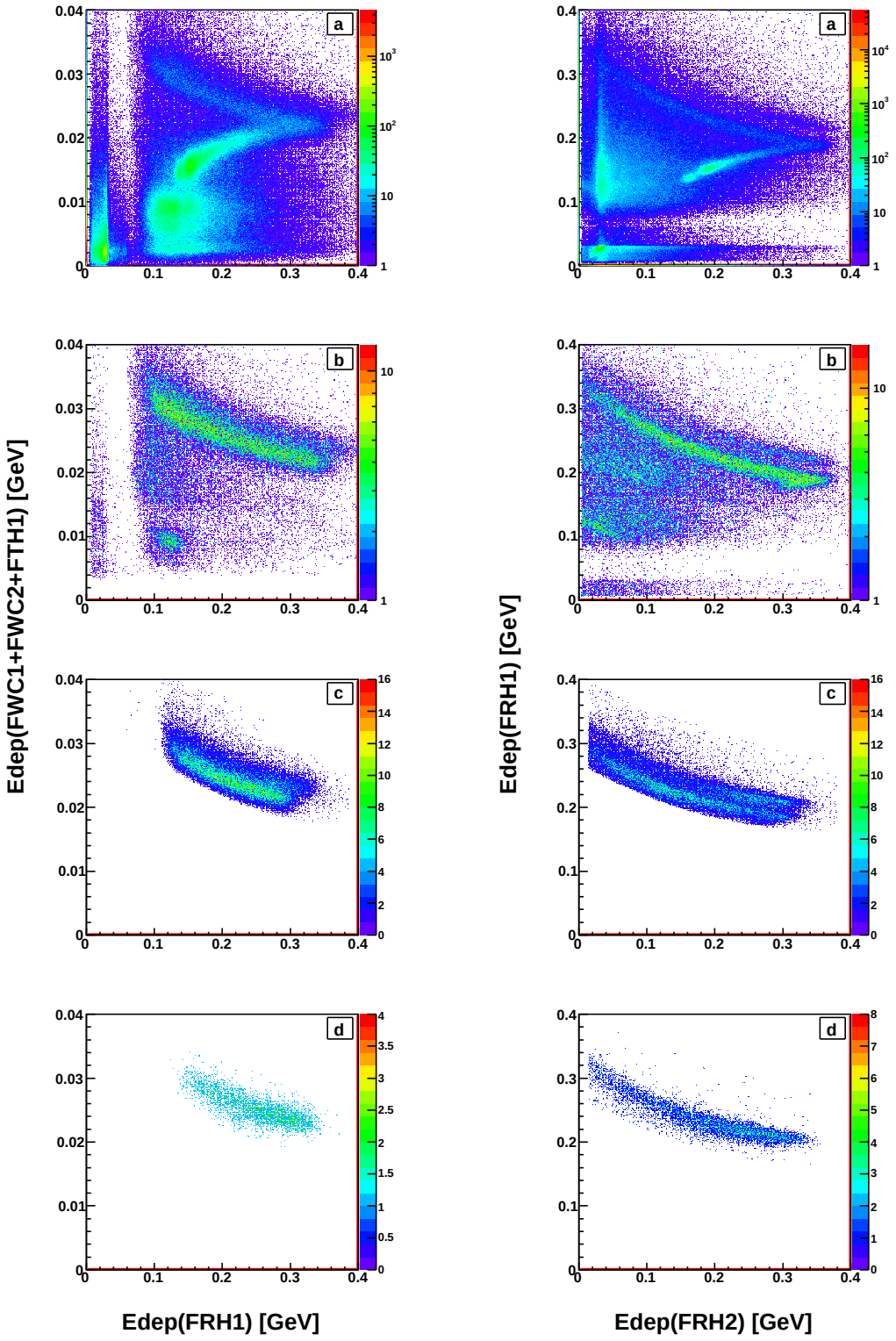

(a) *Tracks stopping in FRH1* **(b)** *Tracks stopping in FRH2*

Figure 5.5: ^{4}He *and* ^{3}He *identification for tracks stopping in FRH1 (left row) and FRH2 (right row): Plots a) show all tracks, b) all tracks which fulfill the basic cuts. The plots are in logarithmic scale and only 10 runs were used, roughly 10% of all data for* $T_d = 1.117$ GeV. *In the last two rows only tracks are plotted with identified* $\pi^0\pi^0$*: c) without further cuts, d) with a cut on the probability function of the kinematic fit* ($Prob(\chi^2, 6) > 0.2$). *Here a linear scale is used.*

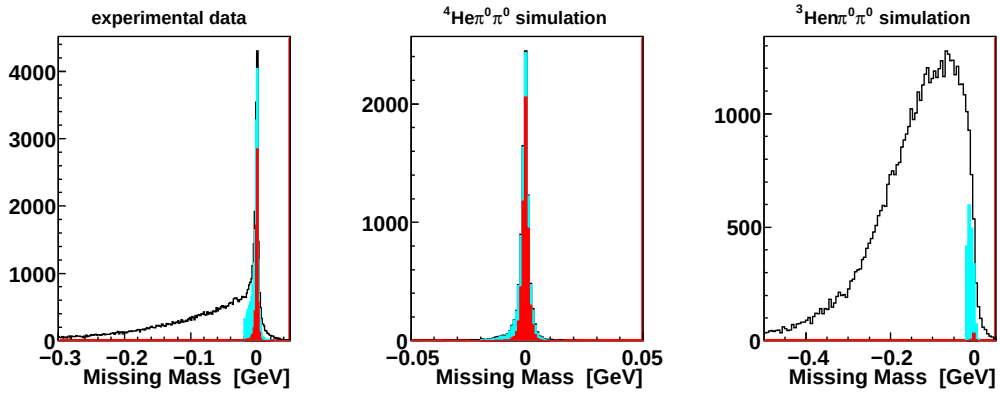

Figure 5.6: *Missing Mass for experimental data (left), a Monte Carlo simulation of* dd $\rightarrow$ ^{4}He$\pi^0\pi^0$ *(middle) and a Monte Carlo simulation of* $dd \rightarrow$ ^{3}He$n\pi^0\pi^0$ *(right). The solid line depicts the spectrum without any cuts except the basic ones and the request for* $\pi^0\pi^0$*. For the cyan shaded area momentum and energy conservation cuts have been applied, and the filled red area marks the events which are left after the kinematic fit (45 events in case of* ^{3}He$n\pi^0\pi^0$*, hardly visible). Note the different scales on the x-axes.*

or some of the background events might be accepted. This imposes a systematic error which is difficult to estimate, since it is hard to check the outcome or compare different cuts.

However it turned out that after $\pi^0\pi^0$ identification and kinematic fit with the assumption that the forward track is a ^{4}He particle, very few ^{3}He particles are left over in the corresponding band. The two lower plots of the figures 5.5b and 5.5a show the same ΔE-ΔE plots as the two upper rows, but only events with identified $\pi^0\pi^0$. First (c) all such tracks are plotted, then (d) a cut on the probability function of the kinematic fit is applied ($Prob(\chi^2, 6) > 0.2$ [6]). Almost all ^{3}He are removed with this cut, thus a tedious ^{4}He/^{3}He separation based on these ΔE-ΔE plots is not necessary. And it is possible to compare different probability cuts and hence understand the systematic effects.

The reason for the strong background reduction by the kinematic fit is that the kinematics for ^{3}He$n\pi\pi$ production, the most probable background from ^{3}He, is very different from that for dd $\rightarrow$ ^{4}He$\pi^0\pi^0$. Figure 5.6 shows the missing mass distribution after the basic cuts are applied and $\pi^0\pi^0$ are identified (but before the kinematic fit) for the experimental data, a Monte Carlo simulation of dd $\rightarrow$ ^{4}He$\pi^0\pi^0$ and a simulation of $dd \rightarrow$ ^{3}He$n\pi^0\pi^0$. The number of events of the two MC simulations is chosen so that the ΔE-ΔE plot of the experimental data and the combination of both simulations look similar.

[6] The function $Prob(a, b)$ gives the probability for the χ^2 value a of a fit with b degrees of freedom. Thus $Prob(\chi^2, 6) > 0.2$ rejects all events with a probability of less or equal than 20% that this particular χ^2 value appears in the kinematic fit of the reaction dd $\rightarrow$ ^{4}He$\pi^0\pi^0$, which has 6 degrees of freedom.

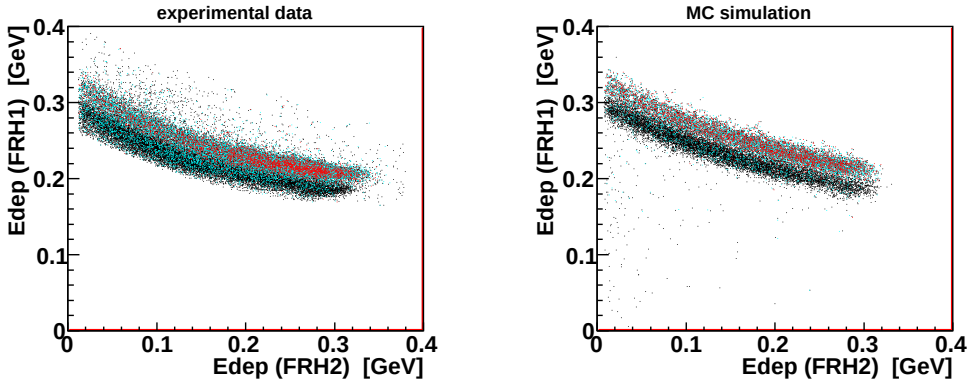

Figure 5.7: *ΔE-ΔE plot for the experimental data (left) and Monte Carlo simulations of* dd → ^{4}He$\pi^0\pi^0$ *and* $dd \rightarrow {}^3\mathrm{He}n\pi^0\pi^0$ *(right). The black dots show the events after the* $\pi^0\pi^0$ *are selected but no further cuts are applied. The blue dots show the events which fulfill the energy and momentum conservation cuts and the red dots show the final result after a cut on the* χ^2 *of the kinematic fit.*

Without any further cuts (solid line) the experimental data and the ^{4}He simulation peak at zero, but the experimental data show a large tail from the ^{3}He background, as expected. On the other hand the $dd \rightarrow {}^3\mathrm{He}n\pi\pi$ distribution is spread over a large area and of course not peaking at zero. If momentum and energy conservation are applied[7] the biggest part of the $dd \rightarrow {}^3\mathrm{He}n\pi\pi$ is cut (cyan area). Applying a cut on the probability function of the kinematic fit ($Prob(\chi^2, 6) > 0.2$) reduces the amount of $dd \rightarrow {}^3\mathrm{He}n\pi^0\pi^0$ even more, leaving only about 0.03% of the original simulated events (red filled area), which is hardly visible.
This is seen also in the ΔE-ΔE plot: Figure 5.7 shows the deposited energy in the FRH1 versus the FRH2 for experimental data and a Monte Carlo simulation of both dd → ^{4}He$\pi^0\pi^0$ and $dd \rightarrow {}^3\mathrm{He}n\pi^0\pi^0$. The same number of events was plotted as in the missing mass plot 5.6. After the cut on momentum and energy conservation almost all ^{3}He is gone and further applying the kinematic fit leaves only very few ^{3}He events.

5.4.2 Central Detector: $\pi^0\pi^0$ Selection

Since a π^0 decays into two photons, four neutral tracks in the CD, which combine into two pairs, each of them having an invariant mass of roughly the π^0 mass, have to be found.
Like in the FD a few basic cuts are applied to the central tracks. All neutral tracks which fulfill these conditions (see table 5.2) are taken into account as possible pho-

[7] Here the following cuts were applied (with MM the total missing mass of the system and ME the total missing energy in GeV, and the momenta in GeV/c): $MM > -0.02$ *and* $ME < 0.01$ *and* $|P^{cm}_{sum}| < 0.2$ *and*
$|Px^{cm}_{sum}| < 0.2$ *and* $|Py^{cm}_{sum}| < 0.2$ *and* $|Pz^{cm}_{sum}| < 0.5$

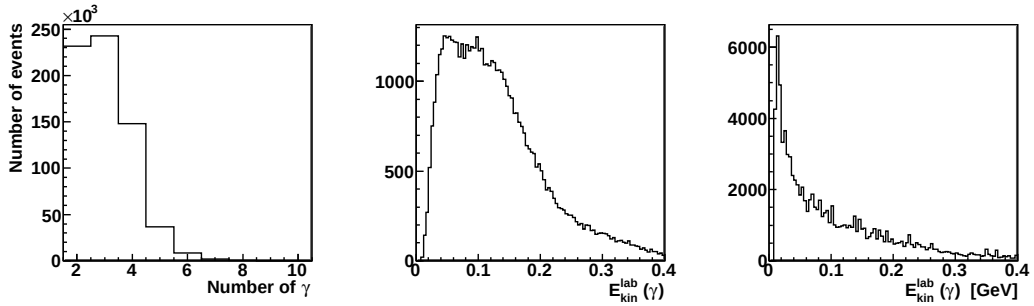

Figure 5.8: *The left plot shows the number of photons which passed the basic cuts. The energy distribution of the photons which are assigned to a π^0 is plotted in the middle, the distribution of the photons which are not assigned to a π^0 on the right.*

tons originating from the π^0 decay. This might be more than four, because there is a sizable photon background. Figure 5.8 shows the number of photons taken into account and their energy distribution. The energy distribution of the photons which are not assigned to a pion peaks at zero with a long tail towards higher energies, while the energy distribution of the photons which are assigned to a pion shows a broad peak at 0.1 GeV.

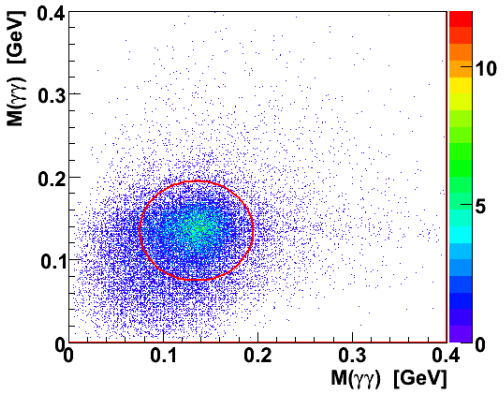

Figure 5.9: *Invariant mass of one γ pair versus the other one before any cuts, thus with a huge background from ^{3}He. The circle indicates the chosen cut around the $\pi^0\pi^0$ point. All events inside this circle are processed through the kinematic fit.*

Both photon pairs should have an invariant mass around the π^0 mass, hence in the plot of one pair versus the other a spike at the $\pi^0\pi^0$ position is expected. This is seen in Fig. 5.9. The background is large because at this stage no separation between ^{3}He and ^{4}He is done. For all combinations which are inside a radius of 60 MeV (indicated in the plot by a circle) a kinematic fit is performed under the assumption that the forward track is ^{4}He. The combination with the smallest χ^2 is used.

Simply taking the two $\gamma\gamma$ pairs which yield the smallest distance to the $\pi^0\pi^0$ point gives the same result as the smallest radius in most cases, but in a few the result is different. Obviously it happens that both combinations give a similar invariant mass and only the requirement to fulfill energy and momentum conservation can distinguish between the correct combination and the random coincidence.

Figure 5.10 shows the sum of the momenta of the ^{4}He and the $\pi^0\pi^0$ system in the center of mass system for the combination with the smallest χ^2 and the one with

the smallest distance to the nominal $\pi^0\pi^0$ point. The values are calculated before the kinematic fit, hence it should be a Gaussian distribution around zero. Clearly the distribution with the smallest distance is broader than the distribution with the smallest χ^2 value.
The time window for the PS is rather large, hence it might happen that tracks, which arrive shortly before or after the actual event, are still inside the time window and are assigned to this event. In this case the track is counted as a charged track, although the initial particle is neutral. These are random coincidences which could spoil the calculation of the total cross section, because the reference reaction $dd \to {}^3\mathrm{He}n$ does not require any signal in the CD. To check how much this affects the total cross section, the usual condition for a neutral track (a signal in SE but no signal in PS and MDC) were loosened to allow also tracks which give a signal in the PS, but no signal in the MDC ("charged neutral tracks").
It turned out that about 10% more events are identified as dd → ^{4}He$\pi^0\pi^0$, but the θ distribution of the "usual neutral tracks" is very different from that of the "charged neutral tracks" (Fig. 5.11). "Charged neutral tracks" are emitted preferably in the forward direction, which is the part of the detector where the MDC efficiency is low, because the number of tubes which are passed decreases, as follows from simple geometrical considerations.
This leads to the assumption that the "charged neutral tracks" are not produced by neutral particles with a PS hit falsely assigned, but rather by charged particles which do not induce a reconstructible track in the MDC. Because there are so many of such tracks, some of them fulfill the requirements to build a pion, but that is a simple random coincidence. This is also supported by the fact that in the case of the "usual neutral tracks" the θ distribution becomes flatter if the combination to a pion is requested, but in the case of the "charged neutral tracks" both distributions, with and without the request of a pion, are very similar.

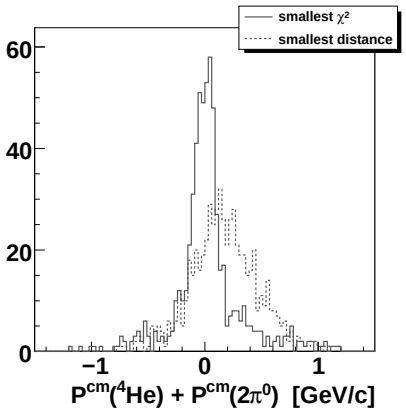

Figure 5.10: *Sum of center of mass momenta of the* ^{4}He *and the* $\pi^0\pi^0$ *system for the* γ *combination with the smallest* χ^2 *(solid red) and the smallest distance to the* $\pi^0\pi^0$ *point (dotted blue).*

5.4.3 Kinematic Fit

Having selected the ^{4}He and the pions, all Lorentz vectors of the particles in the reaction are known and hence all information that is to be known from one event is known. And of course energy and momentum conservation have to be fulfilled. But all energies and angles are measured quantities and have uncertainties. Therefore the measured values can be varied within the errors so that the conservation laws are fulfilled. At the same time the resolution is not only improved, but also the amount

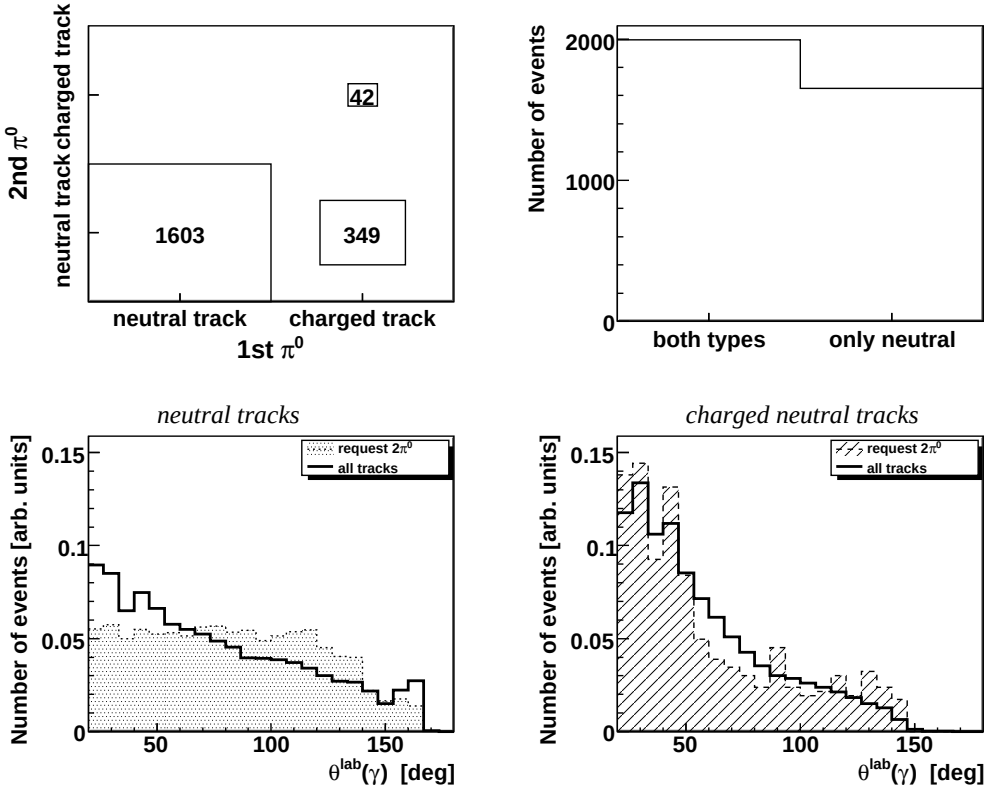

Figure 5.11: *The upper left picture shows the type of the tracks which build the pions if both neutral tracks and charged tracks without MDC information are allowed. The upper right picture shows that the restriction on neutral tracks yields only* 10% *less events. The lower row shows the distribution of the polar angle* θ *with and without restriction on tracks which combine to pions, normalized to 1. The left picture shows the neutral, the right picture the charged tracks without MDC information. If the charged tracks which combine to a pion were falsely identified as charged tracks, their* θ *distribution would look like the distribution for the neutral tracks.*

of background is reduced. This procedure is called kinematic fit and the version used in this work is based on the Lagrangian multipliers method, explained in [BR92]. A description of the algorithm applied in this case can be found in [Kup].

The reaction to fit is $dd \to {}^4\mathrm{He}\,\gamma\gamma\,\gamma\gamma$. Each particle is described by 4 parameters: its mass (1) and its momentum (3). Thus all together $7 \times 4 = 28$ parameters have to be settled.

Beam and target vectors as well as the masses of all particles are fixed values, thus 13 parameters are known already. The input for the fit are the energies and angles of the ^{4}He and the photons (plus the corresponding errors), hence all particles are determined, though 15 parameters are only known within the given errors. Additionally to the conservation laws, two more constraints make sure that the photons build the π^0s, hence the invariant mass of the photon pairs after kinematic fitting is a delta function at the position of the π^0 mass. Thus the fit is performed with in

total 6 over-constraints.

Parameters	d	d	$\rightarrow$	^{4}He	γ_1	γ_2	γ_3	γ_4	#
free	$M, \vec{p}$	$M, \vec{p}$		$M, \vec{p}$	$M, \vec{p}$	$M, \vec{p}$	$M, \vec{p}$	$M, \vec{p}$	28
fixed	$M, \vec{p}$	$M, \vec{p}$		M	M	M	M	M	13
measured				$\vec{p}$	$\vec{p}$	$\vec{p}$	$\vec{p}$	$\vec{p}$	15
constraints:	energy conservation								1
	momentum conservation								3
	invariant mass of $\gamma_1\gamma_2 = M(\pi^0)$								1
	invariant mass of $\gamma_3\gamma_4 = M(\pi^0)$								1
over-constraints	= fixed + measured+ constraints - free								6

Table 5.3: *Constraints of the kinematic fit.*

In an iterative procedure the variables are changed until the constraints are fulfilled, if the fit does not diverge. The output of the fit are the corrected values of the energy and the angles and a χ^2 value for each event. To reduce background, a cut on the χ^2 value or the probability distribution (which can be converted directly into each other) is applied. In this case the cut is done at a probability $> 20\%$ because below this value the probability distribution is steeply rising, whereas above it is more or less flat as can be seen in Fig. 5.12. This figure also shows the large background from ^{3}He: the tail of the $\chi 2$ distribution for the experimental data is very big compared to the one for the Monte Carlo simulation. Since the ^{3}He is not cut before the kinematic fit, but all He are assumed to be ^{4}He, this tail is expected.

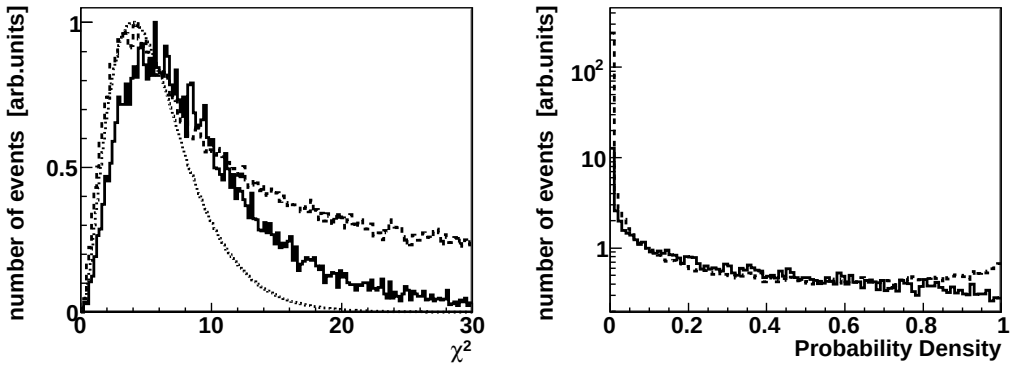

Figure 5.12: *Result of the kinematic fit: The left side shows the χ^2 distribution, the right side the probability distribution for experimental data at $T_d = 1.050$ GeV (red line), a Monte Carlo simulation of* dd $\rightarrow {}^4$He$\pi^0\pi^0$ *(black line) and the theoretical χ^2 distribution for six degrees of freedom (green line). The huge tail for the experimental data due to the ^{3}He background is mirrored in the slight slope in the probability density function.*

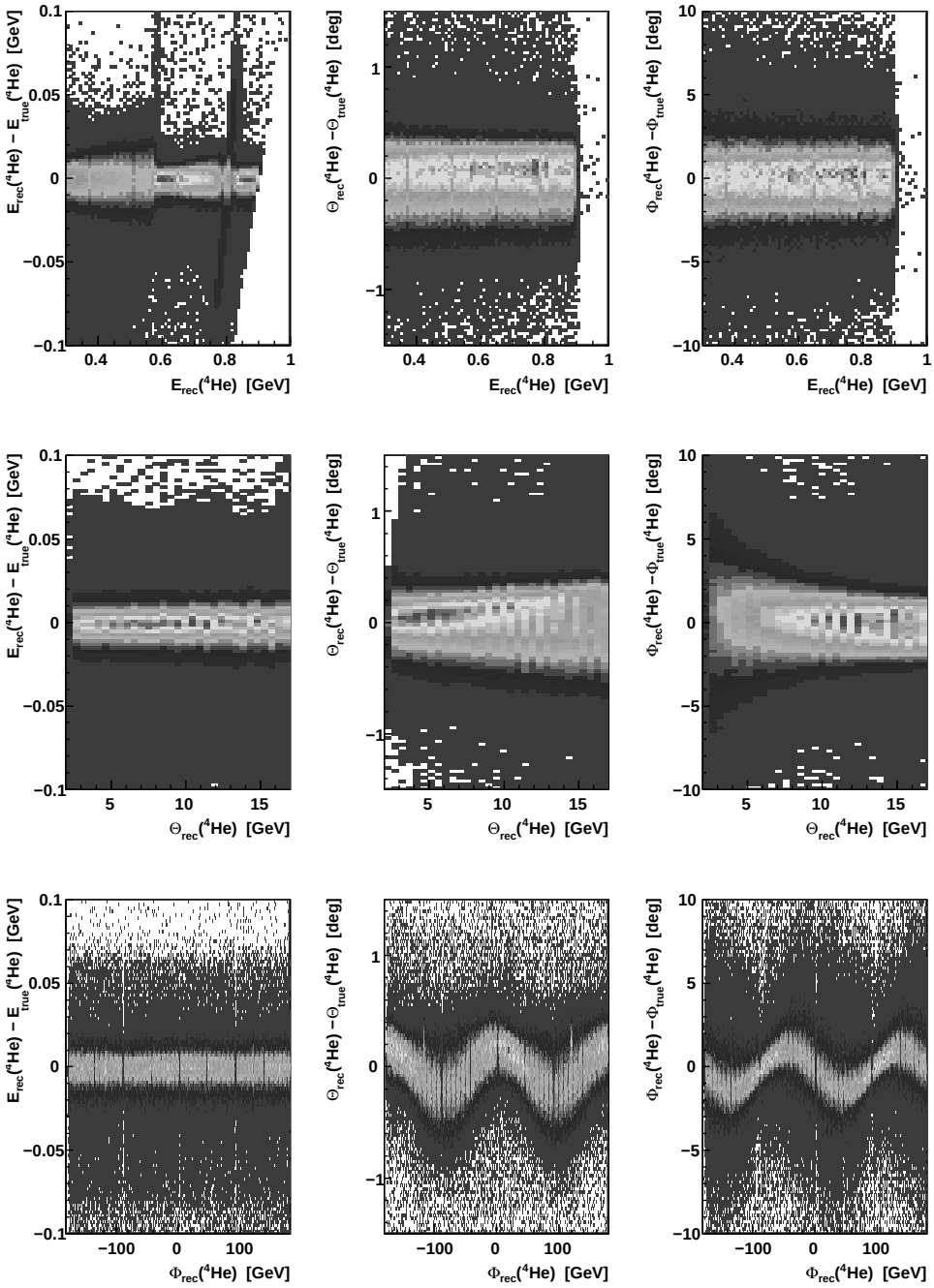

Figure 5.13: *Difference between the true and the reconstructed observables as a function of the kinetic energy E_{kin} (upper row), the polar angle θ (middle row) and the azimuthal angle ϕ for a Monte Carlo simulation of single* ^{4}He *tracks in the FD.*

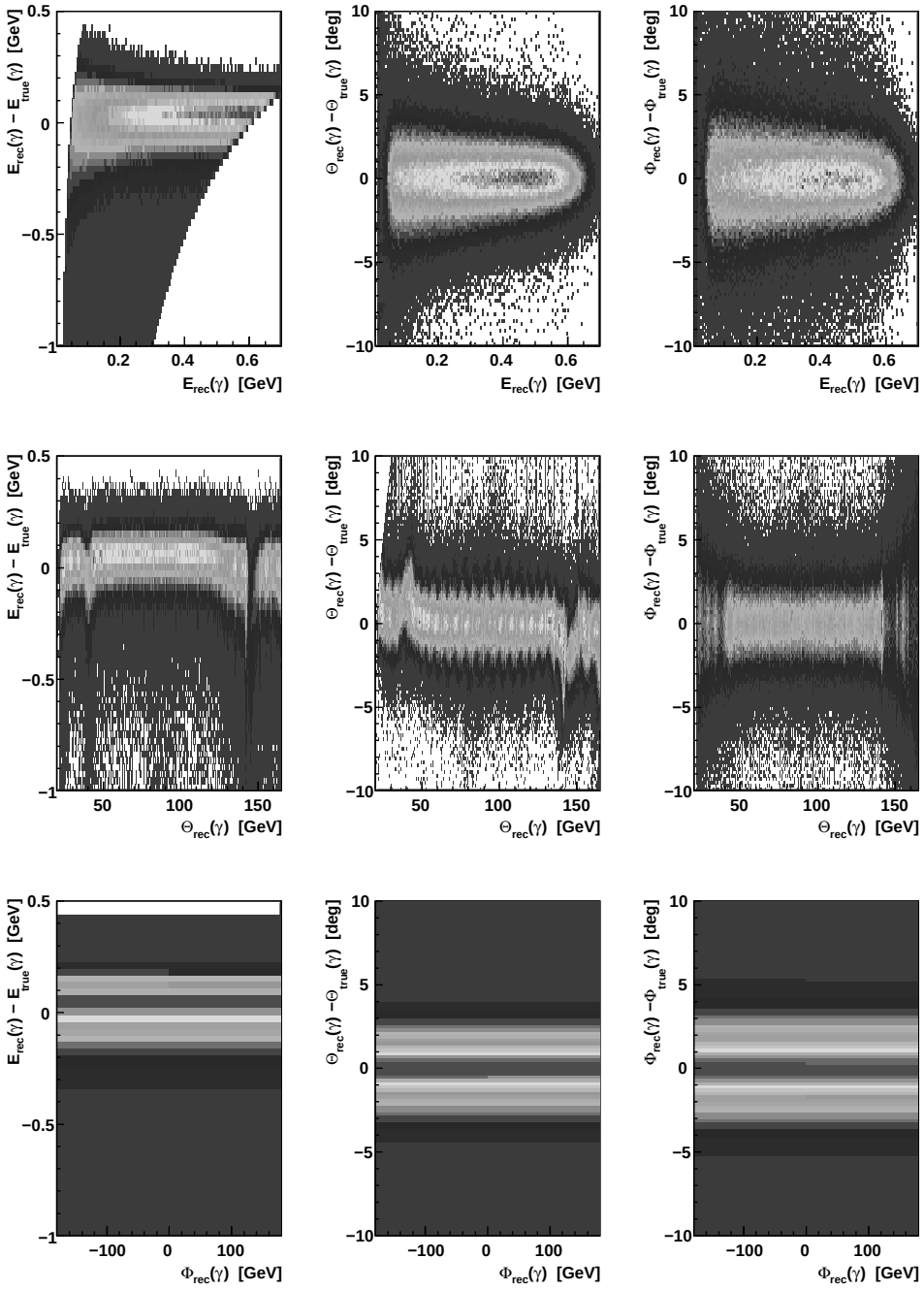

Figure 5.14: *Difference between the true and the reconstructed observables as a function of the kinetic energy E_{kin} (upper row), the polar angle θ (middle row) and the azimuthal angle ϕ for a Monte Carlo simulation of single photon tracks in the CD.*

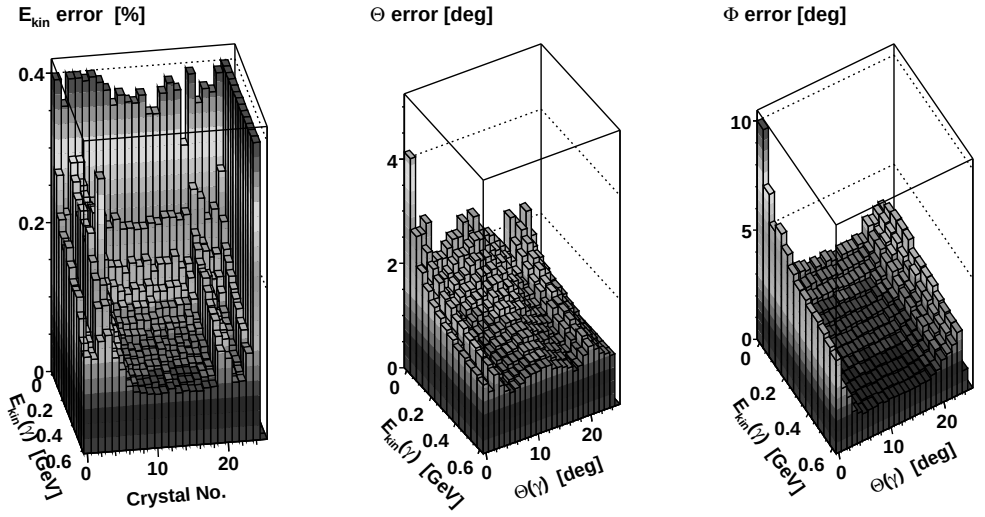

(a) *Errors for photons*

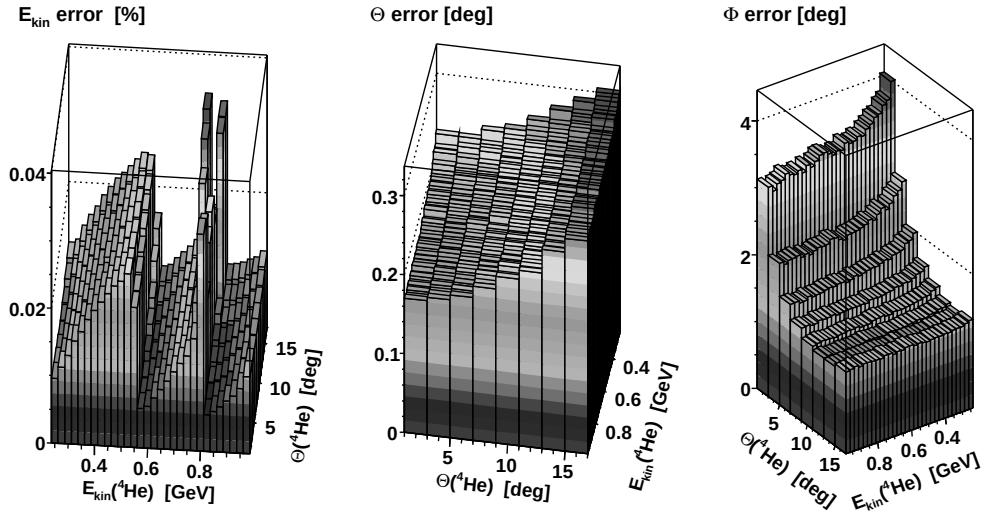

(b) *Errors for* ^{4}He

Error Parameterization

Essential for the kinematical fit is a correct error estimation, especially the relation of the errors for the different observables. If all errors were correct, but 10 times larger than in reality, the corresponding χ^2 distribution would be too small, but the shape would still be the same and in principle the cut on χ^2 could be done similar, but at a different position. However if only one error was a factor 10 too large, this variable would be varied much more compared to the other variables than actually allowed, resulting in a very different (and wrong) result for the corrected variables. To estimate the errors, a Monte Carlo simulation with single ^{4}He tracks in the FD and single photon tracks in the CD, respectively, was created. The difference between the true and the reconstructed value (before the kinematic fit) should be a Gaussian distribution and the standard deviation σ of this Gaussian is used as the error for this

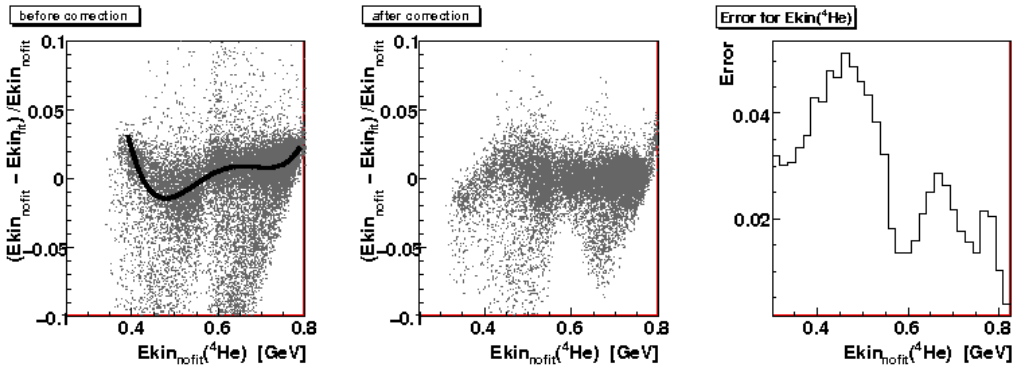

Figure 5.15: *Difference of the kinetic energy of the* ^{4}He *before and after the kinematic fit as a function of the kinetic energy before the fit for experimental data at* T_d = 1.117 GeV. *Left side before the correction, right side afterwards. The solid line depicts the correction function used. The correction is not perfect, but sufficient for the input in the kinematic fit.*

variable. But since the uncertainty might also depend on other variables, the error is parameterized as function of the variables it depends on. Figures 5.13 and 5.14 shows the difference between the true and reconstructed values as a function of the three input variables, the kinetic energy E_{kin}, the polar angle θ and the azimuthal angle ϕ.

The sinusoidal structure in the ϕ dependence of the angular errors is an artefact from the Monte Carlo simulation: the target region is simulated as a rectangular box with certain boundaries. From geometrical considerations follows that the impact of the deviation of the starting point of the track from the $(0, 0)$ point depends on ϕ. A small change in the θ angle is accompanied by a large change in the ϕ angle.

In reality the target region is some rather loosely defined volume, thus this effect should smear out for the experimental data and can be neglected. The errors were parameterized in dependence of the kinetic energy and the polar angle θ in bins of 50 MeV and 2° in case of the ^{4}He and 50 MeV and one crystal width of the SE in case of the photons. The crystal width changes along θ, because the three different parts of the SE consist of differently sized crystals. Because of the separation of the SE in three parts also large uncertainties around the transition regions appear. The energy error is estimated as a relative, the error of the angles as an absolute value.

The reason that some distributions are not centered around zero (e.g. $\theta_{rec} - \theta_{true}(^4\text{He})$) probably is that the position of the detectors in the simulation is slightly different than assumed in the analysis.

In the case of the error of the kinetic energy of the ^{4}He, the error estimated on the Monte Carlo simulation does not describe the true error very well. This is due to the calibration, which at some energies is worse than at others. The course of deposited energy deviates from the Monte Carlo expectations, especially for low energy deposits in the FRH2. Instead of investing huge efforts in finding a better calibration for the nine energies, a correction is introduced on the basis of the kinematic fit: the

difference of the kinetic energy before and after a fit with large errors is parameterized by a function and this is applied as a correction before the final fit. Figure 5.15 shows the relative difference of the kinetic energy of the ^{4}He before and after the kinematic fit as a function of the kinetic energy before the fit for experimental data at $T_d = 1.117$ GeV. The left side shows the result before the correction, together with the correction function. The same distribution after applying the correction is shown in the middle. After the correction at least the part above 0.4 GeV kinetic energy is flat and centered around zero. Certainly another iteration of this procedure would have improved the reconstruction below 0.4 GeV, but already this description is good enough to be fed into the kinematic fit.

The errors are estimated fitting a Gaussian distribution (centered at zero) to the difference before and after the fit as a function of the energy. The θ dependence is rather small and to have enough statistics for reasonable distributions, the parameterization is restricted to the energy dependence. This procedure is done for each energy. Figure 5.15, right side, shows the error of the kinetic energy for ^{4}He for experimental data for $T_d = 1.117$ GeV. For consistency reasons the Monte Carlo error was estimated the same way, thus the errors in Fig. 5.15b, left side, which are totally based on the Monte Carlo simulations, are not used at all.

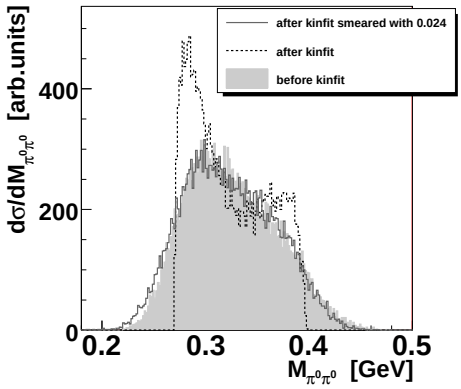

Figure 5.16: *Invariant mass of the $\pi^0\pi^0$ system before (gray area) and after (gray dashed line) the kinematic fit for $T_d = 0.8$ GeV. If a Gaussian smearing is applied with a standard deviation of $\sigma = 24$ MeV (black solid line) on the fitted distribution, the non-fitted one is very well reproduced.*

Having now reduced the ^{3}He background with the help of the kinematic fit, a first look at the invariant mass spectra can be taken. Figure 5.17 shows the distributions before and after the kinematic fit, without efficiency and acceptance corrections. In both cases a cut on the probability distribution at 0.2 is applied. The most significant feature is the strong peak at low $\pi^0\pi^0$ invariant masses, followed by a shoulder toward the higher invariant masses. The invariant mass of the ^{4}Heπ^0 system shows a Lorentzian distribution.

Both invariant masses are affected only a little by the kinematic fit, the non-fitted distributions are just a bit smeared, as expected. However the effect of the smearing is much more pronounced for smaller energies, because there the phase space and hence the energy range covered is smaller. For 0.8 GeV the peak at low invariant masses is smeared so much that it is almost not visible in the distribution before kinfit. This exactly corresponds to a Gaussian smearing with 27 MeV, as seen in Fig. 5.16.

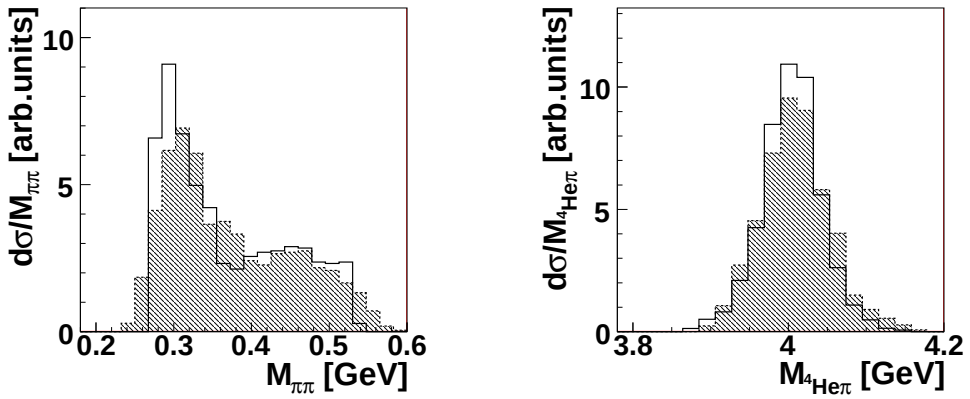

Figure 5.17: *Invariant mass of the $\pi^0\pi^0$ system (left) and ^{4}Heπ^0 system (right) before (gray area) and after (solid line) the kinematic fit.*

5.4.4 Efficiency and Acceptance Corrections

In order to correct the non-perfect geometrical acceptance and the efficiency of the analysis, the data have to be multiplied by the ratio of the simulated Monte Carlo and the reconstructed result. In principle the ratio should be calculated in a four-dimensional space, since a three-body unpolarized reaction is determined with four independent variables. But the statistics necessary for this procedure is far too large compared to the statistics of the data. Instead of e.g. 100 bins in a one-dimensional histogram, 100^4 bins in a four-dimensional histogram would have to be filled.
The usual way is to use one-dimensional histograms, which is fine as long as there is no hole in the acceptance. If a part of the spectrum is not covered, the corrections depend on the model used for the simulation[8]. In this reaction a big part of the backward flying ^{4}He is lost due to the acceptance (see section 5.1.1), whereas the forward flying ^{4}He are well covered. Since the reaction should be forward-backward-symmetric in the center of mass system, the data could be restricted to the forward going ^{4}He. But there is also a very good model available (the ABC resonance model, which will be explained later in section 6.1.2), which can be used as well. And finally at least a two-dimensional correction can be performed and the result compared to the one-dimensional correction. Figure 5.18 shows the invariant masses of the $\pi^0\pi^0$ and the ^{4}Heπ^0 systems and the $cos(\theta^{cm}_{\pi^0\pi^0})$ for different corrections.
The invariant masses are hardly affected whereas the angular distributions differ in the region where the acceptance is low. If the phase space simulation is used for the correction, the angular distribution is far from being symmetric, which is expected since the phase space differs very much from the data and hence it cannot describe the amount of lost events correctly.
Fortunately the model can describe the data well enough, hence this is used for the corrections.

[8]If the model described the data in all observables, the correction would be as good as a multidimensional one with huge statistics.

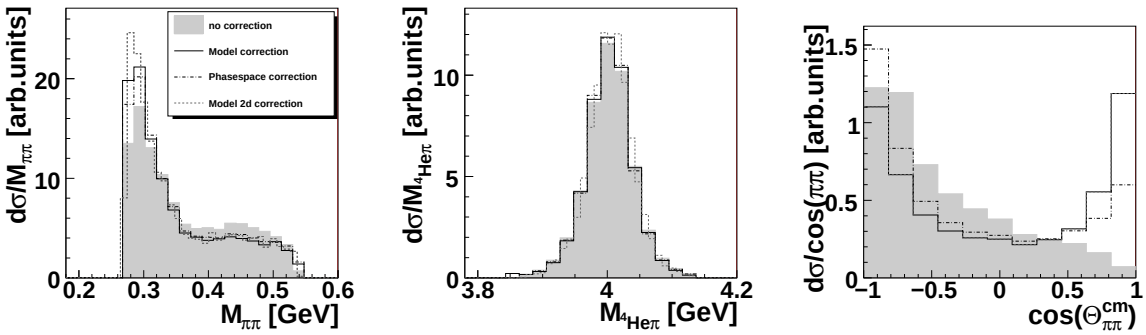

(a) (b) (c)

Figure 5.18: *Differential cross sections for different efficiency and acceptance corrections scaled to fill the same area. The shaded area depicts the uncorrected spectrum. In case of the invariant masses, the one dimensional correction with a phase space simulation (dash-dotted line), a model simulation (solid line) and the two dimensional correction with a model simulation (dotted line) are very similar. Only for the θ^{cm} distribution a difference is seen at large angles, which is expected, since the low acceptance region coincides with this part of the spectrum.*

5.5 Selection of $dd \rightarrow {}^3\mathrm{He}n$ Events

In order to estimate the total cross section, the reaction $dd \rightarrow {}^3\mathrm{He}n$ is used as a reference because it is easy to select and experimental data are available for the normalization [Biz80]. Since it is a binary reaction, the relation between the polar angle θ and the kinetic energy of the ^{3}He is fixed. Furthermore the ^{3}He originating from this reaction have the largest kinetic energy in the pool of ^{3}He particles and are separated from all other reaction products.
Figure 5.19a shows the kinematics of this reaction with the acceptance of the FD indicated. Fortunately the reaction dynamics do not follow the phase space behavior, but it is strongly peaked in forward direction, as is seen in Fig. 5.19b, which shows the transferred momentum squared $t = (P(^3He) - P(beam))^2$ measured by [Biz80], the second scale on top shows the laboratory polar scattering angle θ^{lab}, which is directly translatable into t.
In order to simulate the correct distribution, the t-spectra for the four energies measured by [Biz80] were fitted with a sum of exponentials
$\sigma(t - t_{max}) = \sum_{i=1}^{i=3} a_i * e^{b_i x}$ as in this paper (see Fig. 5.20). After that the energy dependence of the fit parameters was again fitted with hyperbolical functions $par_i(W) = \frac{p_i}{x - q_i} + r_i$, (Fig. 5.21), resulting in an energy dependent parameterization of the t-distribution. The integration of the function for a certain energy gives the total cross section at this energy. Figure 5.20 shows the cross section as a function of the energy together with the four values measured by [Biz80] and the position of the nine energies in the experiment described in this work. The errors are used later on for the error of the absolute normalization of dd $\rightarrow {}^4\mathrm{He}\pi^0\pi^0$. In table 5.4 all

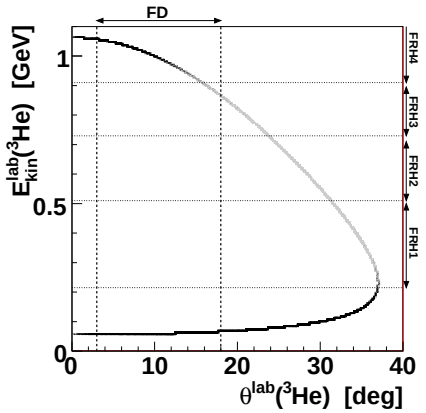

(a) *Kinetic energy in the laboratory system versus the polar scattering angle θ in the laboratory system for a Monte Carlo simulation at $T_d = 1.117$ GeV. The gray line denotes the pure kinematics resulting from energy and momentum conservation, the black dots include the phenomenological model which describes the experimental data.*

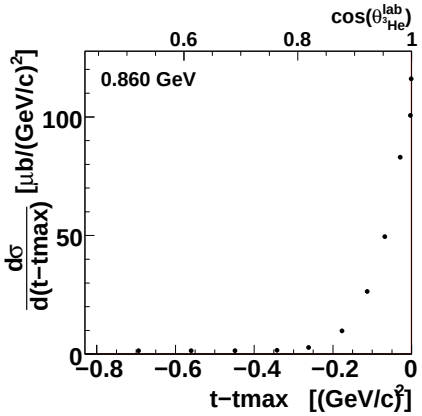

(b) *Measured four-momentum transfer $t - t_{max}$ at a beam energy of 0.86 GeV. The upper scale shows the $cos(\theta^{lab}_{^3\mathrm{He}})$, which is directly related to the transferred momentum squared. It is obvious that the measured $t - t_{max}$ distribution is far from being flat as it would be if the reaction dynamics followed the phase space.*

Figure 5.19: *Normalization reaction $dd \rightarrow {}^3\mathrm{He}n$*

parameters are listed. The fit yields the same value for parameters in the exponents for the t-dependence b_1, b_2 and b_3. It is possible to improve the description of the t-dependence, but in this case the energy dependence cannot be described well. The parameters used present a reasonable compromise.

The selection of $dd \rightarrow {}^3\mathrm{He}n$ is made with the ΔE-ΔE method and the energy dependence of the polar scattering angle θ. Due to the strong angular dependence, the reaction appears in the ΔE-ΔE plot not as a broad band, but rather as one extended point, well separated from the ^{3}He particles originating from different reactions, because these have a smaller kinetic energy. Since $dd \rightarrow {}^3\mathrm{He}n$ is a binary reaction, the relation between the kinetic energy of the ^{3}He and its polar scattering angle θ is fixed, hence in the plot of $E^{lab}_{kin}(^3\mathrm{He})$ versus $\theta^{lab}(^3\mathrm{He})$ this reaction shows up as a line, again well separated from other reactions because the ^{3}He emitted here have the highest possible kinetic energy.

Having a working model for the simulation, it is easy to check which plots are best suited for the $^3\mathrm{He}n$ selection for each energy. Table 5.5 summarizes the kinetic energy range of the ^{3}He, the FRH layer where it stops and the plots used for the selection. Figure 5.23 shows the selection of experimental data for $T_d = 1.117$ GeV.

For the high energies, $T_d = 1.32$ GeV and $T_d = 1.4$ GeV, the selection is done on the basis of FRH4 and FRH5, which were not calibrated for this beam time. Since the kinetic energy reconstruction is made using the polar scattering angle θ, which is much better determined than the deposited energy independent of the layer where

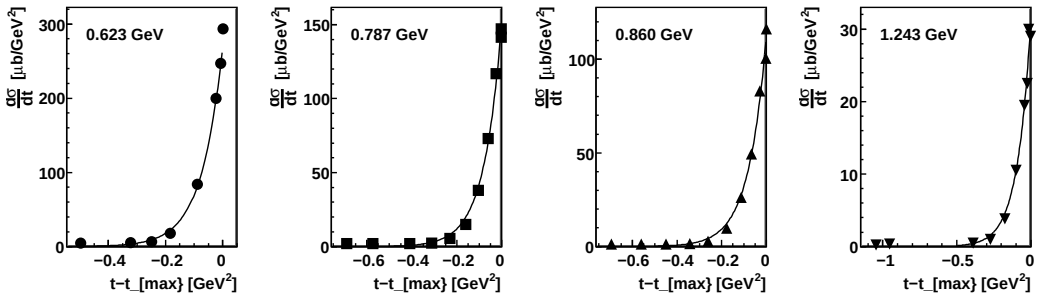

Figure 5.20: *Cross section of* $dd \rightarrow {}^3\mathrm{He}n$ *for four beam energies measured by [Biz80]. The fit to the data is plotted as a solid line.*

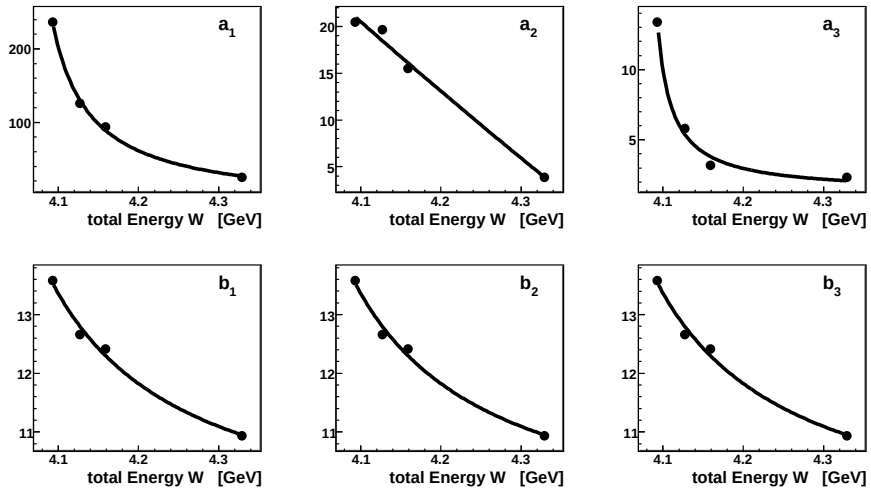

Figure 5.21: *Energy dependence of the fit parameters for the measured cross section of* $dd \rightarrow {}^3\mathrm{He}n$*. The functions fitted here are hyperbolical functions* $f(x) = \frac{a}{x-b} + c$*.*

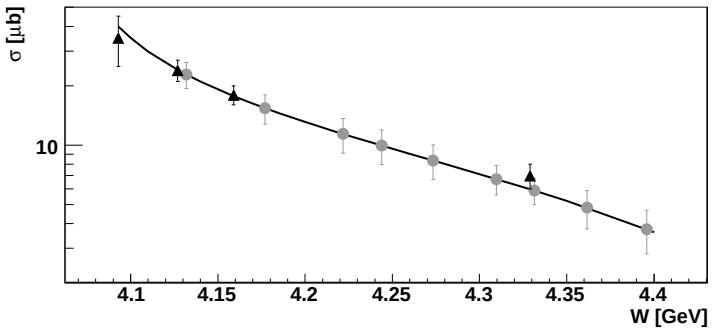

Figure 5.22: *Parameterization of the energy dependence of the total cross section of the reaction* $dd \rightarrow {}^3\mathrm{He}n$*. The triangles show the values measured by [Biz80]. The energies measured in this work are marked with the circles, the error bars indicating the error used for the value of the total cross section.*

	p_i	q_i	r_i
a_1	11.64	4.05	-14.49
b_1	0.78	3.92	9.04
a_2	2327.04	-1.44	-399.27
b_2	0.78	3.92	9.04
a_3	0.22	4.08	1.24
b_3	0.78	3.92	9.04

Table 5.4: *Parameters for the energy and t dependence of the total cross section of the reaction $dd \rightarrow {}^3\mathrm{He}n$. The t dependence is described by the function $\sigma(t-t_{max}) = \sum_{i=1}^{i=3} a_i * e^{b_i x}$ and each parameter is described by a function of the total energy $par_i(W) = \frac{p_i}{x-q_i} + r_i$.*

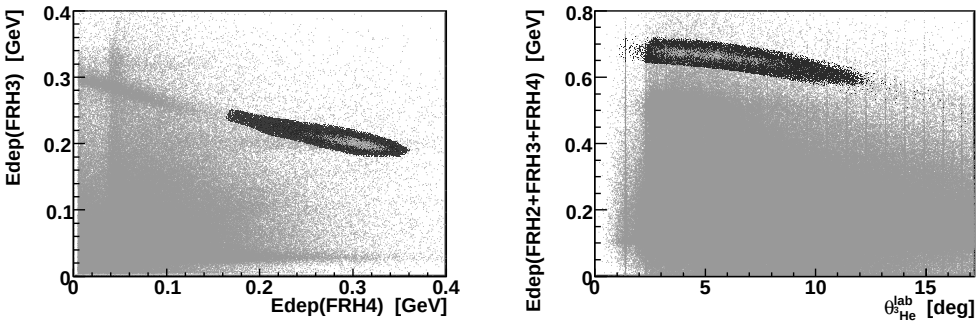

Figure 5.23: *Selection of the reaction $dd \rightarrow {}^3\mathrm{He}n$ at $T_d = 1.117$ GeV. The left side shows the deposited energy in FRH3 versus FRH4, the right side the sum of the deposited energies in FRH2, FRH3 and FRH4 versus the polar scattering angle θ. The gray dots show the events without any selection except the basic cuts (see table 5.2), the blue dots represent the events selected as ${}^3\mathrm{He}n$.*

the particle stops, an energy calibration is not needed in case of ${}^3\mathrm{He}n$. Instead of putting big efforts in a careful energy calibration only to select the ${}^3\mathrm{He}n$ reaction for all elements at once, like for the lower energies, a broader cut is applied and only for some elements a more careful selection is made.
The phenomenological model developed before is simulated and used for the efficiency and acceptance corrections. The experimental result is scaled to the t-distribution expected for this energy according to the model. The result is shown in Fig. 5.24. With Δt being the bin width in the t-spectrum, the scaling factor f is directly related to the integrated luminosity:

$$L_{int} = \frac{1}{f * \Delta t} \tag{5.1}$$

The error of the integrated luminosity is given by the error of the scaling factor f, which depends on the one hand on the statistical fluctuations in the $dd \rightarrow {}^3\mathrm{He}n$ selection $\delta_R^{stat}({}^3\mathrm{He}n) = \sqrt{N({}^3\mathrm{He}n)}$, and on the other hand on the error in the de-

energy [GeV]	stopping layer	ΔE-ΔE plot	Edep - θ plot
0.8	FRH2, FRH3	FRH1 vs FRH2+FRH3	FRH1+FRH2+FRH3 vs θ
0.9	FRH2, FRH3	FRH1 vs FRH2+FRH3	FRH1+FRH2+FRH3 vs θ
1.0	FRH3, FRH4	FRH2 vs FRH3+FRH4	FRH2+FRH3+FRH4 vs θ
1.05	FRH3, FRH4	FRH2 vs FRH3+FRH4	FRH2+FRH3+FRH4 vs θ
1.1117	FRH3, FRH4	FRH3 vs FRH4	FRH2+FRH3+FRH4 vs θ
1.2	FRH4	FRH3 vs FRH4	FRH2+FRH3+FRH4 vs θ
1.25	FRH4, FRH5	FRH3 vs FRH4+FRH5	FRH4+FRH5 vs θ
1.32	FRH5	FRH4 vs FRH5	FRH4+FRH5 vs θ
1.4	FRH5	FRH4 vs FRH5	FRH4+FRH5 vs θ

Table 5.5: *Ranges of the laboratory kinetic energies of the* ^{3}He*, the corresponding FRH layer where the* ^{3}He *stops and the plots which were used for the selection of* $dd \to {}^3\mathrm{He}n$*.*

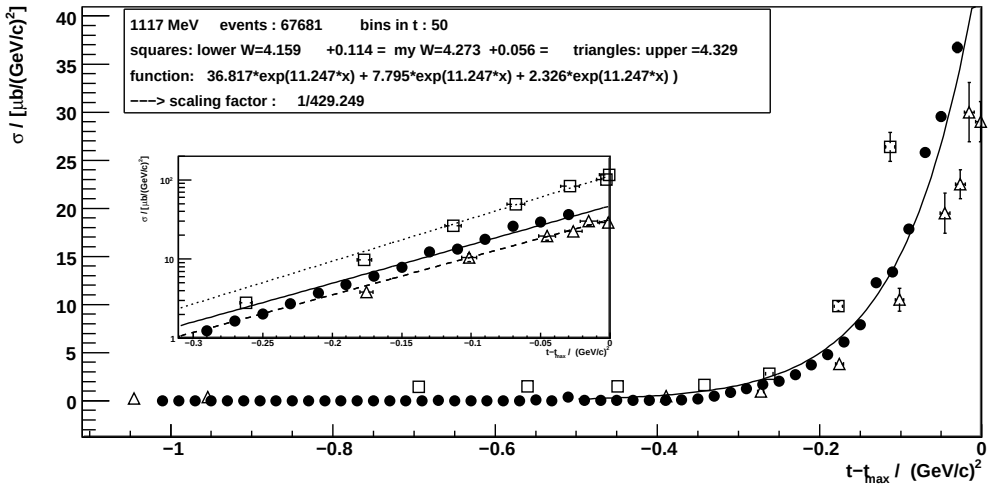

Figure 5.24: *$t - t_{max}$ distribution of the reaction $dd \to {}^3\mathrm{He}n$ at $T_d = 1.117$ GeV. The dots denote the experimental data from the neighboring energies measured in [Biz80]. The solid line corresponds to the expected distribution according to the fit function. The data measured in this work (red squares) are scaled to fit the line.*

scription of the t-distribution. The integral of the t-distribution yields the total cross section and since the shape of the fit is fixed by the shape of the data, the relative error of the total cross section is used as the relative error of the t-distribution[9]. The relative error for the total cross section $\delta_R^\sigma({}^3\mathrm{He}n)$ was estimated as the relative

[9]This means that if the total cross section was 10% larger, the differential cross section would be 10% larger over the whole range in t. This needs not to be the case since the 10% error could result from a different shape of the differential cross section as well, but since the shape of the data points and the t-distribution function fit quite well, it was assumed that the shape is fixed by the fit.

error of the Saclay data of the nearest point multiplied by a factor accounting for the distance to this point. Table 5.6 summarizes the assigned errors.
Thus the error of the integrated luminosity is given by:

$$\delta L = \frac{1}{2\Delta t\, f^2} \cdot \delta f \tag{5.2}$$

$$\delta f = f \cdot (\delta_R^{stat}({}^3\mathrm{He}n) + \delta_R^{\sigma}({}^3\mathrm{He}n)) \tag{5.3}$$

Or, distinguished in statistical and systematic errors:

$$\delta L^{stat} = \frac{1}{2\Delta t\, f^2} \cdot f \cdot \delta_R^{stat}({}^3\mathrm{He}n) \tag{5.4}$$

$$\delta L^{sys} = \frac{1}{2\Delta t\, f^2} \cdot f \cdot \delta_R^{\sigma}({}^3\mathrm{He}n) \tag{5.5}$$

			Saclay [Biz80]			
energy		$\delta_R(\sigma_{tot})$	**energy**		σ_{tot}	$\delta_R(\sigma_{tot})$
			0.62	GeV	35 μb	0.29
0.8	GeV	0.15	0.79	GeV	24 μb	0.16
			0.86	GeV	18 μb	0.11
0.9	GeV	0.17				
1.0	GeV	0.2				
1.05	GeV	0.2				
1.1117	GeV	0.2				
1.2	GeV	0.17				
1.25	GeV	0.15	1.24	GeV	7 μb	0.14
1.32	GeV	0.22				
1.4	GeV	0.25				

Table 5.6: *Relative errors for the total cross section for* $dd \to {}^3\mathrm{He}n$

6 Results

You say you got a real solution
Well, you know
We'd all love to see the plan.
You ask me for a contribution,
Well, you know
We all do what we can.

Revolution, The Beatles [Len68]

This chapter is devoted to the results of the dd $\rightarrow {}^4\mathrm{He}\pi^0\pi^0$ analysis. Since they will be compared to predictions of theoretical models, first these are described. Then differential distributions are discussed in detail for $T_d = 1.117$ GeV as a typical energy in the region of the peak cross section. Note that for a 3-body reaction (with unpolarized beam and target) there are four independent kinematic variables, which give rise to four independent single-differential cross sections. Finally the energy dependence of differential and total cross sections is presented.

6.1 Theoretical Models

6.1.1 The GFW Model for $dd \rightarrow {}^4\mathrm{He}\pi\pi$

Historically the only model attempting to explain explicitly the ABC effect in $dd \rightarrow {}^4\mathrm{He}\pi\pi$ was the so-called Gårdestig-Fäldt-Wilkin (GFW) model [Gar99]. Here the two-pion production is implemented as two free and independent $NN \rightarrow d\pi$ reactions occurring in parallel between different pairs of nucleons from the two deuterons. After that the two final deuterons form the ^{4}He.

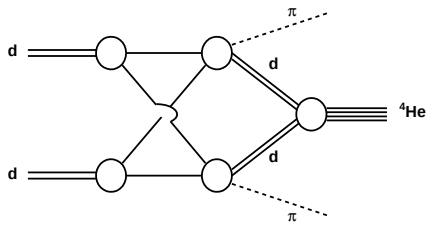

Figure 6.1: *Feynman diagram of the GFW model [Gar99]*

This model was tested in a simplified version on the first exclusive measurements in this field, measured with CELSIUS-WASA [Kel08]. Figure 6.2 shows the invariant masses of the $\pi^0\pi^0$ and the ${}^4\mathrm{He}\pi^0$ system in comparison to a simulation of this model.

The invariant mass of the ${}^4\mathrm{He}\pi$ system is predicted to be broader than the experimental data[1]. Even more striking is the deviation in the invariant mass of the $\pi\pi$ system, where the model predicts an enhancement both at low and at high invari-

[1] In [Kel08] this difference is less pronounced because there no kinematic fit was performed, hence the resolution was worse than in this work.

ant masses, whereas the experimental data show no enhancement at high invariant masses.

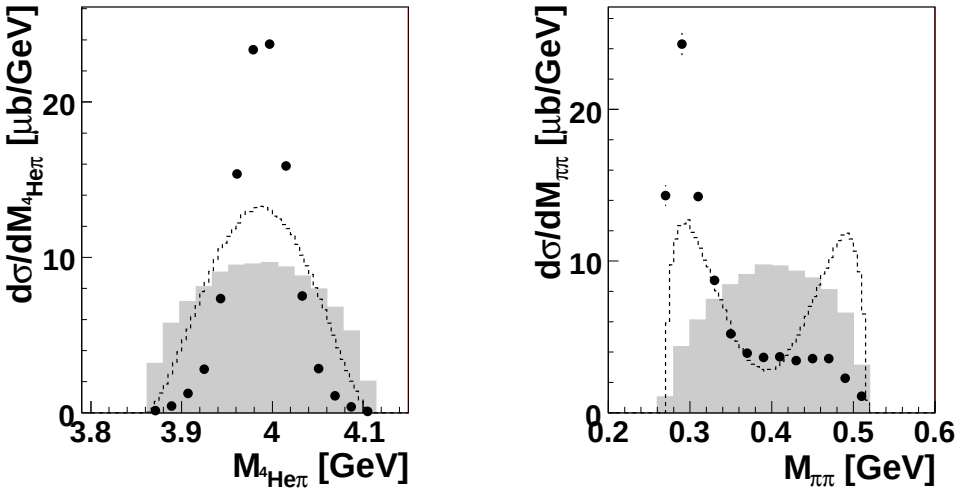

Figure 6.2: *Invariant mass spectrum of the* ^{4}Heπ^0 *(left) and the* $\pi^0\pi^0$ *(right) systems for* $T_d = 1.05$ GeV. *The dots are the experimental data, the gray area marks the phase space simulation and the dashed line a simulation based on the simplified GFW model as applied in [Kel08].*

6.1.2 The ABC Resonance Model

Driven by recent measurements of two pion production at CELSIUS-WASA [Bas09, Kha09, Sko09, Kre10] and WASA-at-COSY [Basc], a new model, the so-called ABC-Resonance model, was developed, which describes these data very well.
In the ABC resonance model the reaction dd $\rightarrow$ ^{4}He$\pi^0\pi^0$ is assumed to take place via the basic ABC reaction $pn \rightarrow d\pi\pi$ plus two nucleons which act as spectators which fuse with the d to form the ^{4}He in a kind of final state interaction. For this reason the model for $pn \rightarrow d\pi\pi$ will be explained first, followed by its adaption to the $dd \rightarrow$ ^{4}He$\pi\pi$ reaction. The description of the models is taken from [CB10].

The t-channel $\Delta\Delta$ Model

The first model which could qualitatively explain the inclusive measurements in the field of the ABC effect was the t-channel $\Delta\Delta$ model [RS73]. In this model the two incoming nucleons of the reaction $pn \rightarrow d\pi\pi$ both are excited to a Δ resonance which subsequently decays into a nucleon and a pion. The two pions are emitted and the nucleons fuse to the deuteron. The Feynman diagram for this process is depicted in Fig. 6.3.
This scenario can be very well tested in the non-fusion two pion production $pp \rightarrow NN\pi\pi$. From isospin decomposition [Sko09] of the total cross sections the t-channel $\Delta\Delta$ excitation is found to be the dominant part for $T_p > 1$ GeV. The only

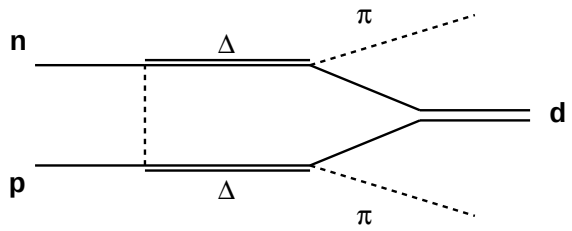

Figure 6.3: *Feynman diagram of the t-channel ΔΔ process for the basic ABC reaction* $pn \rightarrow d\pi\pi$.

other resonances playing a role are the Roper Resonance $N^*(1440)$ at $T_p \leq 1$ GeV and to some extent the $\Delta(1600)$, mainly in the $nn\pi^+\pi^+$ channel.
Also in the fusion reaction $pp \rightarrow d\pi^+\pi^0$ (at similar energies) the t-channel ΔΔ process can explain the experimental data very well, both in the differential and the total cross sections [Kre10], as seen in Fig. 6.4. In this channel, where the $\pi\pi$ system is in isospin $I_{\pi\pi} = 1$, no ABC effect is observed.

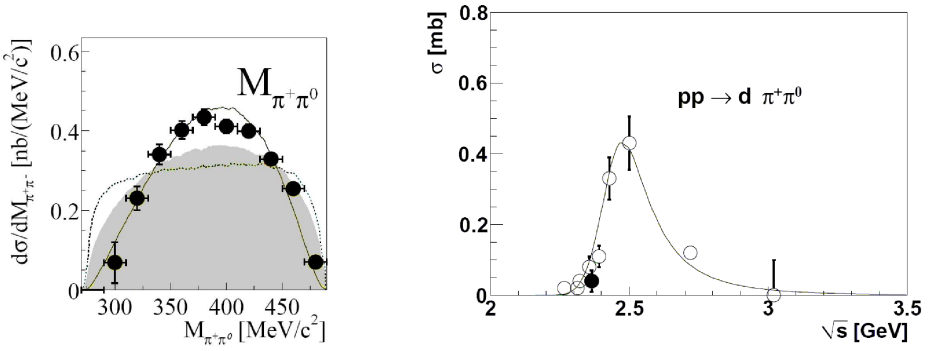

(a) $M_{\pi\pi}$. **(b)** *Total cross section*

Figure 6.4: *The* $pp \rightarrow d\pi^+\pi^0$ *reaction: The solid dots represent the CELSIUS-WASA data [Kre10], the open dots are data from previous measurements. The shaded area marks the phase space simulation, the dotted curve a t-channel ΔΔ calculation à la Risser and Shuster [RS73]. For the solid line the factor* $\vec{\sigma}(\vec{k_1} \times \vec{k_2})$ *was added to account for the production of the vector-isovector pion pair.*

Next this ansatz can be applied to the fusion reaction with the pion pair in isospin state $I = 0$, where the ABC effect was observed.
Generally the cross section is given by [PDG]:

$$d\sigma = \frac{(2\pi)^4}{4p_i\sqrt{s}} |M|^2 \, d\Phi_3 \tag{6.1}$$

with $d\Phi_3$ denoting the 3-body phase space.

The matrix element $M_{\Delta\Delta}$ for the t-channel $\Delta\Delta$ graph is given by:

$$M_{\Delta\Delta} = c\,\frac{e^{i\phi_{\Delta\Delta}}}{q^2 - m_\pi^2}\; m_\Delta \sqrt{\frac{\Gamma_{\Delta_1}\Gamma_{\Delta_2}}{q_{\pi_1}^{N_1\pi_1} q_{\pi_2}^{N_2\pi_2}}}\; D_{\Delta_1}\, D_{\Delta_2} \tag{6.2}$$

with $\phi_{\Delta\Delta} \approx 0$ from a fit to the experimental data and c being an effective coupling constant, which can be extracted from experimental data for the $pp \to d\pi^+\pi^0$ reaction and transferred to $pn \to d\pi^0\pi^0$ via isospin relations. The Δ propagator D_Δ is given by [PDG]

$$D_\Delta = \frac{\sqrt{m_\Delta \Gamma_\Delta / q_\pi^{N\pi}}}{M_{N\pi}^2 - m_\Delta^2 + i m_\Delta \Gamma_\Delta} \tag{6.3}$$

with $q_\pi^{N\pi}$ denoting the momentum of the pion in the $N\pi$ subsystem and $m_\Delta = 1.23\,\mathrm{GeV}$. The momentum dependent width of the Δ is given by:

$$\Gamma_\Delta(q_\pi^{N\pi}) = \gamma\,(q_\pi^{N\pi})^3\,\frac{R^2}{1 + R^2 (q_\pi^{N\pi})^2} \tag{6.4}$$

with $R = 6.3\,(\mathrm{GeV/c})^{-1}$ and $\gamma = 0.74$ as in [Pil67, RS73], i.e. $\Gamma(M_\Delta) = 110$ MeV.

Since in the description of Risser and Shuster no angular dependence is given, the factor $(1 + 3cos(\theta_{\pi_1}^{N_1\pi_1}))(1 + 3cos(\theta_{\pi_2}^{N_2\pi_2}))$, known from the Δ decay, is included. The $M_{\pi\pi}$ distribution following from this ansatz for the reaction $pn \to d\pi\pi$ is shown in Fig. 6.5.

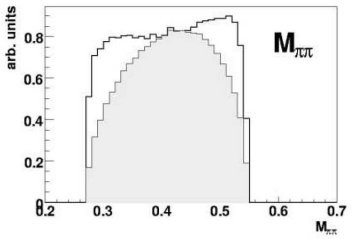

Figure 6.5: *Simulation of the $M_{\pi\pi}$ spectrum for the reaction $pn \to d\pi^0\pi^0$. The shaded area marks the phase space simulation, the solid line a t-channel $\Delta\Delta$ model calculation [Bas06].*

With respect to phase space enhancements both at high and at low invariant $\pi\pi$ masses are predicted. As explained in [RS73], the origin of these enhancements is the term $D_{\Delta_1} D_{\Delta_2}$ which is largest for the two configurations where the two pions move parallel or antiparallel to each other, leading to low and high invariant $\pi\pi$ masses, respectively. This may be related to the relative motion of the two Δ: since the two nucleons end up in a bound state, their relative momentum must be small, thus any relative momentum $q_{\Delta\Delta}$ of the Δs must be carried by the pions (neglecting Fermi motion). Therefore in the case that the relative momentum $q_{\Delta\Delta}$ of the Δs is small, the pions are emitted in parallel, in the case that the relative momentum of the Δs is large, the pions are emitted in antiparallel. The first case is expected to be more prominent when the center of mass energy is below $2\,\mathrm{M}_\Delta$, the latter when the center of mass energy is larger than $2\,\mathrm{M}_\Delta$.

In the reaction $pp \to d\pi^+\pi^0$, where the pion pair has an isospin of $I = 1$ and the ABC effect is not observed, the two enhancements are suppressed due to the factor $(k_1 \times k_2)$, which arises from the fact that the pions have to be in relative p-wave to

obey the Bose-symmetry[2].
As long as only inclusive measurements were available, also the ABC reaction $pn \rightarrow d\,\pi\pi$ was qualitatively well described by this t-channel $\Delta\Delta$-model, however not as well as the non-ABC reactions. Thus at that stage, knowing only the inclusive results, the non-fusion and the fusion reactions seemed to fit together, and the ABC effect in the isospin $I = 0$ channel as well as the non-existence of the ABC effect in the isospin $I = 1$ channel would be explained naturally. However, later it turned out that the exclusive data do not fit into this picture.
As soon as exclusive measurements with sufficient statistics were available, large discrepancies between the predictions and the experimental data were revealed. The high mass peak in the invariant mass of the pion pair is not seen in the experimental data (see Fig. 6.6a). Furthermore the energy dependence of the total cross section of $pn \rightarrow d\pi^0\pi^0$ exhibits a strong resonance-like structure (see Fig. 6.6b), which was neither expected nor described by t-channel $\Delta\Delta$ models.
Hence a new ansatz was pursued in [Bas09], the so-called ABC resonance model, which is able to explain the existing experimental data.

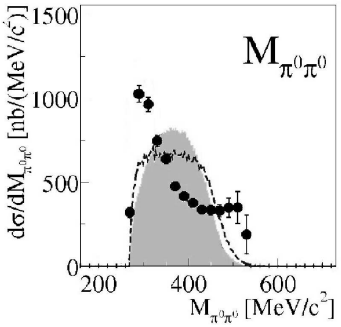

(a) $M_{\pi^0\pi^0}$ *distribution: The shaded area marks the phase space, the dashed line the* $\Delta\Delta$ *simulation. [Kha09].*

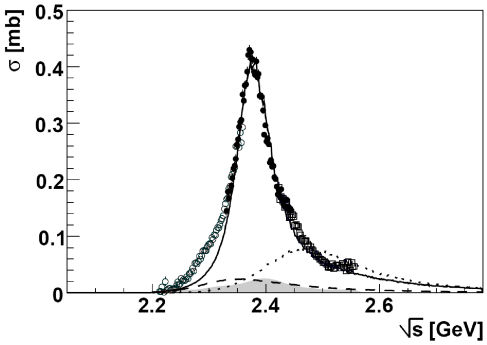

(b) *Total cross section. The solid line denotes the ABC resonance model, the dashed line the contribution from the Roper resonance and the dotted line that from the* $\Delta\Delta$ *process. The shaded area denotes systematic uncertainties.*

Figure 6.6: *The* $pn \rightarrow d\pi^0\pi^0$ *reaction: The solid dots represent the experimental data of CELSIUS-WASA [Kha09] (left) and WASA-at-COSY [Basc] (right).*

The ABC Resonance Model

The new ingredient in the ABC resonance model is an s-channel $\Delta\Delta$ resonance d^* which is excited in the isoscalar pn collision and decays into two Δs, which

[2]In $pp \rightarrow d\pi^+\pi^0$ the isospin of the pion pair is $I = 1$. The pion pair has to obey the Bose symmetry $(-1)^{S+L+I} = 1$. Since the spin of the pions is $S = 0$, L must be an odd number and because the center of mass energy of the system of the regarded reactions is close to the reaction threshold $L = 1$ is the most likely relative angular momentum.

subsequently decay into $N\pi$ as before[3]. The respective Feynman diagram is depicted in Fig. 6.7. The configurations with large relative momenta between the Δs are suppressed and hence the high invariant mass part of the $M_{\pi\pi}$ spectrum is suppressed as well. That way also the resonance-like structure in the total cross section is explained naturally.
The isospin of this resonance must be $I = 0$ because the ABC effect is only visible in the $I = 0$ channel. Since it happens only close to threshold, s-wave behavior between the Δs is assumed, thus $l_{\Delta\Delta} = 0$. The resonance decays into two Δs, thus Fermi statistics must be fulfilled, i.e. $(-1)^{l_{\Delta\Delta}+J+I} = -1$. Hence J must be an odd number, in this case 1 or 3. The angular distributions are clearly in favor of $J = 3$ [CB10, Basc], thus the quantum numbers are consistent only with $I(J^P) = 0(3^+)$.

The cross section is now described by the sum of the t-channel $\Delta\Delta$ amplitude $M_{\Delta\Delta}$, the amplitude resulting from the Roper resonance (N^*1440) M_{Roper} and the s-channel resonance amplitude M_{d^*} [CB10]

$$d\sigma = \frac{(2\pi)^4}{4p_i\sqrt{s}} \sum |M_{d^*} + M_{Roper} + M_{\Delta\Delta}|^2 \, d\Phi_3 \tag{6.5}$$

where the sum runs over the observable spin sub-states m_p, m_n, m_d of proton, neutron and deuteron and over all kinematic variables not considered explicitly in the dependence of the differential cross section $d\sigma$ [CB10].
In the following the essentials of that approach, according to [CB10], will be presented.

t-channel $\Delta\Delta$ Contribution $M_{\Delta\Delta}$

The t-channel $\Delta\Delta$ contribution is calculated as explained above (equation 6.2), however now allowing all possible partial waves, ${}^3S_1$, ${}^3D_1$ and ${}^3D_3$, and using the correct angular dependence based on the angular momentum couplings in entrance and exit channels and the spherical harmonics.

t-channel Roper $N^*(1440)$ Contribution M_{Roper}

The Roper resonance $N^*(1440)$ is considered to be excited by t-channel σ-exchange, which is the dominant contribution. The main decay channel is the direct decay into $N\sigma$ [Sko09], thus in the current description the decay via the Δ resonance is neglected for the sake of simplicity. The matrix element for this process is then given by:

$$M_{Roper} = \frac{e^{i\Phi_{Roper}}}{q^2 - m_\sigma} D_{Roper} \, \Theta_{Roper}(m_p, m_n, m_d, \hat{k}_1, \hat{k}_2) \tag{6.6}$$

with the Roper propagator $D_{Roper} = \frac{c_{Roper}}{M^2_{N\pi\pi} - m^2_{Roper} + i m_{Roper}\Gamma_{Roper}}$ and the relative phase Φ_{Roper}. The latter is fitted to the experimental data and found to be approximately $\pi/2$. Since the considered energies are close to threshold, s-wave is assumed between

[3]Thus it is not a t-channel but a s-channel $\Delta\Delta$ system.

the $N^*(1440)$ and the N intermediate states. Hence only ${}^3S_1$ is likely and the angular dependence $\Theta_{Roper}(m_p, m_n, m_d, \hat{k}_1, \hat{k}_2)$ resulting from this ansatz is just a constant [CB10].

s-channel Resonance Contribution M_{d^*}

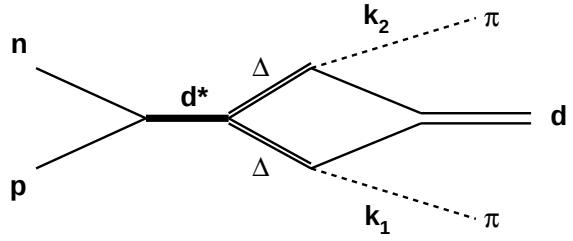

Figure 6.7: *Feynman diagram of excitation and decay of the s-channel resonance d^* in the basic fusion reaction $pn \to d\pi\pi$.*

The matrix element M_{d^*} of the ABC resonance process, which is depicted as Feynman diagram in Fig.6.7, is given by:

$$M_{d^*}(m_p, m_n, m_d, \hat{k}_1, \hat{k}_2) \;=\; M^0_{d^*}\; \Theta_{d^*}(m_p, m_n, m_d, \hat{k}_1, \hat{k}_2) \tag{6.7}$$

where Θ_{d^*} denotes the angular dependence, again obtained with the angular momentum couplings and the spherical harmonics.

$M^0_{d^*}$ is the product of the Δ propagators D_Δ, as in equations 6.3 and 6.4, and the Breit-Wigner-amplitude of the s-channel resonance:

$$M^0_{d^*} \;=\; \frac{m_{d^*}\sqrt{f\,\Gamma_i\,\Gamma_{\Delta\Delta}}}{s \;-\; m^2_{d^*} \;+\; i m_{d^*}\Gamma_{d^*}}\, D_{\Delta_1}\, D_{\Delta_2} \tag{6.8}$$

with the mass and total width of the resonance $m^2_{d^*} \approx 2.38$ GeV and $\Gamma_{d^*} \approx 70$ MeV at $s = m^2_{d^*}$.
The flux factor f of the Breit-Wigner resonance is given by

$$f \;=\; \frac{s}{p_i\, p_f}\,\frac{2J+1}{(2S_1+1)(2S_2+1)} \tag{6.9}$$

with S_1 and S_2 being the initial nucleon spins and p_i the initial momentum. $p_f = q_{\Delta\Delta}/2$ denotes the momentum of each Δ in the $\Delta\Delta$ system, where the s-channel resonance decays to [CB10].
Γ_i and $\Gamma_{\Delta\Delta}$ denote the partial widths for formation and decay of the resonance and are proportional to the square of the respective coupling constants g_{pn} and $g_{\Delta\Delta}$. Since the spin J of the resonance is 3, the width Γ_i is given by [Pil67, HA94, Tei97]:

$$\Gamma_i \;=\; g^2_{np}\, p_i^5\, F(p_i) \tag{6.10}$$

where the form-factor $F(p_i)$ accounts for potential barriers etc. The relative change of p_i is small over the resonance region, because the pn threshold is far below the energies regarded here, thus Γ_i can be assumed to be constant.
Similarly $\Gamma_{\Delta\Delta}$, assuming s-wave decay, is described by:

$$\Gamma_{\Delta\Delta} = g^2_{\Delta\Delta}\, q_{\Delta\Delta}\, F(q_{\Delta\Delta})^2 \tag{6.11}$$

Here the monopole form factor $F(q_{\Delta\Delta}) = (\frac{\Lambda^2}{\Lambda^2+q^2_{\Delta\Delta}})^2$ [Tei97], naively accounting for the finite dimensions of the $\Delta\Delta$ system emerging from the resonance, introduces a $1/q_{\Delta\Delta}$ dependence. Hence this factor suppresses the constellations with a large relative momentum between the two Δs, and, as explained above, hereby the pion pairs with large $q_{\pi\pi}$ and invariant mass, respectively. The cutoff parameter Λ is fitted to reproduce the experimental data. The best result is gained with $\Lambda = 0.4$ (GeV/c)^2, which, since a monopole form factor is used, corresponds to a size of $r = \frac{\hbar\sqrt{6}}{\Lambda} \approx 1.2$ fm [CB10].
The total width Γ_{d^*} of the resonance is given by [CB10]:

$$\Gamma_{d^*} = \Gamma_i + \sum \Gamma_f \approx \Gamma_0 + \gamma_{d^*} \int q_{\Delta\Delta} F^2(q_{\Delta\Delta}) |D_{\Delta_1} D_{\Delta_2}|^2 \tag{6.12}$$

where the sum runs over all possible $q_{\Delta\Delta}$, m_1^2 and m_2^2, where m_i denotes the invariant mass of the $N\pi$ system forming the Δ_i. Here Γ_0 denotes the partial width for the decay into NN and $NN\pi$. Since the energy range of the ABC effect is well above the respective thresholds, this width can be taken as a constant. In can be estimated to a value of 30 MeV [CB10].
The term γ_{d^*} represents the decays into $d\pi\pi$ and $NN\pi\pi$. It contains among others the (unknown) coupling constant $g_{\Delta\Delta}$ and the strength of the decays into the unbound channels. It is adjusted so that the total width fits to the experimentally found width of $\Gamma_{d^*}(s = m^2_{d^*}) = 70$ MeV.

With these ingredients the experimental data can be described amazingly well. Figure 6.8 shows the Dalitz plot for the reaction $pn \to d\pi^0\pi^0$ at $\sqrt{s} = 2.38$ GeV and $\sqrt{s} = 2.5$ GeV. The left side shows the experimental data, the right side the Monte Carlo simulation of the ABC resonance model. Both, the narrow band in the invariant mass of $d\pi$ and the structure in the invariant mass of the two pions, are well reproduced by the simulation. At the higher energy the $\Delta\Delta$ process starts to play a role, which causes a bump also at high $M_{\pi\pi}$ values. The total cross section of this reaction is seen above in Fig. 6.6b. The ABC resonance model describes the data for both total and differential cross section very well.

Extension to dd $\to {}^4$He$\pi^0\pi^0$

To extend the ABC resonance (and similarly the t-channel $\Delta\Delta$) model from $pn \to d\pi\pi$ to dd $\to {}^4$He$\pi^0\pi^0$ the simplest way is to assume the momenta of the four participating nucleons to be 1/2 of the momenta of the two deuterons in the

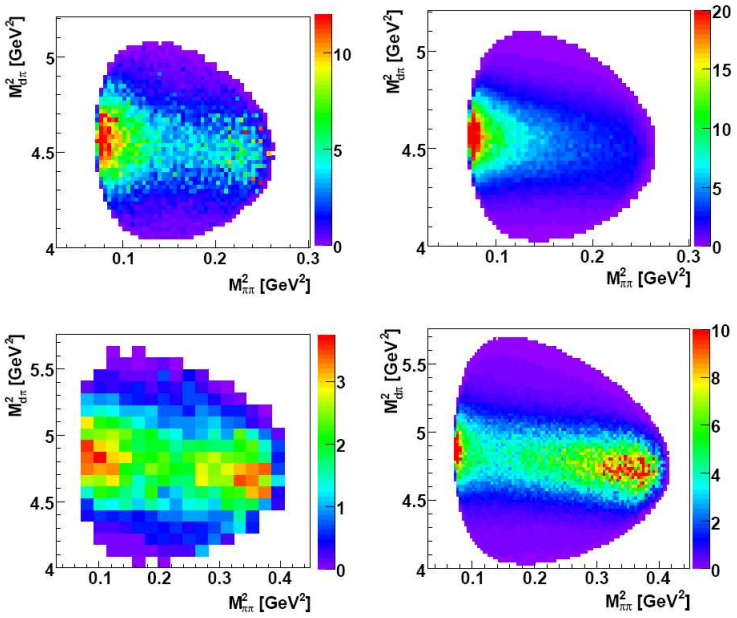

Figure 6.8: *$pn \to d\pi^0\pi^0$: Dalitz plots for $\sqrt{s} = 2.38$ GeV (upper row) and $\sqrt{s} = 2.5$ GeV (lower row). Left side shows the experimental data, right side the Monte Carlo simulations using equation 6.5. (plots taken from [Basc])*

initial channel and 1/4 of the ^{4}He momentum for the nucleons in the final channel, i.e. to neglect the Fermi motion of all participating nuclei. With these momenta the cross section according to Eq. 6.5 can be calculated.
In a more sophisticated, and more realistic, ansatz the momenta are calculated assuming a Fermi distribution inside the nuclei. For the initial nucleons the deuteron wave function is used, which gives the momentum distribution:

$$\wp(p) \propto [\frac{p \cdot (k^2 - \beta^2)}{(p^2 + \beta^2)(p^2 + k^2)}]^2 \tag{6.13}$$

This is based on the Hulthen wave function [Fri75], with $k = 0.26$ GeV/c and $\beta = 0.0456$ GeV/c.
For the nucleons forming the ^{4}He the momentum distribution is described by a Gaussian:

$$\wp(p) \propto (p \cdot e^{-(p/\lambda)^2})^2 \tag{6.14}$$

with $\lambda = 0.2$ GeV, which is obtained from a fit to the experimental charge radius of ^{4}He.
The mass, width Γ_R and the form factor parameter Λ of the resonance might be different in a medium compared to the clean case, thus these parameters can be adjusted. Additionally there are two parameters for each matrix element in equation 6.5: the strength of a particular matrix element ρ and its phase ϕ. The strength ρ is the combination of all constant factors like coupling constants etc. To some extent it is known, but can be varied in certain ranges. The phase ϕ is a unknown and hence

free parameter; it is measured in respect to the resonance phase. Furthermore the t-channel $\Delta\Delta$ amplitude appears in three partial waves, $^3S_1$, $^3D_1$ and $^3D_3$, each of them having different parameters ρ and ϕ.

Parameter		Value
ABC Resonance	M_R	2.34 GeV
	$\Gamma_R(s = M_R)$	0.124 GeV
	Λ	0.17 GeV/c
	ρ_R	15
Roper Resonance	ρ_{Roper}	6
	ϕ_{Roper}	$\pi/1 = 2$
t-channel $\Delta\Delta$ $^3S_1$	ρ	0
	ϕ	-
t-channel $\Delta\Delta$ $^3D_1$	ρ	6
	ϕ	0
t-channel $\Delta\Delta$ $^3D_3$	ρ	1.6
	ϕ	0

Table 6.1: *Parameters for the ABC resonance model for the reaction* $\mathrm{dd} \to {}^4\mathrm{He}\pi^0\pi^0$. *[Basb] ($\rho$ and ϕ are dimensionless)*

The parameters which yield the best description of the experimental data are given in table 6.1 [Basb].
In section 5.4.4 the efficiency and acceptance corrections based on different models are compared. The result is almost independent of the model used. The invariant masses do not change at all, only the angular distributions become less symmetric when a model is used which does not describe the invariant masses. Hence the results presented on the following pages are acceptance and efficiency corrected with the ABC resonance model, since it describes the data on a quantitative level and hence qualifies for a self-consistent data analysis.

6.2 Invariant Mass Distribution

The invariant mass of a system is a Lorentz-invariant quantity. It is determined by the square of the four-vector for the respective system: $M = \sqrt{E_{tot}^2 - p_x^2 - p_y^2 - p_z^2}$. In case of an unpolarized three body reaction, as in this work, three invariant mass distributions are possible: $M_{\pi_1\pi_2}$, $M_{^4\mathrm{He}\pi_1}$ and $M_{^4\mathrm{He}\pi_2}$, which reduces to two distributions in case of two neutral (indistinguishable) pions.

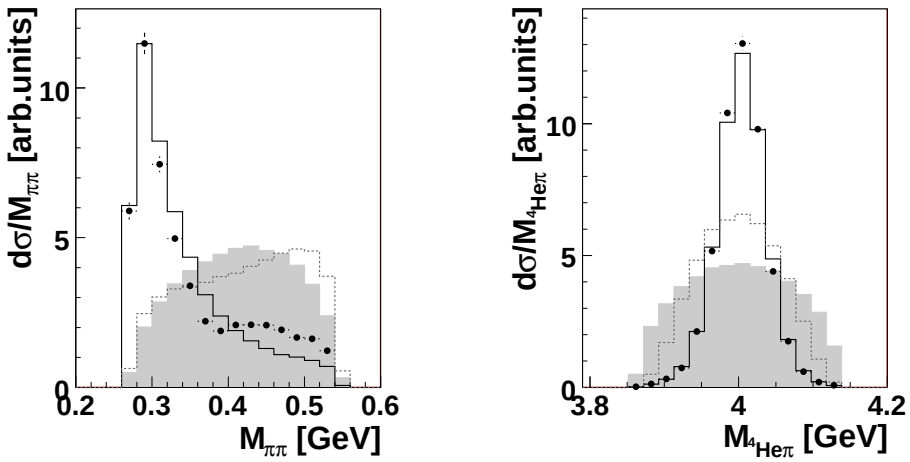

Figure 6.9: *Invariant Mass distributions of the $\pi^0\pi^0$ and $^4\mathrm{He}\pi^0$ systems for $T_d = 1.117$ GeV. The black dots represent the data of this work, the shaded area the phase space and the solid line the ABC resonance model and the dotted line the t-channel $\Delta\Delta$ simulation.*

Figure 6.9 shows the invariant mass distributions of the $\pi^0\pi^0$-system and the $^4\mathrm{He}\pi^0$-system after acceptance correction in comparison with the phase space and the ABC resonance model and the t-channel $\Delta\Delta$ simulation. The $\pi^0\pi^0$ invariant mass shows a strong peak at low invariant masses, followed by a broad shoulder towards higher invariant masses. It clearly deviates from phase space, as expected from previous experiments. Also the t-channel $\Delta\Delta$ calculation predicts a very different behavior with slight enhancements at high and low $M_{\pi^0\pi^0}$. However the ABC resonance model can reproduce the main ingredients, namely the strong narrow peak at low invariant masses, with no peak at high invariant masses.
The invariant mass of the $^4\mathrm{He}\pi^0$ system is much narrower than phase space as expected in case of a $\Delta\Delta$ excitation. However, it is even narrower than the expectations following from the t-channel $\Delta\Delta$ process. The reason is seen in Fig. 6.10 which shows the Dalitz plot $M^2_{^4\mathrm{He}\pi^0}$ versus $M^2_{\pi^0\pi^0}$ for phase space, ABC resonance model simulation and the experimental data. The strong enhancement at low $M_{\pi^0\pi^0}$ practically restricts the available phase space for $M_{^4\mathrm{He}\pi^0}$ to the region which is covered by the low $M_{\pi^0\pi^0}$ peak. In that part the width of the Dalitz plot in $M^2_{^4\mathrm{He}\pi^0}$ is narrower than in the center, especially on the very edge of the kinematic region, where the $M_{\pi^0\pi^0}$ peak is located.

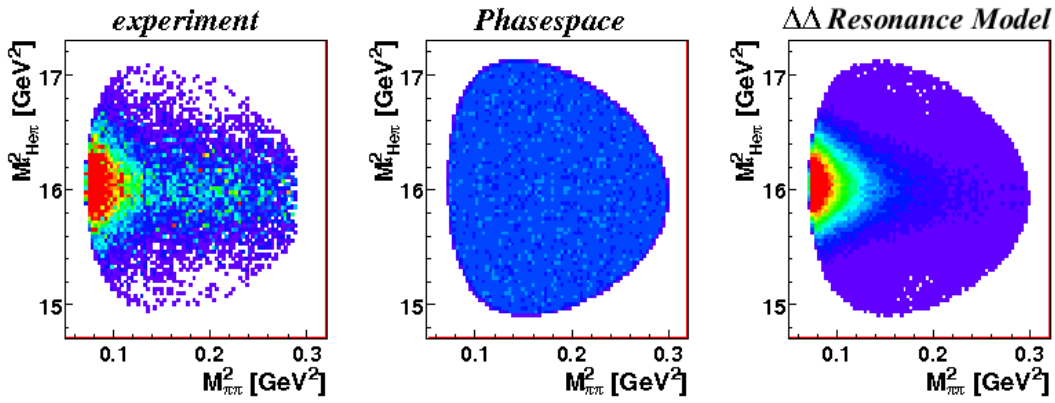

Figure 6.10: *Dalitz plot* $M^2_{^4He\pi^0}$ *versus* $M^2_{\pi^0\pi^0}$ *for* $T_d = 1.117$ GeV.

6.2.1 Comparison to CELSIUS-WASA Results at 1.029 GeV

The same reaction was measured before at CELSIUS-WASA at a beam energy of 1.029 GeV ([Kel08, Kel09]). In that work not the invariant mass of the $\pi^0\pi^0$ system is given, but the missing mass of the ^{4}He. Both are identical, if the kinematic conditions are fulfilled. But since no kinematic fit was performed in that work, they do not need to be the same. Figure 6.11 shows the ^{4}He missing mass before kinematic fit and before efficiency and acceptance corrections[4] both for the CELSIUS-WASA result and the result of this work at 1.05 GeV. The distributions are very similar, both showing the pronounced peak at low $M_{\pi^0\pi^0}$ and a shoulder toward higher invariant masses.

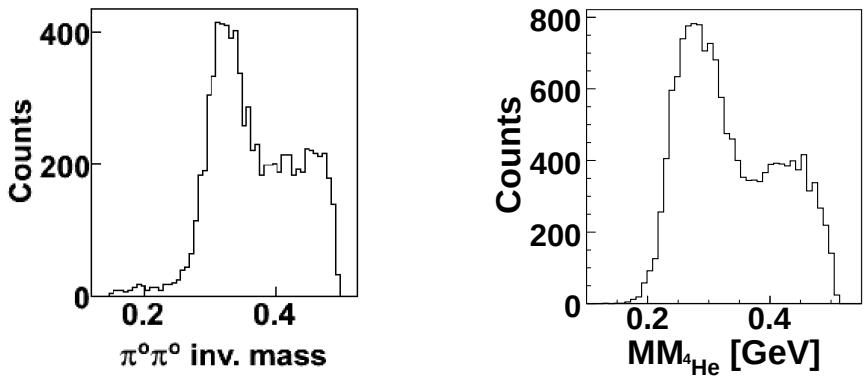

Figure 6.11: ^{4}He *Missing mass distribution before kinematic fit and efficiency and acceptance corrections. The left side shows the result for 1.029 GeV from CELSIUS-WASA [Kel08], the right side the result for 1.05 GeV from this work.*

[4] If the kinematic conditions are not fulfilled, the acceptance and efficiency corrections could in principle lead to artefacts from events which are outside the boundary and simply rejected by the correction.

6.3 Angular Distributions

For each particle (and particle system) one can plot angular distributions for different coordinate systems and several rest frames, like the center of mass system (cm), the laboratory system (lab), the $\pi^0\pi^0$ system and so on. All these distributions show certain information, here the most interesting distributions (see Fig. 6.12) will be discussed:

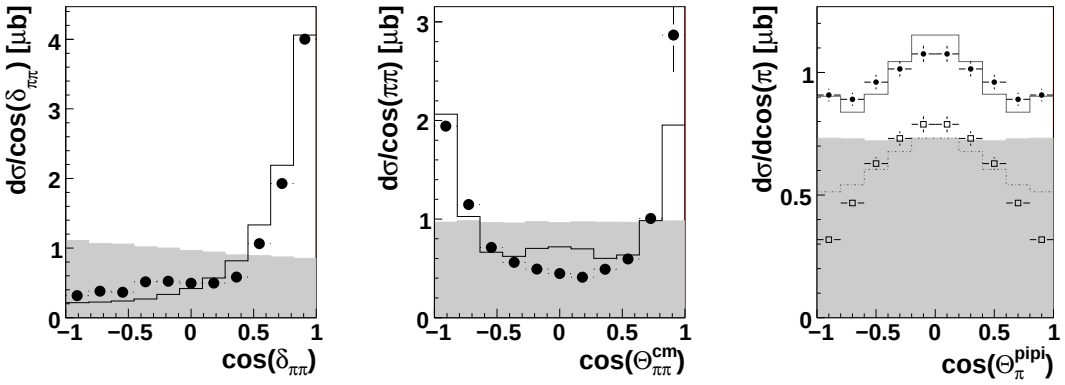

Figure 6.12: *Angular distributions for $T_d = 1.117$ GeV. The left plot shows the opening angle between the two pions in the cm system, the middle plot shows the polar scattering angle of the pion pair in the cm system and the right picture shows the angle of pions in the $\pi^0\pi^0$ subsystem. The dots represent the experimental data of this work, the shaded area marks the phase space and the solid line the ABC resonance model simulation. The open rectangles (dash-dotted line) in the cos$(\Theta_\pi^{\pi\pi})$ distribution are for the constraint $M_{\pi^0\pi^0} < 0.34$ GeV (low-mass enhancement region).*

$\delta^{cm}_{\pi^0\pi^0}$ is the opening angle between the two π^0 momentum vectors in the cm system. The experimental distribution is strongly peaked towards low relative angles, thus low relative momenta. Since low relative momenta correspond to low invariant masses, this peak correlates directly to the peak at low $\pi^0\pi^0$ invariant masses.

$\theta^{cm}_{\pi^0\pi^0}$ is the polar scattering angle of the $\pi^0\pi^0$ system in the cm frame. By kinematics it is mirrored to the θ angle for the ^{4}He. The distribution exhibits a strong "smiling face" as seen also in earlier measurements of the ABC effect. This follows from the angular distribution in the $\Delta\Delta$ system.

In the reaction dd $\rightarrow$ ^{4}He$\pi^0\pi^0$ it must be symmetric about 90° since the entrance channel is symmetric. Unfortunately the acceptance of the WASA detector is very low for forward going $\pi^0\pi^0$ pairs, because in this case the probability that at least one of the emitted photons is going in the forward region where it cannot be detected, is very high. This is clearly seen in the distribution before efficiency and acceptance correction in Fig. 6.14a. In this

region the accuracy of the model used for the corrections is crucial. Since the model is adjusted to fit best to all energies, it is not perfect for each energy, which shows up in the slight asymmetry of the corrected data.

$\theta_{\pi^0}^{\pi^0\pi^0}$ is the scattering angle in the $\pi^0\pi^0$ subsystem where the coordinate system is chosen such that the z-axis corresponds to the beam axis. This is the so-called Pseudo-Jackson frame[5] which is well suited for the study of the contributing partial waves in the respective subsystem. The full angular distribution shows a "sad face", i.e. the cross section is at maximum at values around $cos(\theta_{\pi^0}^{\pi^0\pi^0}) = 0$ and smaller at $cos(\theta_{\pi^0}^{\pi^0\pi^0}) = 1$ and $cos(\theta_{\pi^0}^{\pi^0\pi^0}) = -1$, which becomes steeper if only the part in the low mass peak of the $\pi^0\pi^0$ system is plotted. However, if this angle is plotted as a function of the invariant mass $M_{\pi^0\pi^0}$ of the $\pi^0\pi^0$ system it turns out that outside the peak in $M_{\pi^0\pi^0}$ the distribution turns around into a "smiling face" (see Fig. 6.13). The Monte Carlo simulation of the ABC resonance model also shows a "sad face" in the peak region, though much less pronounced, and underestimates the contribution at larger $M_{\pi^0\pi^0}$. For the overall shape of the distribution the interplay between the low and the high $M_{\pi^0\pi^0}$ part plays a crucial role, thus using different models for the corrections give somewhat different results for the shape of the full distribution, although the 2-dimensional plot changes only slightly.

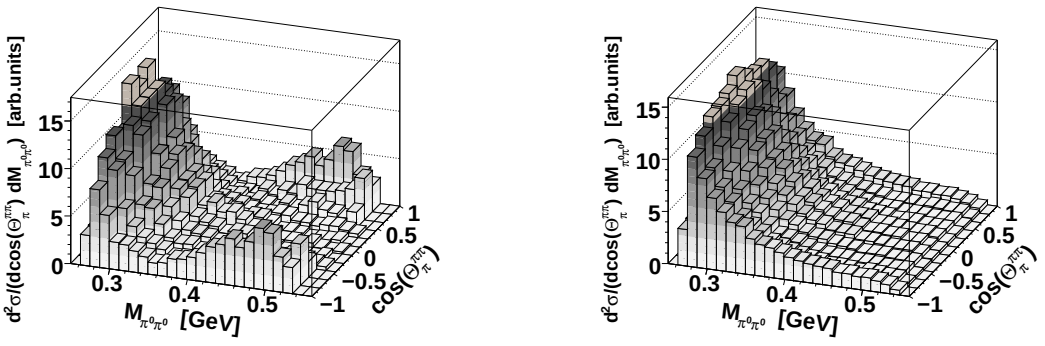

(a) *experimental data* **(b)** *ABC Resonance Model*

Figure 6.13: *Invariant mass $M_{\pi^0\pi^0}$ of the $\pi^0\pi^0$ pair versus the polar scattering angle $\Theta_{\pi^0}^{\pi^0\pi^0}$ of any of the π^0s in the $\pi^0\pi^0$ subsystem.*

The 2-dimensional plot of the laboratory kinetic energy of the ^{4}He versus the polar scattering angle θ of ^{4}He (Fig. 6.14) summarizes several informations in one plot, as explained at hand of Fig. 5.2a (section 5.1.1). The strong population of the outer rim of the kinematic ellipse corresponds to the low mass enhancement in $M_{\pi^0\pi^0}$.
At kinetic energies below 0.4 GeV practically no events are measured, because the probability to lose at least one γ to the forward detector is very high. If no events

[5] In the usual Jackson frame also the beam axis is transformed into the $\pi^0\pi^0$ rest frame.

at all are measured in a regime, efficiency and acceptance corrections cannot be applied.

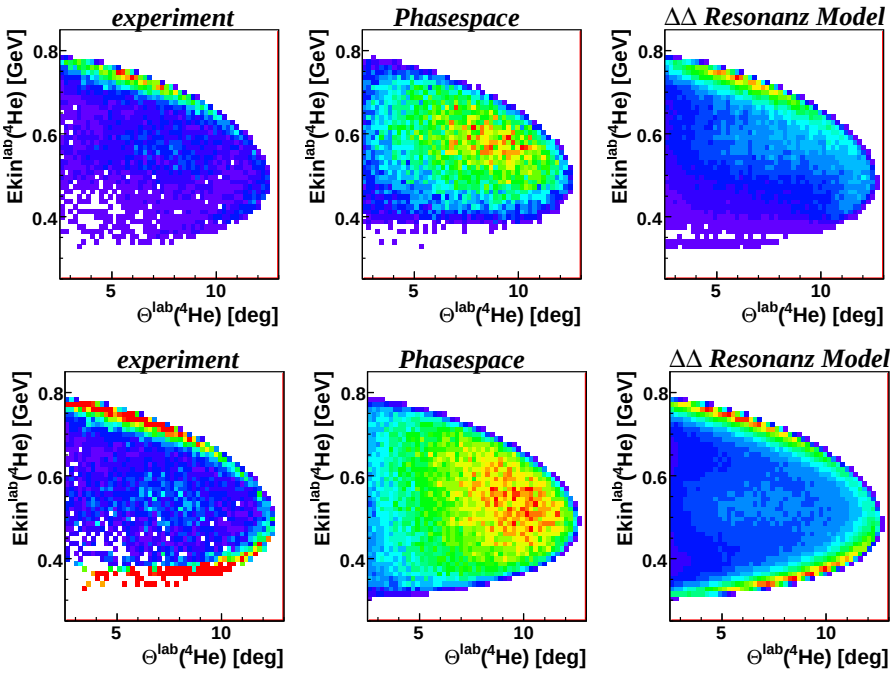

Figure 6.14: *Kinetic energy of the* ^{4}He *versus its polar scattering angle* θ *in the laboratory frame before (upper row) and after efficiency and acceptance corrections (lower row) for experimental and simulated data. The rim at the outer border corresponds to the peak at low invariant* $\pi^0\pi^0$ *masses.*

6.4 Energy Dependence of the Differential Cross Sections

6.4.1 $M_{\pi^0\pi^0}$ and $M_{^4\mathrm{He}\pi^0}$ Distributions

In the reaction $pn \rightarrow d\pi^0\pi^0$ the total cross section shows a peak structure, which is correlated with the low-mass peak in the $M_{\pi^0\pi^0}$ spectrum. At energies above the peak structure in the total cross section the low-mass peak decreases and a second peak at high $M_{\pi^0\pi^0}$ arises. The latter is the signature of the t-channel $\Delta\Delta$ excitation. In case of the fusion to ^{4}He, which is investigated in this work, the changes with the energy of the system are much less pronounced. Figures 6.16 - 6.18 show Dalitz plots as well as their square-root projections, the distributions of the invariant masses of the $\pi^0\pi^0$ and $^4\mathrm{He}\pi^0$ systems for all measured energies.
The $M_{^4\mathrm{He}\pi^0}$ distribution stays in principle the same over the whole energy regime. It is always much narrower than the phase space simulation, which is expected, since the $\Delta\Delta$ excitation should play a crucial role at all measured energies - independent of whether the underlying process is a s-channel or a t-channel process. But it is also

narrower than the expectations from the t-channel ΔΔ process. Since the narrow width is connected to the low-mass peak in the $M_{\pi^0\pi^0}$ spectrum, this fits to the fact, that also the $M_{\pi^0\pi^0}$ distribution changes only in details. At all energies the strong peak at low invariant masses is the main feature. Contributions from the Roper excitation are possibly seen at 0.8 and 0.9 GeV and the t-channel ΔΔ excitations contributes possibly at the higher energies by some small amount.
In the ABC resonance model that would mean that the resonance is broader than in the basic reaction and that the contribution from t-channel ΔΔ excitation is much less in the fusion to ^{4}He than in the fusion to d. Inside a nuclear medium two effects can broaden a resonance: by collision damping another decay branch is possible and its width is added to the total width of the resonance. Additionally the Fermi momentum inside a nucleus broadens the width of the resonance - the more the stronger the nuclear binding is.

6.4.2 Dalitz Plot $M_{^4\mathrm{He}\pi^0_1}$ versus $M_{^4\mathrm{He}\pi^0_2}$

If the Dalitz plots $M_{^4\mathrm{He}\pi^0_1}$ versus $M_{^4\mathrm{He}\pi^0_2}$ for all energies are plotted in a single picture, the development of the Δ resonance in the system can be observed. For each energy it is a very narrow ellipse with a significant enhancement at the upper edge in diagonal direction which reflects in the $\pi^0\pi^0$ invariant mass distribution. However this enhancement is hardly visible since the ellipse is so narrow. The ellipse is getting longer with increasing energy, while the width broadens only slightly.
Fig. 6.15 shows this plot for the experimental result, the ABC resonance model and the t-channel ΔΔ process. Obviously the ABC resonance model describes the data very well. Over the full energy range both show a narrow enhancement in the center of the ellipse, in contrast to the t-channel process, where the central peak broadens significantly above the nominal on-shell ΔΔ mass.

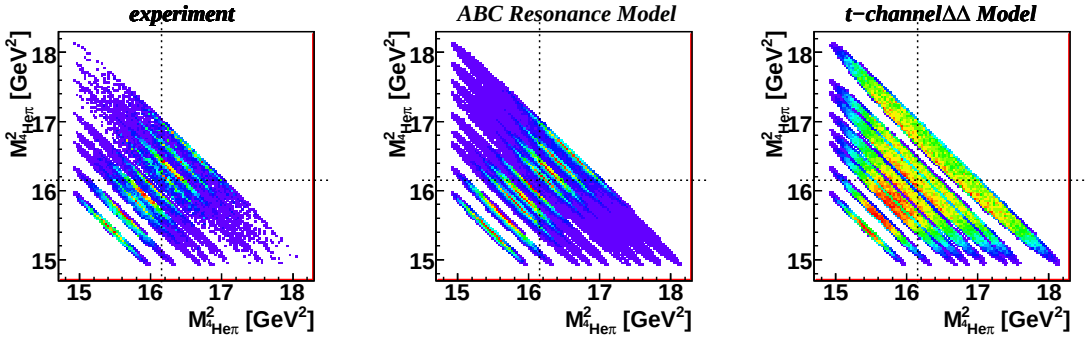

Figure 6.15: *Dalitz plot $M^2_{^4He\pi^0}$ versus $M^2_{^4\mathrm{He}\pi^0}$, all measured energies. The dotted line crossing marks the on-shell ΔΔ mass.*

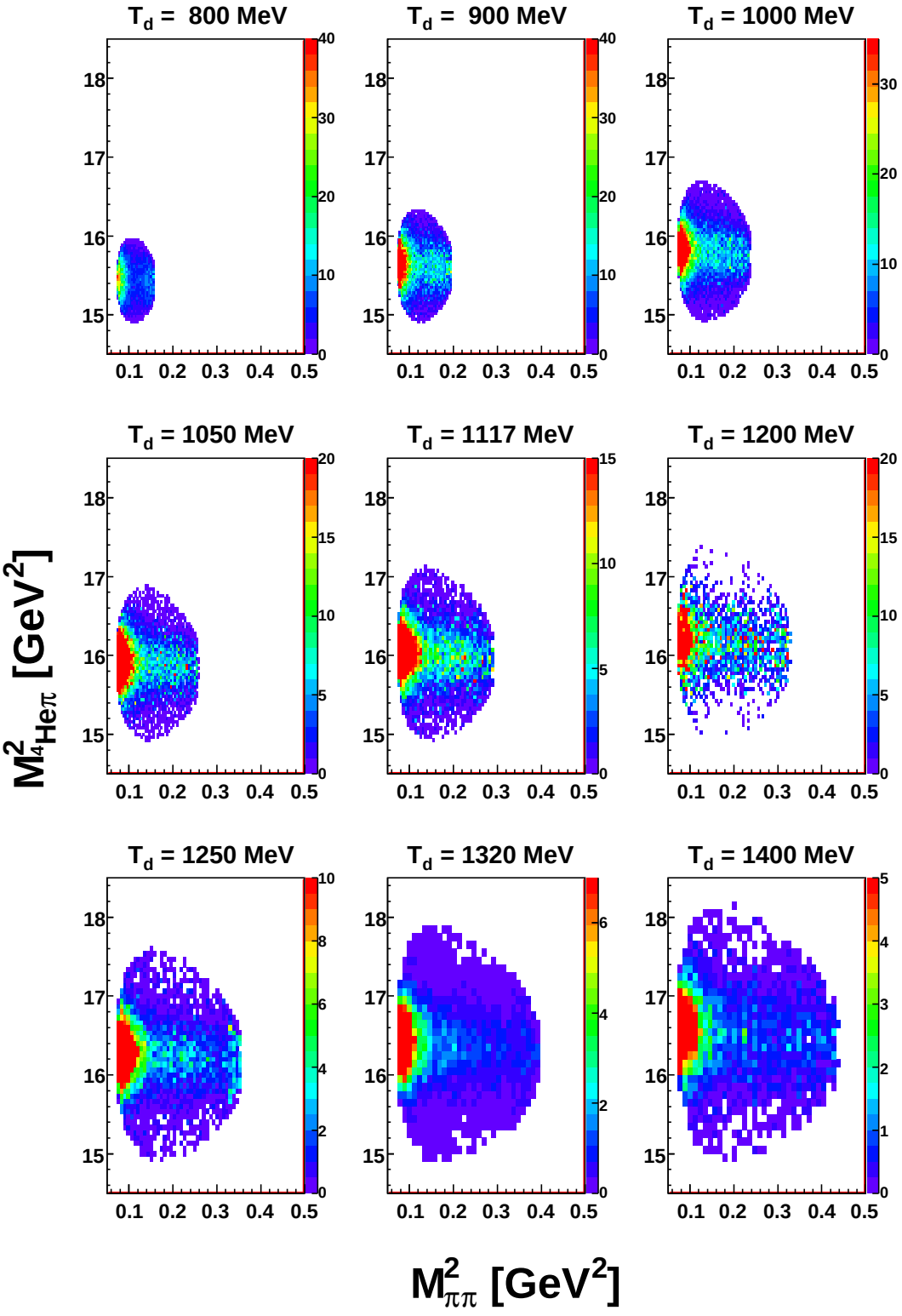

Figure 6.16: *Dalitz plot $M^2_{^4He\pi^0}$ versus $M^2_{\pi^0\pi^0}$ for $T_d = 1.117$ GeV for all energies. The evolution of the available phase space is nicely seen in the areal expansion of the Dalitz plots (note that the scale for the Dalitz plots is the same for all energies, while it is adjusted to each energy in case of the invariant masses).*

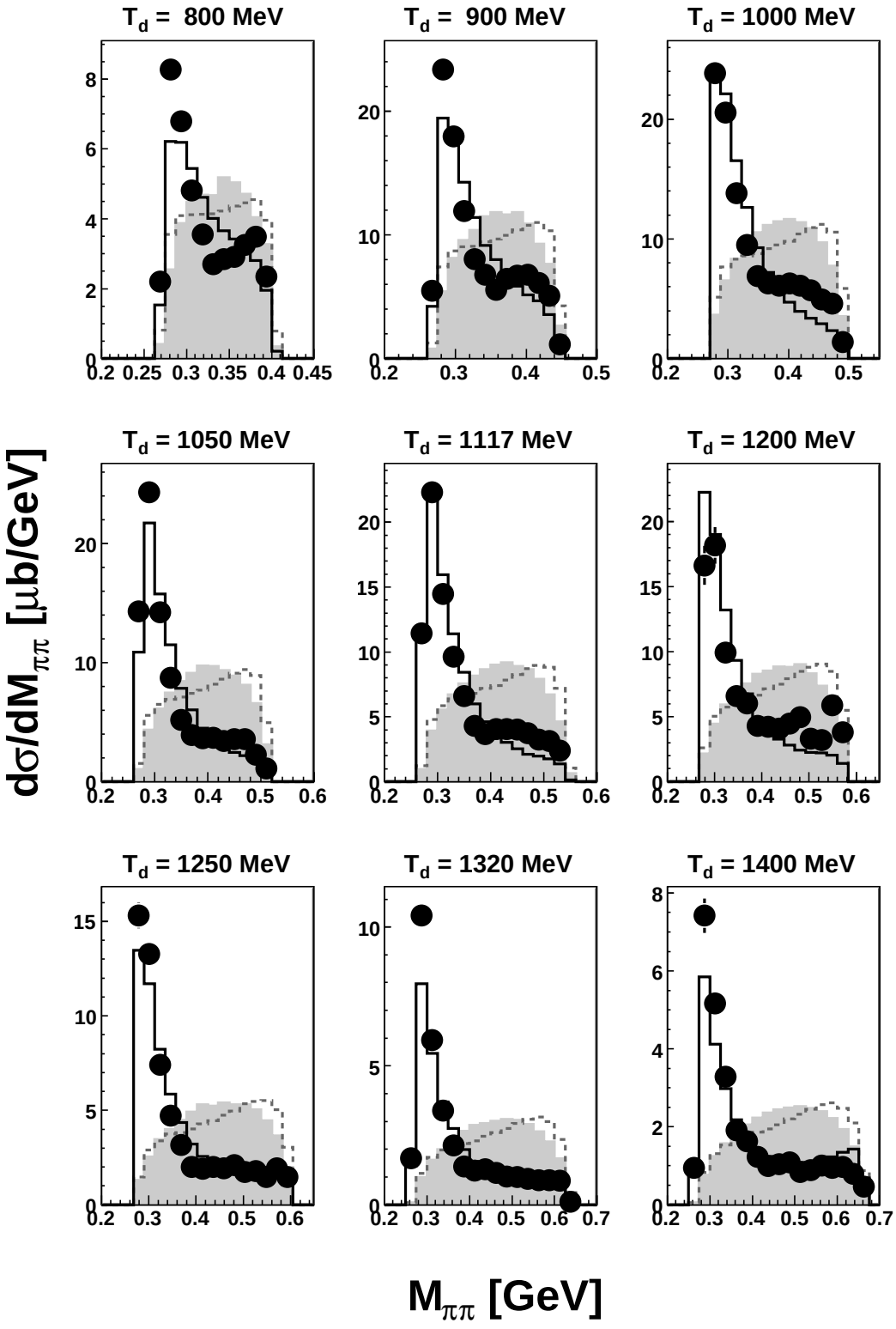

Figure 6.17: *$M_{\pi^0\pi^0}$ distribution for all energies. The dots represent the data, the shaded area the phase space, the solid line the ABC resonance model and the dotted line the t-channel $\Delta\Delta$ simulation.*

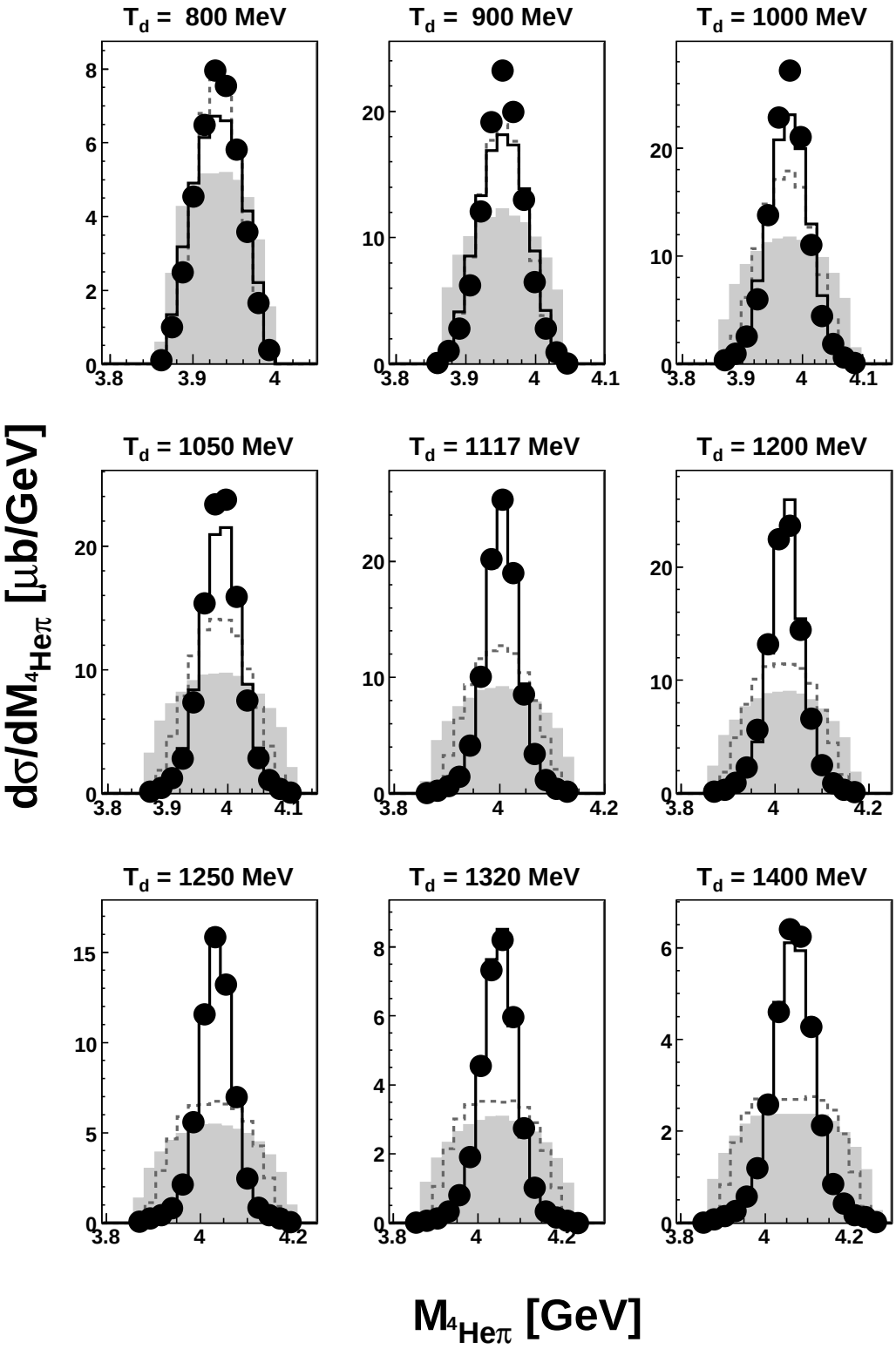

Figure 6.18: *$M_{^4\mathrm{He}\pi^0}$ distribution for all energies. The dots represent the data, the shaded area the phase space, the solid line the ABC resonance model and the dotted line the t-channel $\Delta\Delta$ simulation.*

6.4.3 Angular Distributions

Since the opening angle between the pions $\delta^{cm}_{\pi^0\pi^0}$ is directly related to $M_{\pi^0\pi^0}$, its distribution shows the same behavior as the invariant masses. Over the full energy range a strong enhancement at small angles is seen.
The distribution of $\Theta^{cm}_{\pi^0\pi^0}$ does not change much over the energy range. It is always a "smiling face". The asymmetry at $T_d = 1.2$ GeV might originate from the bad beam conditions during the measurements.
For $\theta^{\pi^0\pi^0}_{\pi^0}$ the distributions yield for all energies a "sad face" at small $M_{\pi^0\pi^0}$, in the region of the enhancement in the spectrum of the invariant mass $M_{\pi^0\pi^0}$ of the $\pi^0\pi^0$ system, which turns around into a "smiling face" at larger $M_{\pi^0\pi^0}$.

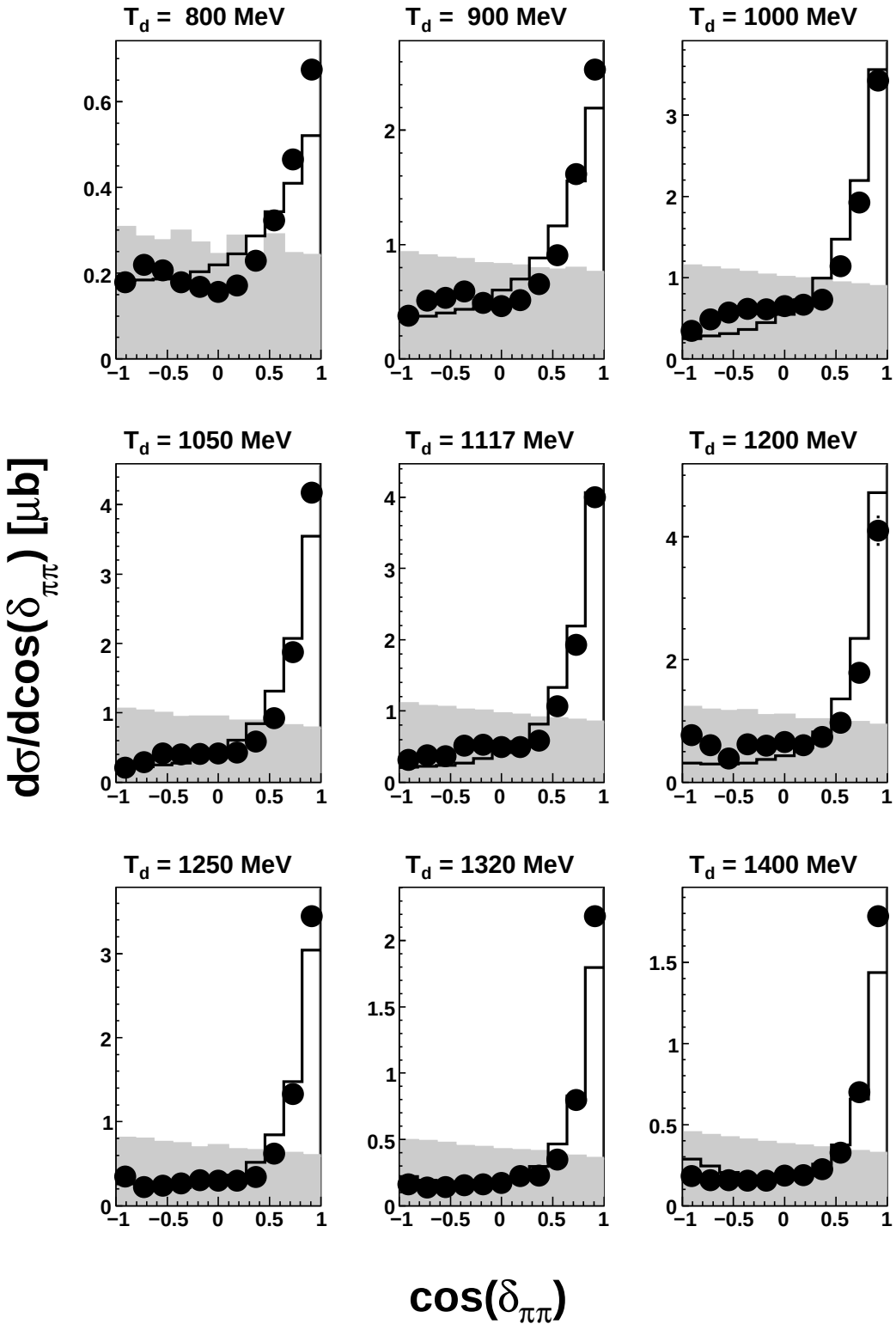

Figure 6.19: *Distribution of the opening angle $\delta^{cm}_{\pi^0\pi^0}$ between the pions in the center of mass system for all measured energies. The dots represent the data, the shaded area the phase space and the solid line the ABC resonance model simulation.*

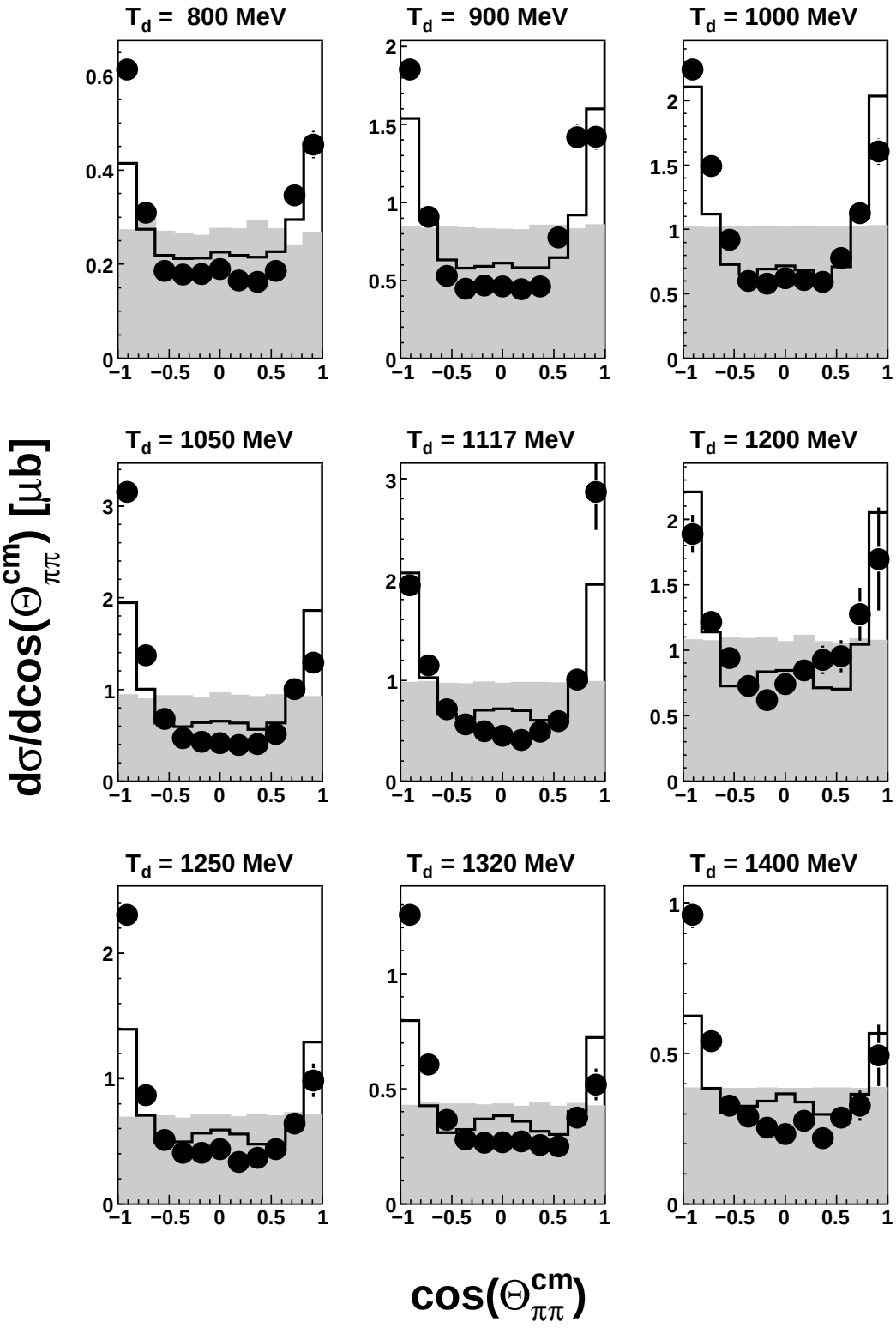

Figure 6.20: *Distribution of the $\pi^0\pi^0$ center of mass angle $\Theta^{cm}_{\pi^0\pi^0}$ for all measured energies. The dots represent the data, the shaded area the phase space and the solid line the ABC resonance model simulation.*

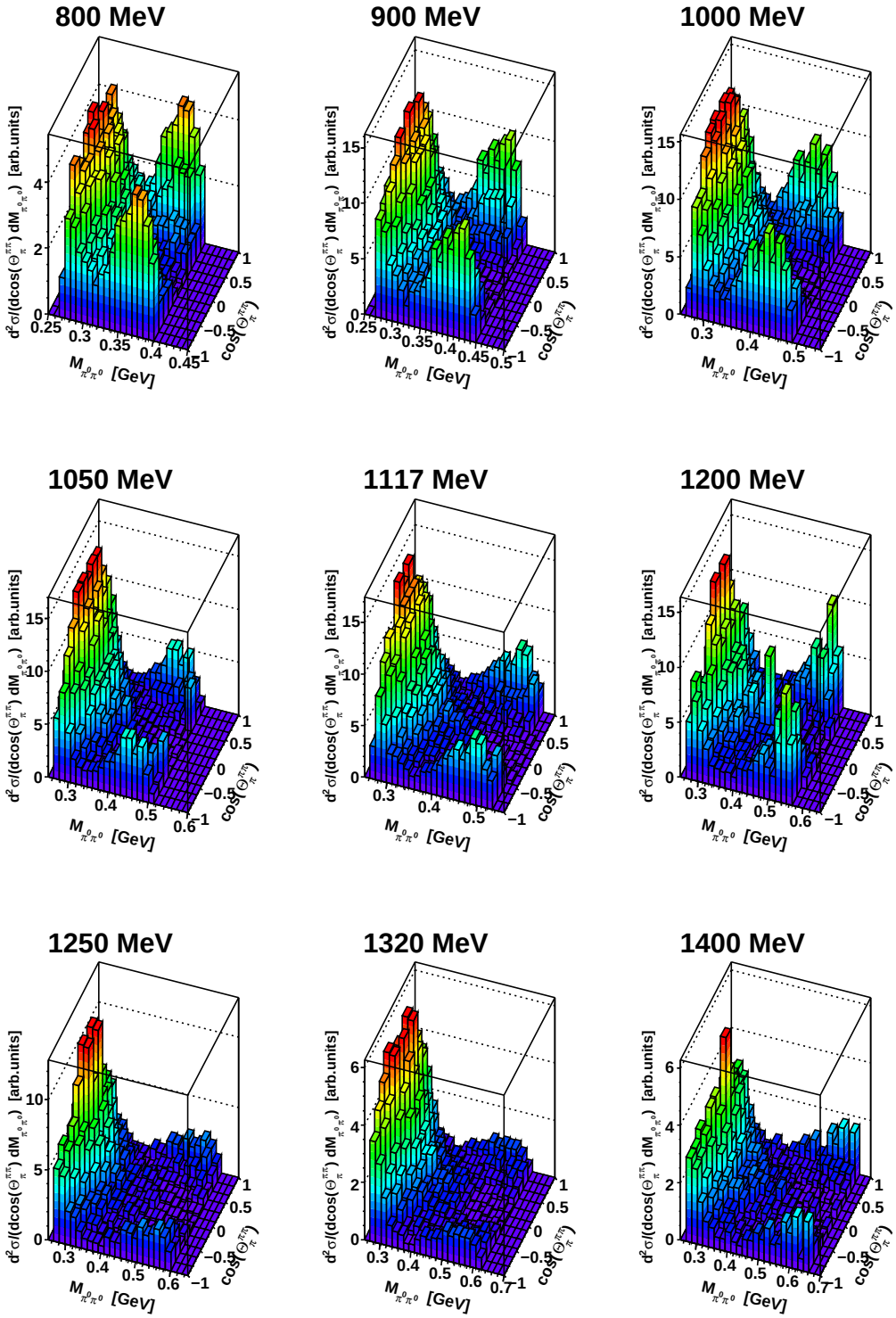

Figure 6.21: *Distribution of the polar scattering angle* $\theta^{\pi^0\pi^0}_{\pi^0}$ *of any pion in the* $\pi^0\pi^0$ *subsystem versus the invariant mass* $M_{\pi^0\pi^0}$ *of the* $\pi^0\pi^0$ *system for all measured energies. Clearly seen is the different curvature for small and large* $M_{\pi^0\pi^0}$.

6.5 Absolute Normalization

The number of reconstructed measured events N_{exp} is related to the total cross section σ by:

$$N_{exp} = \sigma \cdot L_{int} \cdot \epsilon_{eff-acc} \tag{6.15}$$

Here $\epsilon_{eff-acc}$ denotes the efficiency and acceptance corrections due to the detector geometry and the analysis, and $L_{int} = \int L \cdot \epsilon \cdot dt$ the time integrated luminosity.
The former can be estimated using Monte Carlo simulations, which is a reliable method provided that either the reaction model is realistic or the whole phase space is measured. The estimation of L_{int}, however, is rather difficult because ϵ incorporates all the imperfections in the experiment like the DAQ dead-time, the trigger inefficiencies, the cycle structure of the beam and the pellet frequency.
A much easier and more reliable way is to deduce the integrated cross section by means of a known reaction. In the case that both reactions, the one of interest and the normalization reaction, are measured with the same trigger simultaneously, all instrumental imperfections L_{int} depends on are exactly the same for both reactions. Hence the cross sections are related by:

$$\frac{\sigma}{\sigma^{known}} = \frac{\epsilon^{known}_{eff-acc}\ N_{exp}}{N^{known}_{exp}\ \epsilon_{eff-acc}} \tag{6.16}$$

In the case of dd $\rightarrow$ ^{4}He$\pi^0\pi^0$ the reaction dd $\rightarrow$ ^{3}Hen is a good normalization reaction. In Saclay this reaction was measured at four energies not too far away from the nine energies measured for this work (see Fig. 5.22). The selection of dd $\rightarrow$ ^{3}Hen is described in section 5.5.
Problems arise from the fact, that the ^{3}He particles emitted in this reaction have larger kinetic energies than the ^{4}He particles and punch through the detector layers, where the ^{4}He is stopped. This shows up in two points:

Threshold on FRH1: The deposited energy in the first FRH is substantially lower for dd $\rightarrow$ ^{3}Hen than for dd $\rightarrow$ ^{4}He$\pi^0\pi^0$. Since the trigger was adjusted for measuring dd $\rightarrow$ ^{4}He$\pi^0\pi^0$, the threshold on FRH1 was rather large. It turned out that at some energies the threshold was too high for some elements and hence cut dd $\rightarrow$ ^{3}Hen events. Luckily, for most elements the threshold was low enough so that everything was measured[6].

Veto included in the trigger: At some beam energies the trigger included a veto on a FRH layer, which was not reached by ^{4}He ejectiles from the dd $\rightarrow$ ^{4}He$\pi^0\pi^0$ reaction but by ^{3}He ejectiles from the dd $\rightarrow$ ^{3}Hen reaction. In this case, the main trigger could not be used for the normalization. For 0.9 GeV unfortunately no other trigger was set up which gave reasonable large statistics. Only a single run was taken without the veto. Thus this run was used for the normalization. Accordingly the number of available events here is much lower than at the other beam energies where the main trigger could be used.

[6]There is only one common threshold value to set for 16 elements of the FRH.

Several runs had to be omitted for the absolute normalization, because the conditions, like beam current, pellet rate or detector performance varied too much. Table 6.2 summarizes for each beam energy which detector elements had to be omitted and how many events could be used for the determination of the total cross section.

T_d /GeV	omitted elements		number of events		remark
	^{3}Hen	^{4}He$\pi^0\pi^0$	^{3}Hen	^{4}He$\pi^0\pi^0$	
0.800	19, 24	-	63632	620	
0.900	23	23	1296	62	only run 5146
1.000	-	-	973	73	only runs 3854-3905
1.050	4	1, 24	446872	29324	
1.117	4, 18, 19, 24	24	62768	6862	
1.200	3, 4, 10, 15-18, 24		7493	444	only runs 4170-4210
1.250	4, 18, 19, 24	-	51778	5915	
1.320	all except 2,6,8,9	-	20761	7735	
1.400	all except 11,15,20	-	5649	3518	

Table 6.2: *Conditions used for the determination of the absolute cross section. In case of 1.32 and 1.4 GeV the* ^{3}Hen *selection was carried out only for a few detector elements (see section 5.5).*

6.5.1 Error Estimation

The error of the total cross section is given by the statistical and the systematic errors of the ^{4}He$\pi^0\pi^0$ events and the integrated luminosity.

Statistical Error

According to the usual error propagation, the statistical error of the total cross section is given by:

$$\delta^{stat}(\sigma) = \sigma \sqrt{(\frac{\delta^{stat}(N_{^4\mathrm{He}\pi^0\pi^0})}{N})^2 + (\frac{\delta^{stat}(L)}{L})^2} \tag{6.17}$$

Here $\delta^{stat}(N_{^4\mathrm{He}\pi^0\pi^0})$ denotes the uncertainty originating from simple statistical fluctuations ($\Delta N = \sqrt{N}$) of the number of measured events. The number of measured events as well as the number of simulated and reconstructed events are taken into account, although the error for the latter is usually negligible, since the number of measured events is usually much smaller than that of the simulated events.
$\delta^{stat}(L)$ denotes the uncertainty in the luminosity determination, which is described in section 5.5.

Systematic Error

The probability cut in the selection of ^{4}He$\pi^0\pi^0$ events comprises a systematic uncertainty. To estimate this effect, the cut was varied between 0.05 and 0.35 (0.2 being the one used in general for the differential cross sections). The distance between the smallest and the largest cross section is assigned as error. Appendix 9.6 shows the respective plots.

Changes in the differential luminosity might have an impact on the total cross section because, e.g., the gains of the PMTs are rate dependent or the trigger gets spoiled by a larger amount of background. The gains might also change due to temperature changes or high voltage jumps. In order to estimate the time dependence of the results for the total cross section, the total cross section is calculated run wise. In most cases the total cross sections are consistent within the error bars. The respective plots can be found in the appendix 9.7. In case of $T_d = 0.9$ GeV this check is of course not possible, since only one run can be used to estimate to total cross section.

The error of the luminosity due to the error of the total cross section given by the ^{3}Hen data from [Biz80] (see table 5.6) is regarded as a systematic error and added in quadrature to the systematic error arising from the ^{4}He$\pi^0\pi^0$ analysis.

Commissioning Beam Time

It was possible to extract differential distributions also from the two beam energies which were measured during the commissioning beam time, $T_d = 1.0$ GeV and $T_d = 1.2$ GeV. Unfortunately the γ detection efficiency was bad during one part of the beam time due to bad beam or target conditions (see Appendix 9.8). This caused a lower efficiency for the dd $\rightarrow$ ^{4}He$\pi^0\pi^0$ reaction, thus this part of the beam time could not be used for the absolute normalization.

For $T_d = 1.0$ GeV enough statistics was collected during the good part of the beam time, thus the total cross section is estimated on the basis of these runs, resulting in a relatively large statistical error for the cross section.

For $T_d = 1.2$ GeV this was not possible. In order to give an estimate of the total cross section the value obtained from the second part of the beam time was corrected by a factor estimated on basis of the 1.0 GeV data, where both parts of the beam time can be compared (see Appendix 9.8), assuming the detector efficiency was the same for both energies. From this follows that the actual number of the cross section is larger than the measured one by a factor of 2.17 ± 0.83. Here the large error is purely statistical due to the relatively few events available for the cross section determination. Furthermore it is not clear if the assumption that the detector efficiency was approximately constant over each part of the beam time is correct. Hence the total cross section for $T_d = 1.2$ GeV must rather be considered as an educated guess.

6.5.2 Total Cross Section

Finally the total cross sections for the nine measured energies are given in table 6.3 and plotted in Fig. 6.22 together with phase space, ΔΔ process and ABC-resonance model calculations. The results from this work are represented by the filled blue circles (the $T_d = 1.2$ GeV estimate is shown by an open circle in light blue). The colored symbols show the experimental data published from different groups. The only other result from exclusive measurements, the CELSIUS-WASA point at 1.029 GeV, is in good agreement with the results presented here. The Saclay point at 1.25 GeV, which is much lower than the result obtained in this work, was extracted from inclusive measurements, hence a deviation is not too serious.

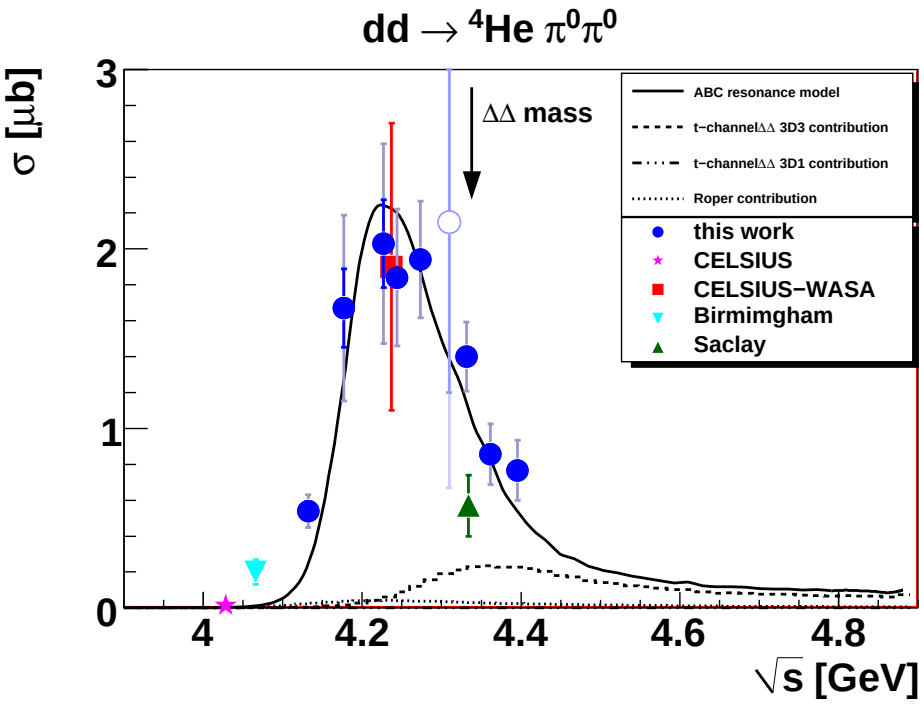

Figure 6.22: *Total cross section of the reaction* dd $\rightarrow$ ^{4}He$\pi^0\pi^0$ *as a function of the total energy* $\sqrt{s}$*. The blue dots mark the result of this work. The other symbols denote previous experiments [Kel09, Bar97, Cha66, Ban76]. The open circle marks the estimated cross section at 1.2 GeV.*

As expected from the situation in the $pn \rightarrow d\pi^0\pi^0$ reaction, the total cross section of the dd $\rightarrow$ ^{4}He$\pi^0\pi^0$ reaction is strongly energy dependent, showing a peak at a total energy of $\sqrt{s} \approx 4.25$ GeV, which corresponds to a beam energy of $T_d \approx 1.05$ GeV. As in the differential distributions neither phase space nor the t-channel ΔΔ model describe this effect. However the ABC resonance model fits very well to the experimental result: both the position and the width of the peak are reproduced.

energy		σ_{tot}	δ^{stat}	δ^{sys}	
0.8	GeV	0.54	$\pm$ 0.023	$\pm$ 0.068	μb
0.9	GeV	1.67	$\pm$ 0.219	$\pm$ 0.298	μb
1.0	GeV	0.79	$\pm$ 0.244	$\pm$ 0.312	μb
1.05	GeV	1.84	$\pm$ 0.038	$\pm$ 0.343	μb
1.1117	GeV	1.94	$\pm$ 0.044	$\pm$ 0.281	μb
1.2	GeV	2.15	$\pm$ 0.95	$\pm$ 0.53	μb
1.25	GeV	1.40	$\pm$ 0.033	$\pm$ 0.160	μb
1.32	GeV	0.86	$\pm$ 0.019	$\pm$ 0.150	μb
1.4	GeV	0.77	$\pm$ 0.027	$\pm$ 0.141	μb

Table 6.3: *Total cross sections for the nine measured energies and the estimated errors.*

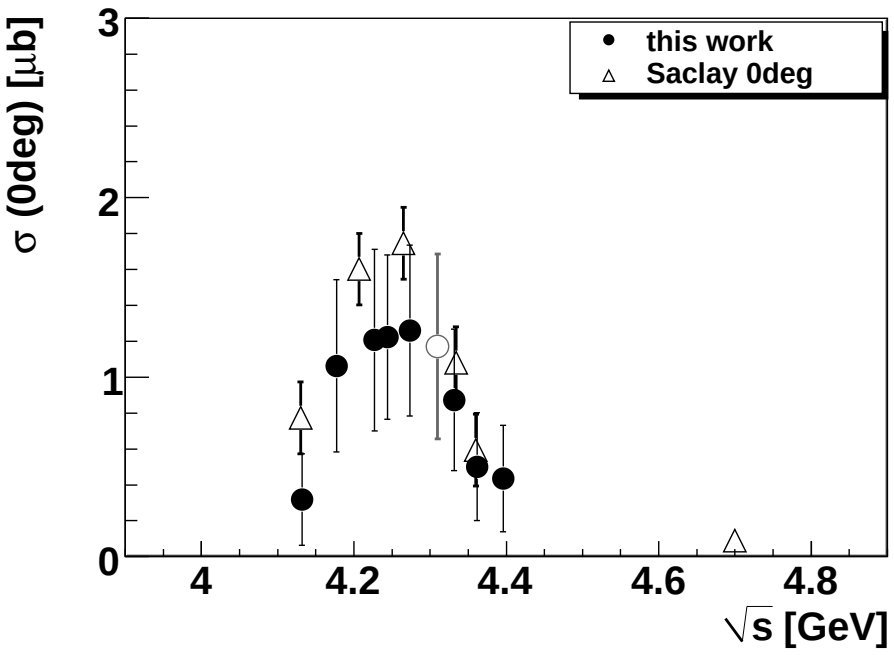

Figure 6.23: *Absolute cross section at $\theta^{cm}_{^4\mathrm{He}} = 0$ as a function of the beam energy. The blue dots represent the results of this work, the triangles the results from inclusive measurements from Saclay [Ban76], renormalized by a factor of 1.8.*

The only other measurements showing the energy dependence of the absolute cross section in the regarded range are inclusive measurements at $\theta^{cm}_{^4\mathrm{He}} = 0^\circ$ or 180° by [Ban76]. In order to compare the results found here to these data, the average value of $\theta^{cm}_{^4\mathrm{He}} = 0^\circ$ and $\theta^{cm}_{^4\mathrm{He}} = 180^\circ$ is used[7]. Since the WASA detector cannot measure at

[7]Since the two incident particles are identical, the $\theta^{cm}_{^4\mathrm{He}}$ distribution must be symmetric about 90°

exactly 0°, the absolute cross section at very small angles is not well determined. To overcome this problem, the cross section was taken in a larger interval from $\theta^{cm}_{^4\mathrm{He}} = [0°, 28°]$ and $\theta^{cm}_{^4\mathrm{He}} = [152°, 180°]$, respectively.
Since the Saclay values result from inclusive measurements, the absolute value of the cross section might be different, but the energy dependence itself should be similar. Indeed the behavior is very similar, as seen in Fig. 6.23, where both, the Saclay results and those presented in this work, are plotted. Here an overall scale factor was applied to the Saclay data points. Also here a broad peak with a maximum at around $T_d = 1$ GeV beam energy is seen.
Since it is assumed that the ABC effect in all observed channels, $pn \to d\pi\pi$, $pd \to {}^3\mathrm{He}\pi\pi$ and $dd \to {}^4\mathrm{He}\pi\pi$, is based on the same process, the energy dependence of the total cross section should show a similar behavior as well. To check that, the total cross section is plotted in Fig. 6.24 as a function of the excess energy, thus the available energy above the reaction threshold. The $pn \to d\pi^0\pi^0$ data are taken from the most recent exclusive measurement from WASA-at-COSY[Basc].

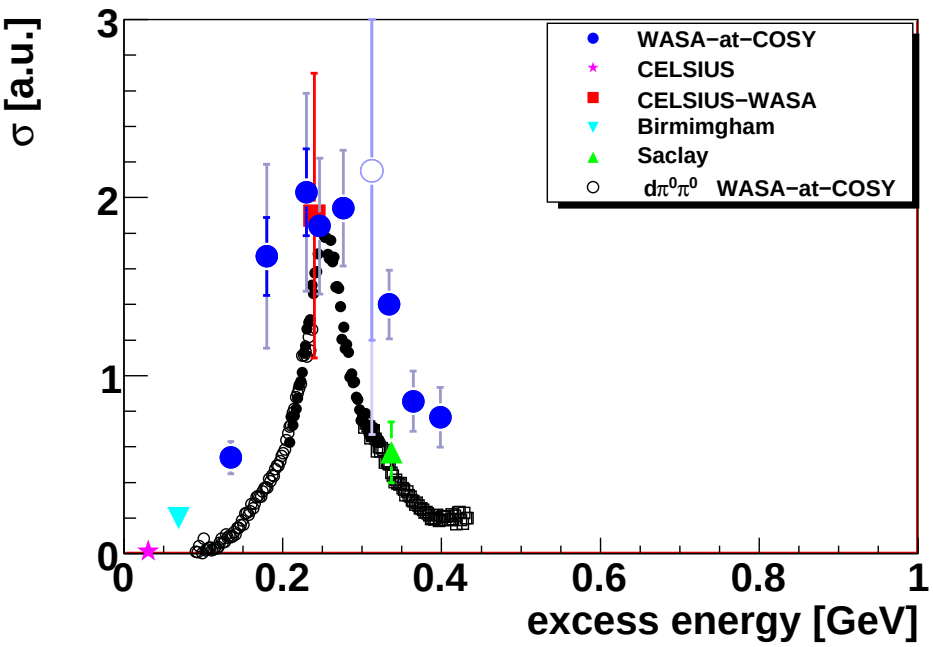

Figure 6.24: *Total cross section of the reactions* dd $\to {}^4\mathrm{He}\pi^0\pi^0$ *(blue symbols) and* $pn \to d\pi^0\pi^0$ *(black dots), rescaled by a factor of 2 as a function of the excess energy* $(\sqrt{s} - E_{threshold})$.

Indeed the results are very similar. In both cases the total cross section exhibits a peak at roughly the same position, approximately 80 MeV below the $\Delta\Delta$ threshold. However, the peak in dd $\to {}^4\mathrm{He}\pi^0\pi^0$ seems to be shifted slightly towards lower energies, which would correspond to a smaller mass of the resonance. The effect that the effective mass of a resonance changes inside a nuclear medium is well-known from studies of the Δ resonance in nuclei [EW88]. In the basic reaction the

peak is much narrower, due to the reduced Fermi motion effect and inside a nuclear medium partners for collisions are available, which cause a shorter lifetime and hence a larger width (collision damping) [EW88].
The large width in dd $\rightarrow {}^4\mathrm{He}\pi^0\pi^0$ is also mirrored in the differential distributions, where the part attributed to the resonance dominates over the whole measured energy region.

To summarize, in the region of the ABC effect both the basic double-pionic fusion to deuteron, $pn \rightarrow d\pi^0\pi^0$, and the fusion to helium, dd $\rightarrow {}^4\mathrm{He}\pi^0\pi^0$, appear to be dominated by the same process. The exclusive results presented here for the fusion to helium as well as the recent exclusive results for $pn \rightarrow d\pi^0\pi^0$ [Basc] are well reproduced by the ABC resonance model, i.e. an intermediate excitation of a s-channel resonance in pn and $\Delta\Delta$ systems.

7 Summary

Now You all know the bards and their songs
When hours have gone by I'll close my eyes

The Bard's Song, Blind Guardian [BG92]

The energy dependence of the double-pionic fusion to ^{4}He was studied for the first time in exclusive experiments. At nine beam energies in the regime of the ABC effect both the differential and total cross sections of the reaction $dd \rightarrow {}^4\mathrm{He}\pi^0\pi^0$ were obtained.
To perform these measurements with the WASA facility at COSY, several detector components were upgraded. Design, manufacturing and installation of the new FWC and the new FVH have been described in the first part of this work. The second part covers the analysis and the results of the reaction $dd \rightarrow {}^4\mathrm{He}\pi^0\pi^0$.
The data presented here show:

- a very strong and narrow peak in the $M_{\pi^0\pi^0}$ spectrum at small $M_{\pi^0\pi^0}$ values over the full energy range,
- a very narrow distribution of the invariant mass of the ^{4}Heπ^0 system, which is even narrower than naively expected from the width of the Δ excitation,
- a strong energy dependence of the total cross section with a peak approximately 80 MeV below the nominal $\Delta\Delta$ mass.

These results are in agreement with the only previous exclusive measurement at $T_d = 1.029$ GeV by CELSIUS-WASA [Kel09], :
The models previously used to describe the double-pionic fusion, developed on inclusive measurements, cannot describe the features of the exclusive data. Obviously the additional knowledge gained from the exclusive measurements is crucial for the understanding of the ABC effect.
The comparison with the recent exclusive measurements of the double-pionic fusion to the deuteron demonstrates that both reactions are based on the same underlying process: In both cases the peak in the total cross section is at a comparable position, and the $M_{\pi^0\pi^0}$ spectrum shows the same striking low-mass enhancement. However in the fusion to ^{4}He the low-mass peak in the $M_{\pi^0\pi^0}$ spectrum is even stronger and the by far dominant part over the full measured energy range. The width is larger, which may be explained by Fermi motion and collision damping inside a nuclear medium.
These findings indicate a resonance in the $\Delta\Delta$ system which dominates the fusion process not only in the basic reaction $pn \rightarrow d\pi\pi$ but also in the fusion to heavier nuclei. And in fact the recently developed ABC resonance model [Basc] describes both results on the basic reaction and the results presented here amazingly well.

8 *Outlook*

> And the winds of change are
> blowing, blowing
> Gathering more and more leaves in
> its path,
> As time goes past
>
> Winds of Change,
> Eric Burdon & The Animals
> [Bur67]

To further increase the understanding of hadron physics, new experiments have to be carried out. The next upgrade of the WASA detector is already worked on: a DIRC (**D**etection of **I**nternally **R**eflected **C**herenkov light) detector can improve the energy resolution of fast protons and pions on the forward detector significantly. A similar detector was installed at the BaBar experiment [Ada05] and worked very well. Due to the limitations in space the anticipated design at WASA is very different in comparison to the BaBar DIRC. However, a DIRC design as anticipated in WASA is planned as a part of the PANDA detector at FAIR, thus any developments for WASA will also be helpful for the future PANDA detector.

Focusing on the ABC effect the next step is the analysis of the fusion to ^{4}He with charged pions $dd \to {}^4\mathrm{He}\pi^+\pi^-$. The respective data can be extracted from the same data sample as was used for the neutral channel presented here. It will allow additional tests of the present understanding of the double-pionic fusion to ^{4}He.
The analysis of the $pd \to {}^3\mathrm{He}\pi\pi$ reaction is already going on and will be presented in the PhD thesis of E. Perez del Rio [Per06]. At a single energy exclusive data already exist and show the same behavior as the $pn \to d\pi^0\pi^0$ and $dd \to {}^4\mathrm{He}\pi^0\pi^0$ reactions. But the investigation of the energy dependence will deepen the understanding of the ABC effect.
Fusion experiments to heavier nuclei, like the fusion to oxygen with a deuteron beam and a nitrogen target, are in principle possible also with the WASA detector, however several changes of the target and the detector system would be necessary.
Fruitful discussions with theorists about the nature of the ABC effect are ongoing, fed by the very active research on the ABC topic in all double pion production channels up to the fusion of ^{4}He. The results presented in this thesis will help to fully unveil the now 50 year old ABC puzzle.

9 *Appendix*

9.1 List of Acronyms

ADC	**A**nalog to **D**igital **C**onverter
ANKE	**A**pparat zum Studium von **N**ukleon- und **K**aon-**E**jektilen
CD	**C**entral **D**etector
CELSIUS	**C**ooling with **El**ectrons and **S**toring of **I**ons form **U**ppsala **S**ynchrocyclotron
COSY	**CO**oler **SY**nchrotron
DAQ	**D**ata **Aq**uisition
FD	**F**orward **D**etector
FPC	**F**orward **P**roportional **C**hamber
FRH	**F**orward **R**ange **H**odoscope
FRH1/2/3/4/5	1st/2nd/3rd/4th/5th layer of the FRH
FRI	**F**orward **R**ange **I**ntermediate Hodoscope
FTH	**F**orward **T**rigger **H**odoscope
FVH	**F**orward **V**eto **H**odoscope
FWC	**F**orward **W**indow **C**ounter
FWC1/2	1st/2nd layer of the FWC
FWHM	**F**ull **W**idth **H**alf **M**aximum
MC	**M**onte **C**arlo simulations
MDC	**M**ini **D**rift **C**hamber
PMT	**P**hoto**m**ultiplier **T**ube
PS	**P**lastic **S**cintillator barrel
PSB	**P**lastic **S**cintillator barrel **B**ackward
PSC	**P**lastic **S**cintillator barrel **C**entral
PSF	**P**lastic **S**cintillator barrel **F**orward
SE	**S**cintillating **E**lectromagnetic calorimenter
SEC	**S**cintillating **E**lectromagnetic calorimenter **C**entral part
TDC	**T**ime to **D**igital **C**onverter
TOF	**T**ime **O**f **F**light
WASA	**W**ide **A**ngle **S**hower **A**pparatur

9.2 Kinematics of dd → ^{4}He$\pi^0\pi^0$

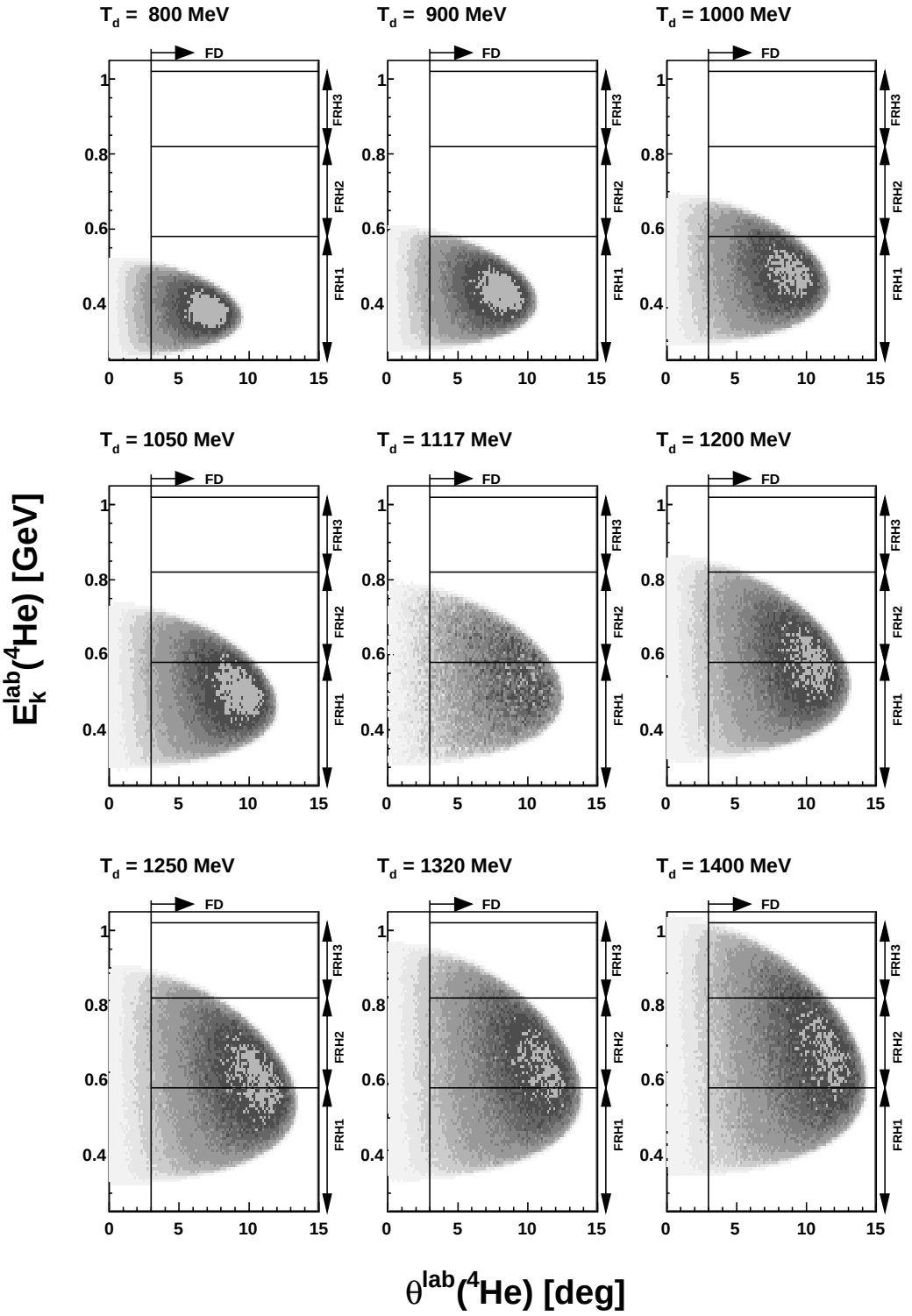

Figure 9.1: *Simulated laboratory kinetic energy versus the laboratory scattering angle θ of the ^{4}He for all measured energies.*

9.3 Analysis of $dd \rightarrow {}^4He\pi^0\pi^0$

The following pages show plots to judge the results of the analysis for each energy. The first rows show the ΔE-ΔE plots for tracks stopping in FRH1 (left) and punching through FRH1 (right). The colored dots show the events finally used after the kinematic fit.
The second rows show the χ^2 and $Prob(\chi^2, ndf = 6)$ distributions. The black lines denote the Monte Carlo simulations, the green line the theoretical χ^2 distribution for ndf=6 and the red lines denote the experimental data.
The third row depicts the invariant masses of the $\pi^0\pi^0$ (left) and the ${}^4He\pi^0$ (right) system before (shaded area) and after the kinematic fit for experimental data.
The fourth rows show the invariant mass of the $\pi^0\pi^0$ (left) and the ${}^4He\pi^0$ (right) and $cos(\theta^{cm}_{\pi^0\pi^0})$ before efficiency and acceptance corrections (shaded area) and after the corrections. The red lines denote the 1-dimensional correction with the $\Delta\Delta$-resonance model, the blue lines the 1-dimensional correction with a phases pace simulation and the black lines the 2-dimensional correction based on the $\Delta\Delta$-resonance model simulation.

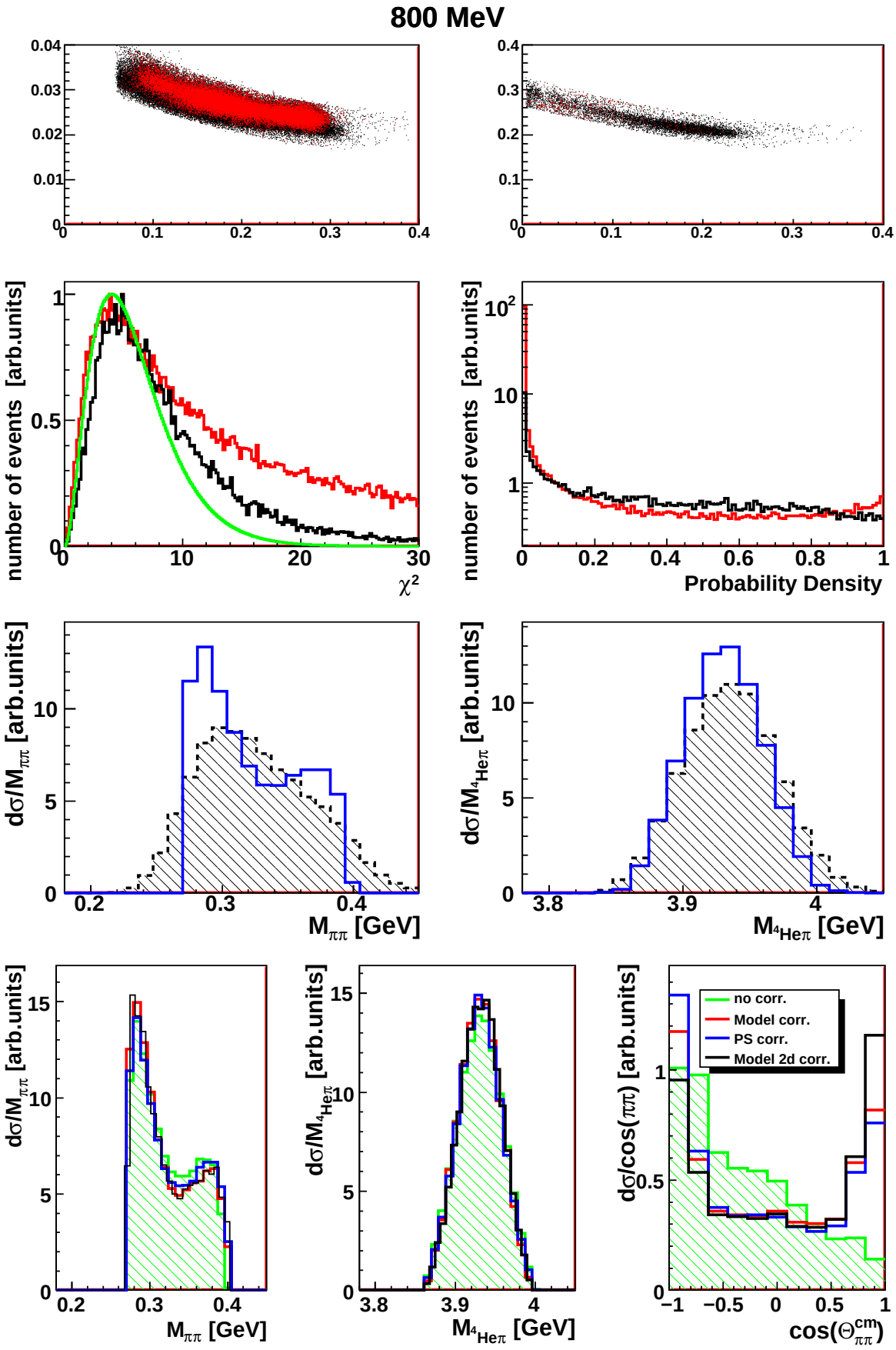

Figure 9.2: *Analysis plots for* dd → ^{4}He$\pi^0\pi^0$ *at* $T_d = 0.8$ *GeV*

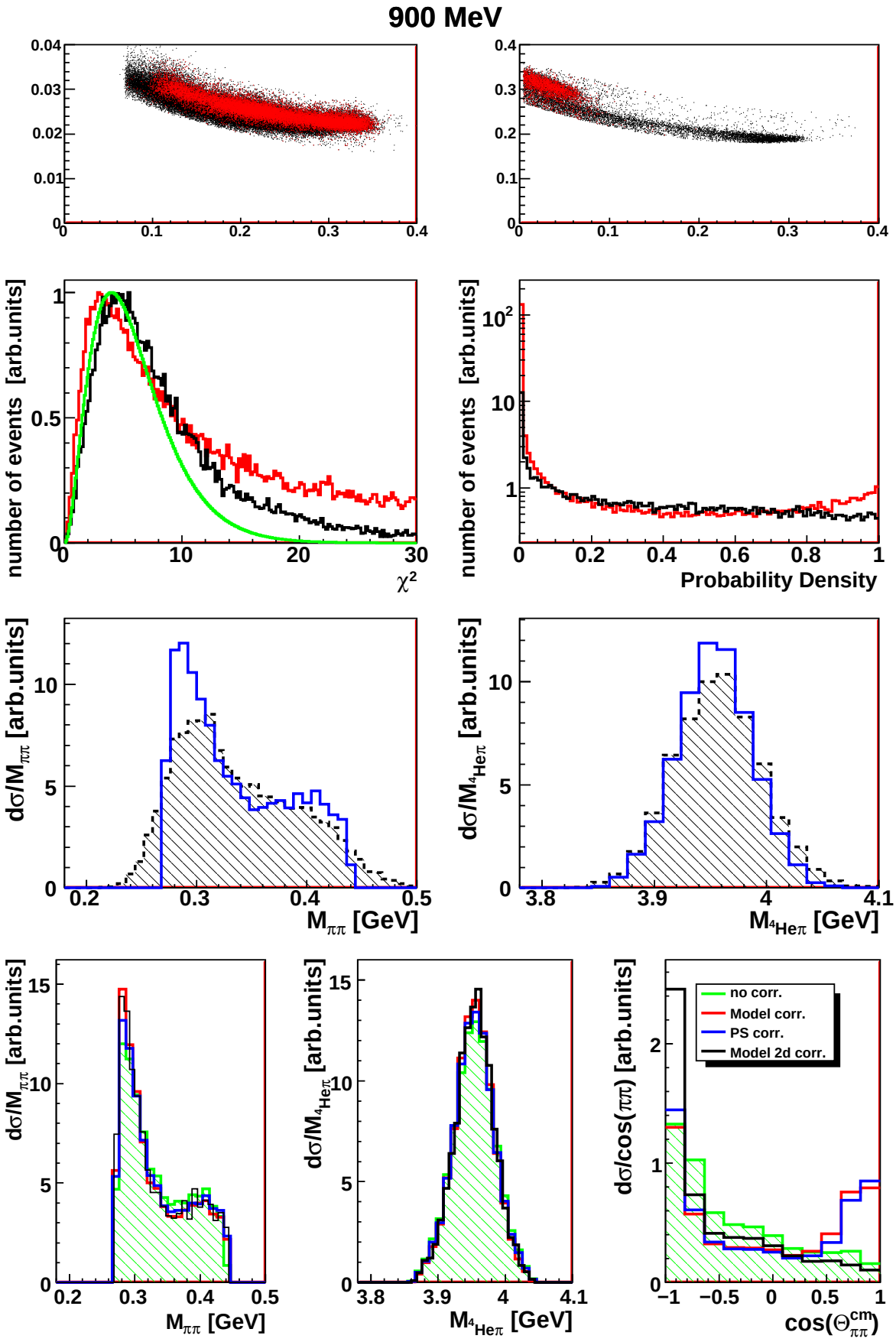

Figure 9.3: *Analysis plots for* $\mathrm{dd} \to {}^4\mathrm{He}\pi^0\pi^0$ *at* $T_d = 0.9$ *GeV*

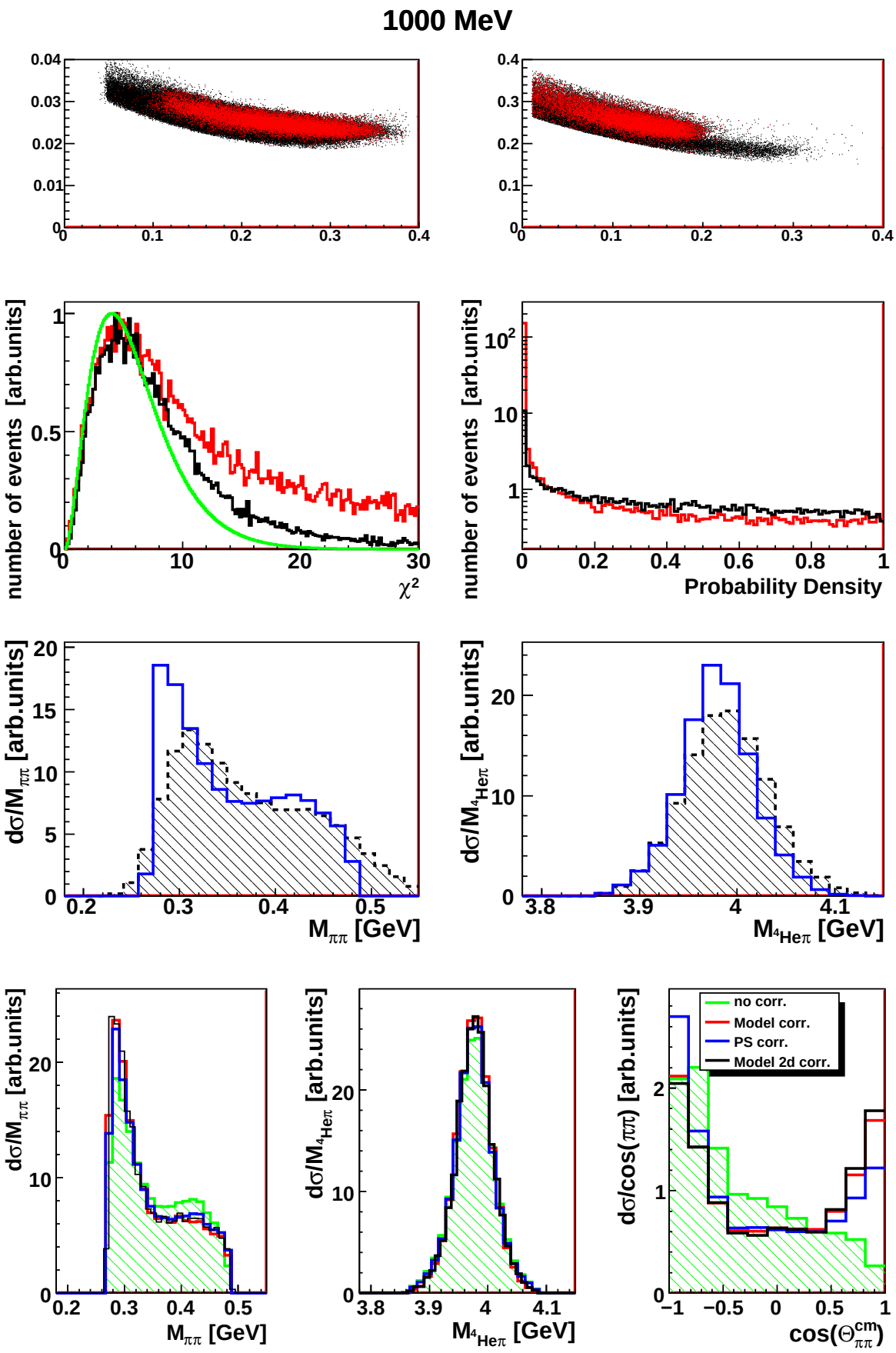

Figure 9.4: *Analysis plots for* dd → ^{4}He$\pi^0\pi^0$ *at* $T_d = 1.0$ *GeV*

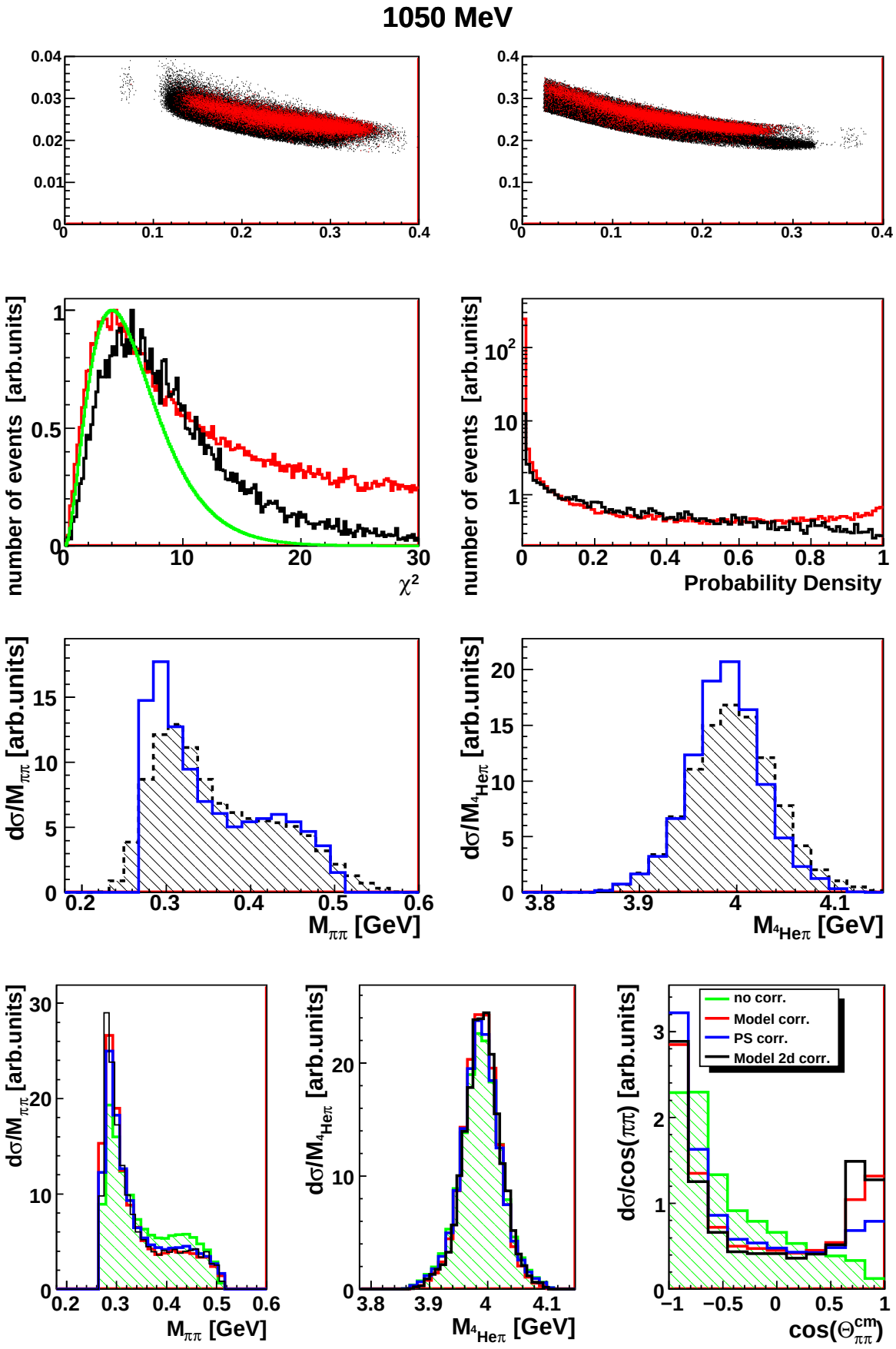

Figure 9.5: *Analysis plots for* $\mathrm{dd} \to {}^4\mathrm{He}\pi^0\pi^0$ *at* $T_d = 1.05$ *GeV*

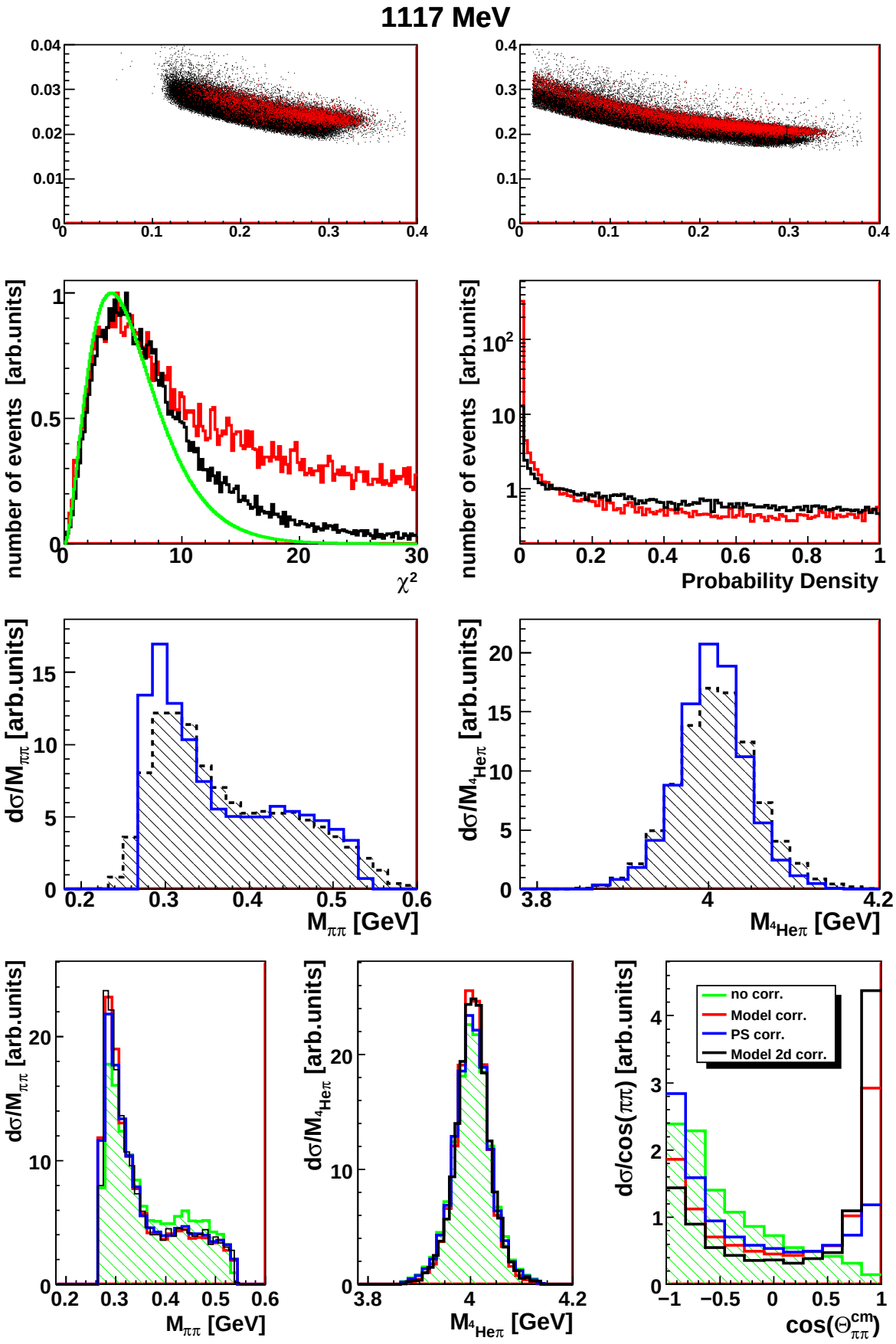

Figure 9.6: *Analysis plots for* dd → ^{4}He$\pi^0\pi^0$ *at* $T_d = 1.117$ *GeV*

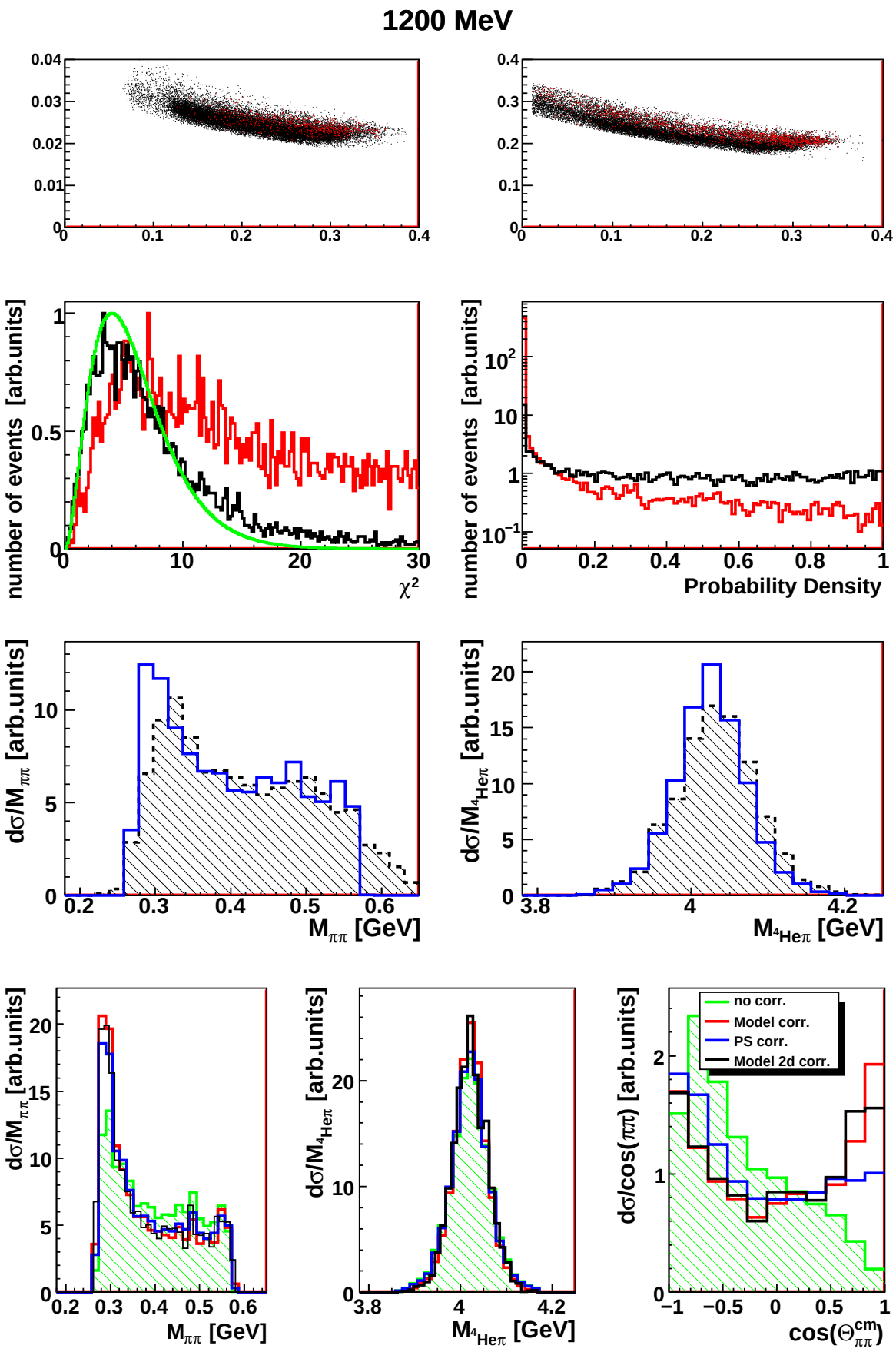

Figure 9.7: *Analysis plots for* $\mathrm{dd} \to {}^4\mathrm{He}\pi^0\pi^0$ *at* $T_d = 1.2$ *GeV*

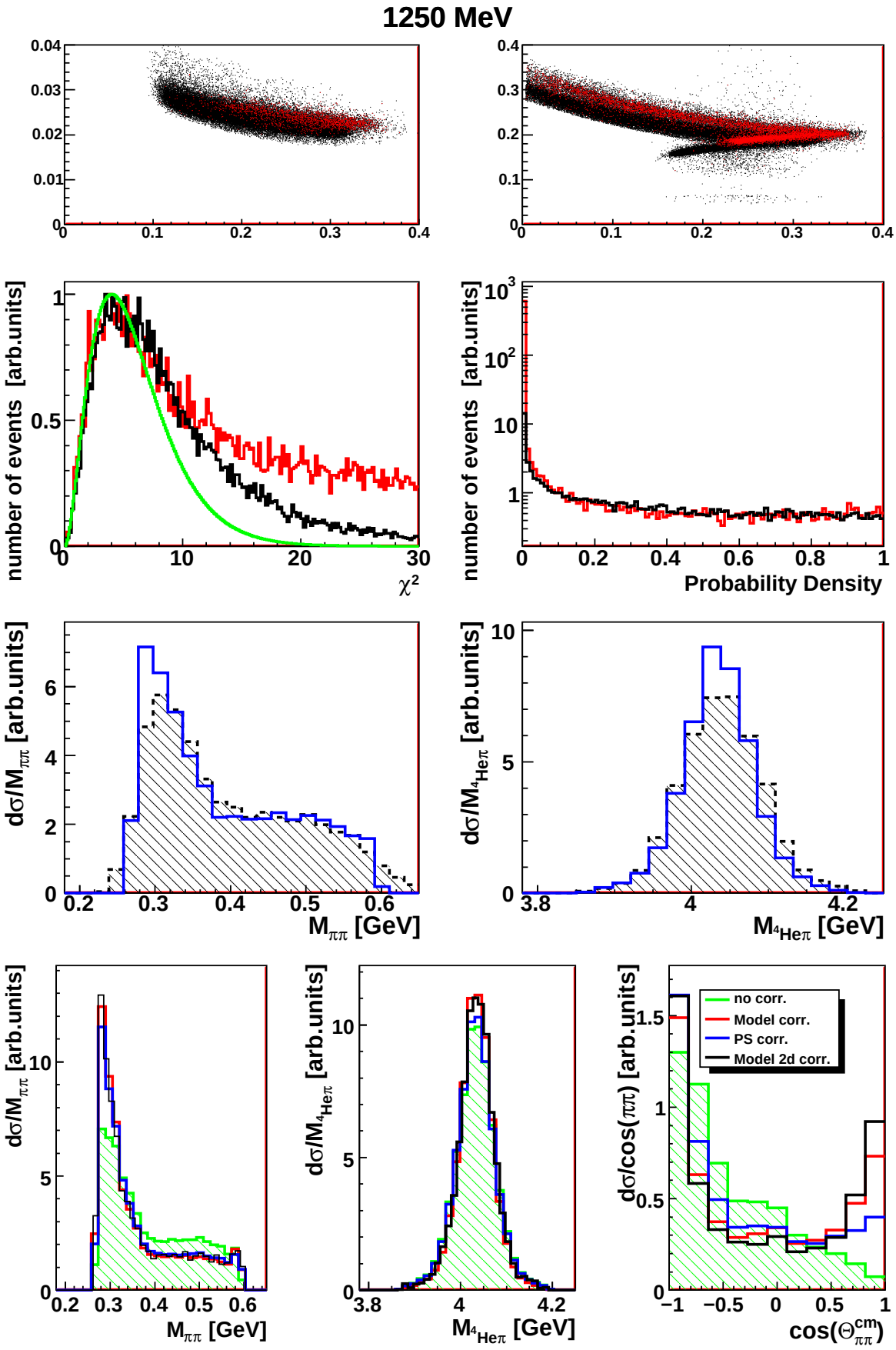

Figure 9.8: *Analysis plots for* dd → ^{4}He$\pi^0\pi^0$ *at* $T_d = 1.25$ *GeV*

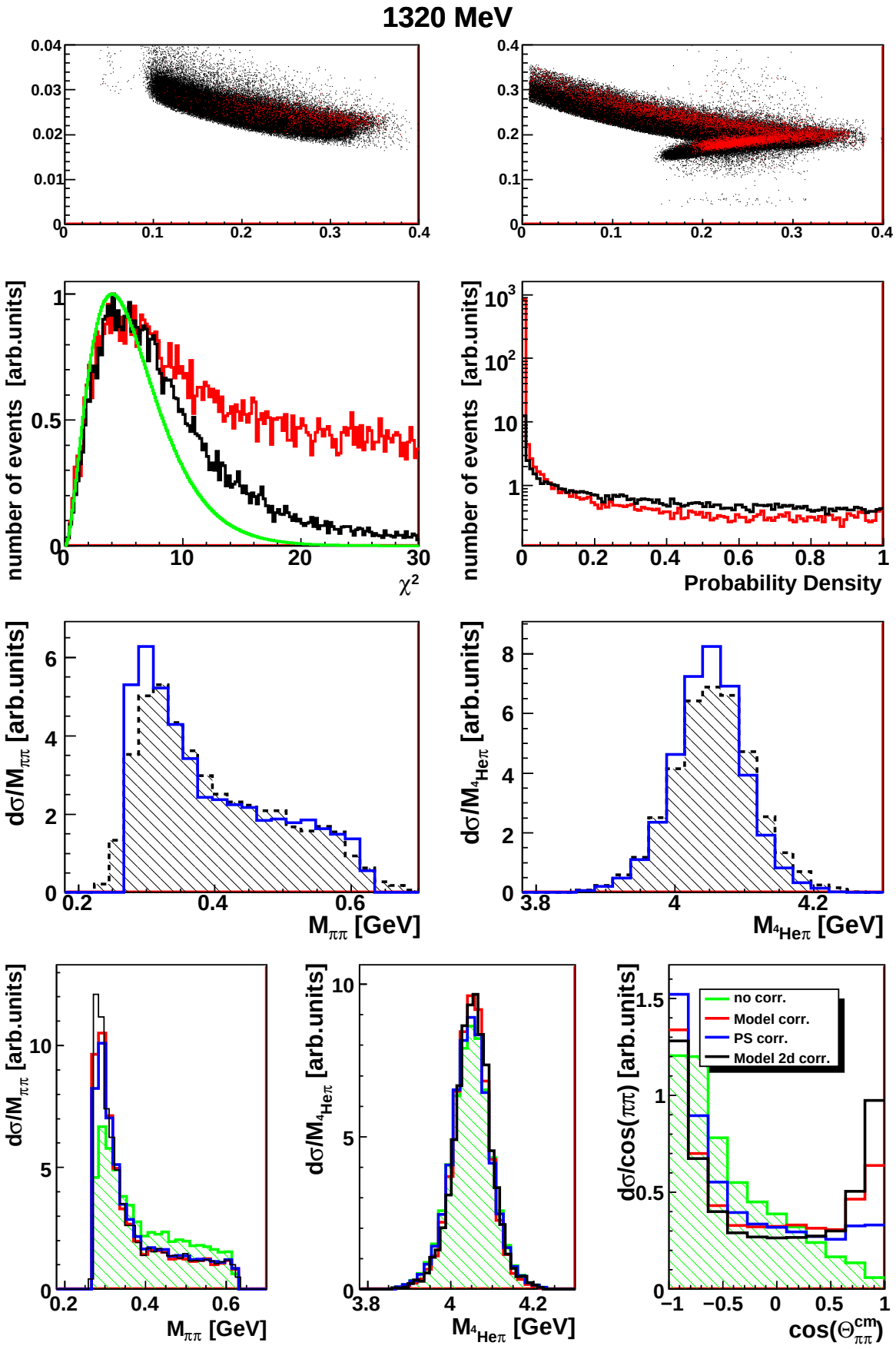

Figure 9.9: *Analysis plots for* $\mathrm{dd} \to {}^4\mathrm{He}\pi^0\pi^0$ *at* $T_d = 1.32$ *GeV*

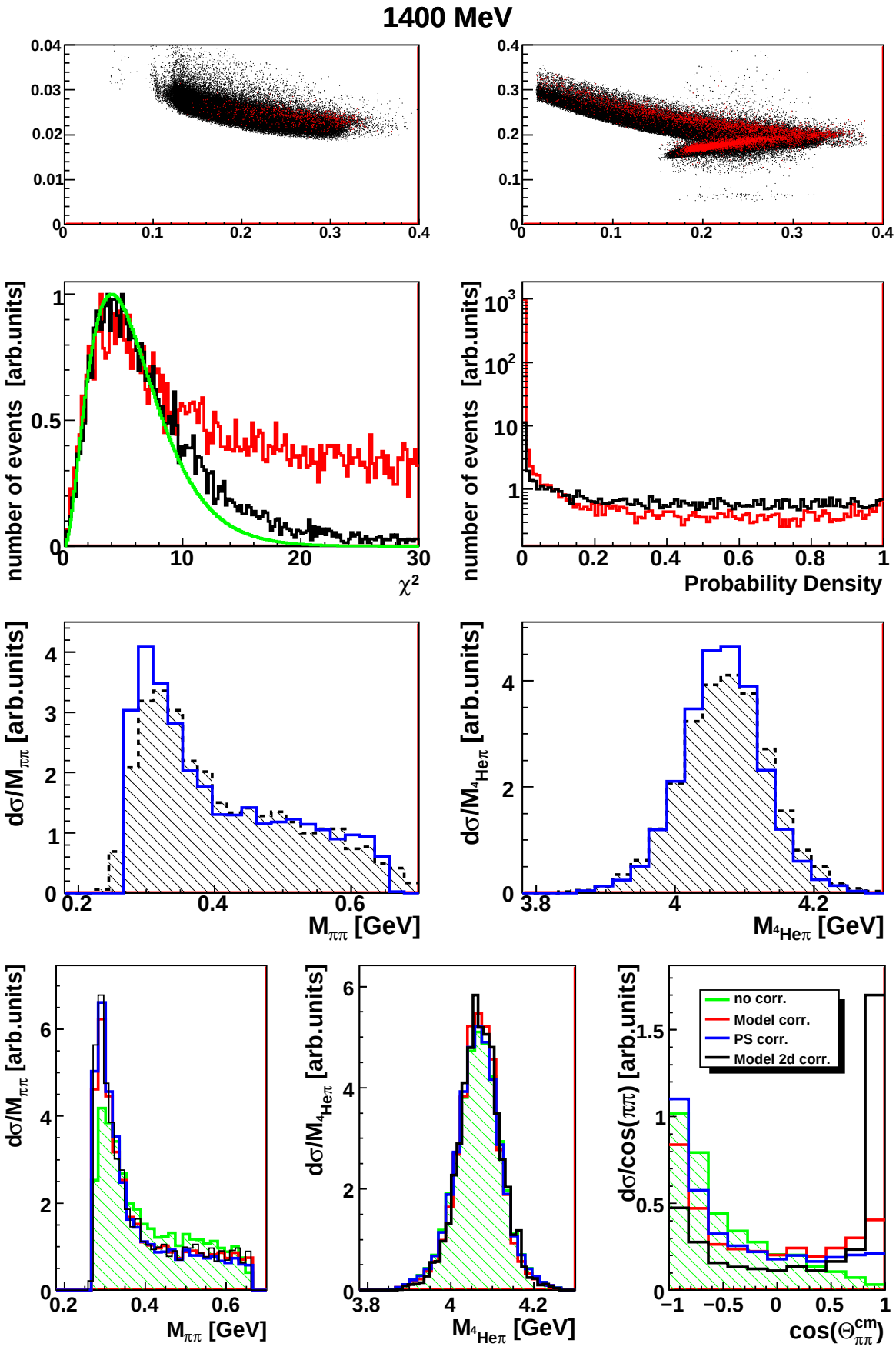

Figure 9.10: *Analysis plots for* dd → ^{4}He$\pi^0\pi^0$ *at* $T_d = 1.4$ *GeV*

9.4 Analysis of $dd \rightarrow {}^3\mathrm{He}n$

The following pages show plots to judge the results of the analysis of $dd \rightarrow {}^3\mathrm{He}n$ for each energy.
The first rows show the ΔE-ΔE plot (left) and the $\Delta E - \theta$ plot (right) all events (grey) and for the ${}^3\mathrm{He}n$ selection (colored).
The second row, left picture, shows the missing mass of the identified ${}^3\mathrm{He}$

$$MM = \sqrt{(E(beam) + E(target) + E({}^3\mathrm{He}))^2 - (\vec{p}(beam) + \vec{p}(target) + \vec{p}({}^3\mathrm{He}))^2} \tag{9.1}$$

This observable should be equal to the mass of the neutron (0.94 GeV).
The right plot in the second row shows the θ distribution as a function of the FRH1 element number. Here some elements seem to be cut partly due to the threshold in FRH1.
The third row shows the $t - t_{max}$ distribution for the measured energy (circles) and the Saclay energy below (squares) and above (triangles). The solid line marks the fit.
In the last row the same picture is plotted in logarithmic scale on the y-axis and a smaller range in $t - t_{max}$.
At $T_d = 1.32$ GeV and $T_d = 1.4\,\mathrm{GeV}$ the missing mass reconstruction is worse because the FRH layer where the particle stops are not calibrated and the reconstruction uncertainty for the used layers is large because the particle is too fast.

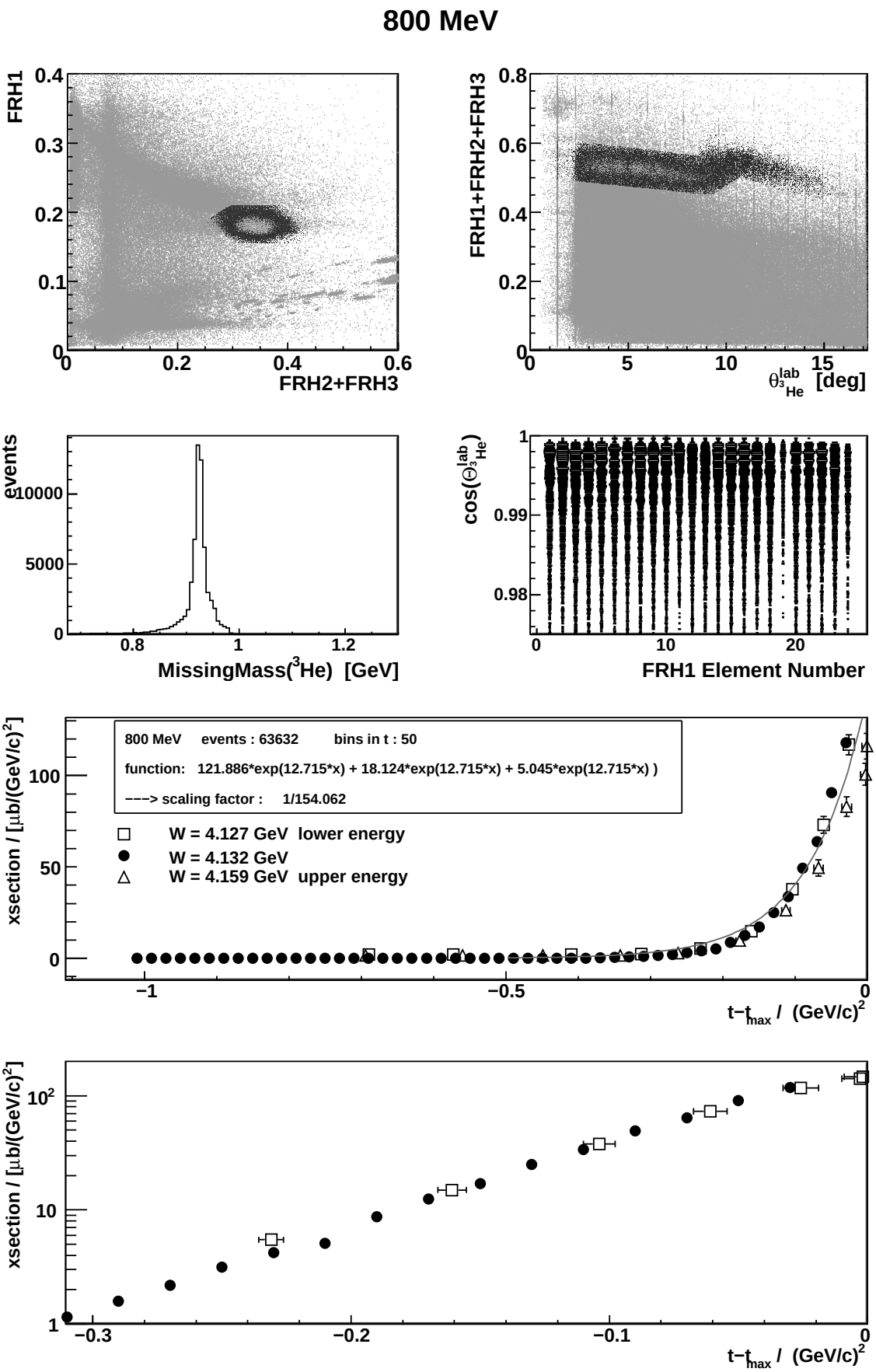

Figure 9.11: *Analysis plots for* $dd \to {}^3\mathrm{He}n$ *at* $T_d = 0.8$ *GeV*

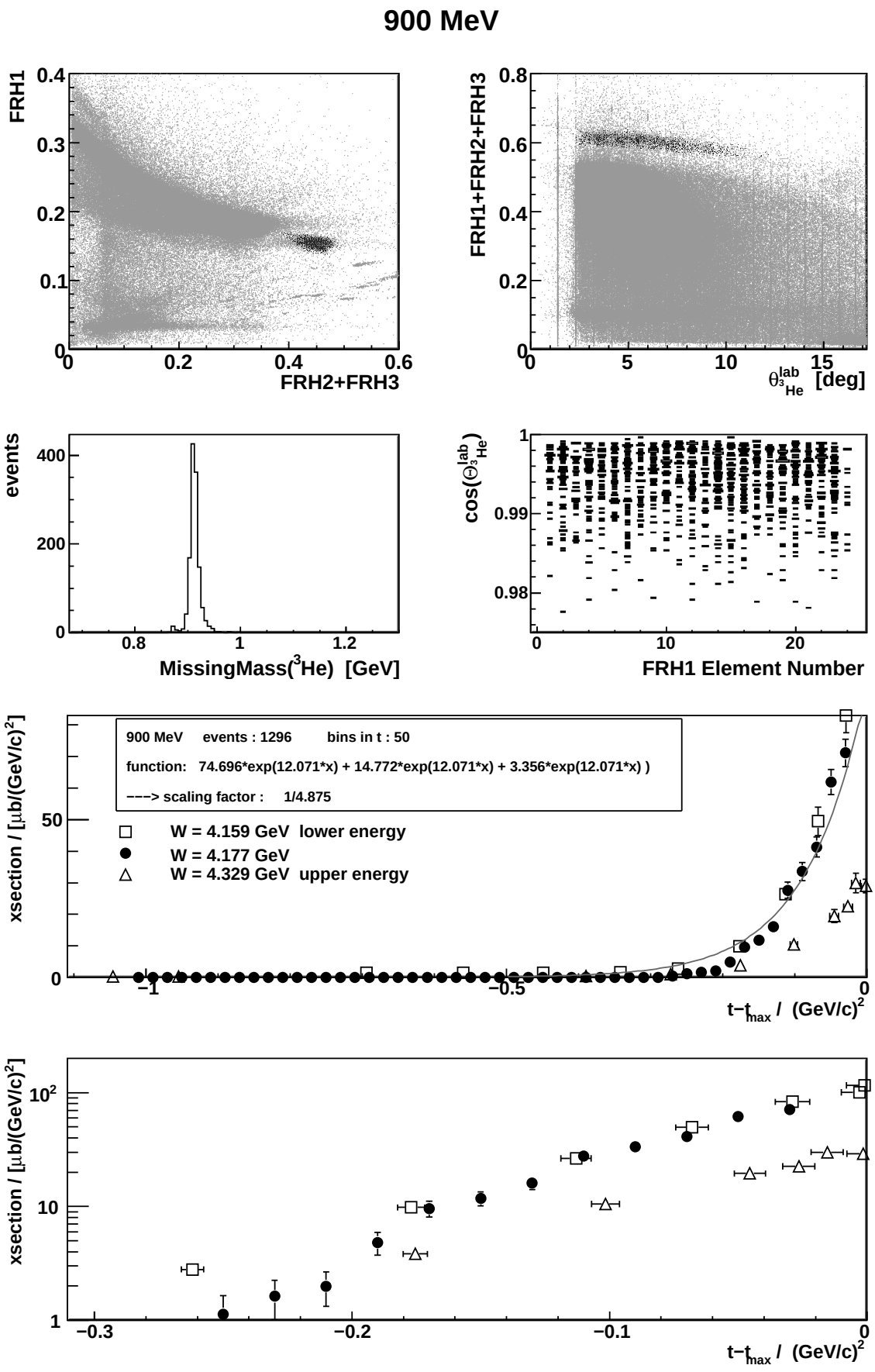

Figure 9.12: *Analysis plots for* $dd \rightarrow {}^{3}\mathrm{He}n$ *at* $T_d = 0.9$ *GeV*

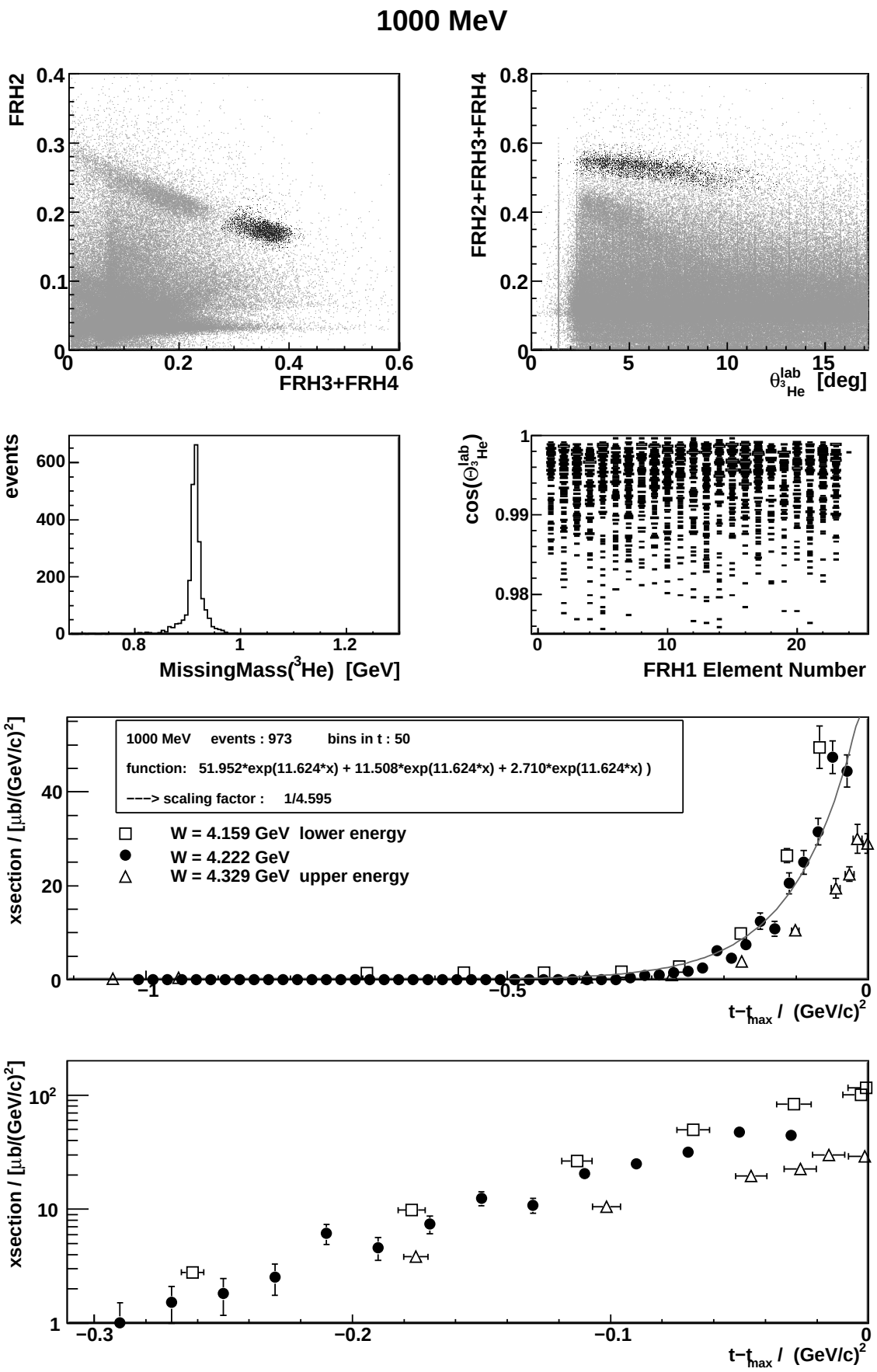

Figure 9.13: *Analysis plots for* $dd \to {}^3\mathrm{He}n$ *at* $T_d = 1.0$ *GeV*

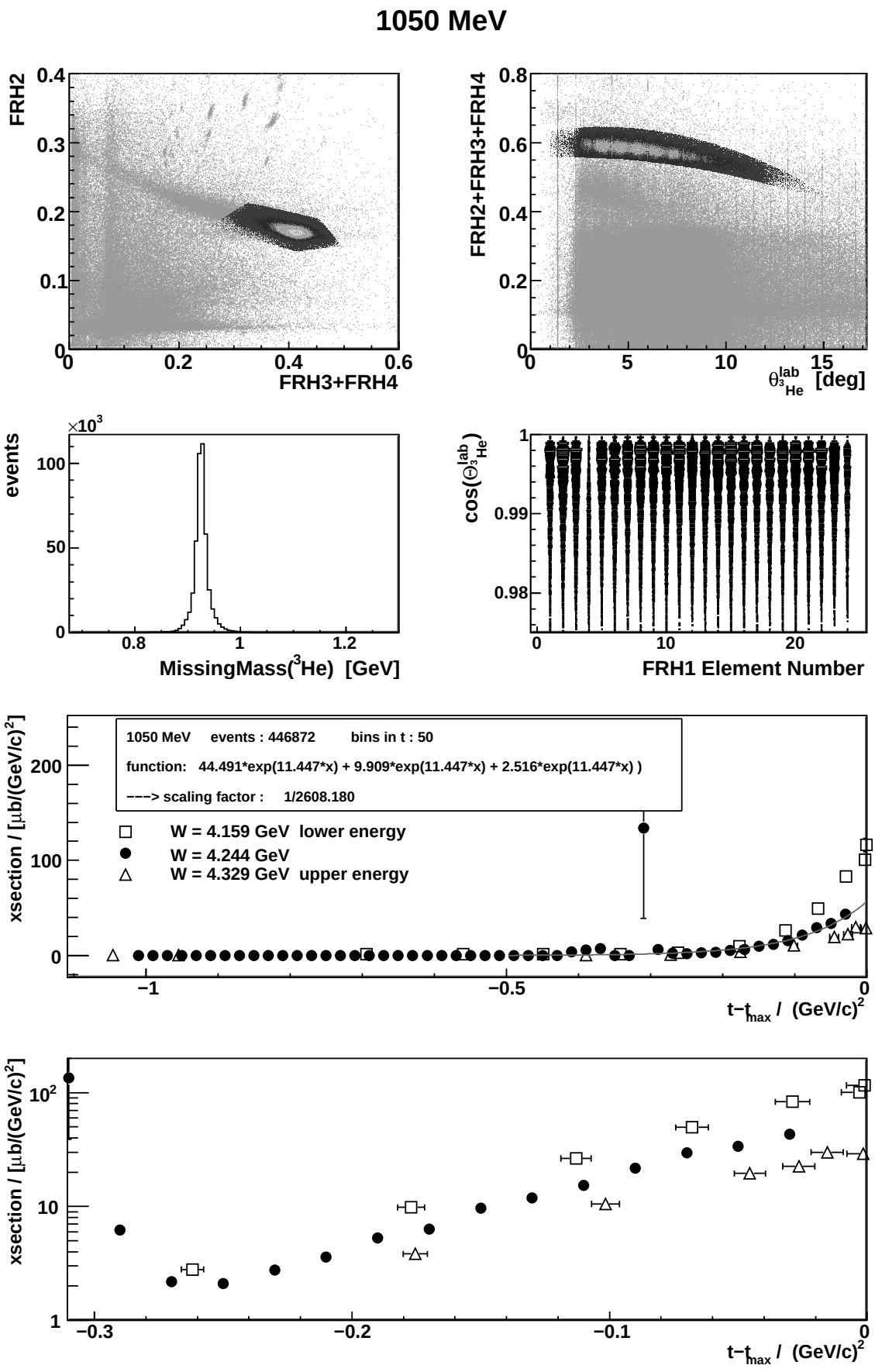

Figure 9.14: *Analysis plots for* $dd \to {}^3\mathrm{He}n$ *at* $T_d = 1.05$ *GeV*

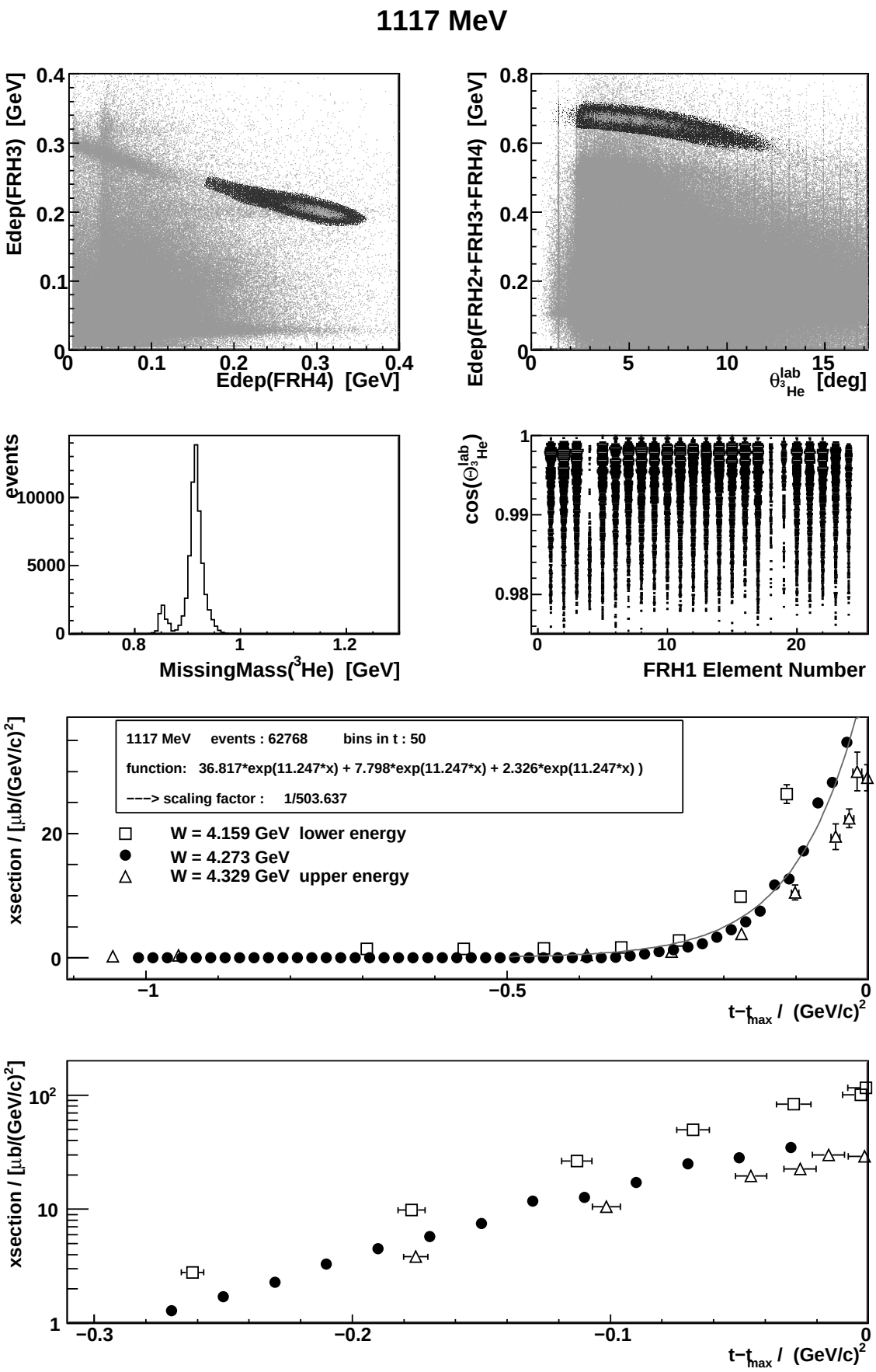

Figure 9.15: *Analysis plots for* $dd \rightarrow {}^3\mathrm{He}n$ *at* $T_d = 1.117$ *GeV*

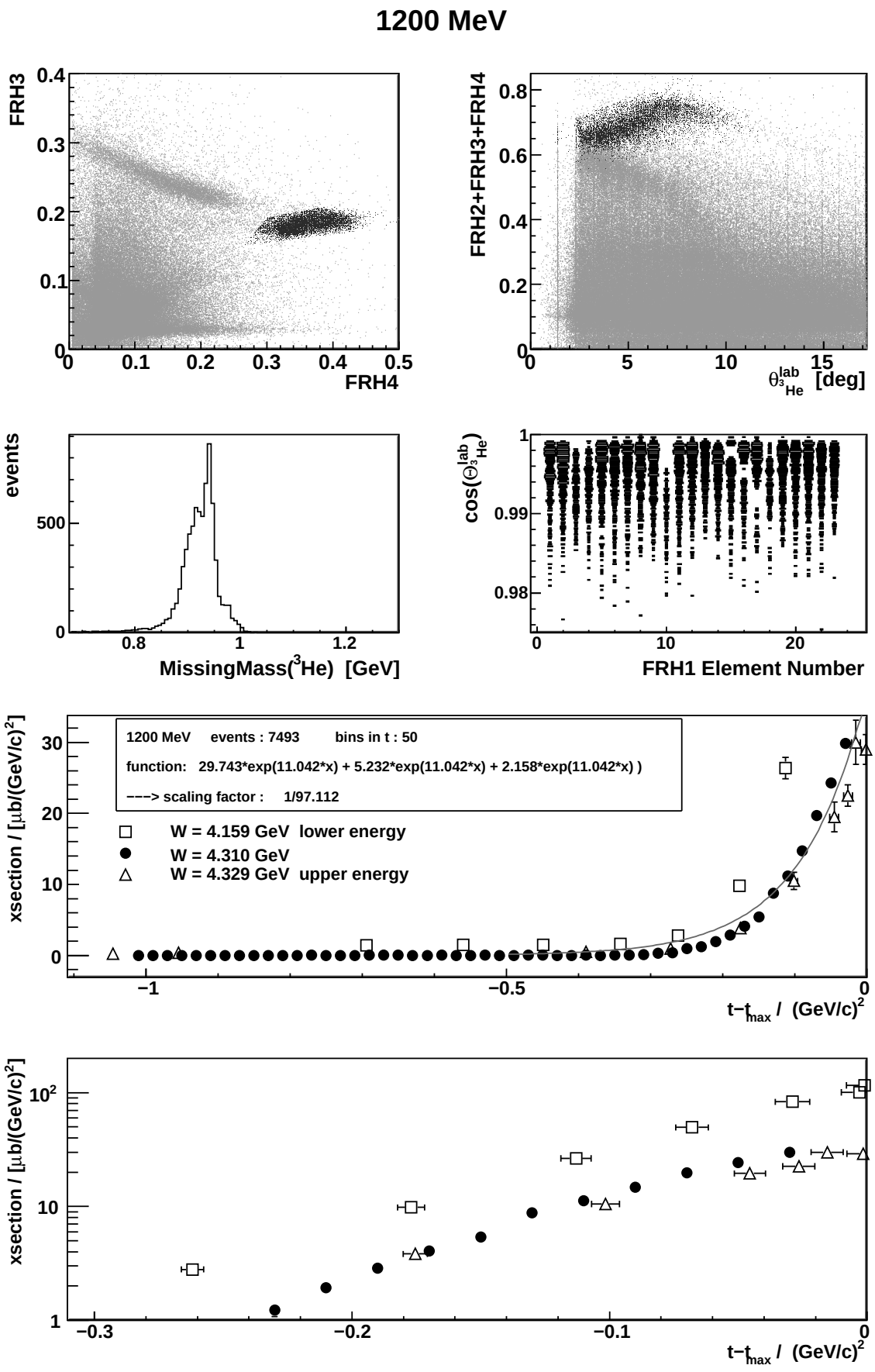

Figure 9.16: *Analysis plots for* $dd \rightarrow {}^3\mathrm{He}n$ *at* $T_d = 1.2$ *GeV.*

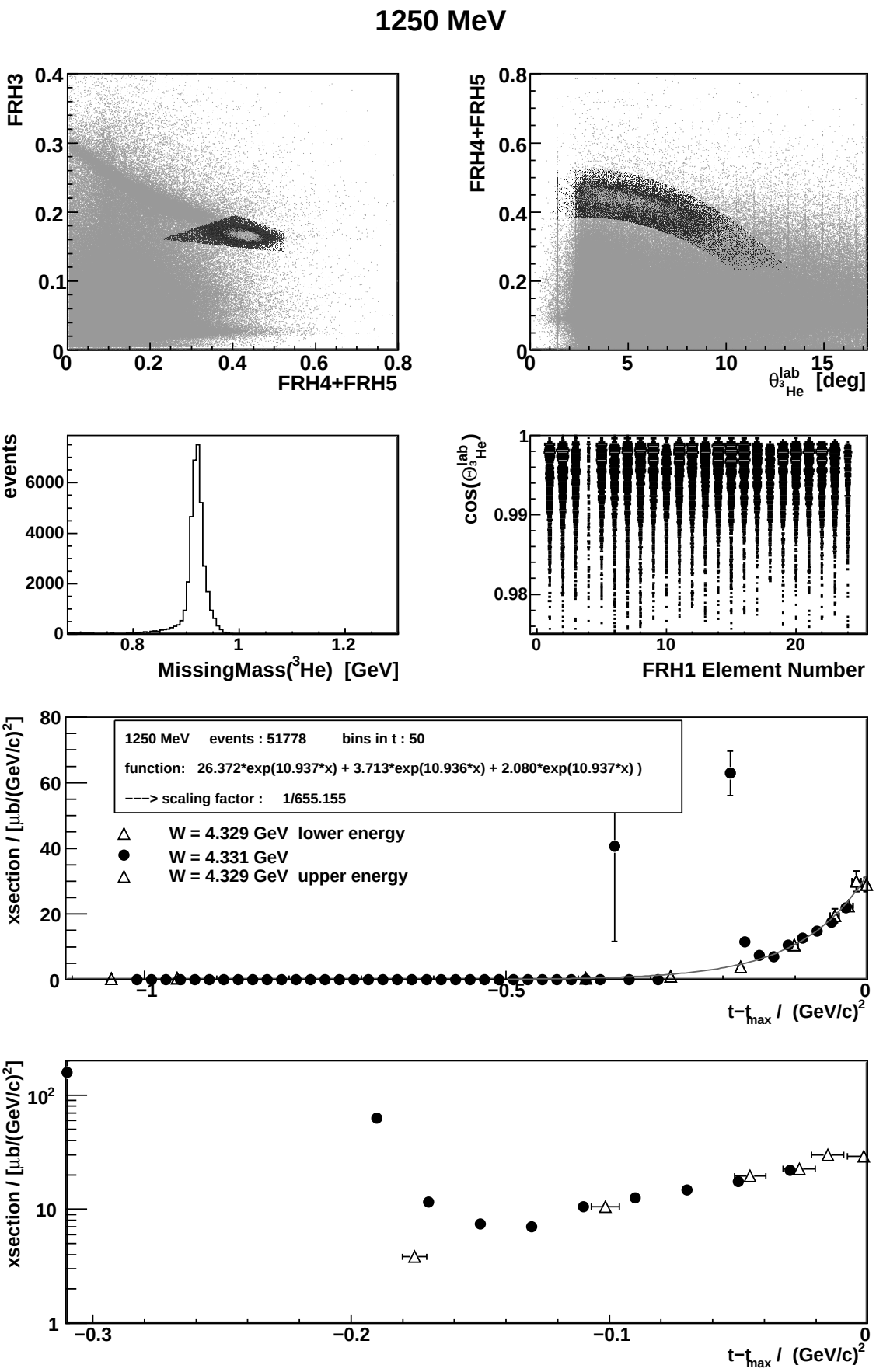

Figure 9.17: *Analysis plots for* $dd \rightarrow {}^3\mathrm{He}n$ *at* $T_d = 1.25\ GeV$

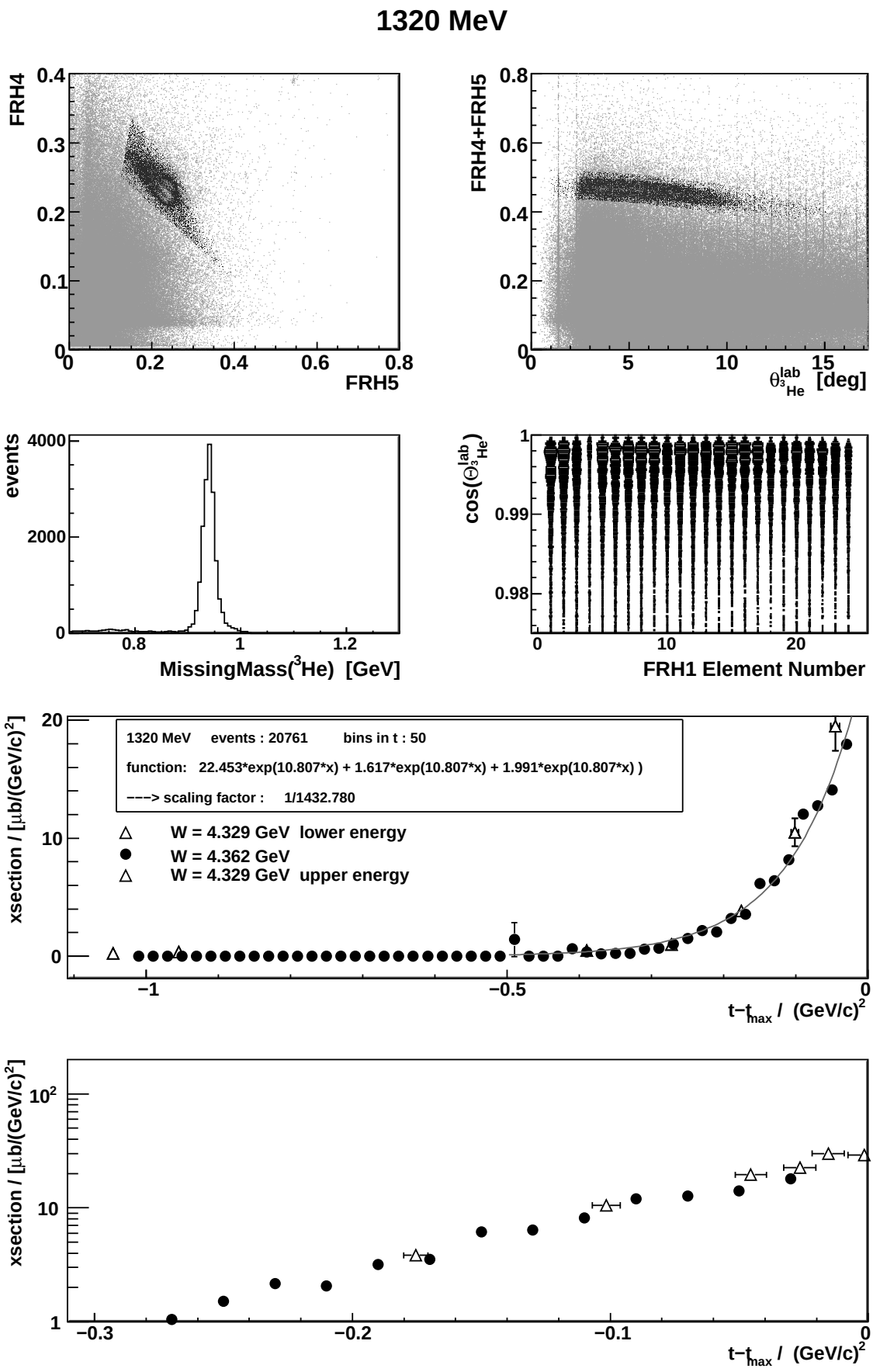

Figure 9.18: *Analysis plots for* $dd \rightarrow {}^3\mathrm{He}n$ *at* $T_d = 1.32$ *GeV*

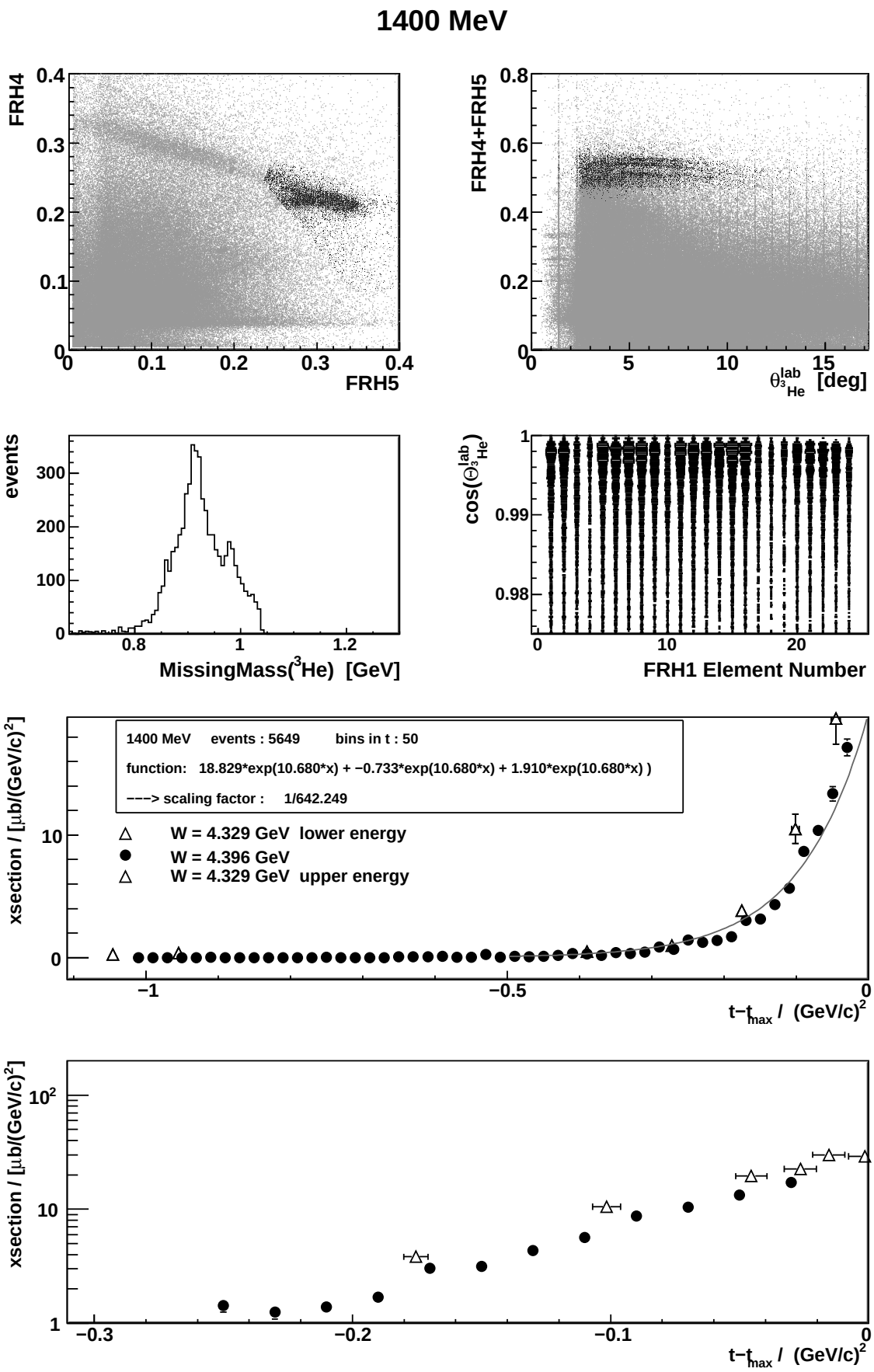

Figure 9.19: *Analysis plots for* $dd \rightarrow {}^3\mathrm{He}n$ *at* $T_d = 1.4$ *GeV.*

9.5 Differential Distributions with Phase Space Correction

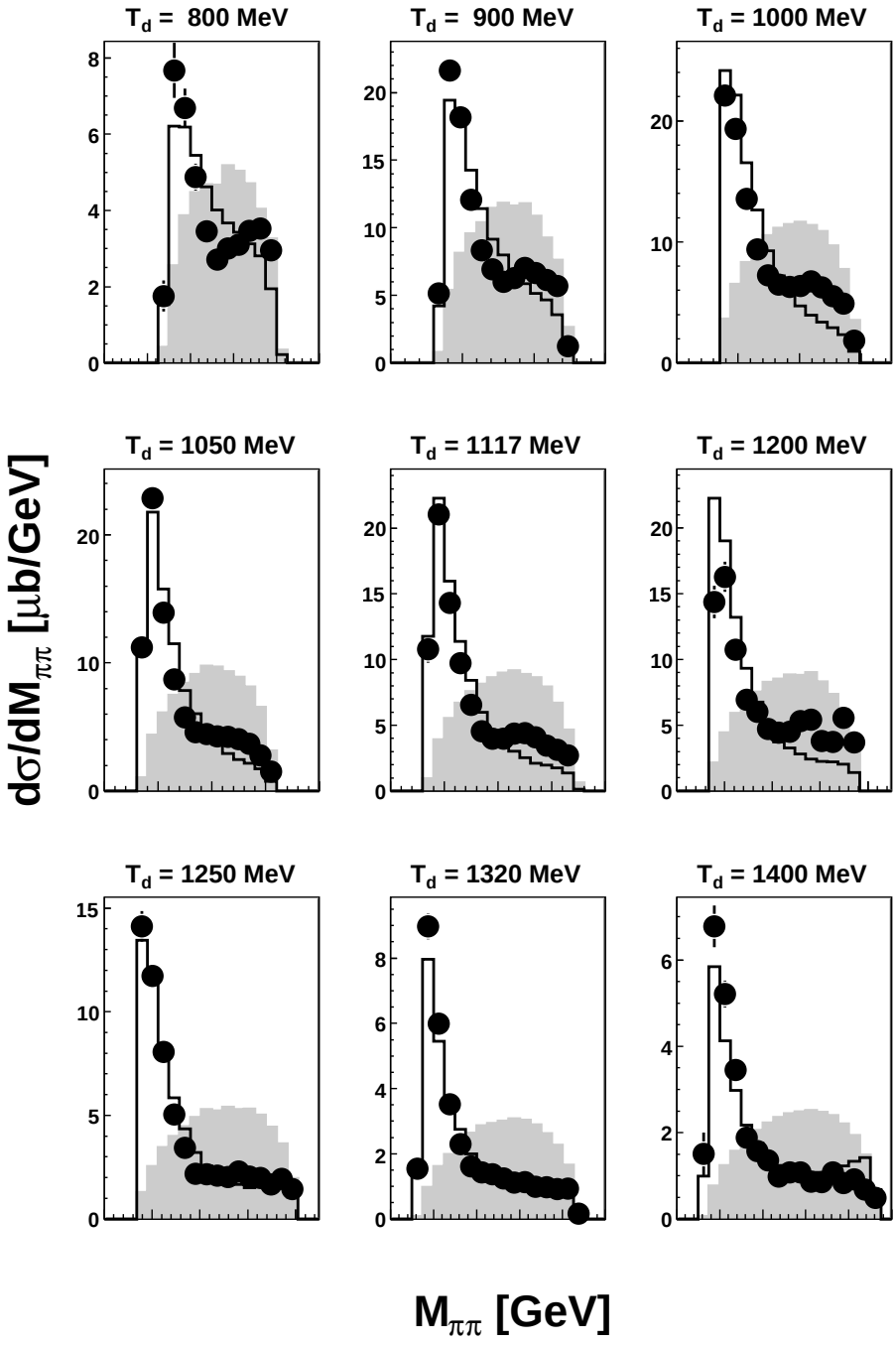

Figure 9.20: *$M_{\pi^0\pi^0}$ distribution for all energies. The dots represent the data, the shaded area the phasespace and the solid line the ABC resonance model and the gray dotted line the t-channel $\Delta\Delta$ simulation. Here the corrections are performed with a phase space simulation.*

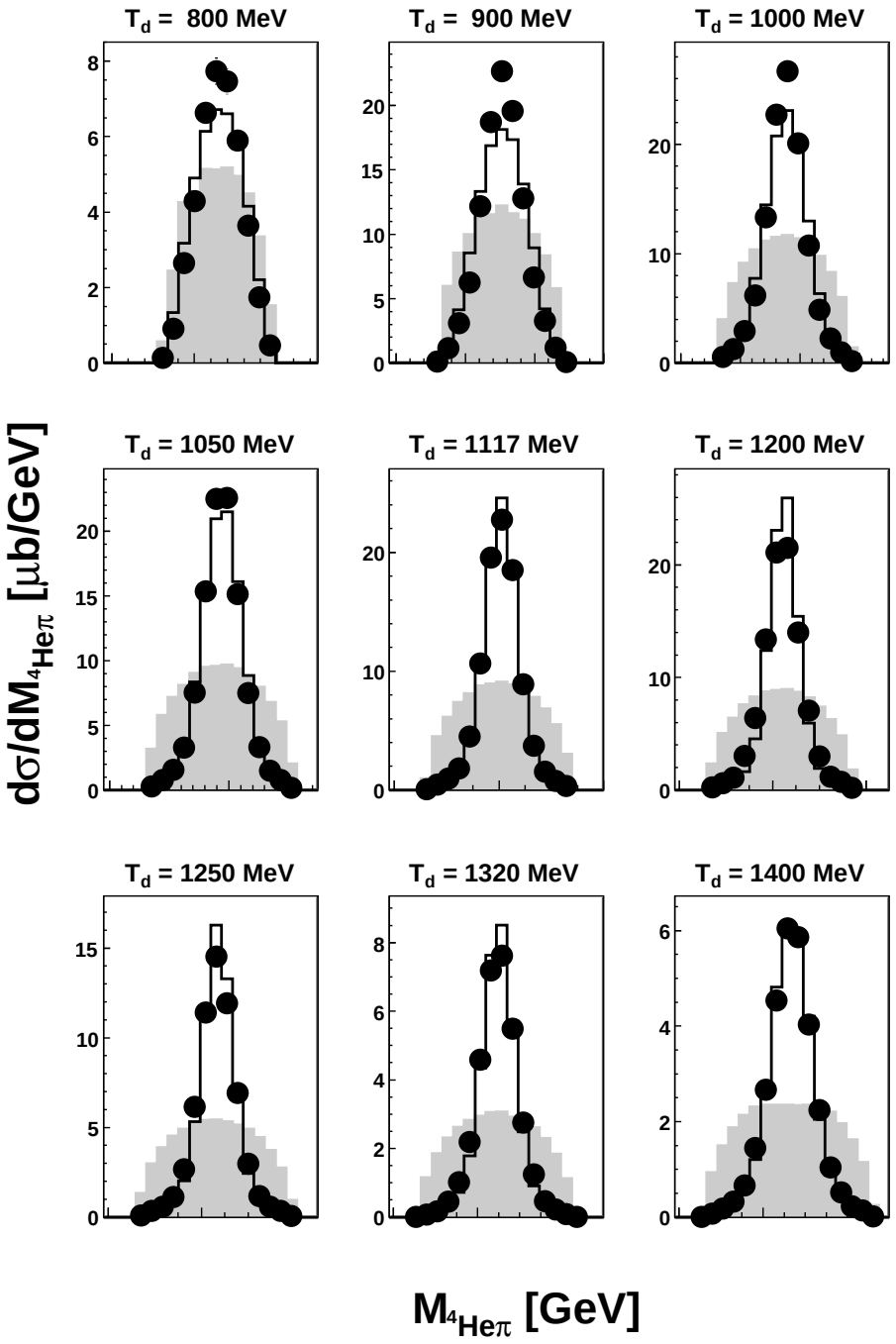

Figure 9.21: *$M_{^4\mathrm{He}\pi^0}$ distribution for all energies. The dots represent the data, the shaded area the phasespace and the solid line the ABC resonance model and the gray dotted line the t-channel $\Delta\Delta$ simulation. Here the corrections are performed with a phase space simulation.*

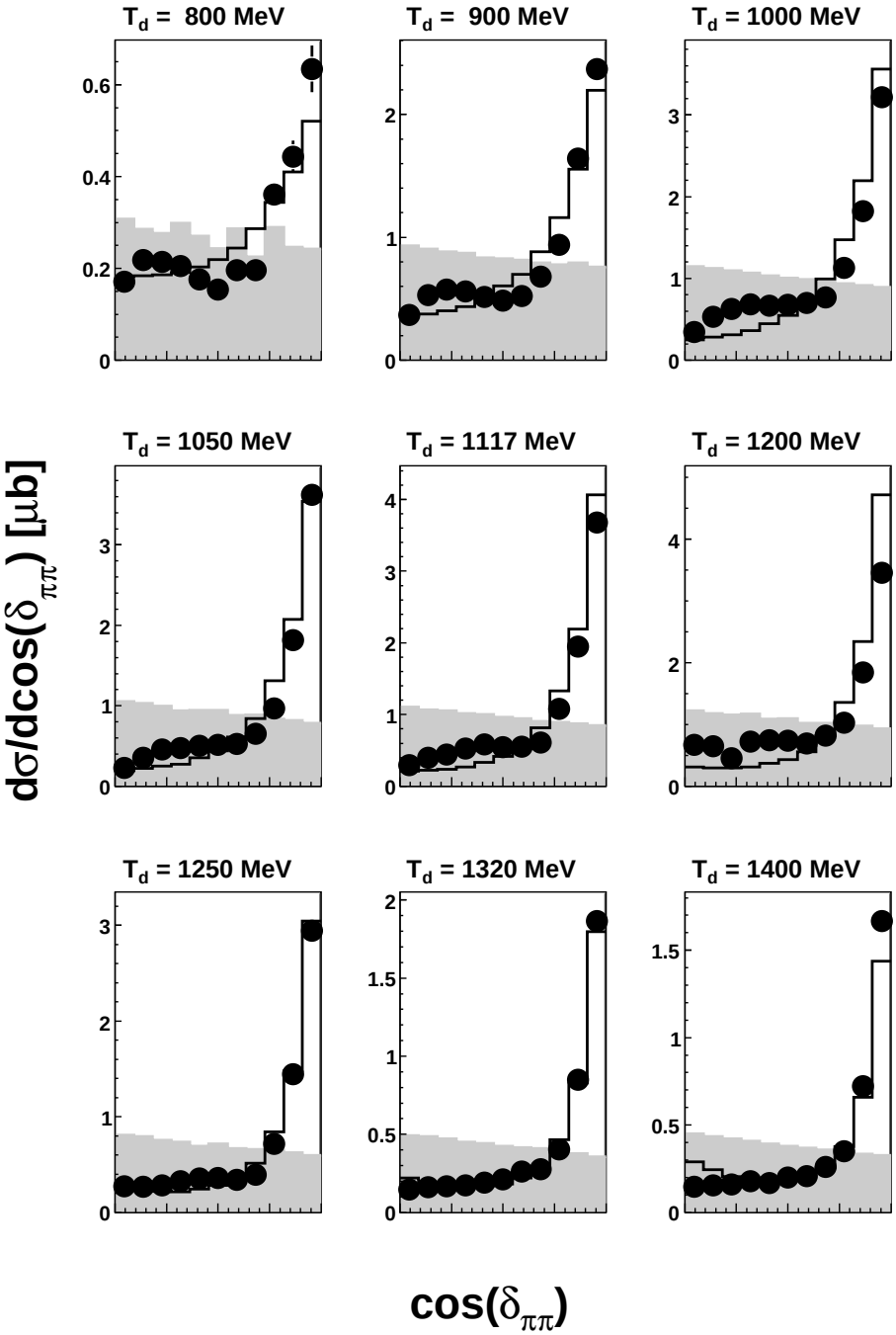

Figure 9.22: *Distribution of the opening angle $\delta^{cm}_{\pi^0\pi^0}$ between the pions in the center of mass system for all measured energies. The dots represent the data, the shaded area the phase space and the solid line the ABC resonance model simulation. Here the corrections are performed with a phase space simulation.*

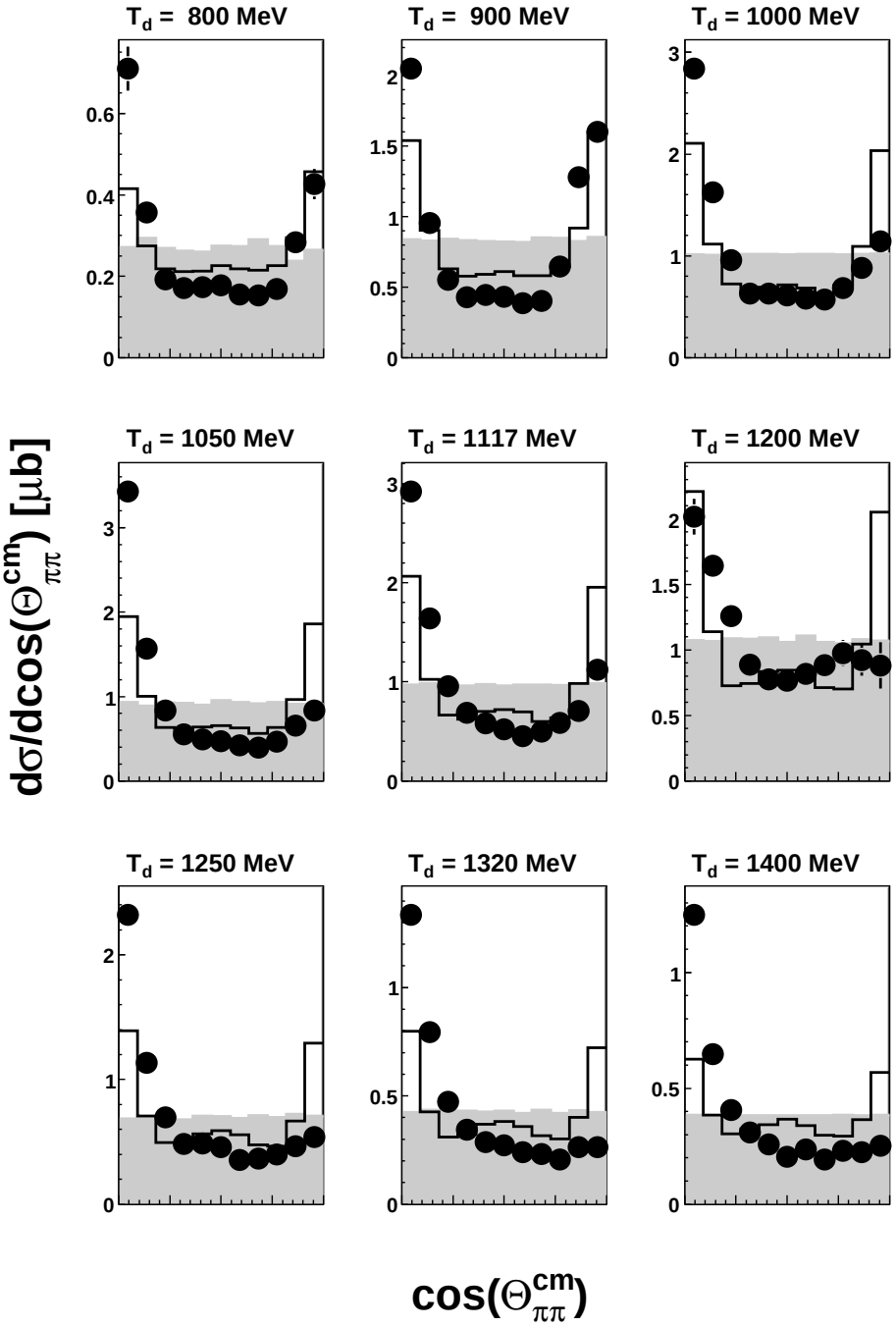

Figure 9.23: *Distribution of the $\pi^0\pi^0$ center of mass angle $\Theta^{cm}_{\pi^0\pi^0}$ for all measured energies. The dots represent the data, the shaded area the phasespace and the solid line the ABC resonance model simulation. Here the corrections are performed with a phase space simulation.*

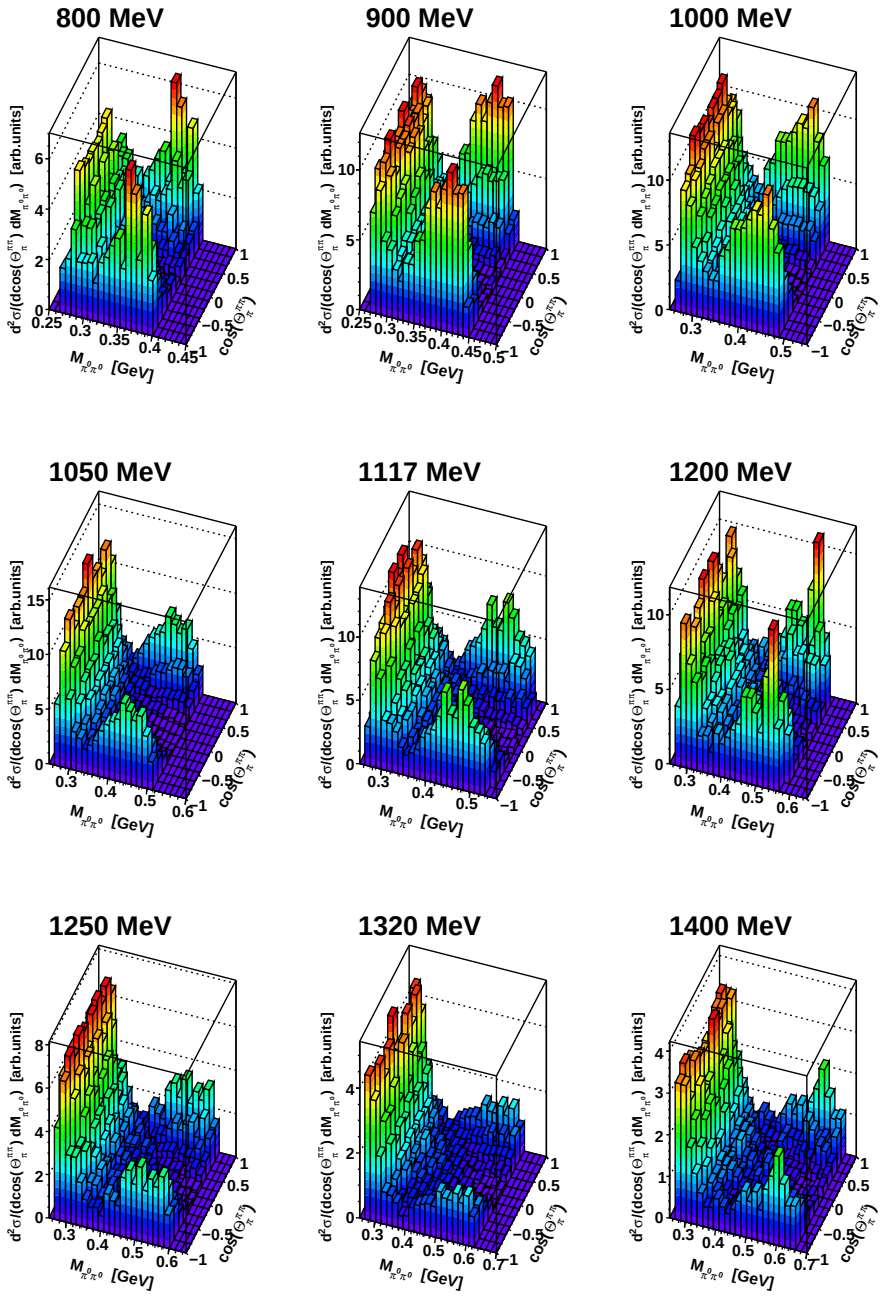

Figure 9.24: *Distribution of the polar scattering angle $\theta^{\pi^0\pi^0}_{\pi^0}$ of any pion in the $\pi^0\pi^0$ subsystem versus the invariant mass $M_{\pi^0\pi^0}$ of the $\pi^0\pi^0$ system for all measured energies. Here the corrections are performed with a phase space simulation.*

9.6 Total Cross Section of dd → ^{4}He$\pi^0\pi^0$ as Function of the Probability Cut

The following pages show the total cross section as a function of the cut on the probability function. The right side shows the probability function for the experimental data (solid line) and a Monte Carlo simulation.

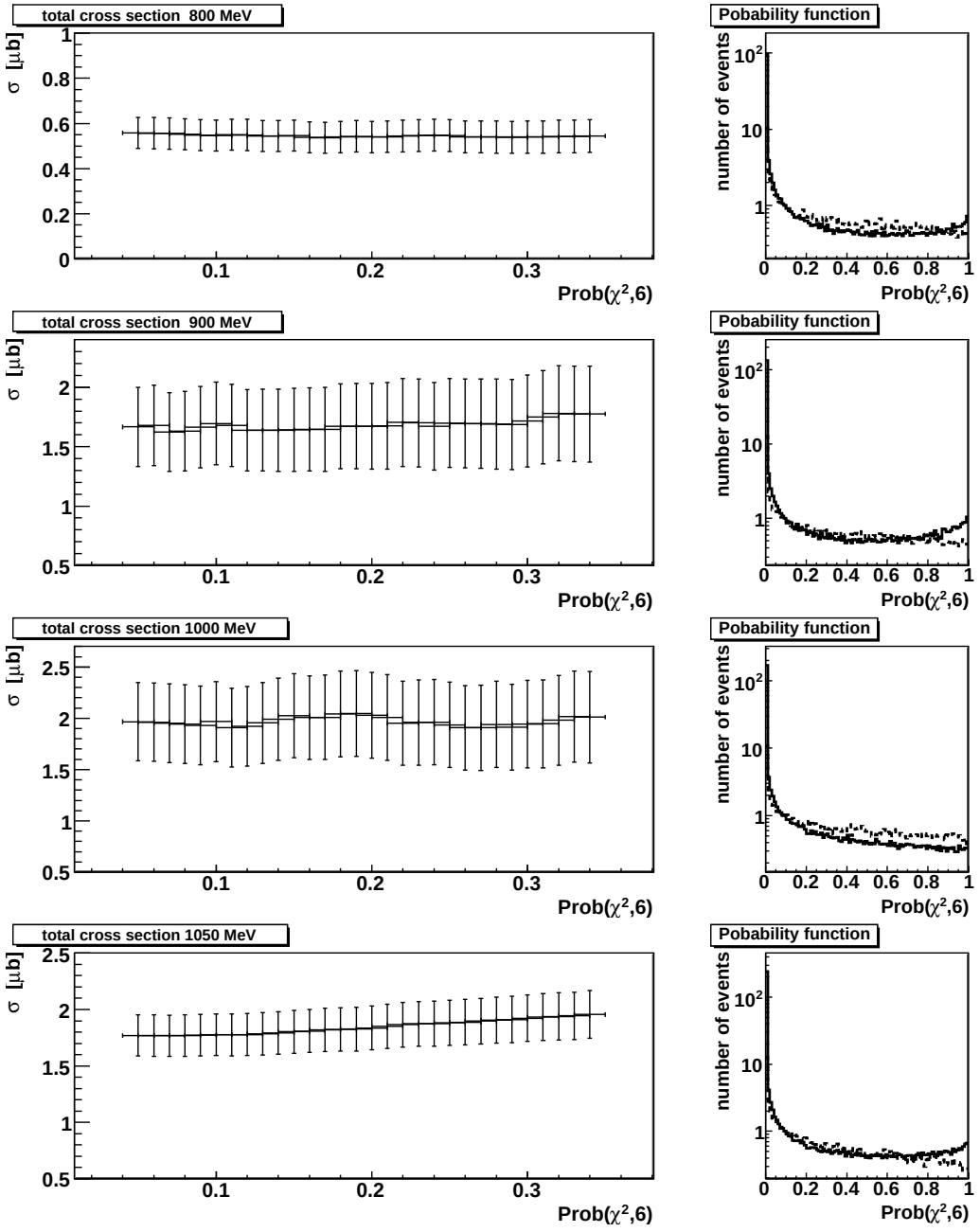

Figure 9.25: *Total cross sections as a function of the probability cut.*

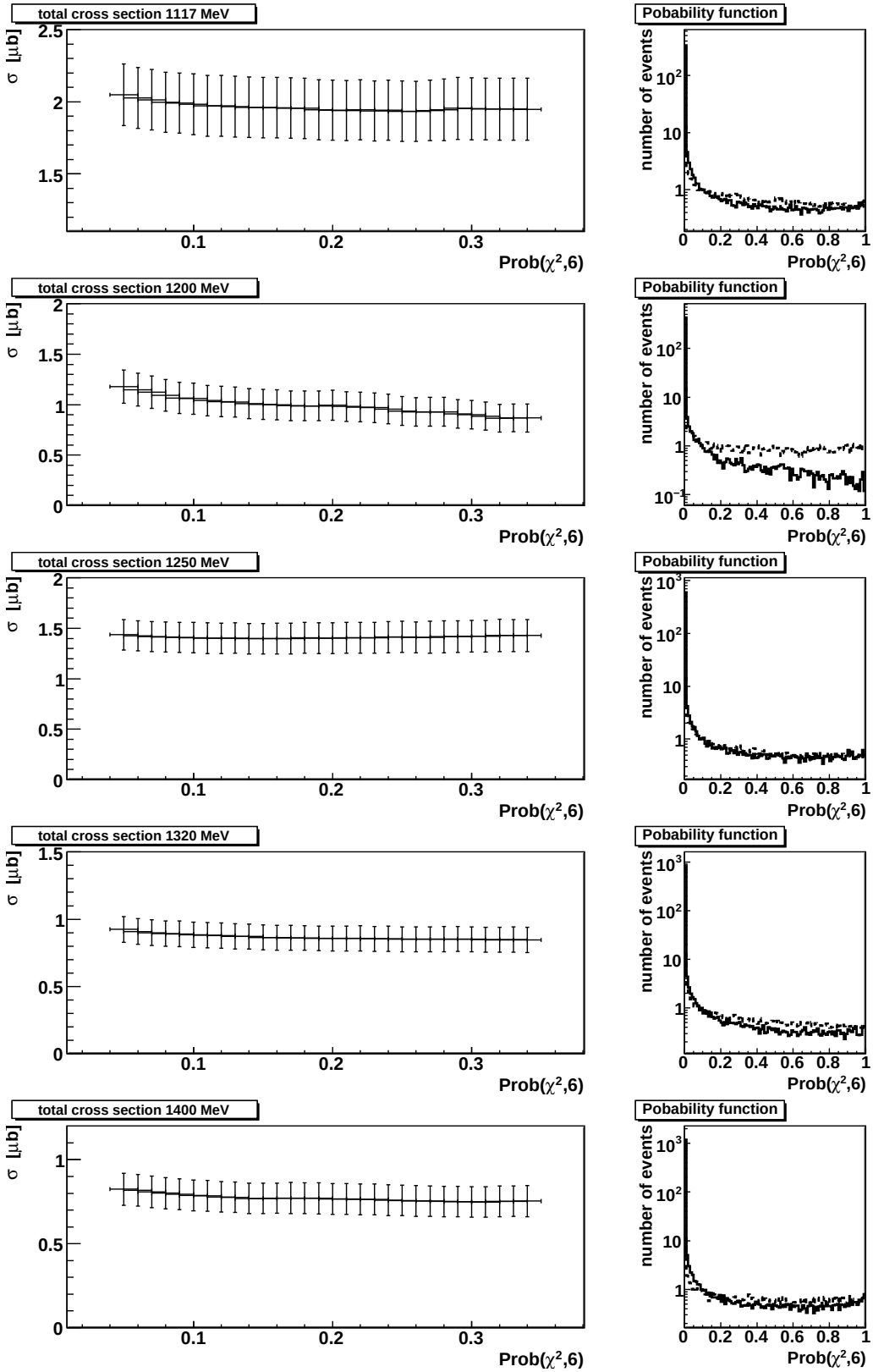

Figure 9.26: *Total cross sections as a function of the probability cut.*

9.7 Total Cross Section of dd → ^{4}He$\pi^0\pi^0$ as Function of the Run Number

The following pages show the total cross section as a function of the run number. The width of the error bars in x-direction marks the number of runs combined for one point. The right side shows the projection on the y-axis., where the values are weighted with $1/(\Delta\sigma)^2$. In case of 1.0 GeV the projection of the first part of the beam time (runs 3854 to 3905) is represented by the solid line, that of the second part (runs 4091 to 4165) by the dashed line.

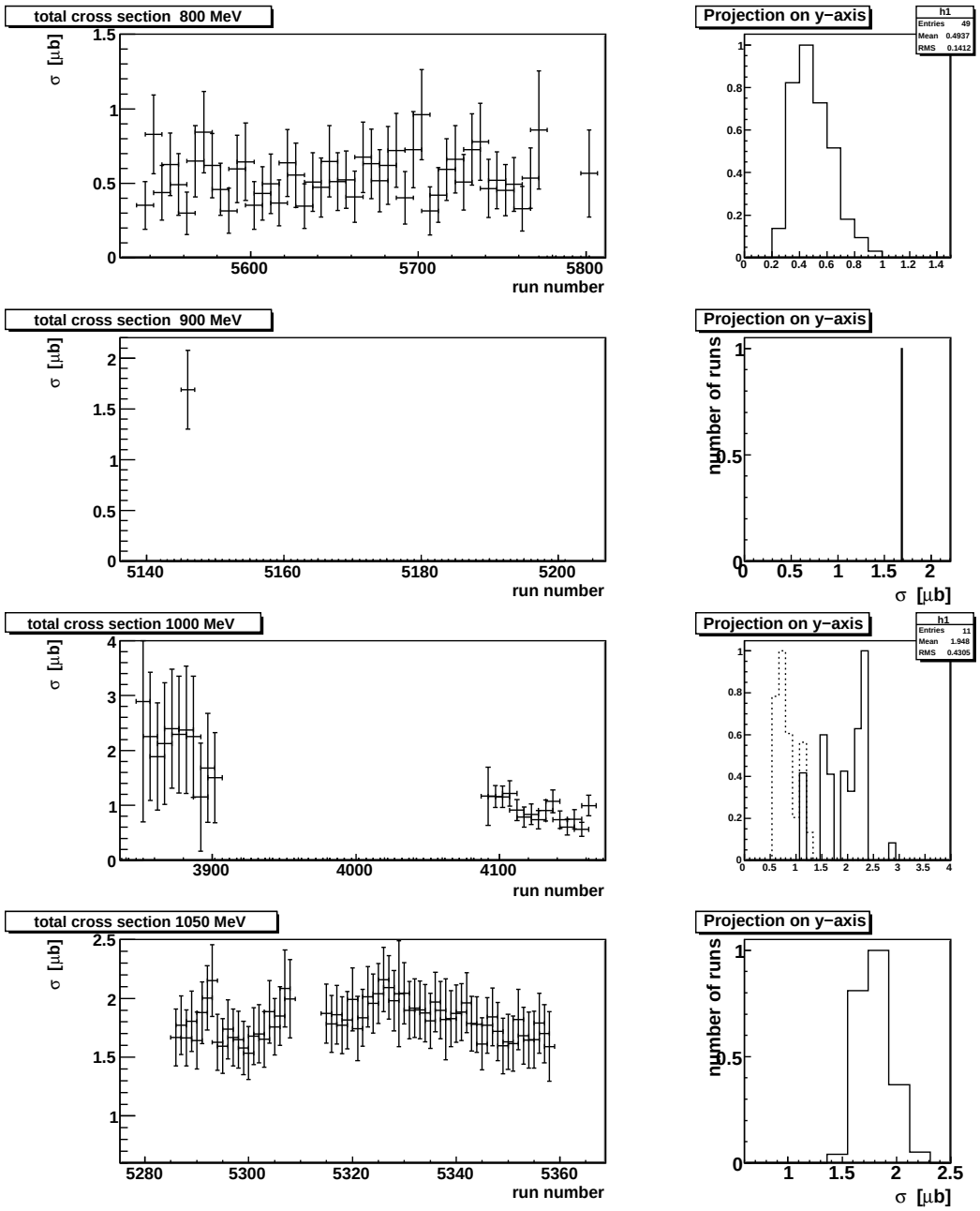

Figure 9.27: *Total cross sections as a function of the run number.*

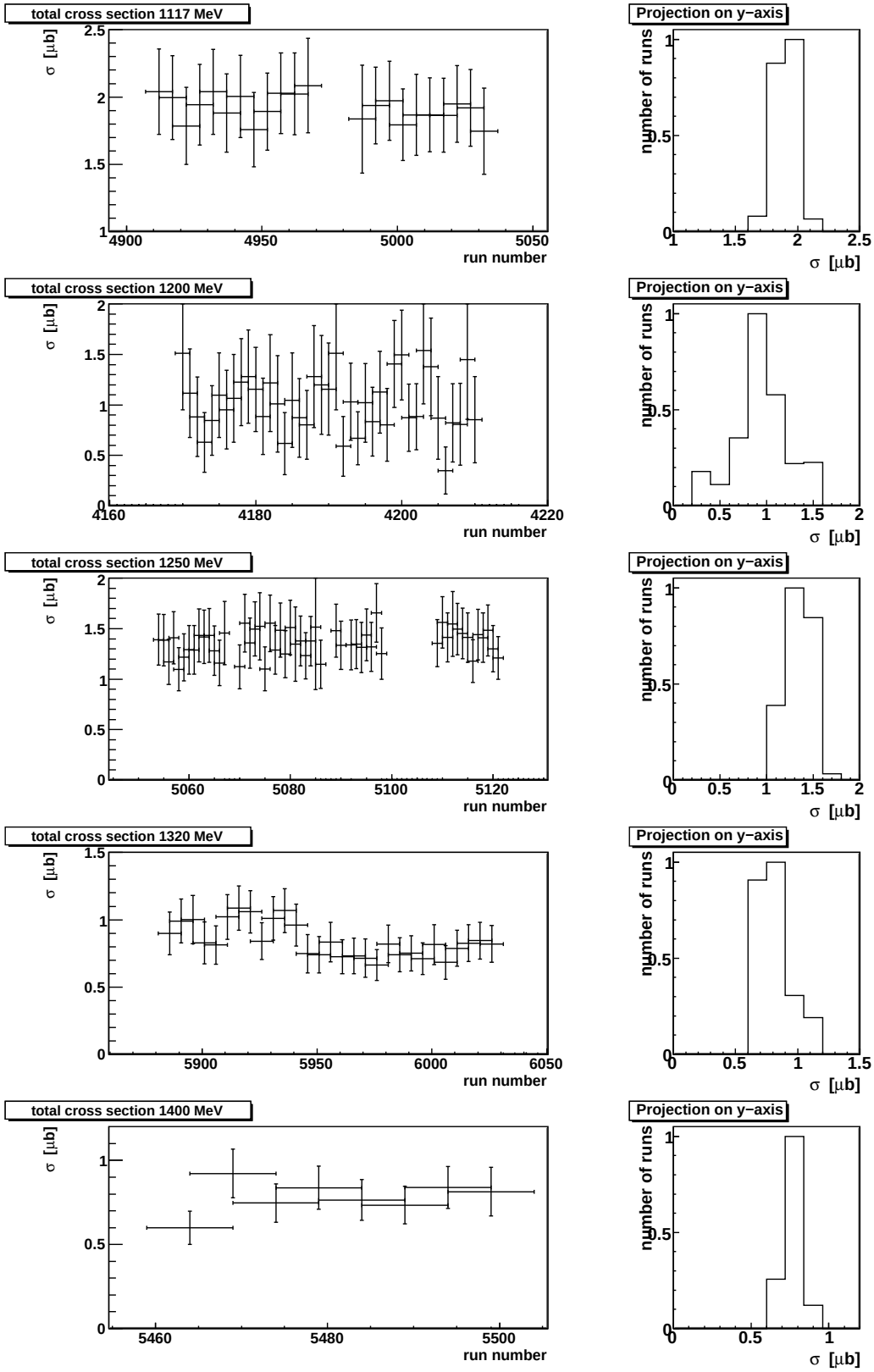

Figure 9.28: *Total cross sections as a function of the run number.*

9.8 Commissioning Beam Time: 1.0 and 1.2 GeV

During the commissioning beam time for the newly installed detectors two beam energies were used, 1.0 and 1.2 GeV, which can be analyzed as well. Both were obtained in two parts distributed over the two weeks of beam time. The first part was meant for tests of the triggers and the detectors, the second part for data production.

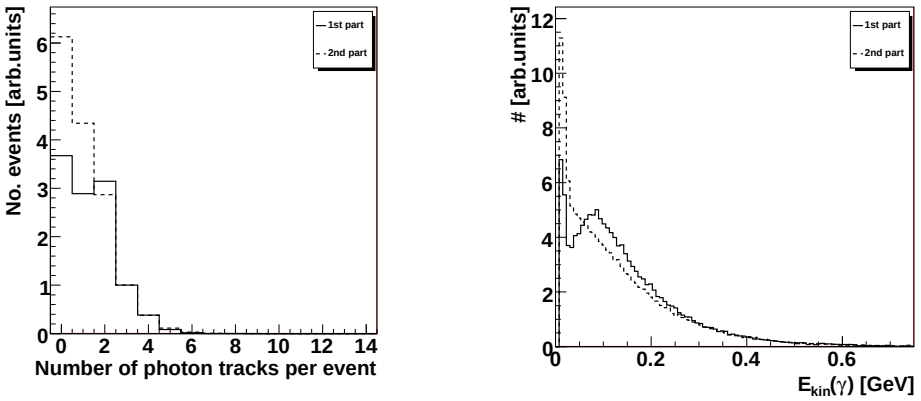

(a) *Number of photon tracks per event.*

(b) *Kinetic energy distribution of the photons from the π^0 decay.*

Figure 9.29: *Comparison of first and second parts of the beam time for the 1.0 GeV measurements. The solid line represents the first part of the beam time, the dashed line the second part.*

Unfortunately the detector performance turned out to be much worse in the second part. Apparently photons from π^0 decay were lost and low energetic photons flooded the detector. The reason might be that due to bad beam and target conditions the interaction point was no longer a rather confined region around $x = y = z = 0$, but extended over a much larger area. In such a 'beam gas' situation especially the z-position is expected to vary, which would affect the ^{4}He particles only slightly, since they are anyway going in the forward direction. The photons on the other hand would be lost in the forward and backward holes and their paths through the detector would be very different.
The following plots always show the result for 1.0 GeV since here the statistics is larger, but similar plots for 1.2 GeV show the same effect. Fig. 9.29a shows the distribution of detected γ tracks in the first (solid line) and second part (dashed line) of the beam time. The number of events with one or zero tracks is much larger in the second part of the beam time. The effect is even more clearly seen in the energy distribution of the photons which are assigned to a π^0 (Fig. 9.29b). All tracks in this plot can be sorted to pairs which give a mass similar to the π^0 mass (maximal 30 MeV deviation), however there is always an admixture of random coincidences. But the amount of random coincidences in the second part is much higher than in the first part: While the distribution from the first part of the beam time (solid line)

shows a peak at approximately 100 MeV, this peak is not seen in the second part of the beam time (dashed line). This peak is expected when the π^0 with a mass of 130 MeV decays, since the two γs share the energy, one getting a bit more than the other one. The smooth distribution with the strong rise at small energies in the second part just tells that most γ pairs which are attributed to a π^0 are actually just random coincidences.

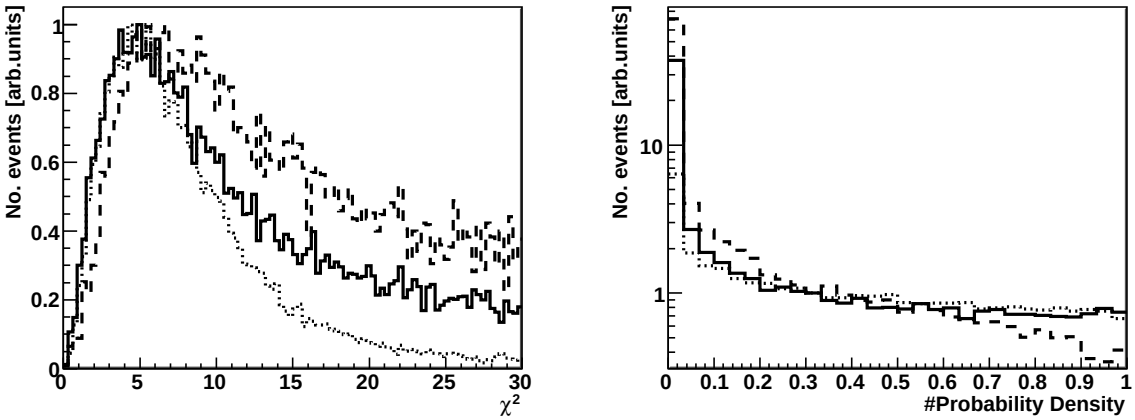

Figure 9.30: χ^2 *and probability distribution for 1.0 GeV for the first (solid line) and the second (dashed line) part of the beam time and MC simulations (dotted line)*

Of course energy and momentum conservation including both pions and the ^{4}He will (in most cases) not be fulfilled, since there is no reason why e.g. the angle of the falsely identified π^0 should follow the restrictions given by the angle of the ^{4}He. Consequently the χ^2 distribution will have a much bigger tail towards high χ^2 values, as indeed is the case - see Fig 9.30.
If ^{4}He events are selected element by element with the $\Delta E - \Delta E$ method (FRH1 versus FRH2) in principle 1/3 of the selected events should survive the kinematic fit, the rest being $dd \rightarrow {}^4\mathrm{He}\pi^+\pi^-$ since nothing else is possible at these energies[1]. The number of events which pass the kinematic fit and the more detailed analysis will be still smaller (e.g. some of the ^{4}He particles are actually ^{3}He particles, some γ are lost in the forward detector). Fig. 9.31 shows selected ^{4}He events (green marker) and the subsample of these which passed the $\chi^2 < 10$ cut (red marker). In case of the second part of the beam time apparently much less events survive although ^{4}He is already selected. This proves again that the problem is connected with the photon reconstruction, not with the ^{4}He identification.
At least this problem does not depend on the γ angle, thus the differential distributions are still correct, as seen in Fig. 9.32. Therefore for the differential distributions both parts can be used to increase the statistics.
However the number of dd $\rightarrow {}^4\mathrm{He}\pi^0\pi^0$ events is reduced compared to the number of $dd \rightarrow {}^3\mathrm{He}n$ events used for the normalization, since the latter reaction is identified

[1] At 1.2 GeV also $dd \rightarrow {}^4\mathrm{He}\eta$ is possible, but the cross section is much smaller.

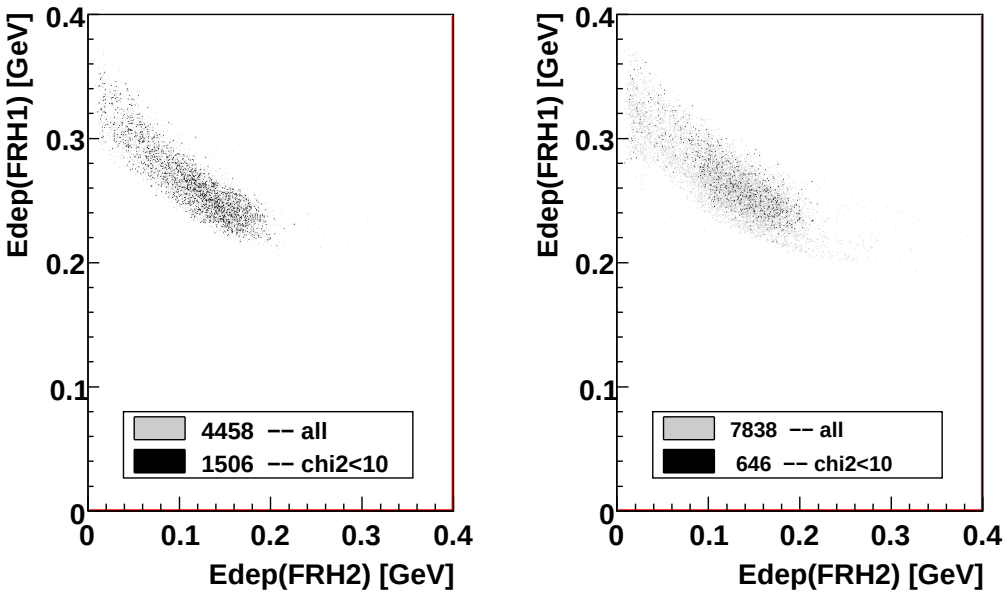

Figure 9.31: *Deposited energy in FRH1 versus FRH2 for selected* ^{4}He *events (green) in comparison with those which survived the kinematic fit (red) at 1.0 GeV. The left side shows the first part of the beam time, the right side the second part. Here all triggers were used, whereas for the estimation of the ratio only the trigger used for the normalization is allowed*

solely with the ^{3}He in the forward detector. Hence the total cross section obtained with the second part of the beam time is too small and cannot be used.

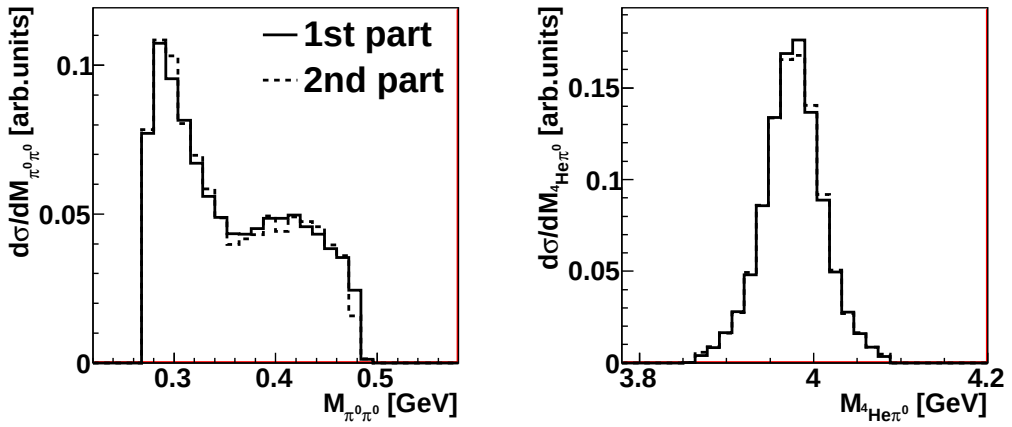

Figure 9.32: *Invariant mass of* $\pi^0\pi^0$ *(left) and the* ^{4}Heπ^0 *(right) systems after the kinematic fit for 1.0 GeV before efficiency and acceptance corrections. The solid red line marks the first, the dashed black line the second part of the beam time*

In case of 1.0 GeV, the statistics is large enough that the first part of the beam time suffices for the absolute normalization, but in case of 1.2 GeV the changes of detector parameters in the first part, which was planned only for tests, are so big and frequent that it cannot be used.
In order to still get an estimate of the total cross section, the values for 1.0 GeV obtained in the first and the second part of the beam time are compared to estimate a correction factor F for the absolute normalization. For 1.2 GeV the total cross section is estimated based on the second part of the beam time and this value is then corrected with the factor based on 1.0 GeV.

$$F = \frac{\sigma_{1.0\ GeV}(1st\,part)}{\sigma_{1.0\ GeV}(2nd\,part)} = 2.17 \pm 0.83 \tag{9.2}$$

Of course this can only be a rough estimate with large uncertainties. Besides the statistical uncertainties given here, based on the errors for the two cross section values, it is not proven that the inefficiency was the same for all runs of the second part of the beam time and that it affects both energies in the same way, given the different ranges of the particles at different energies.
This method allows a rough estimation of the total cross section also for the 1.2 GeV data.

9.9 Technical Drawings for the new FWC

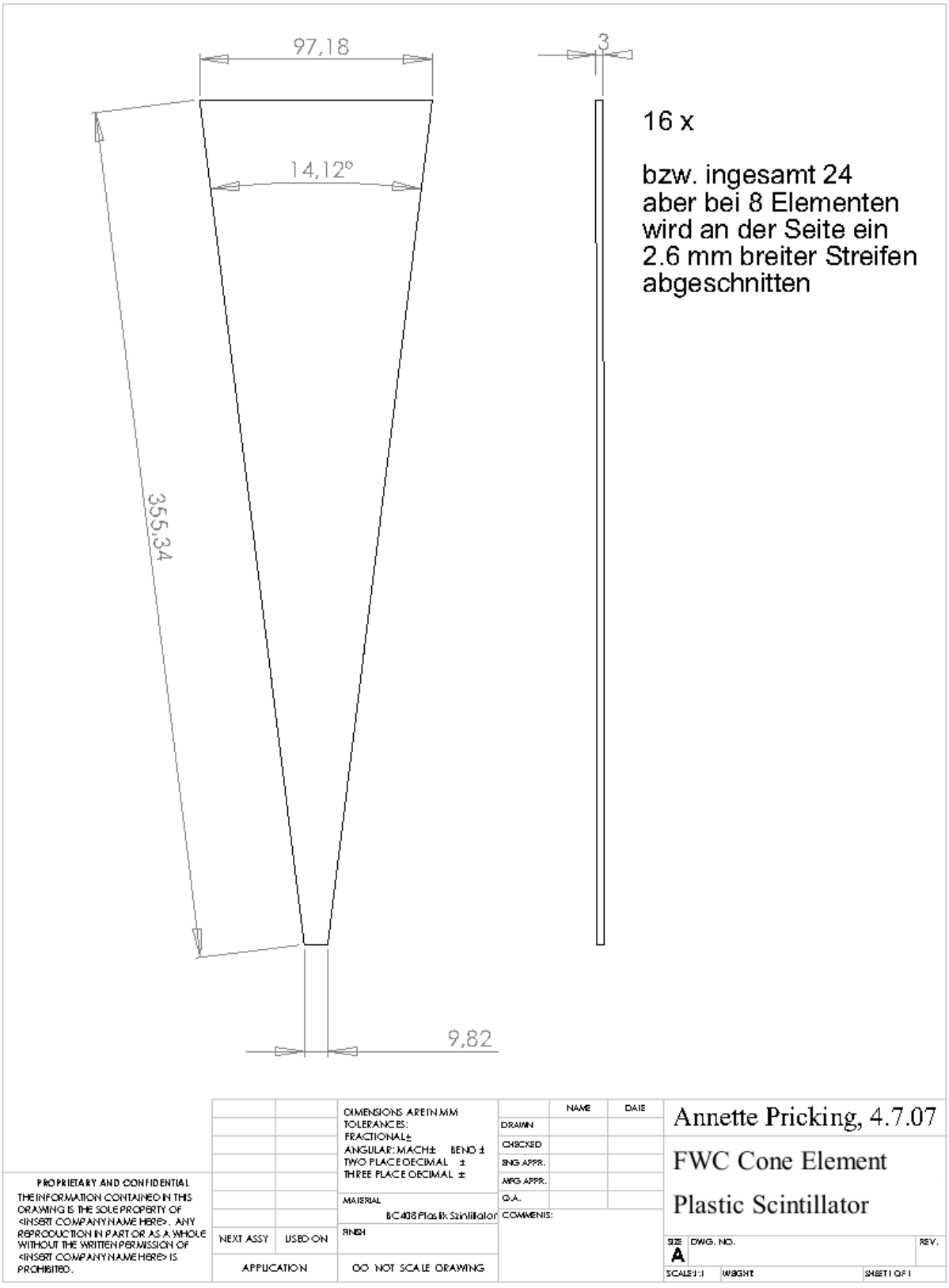

Figure 9.33: *FWC: Element of the conical layer*

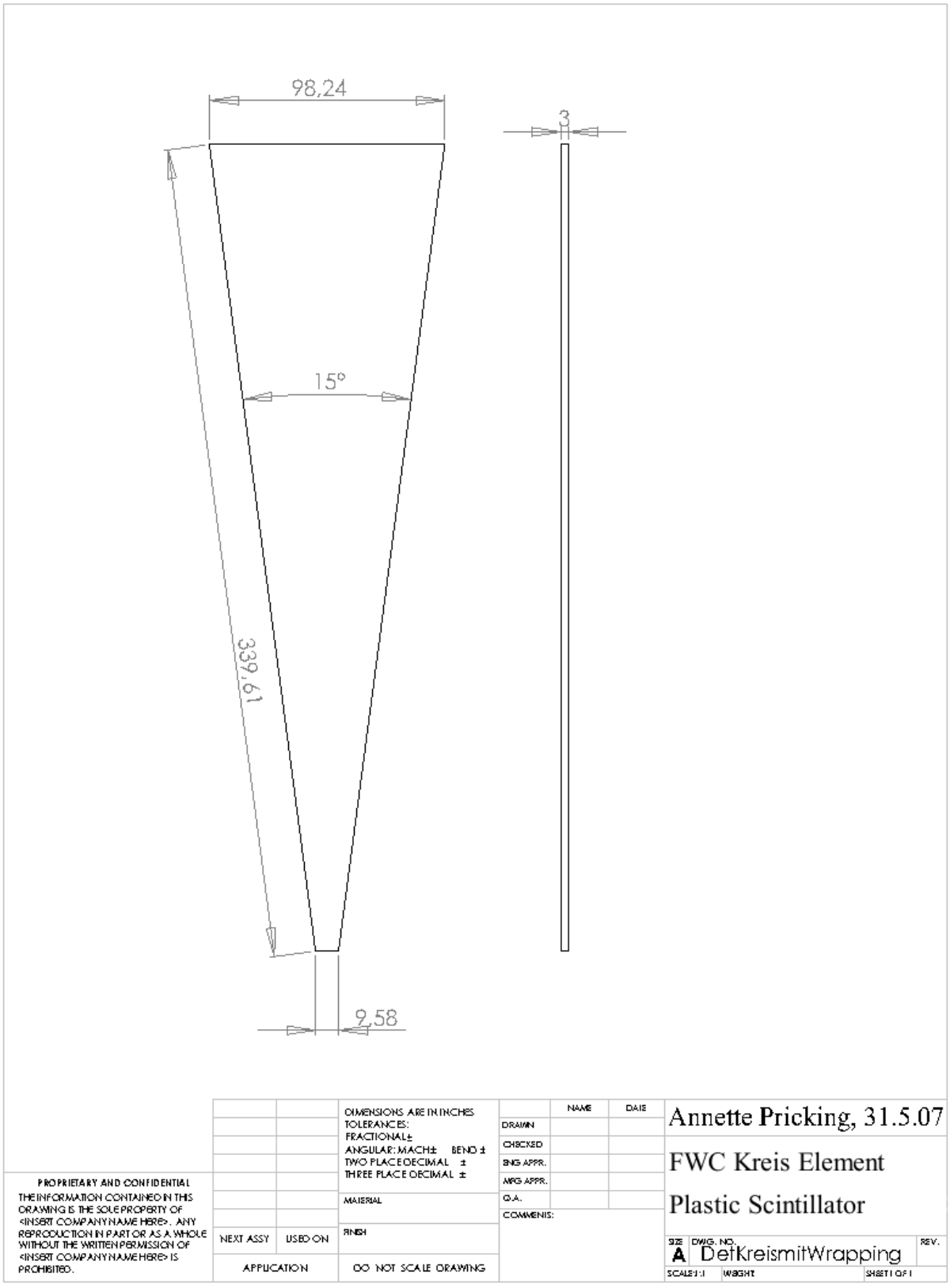

Figure 9.34: *FWC: Element of the planar layer*

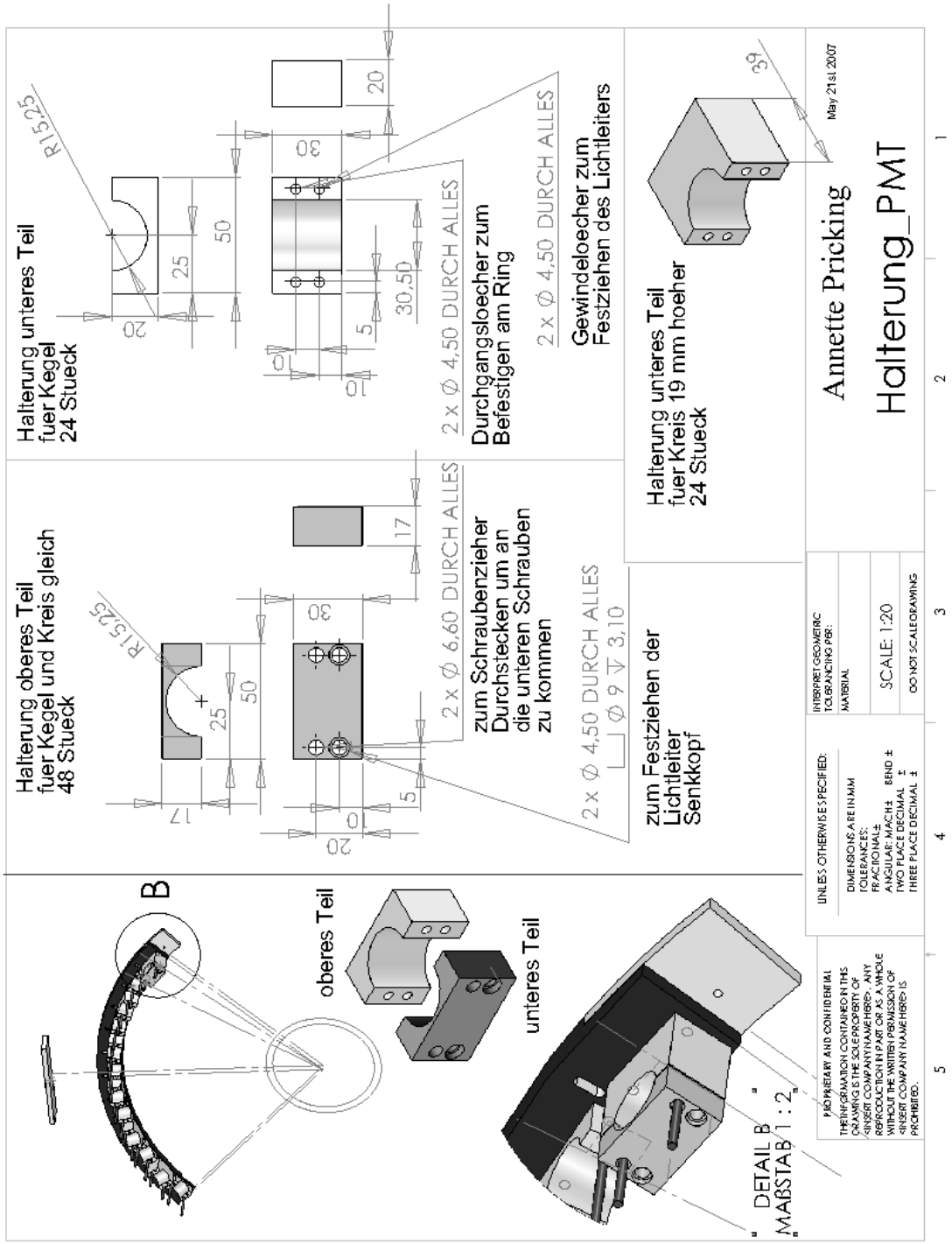

Figure 9.35: *Holding structure for the PMTs. It is the same both for the conical and the planar layer, except that the lower part, which is connected to the ring, is 19 mm longer in case of the planar layer.*

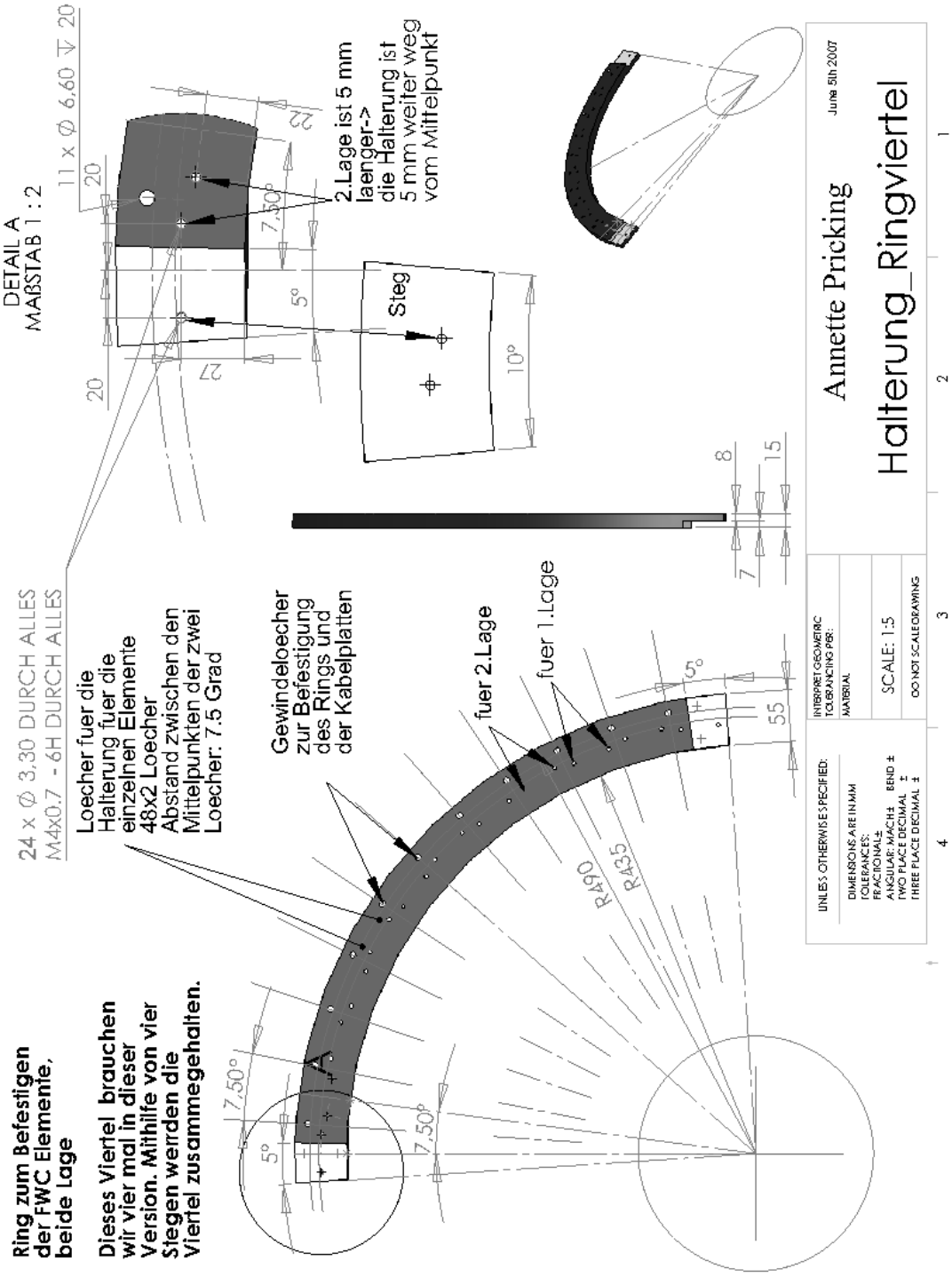

Figure 9.36: *Overall holding structure: the ring is mounted at the WASA support frame and the holding devices for the PMTs are connected to this ring. The devices are mounted so that their center lines are 7.5° apart from each other. Every second device mounted is 5 mm further inside because these parts are meant for the inner layer which is 5 mm shorter.*

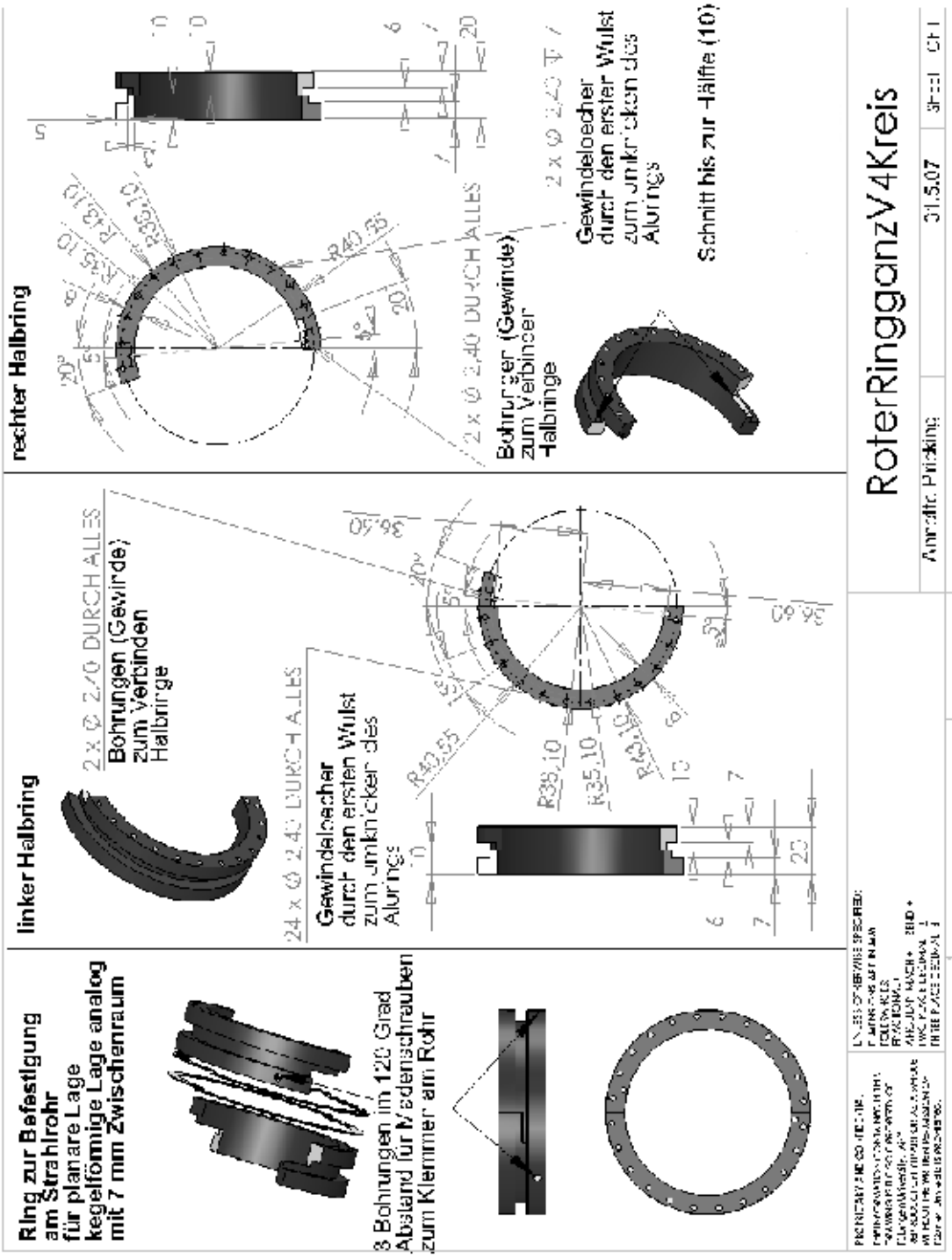

Figure 9.37: *Ring at the beampipe to fix the tip of the elements. The silicon ring and the aluminium saw-tooth ring, which allow a fixation for each element, turned out to be not necessary.*

9.10 Technical Drawings for the new FVH

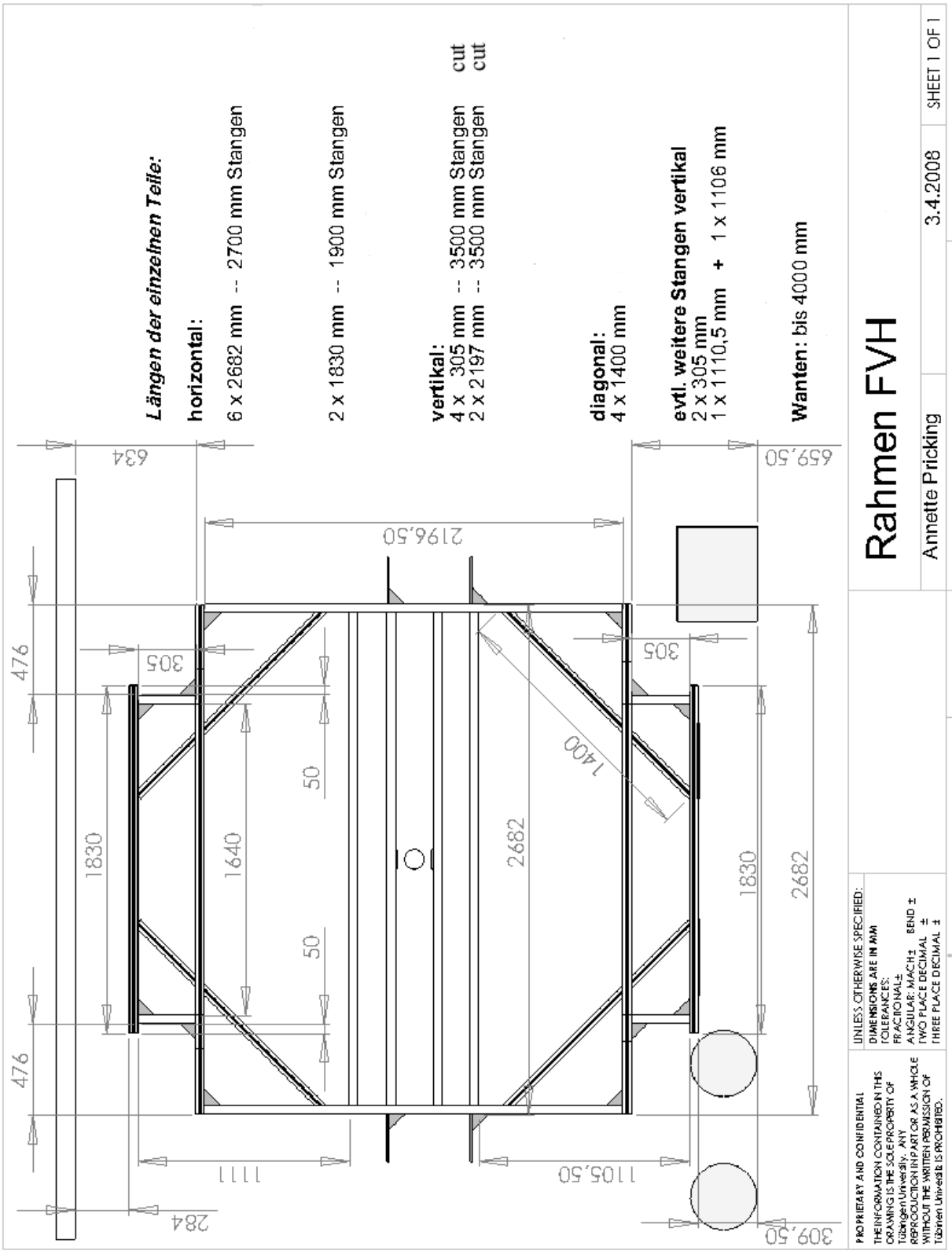

Figure 9.38: *Supporting frame for the new FVH*

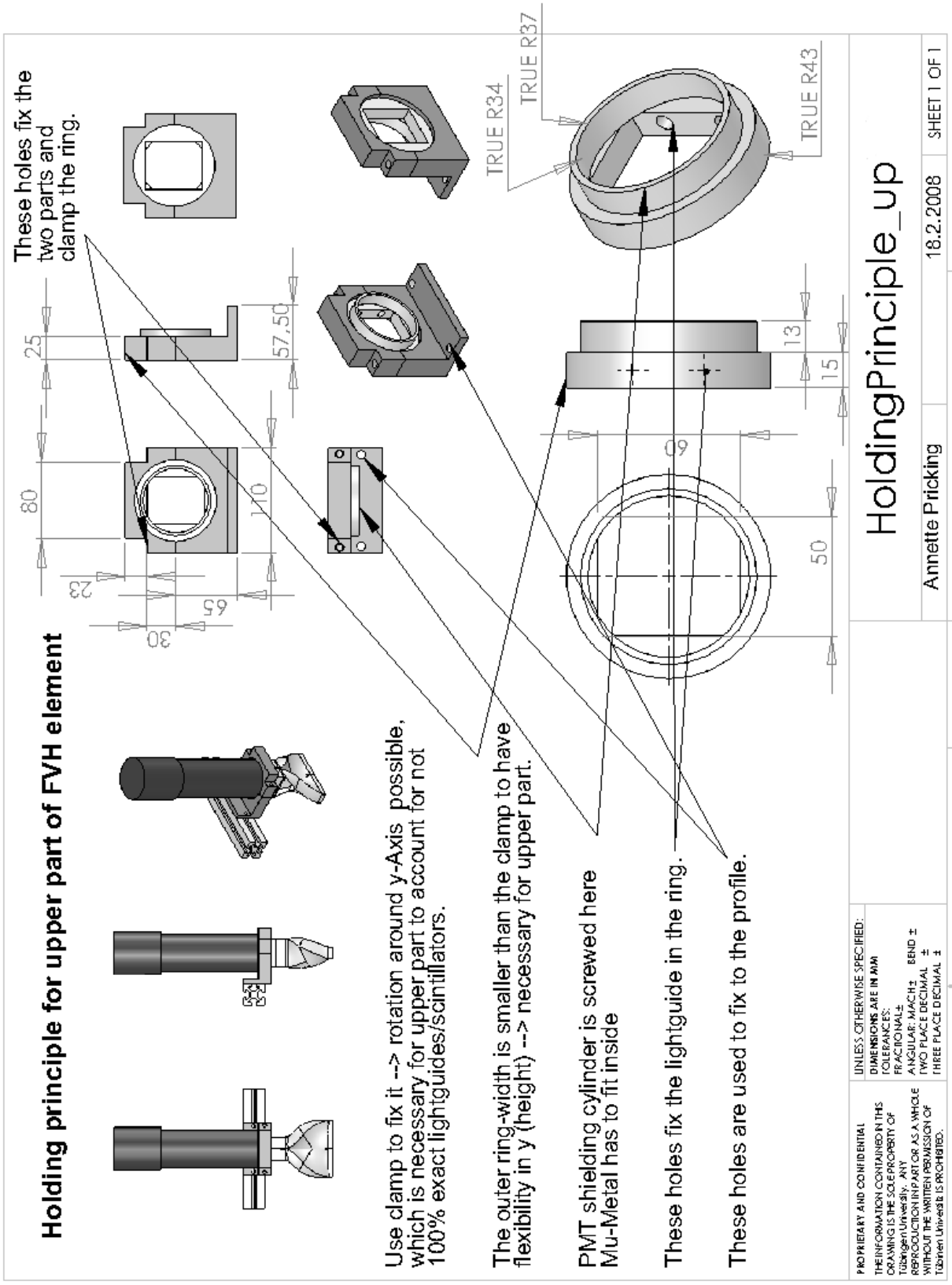

Figure 9.39: *Holding principle of the new FVH, top*

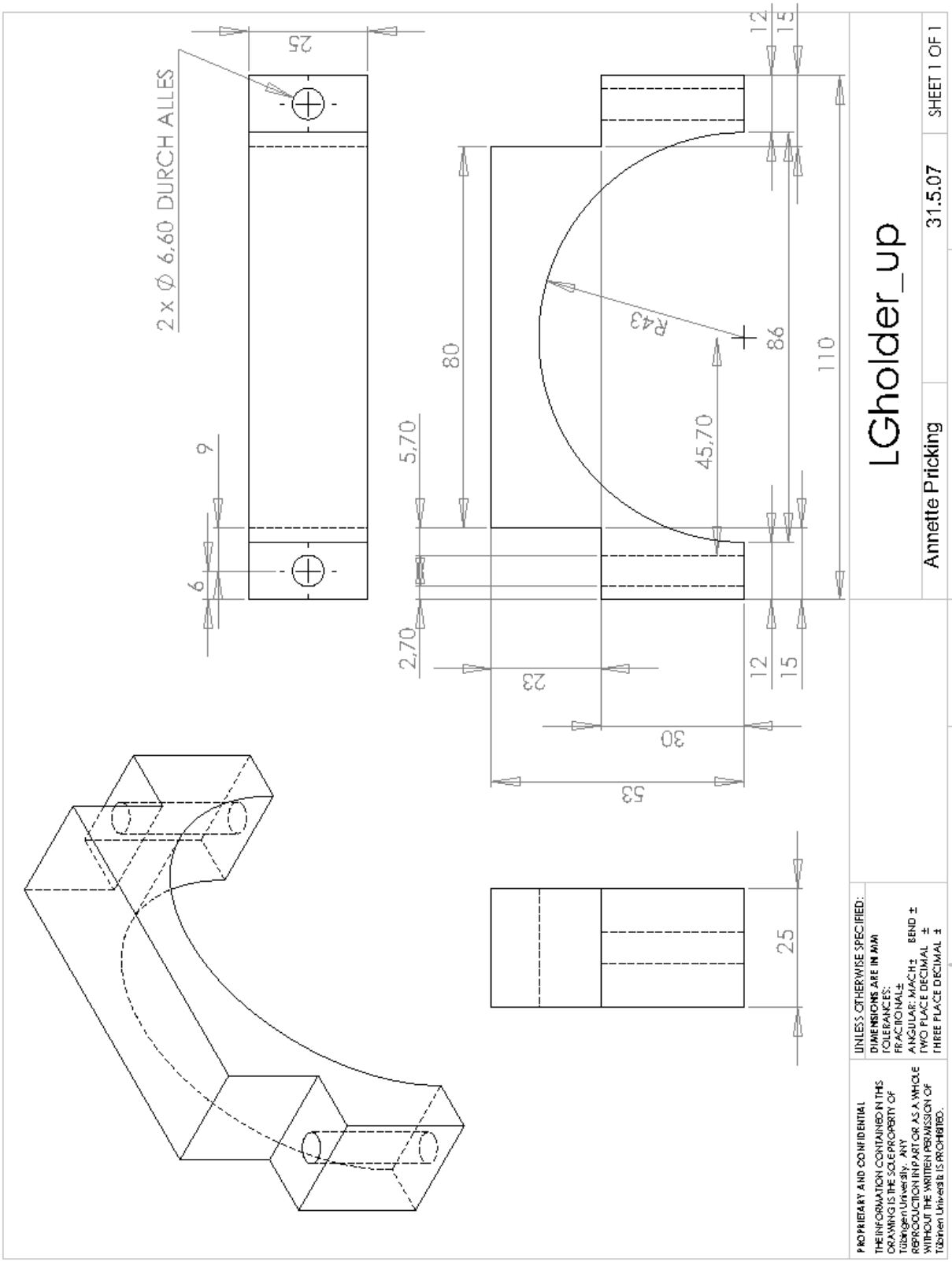

Figure 9.40: *Holder for the lightguide, part1, top*

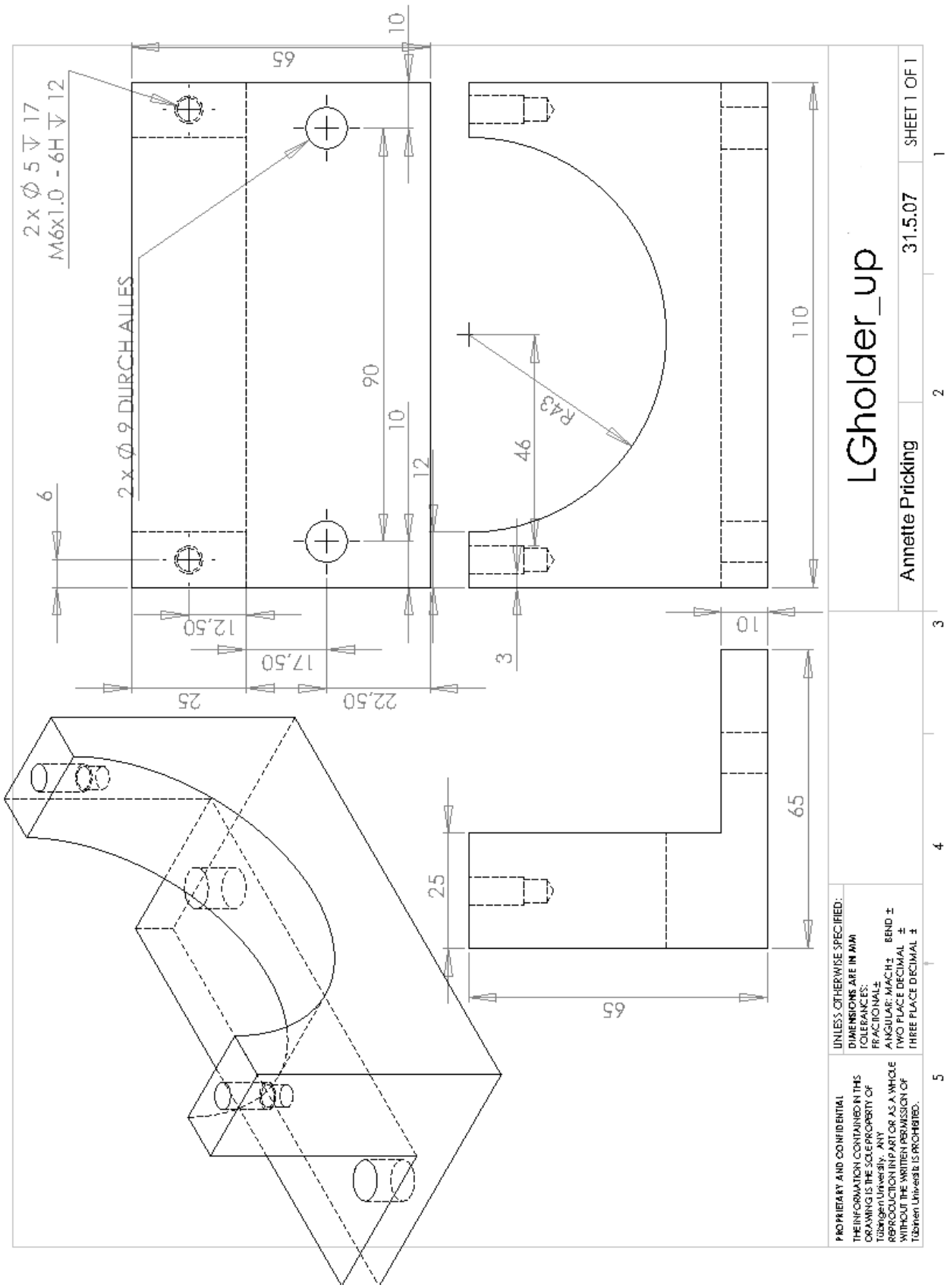

Figure 9.41: *Holder for the lightguide, part2, top*

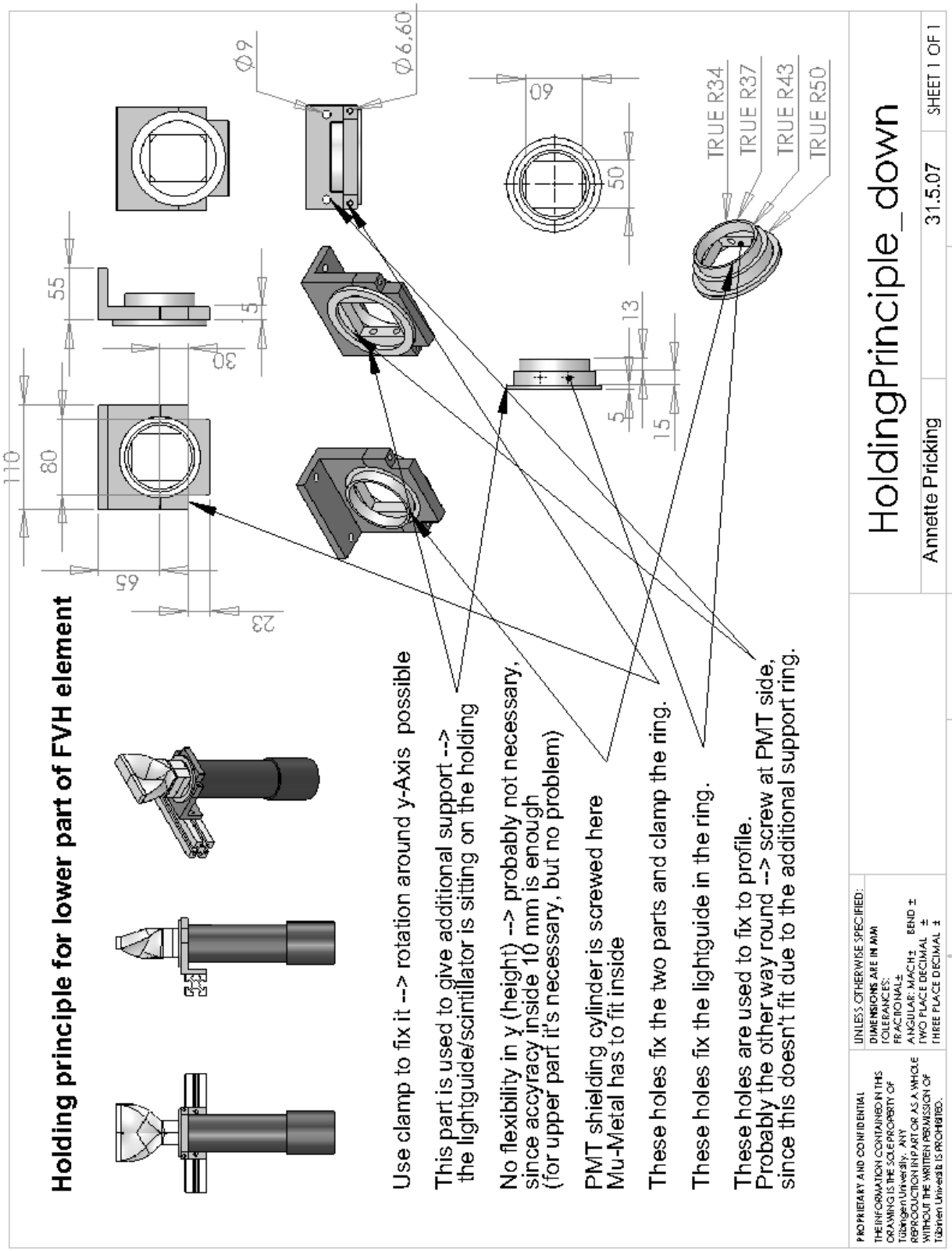

Figure 9.42: *Holding principle of the new FVH, bottom*

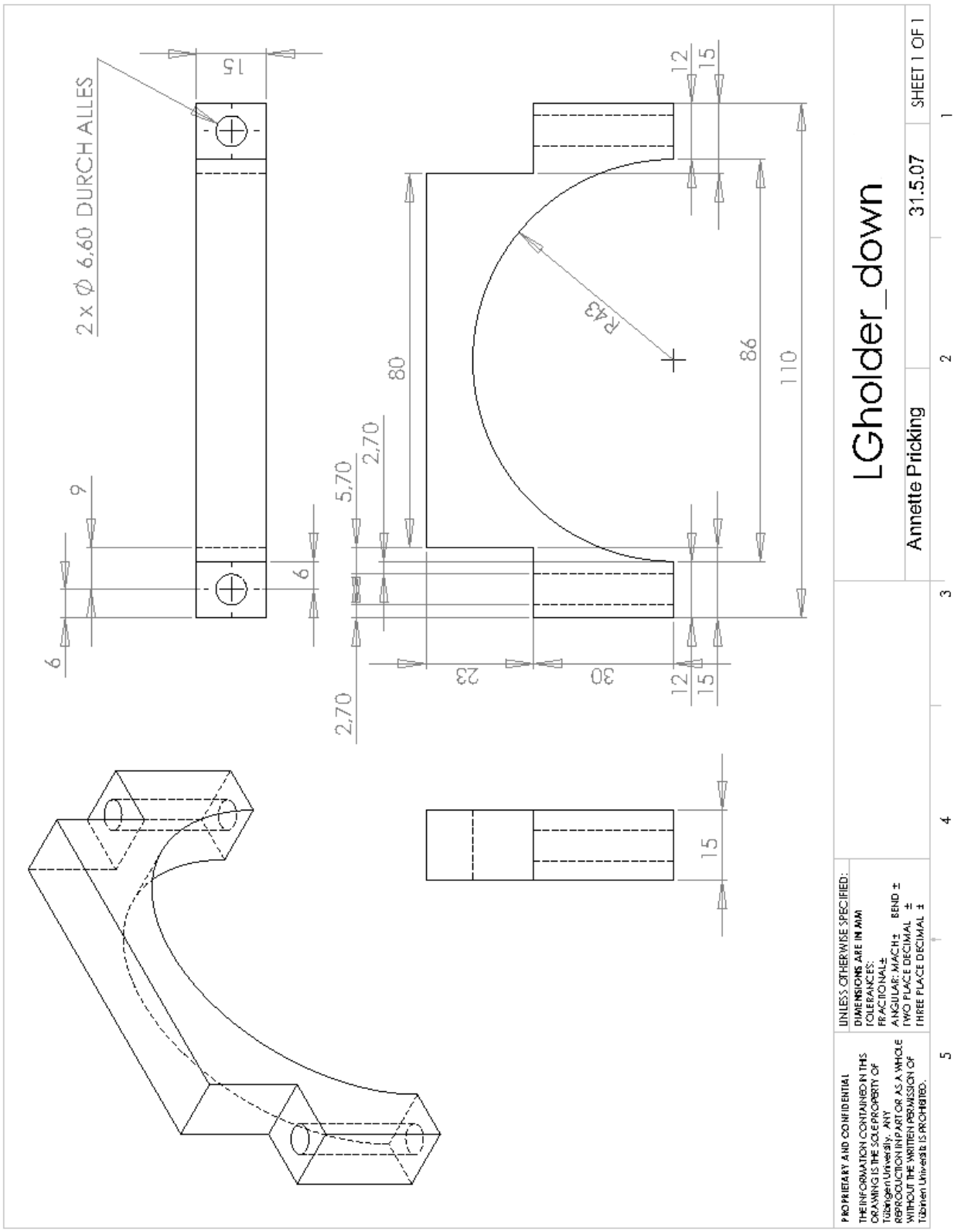

Figure 9.43: *Holder for the lightguide, part1, bottom*

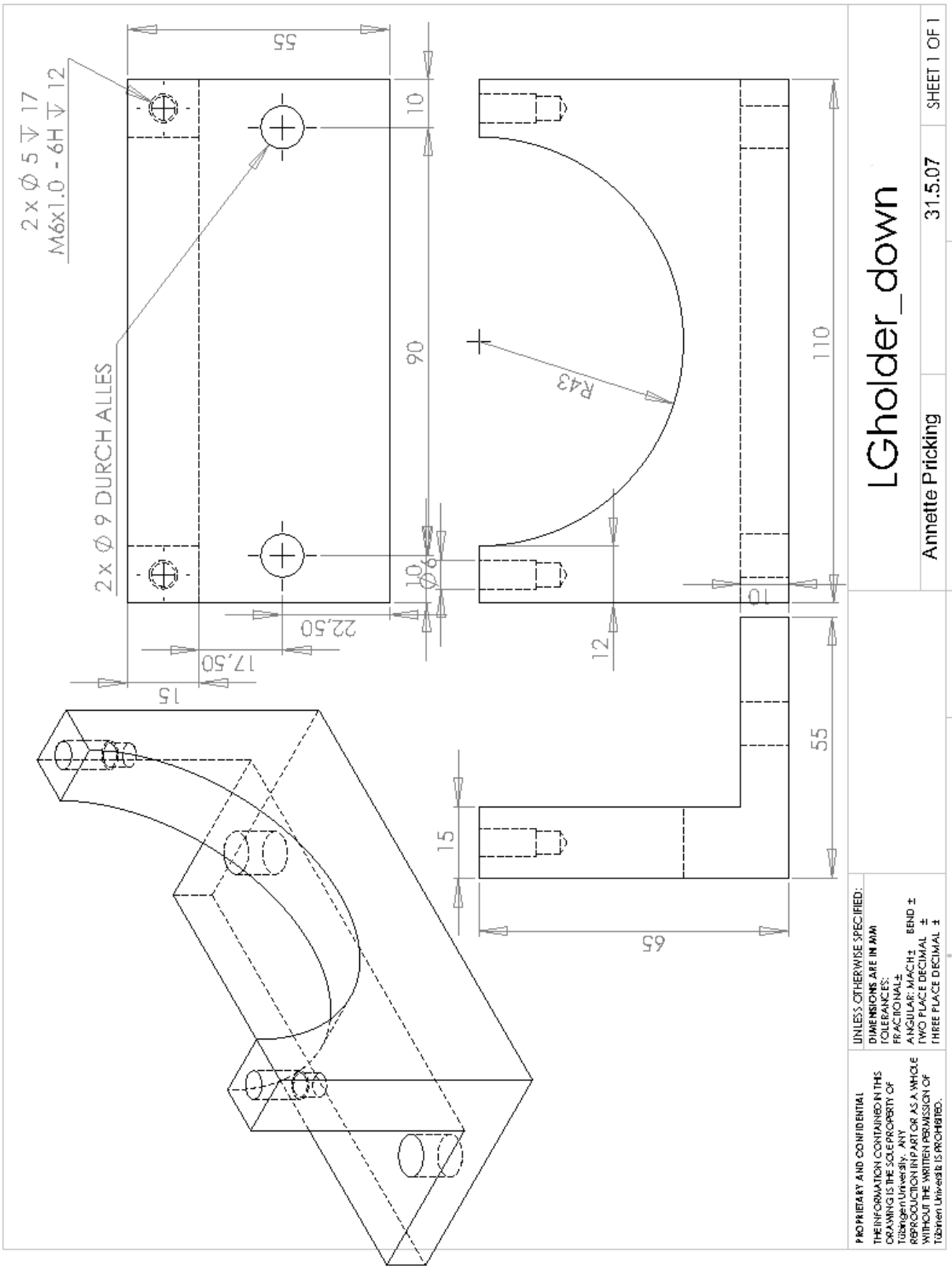

Figure 9.44: *Holder for the lightguide, part2, down*

Bibliography

[ABC60] A. Abashian, N.E. Booth, and K.M. Crowe, *Possible Anomaly in Meson Production in p+d Collisions*, Phys. Rev. Lett. **5** (1960), 258–260.

[Abd80] A. Abdivaliev et al., *Analysis of the Production Mechanism of narrow Enhancements in the Effective Mass Spectrum (pi+ pi-) in the Reaction n p → d pi+ pi- at a Neutron incident momentum of P(n) = 1.73-GeV/c*, Nucl. Phys. **B168** (1980), 385.

[Ada04] H.H. Adam et al., *Proposal for the Wide Angle Shower Apparatus (WASA) at COSY-Juelich-'WASA at COSY'*, 2004.

[Ada05] I. Adam et al., *The DIRC particle identification system for the BaBar experiment*, Nucl. Instrum. Meth. **A538** (2005), 281–357.

[And00] M. Andersson et al., *Isospin resolved double pion production in the reaction p+d→ 3He+2pi*, Physics Letters B **485** (2000), no. 4, 327 – 333.

[Aza10] T. Azaryan, *Study of the pd→ pd X reaction in the ABC effect region*, DPG, 2010.

[Ban71] Banaigs, J. et al., *Observation of the abc effect and of a structure at 450 mev in mesonic missing-mass spectra. (in french)*, Nucl. Phys. **B28** (1971), 509–527.

[Ban73] Banaigs, J. et al., *abc and def effects in the reaction d p → he-3 (mm)0 - position, width, isospin, angular and energy distributions*, Nucl. Phys. **B67** (1973), 1–36.

[Ban76] Banaigs, J. et al., *Production of I = 0 Mesonic States in the Reaction d d → He-4 x*, Nucl. Phys. **B105** (1976), 52.

[Bar73] Bar-Nir, I. et al., *Analysis of the reaction n p → d pi+ pi- below 3.5 gev/c*, Nucl. Phys. **B54** (1973), 17–28.

[Bar97] C. Bargholtz et al., *The inclusive reaction d + d → He-4 + X 29-MeV above the 2pi0 threshold*, Phys. Lett. **B398** (1997), 264–268.

[Bar08] C. Bargholtz et al., *The WASA Detector Facility at CELSIUS*, Nucl. Instrum. Meth. **A594:339-350** (2008).

[Basa] M. Bashkanov et al., *The ABC Effect in Double-Pionic Nuclear Fusion and a pn Resonance as its Possible Origin*, Proc. PANIC08, Elseview 239 (2009)

[Basb] M. Bashkanov, private communication.

[Basc] Bashkanov, M. et al., *The ABC Effect in the Basic Double-Pionic Fusion - Signature of a Resonance in Proton-Neutron and $\Delta\Delta$ Systems*, in preparation.

[Bas06] M. Bashkanov, *Double Pionic Fusion: Towards an Understanding of the ABC Puzzle by Exclusive Measurements*, Dissertation, Eberhard-Karls-Universität Tübingen, 2006.

[Bas09] M. Bashkanov et al., *Double-Pionic Fusion of Nuclear Systems and the ABC Effect – Aproaching a Puzzle by Exclusive and Kinematically Complete Measurements*, Phys. Rev. Lett. **102** (2009), 052301.

[Bel99] Bellemann, F. et al., *Pion pion p wave dominance in the He-3 + p d reaction near threshold*, Phys. Rev. **C60** (1999), 061002.

[Ber08] F. Bergmann et al., *The WASA-at-COSY pellet target*, IKP / COSY Annual Report (2008).

[BG92] H.Küsch, A.Olbrich, *The bards's song (in the forest)*, The Bard's Song, single, Virgin, 1992, recorded by Blind Guardian.

[BIC] BICRON, BC408 data sheet.

[Biz80] G. Bizard et al., *Experimental study and baryonic exchange interpretation of the reaction $H2(d,n)He3$ in the intermediate energy region*, Phys. Rev. C **22** (1980), no. 4, 1632–1637.

[Bon68] M. Bonfire, *Born to be wild*, Born To Be Wild, vinyl single, Dunhill, RCA, 1968.

[BR92] P.R. Bevington and D.K. Robinson, *Data reduction and error analysis for the Physical Science, 2nd edition*, Mc-Graw-Hill, 1992.

[Bro95] W. Brodowski, *Design und Aufbau einer Vetowand für den WASA/PROMICE-Detektor am CELSIUS SPeicherring und erste Messungen der Reaktion pp→ pp pi+pi-*, Diplomarbeit, Eberhard-Karls-Universität Tübingen, 1995.

[Bur67] E. Burdon, *Winds of change*, Winds of ChangeHey, studio album, MGM, 1967, recorded by Eric Burdon & The Animals.

[Cal96] H. Calen et al., *Detector setup for a storage ring with an internal target*, Nucl. Instrum. Meth. **A379** (1996), 57–75.

[CER] CERN, *Root*, cern.root.ch.

[Cha66] C. Chapman et al., *Observation of the Reaction $d + d \rightarrow^4 He2\pi$ at 1.69 GeV/c*, Phys. Lett. **21** (1966), no. 4, 465–467.

[Dah94] M. Dahmen et al., *A three layer circular scintillator hodoscope*, Nucl. Instrum. Meth. **A348** (1994), 97–104.

[ELJ] ELJEN Technology, EJ-200 data sheet.

[EW88] T. Ericson and W. Weise, *Pions and nuclei*, Oxford University Press, 1988.

[FP74] B. Fisher, B. Preston, *You are so beautiful*, You Are So Beautiful, vinyl single, *A&M*, 1974, recorded by Joe Cocker.

[Fri75] A. Fridman, *The Deuteron as Target in High Energy Reactions*, Fortschritte der Physik **23** (1975), 243–315.

[Har69] G. Harrison, *Here comes the sun*, Abbey Road, album, Apple Records, 1969.

[Gar99] A. Gardestig, and G. Faldt, and C. Wilkin, *Structure in two-pion production in the $dd \rightarrow \alpha X$ reaction*, Phys. Rev. **C59** (1999), 2608–2618.

[Geb09] R. Gebel, R. Maier, and H. Stockhorst, *Barrier-bucket RF tests*, IKP/COSY Annual Report **4282** (2009).

[CB10] H. Clement and M. Bashkanov, *Model Description of the $pn \rightarrow R \rightarrow \Delta\Delta \rightarrow d\pi^0\pi^0$ Reaction and its Confrontation with WASA-at-COSY Data* (2010).

[HA94] S. Huber and J. Aichelin, *Production of Delta and N* resonances in the one boson exchange model*, Nucl. Phys. **A573** (1994), 587–625.

[Hal69] J.H. Hall, and T.A. Murray, and L. Riddiford, *Evidence for a low-energy S wave pi pi interaction and a possible doubly charged dibaryon enhancement*, Nucl. Phys. **B12** (1969), 573–585.

[HHM03] V. Hejny, M. Hartmann, and A. Mussgille, *Rootsorter: A new analysis framework for anke*, IKP / COSY Annual Report 2002 **Jül-4052** (2003).

[Jac04] M. Jacewicz, *Measurement of the reaction $pp \rightarrow \pi^+\pi^-\pi^0$ with CELSIUS/WASA at 1.36 GeV*, Dissertation, Uppsala University, 2004.

[Kel08] S. Keleta, *Double Pion Production in the $dd \rightarrow \alpha 2\pi$ Reaction*, Dissertation, Uppsala University, 2008.

[Kel09] S. Keleta et al., *Exclusive measurement of two-pion production in the $dd \rightarrow^4 He\pi\pi$ reaction*, Nucl. Phys. **A825** (2009), 71–90.

[Kha09] O. Khakimova, *The ABC Effect in the Double-Pionic Fusion to Deuterium*, Dissertation, Eberhard-Karls-Universität Tübingen, 2009.

[Koc04] I. Koch, *Measurement of 2pi0 and 3pi0 production in proton-proton collisions at a center of mass energy of 2.465 GeV*, Dissertation, Uppsala University, 2004.

[Kre10] F. Kren et al., *Exclusive Measurements of $pp \to d\pi^+\pi^0$: Double-Pionic Fusion without ABC Effect*, Phys. Lett. **B684** (2010), 110–113.

[Kup] A. Kupcs, private communication.

[Len67] J. Lennon, P. McCartney, *With a little help from my friends*, With a little Help From My Friends, studio album, A&M, 1967, recorded by Joe Cocker.

[Len69] J. Lennon, P. McCartney, *The Long And Winding Road*, The Long and Winding Road, vinyl single, Apple Records, 1969.

[Len68] J. Lennon, P. McCartney, *Revolution*, Hey Jude, vinyl single, Apple Records, 1968.

[Mai97a] R. Maier, *Cooler synchrotron COSY: Performance and perspectives*, Nucl. Instrum. Meth. **A390** (1997), 1–8.

[Mai97b] R. Maier et al., *Cooler synchrotron COSY*, Nucl. Phys. **A626** (1997), 395c–403c.

[Mar71] D. Marcuse, *Compression of a bundle of light rays*, Applied Optics **10** (1971), no. 3, 494–497.

[Mes99] O. Messner, *Design and Setup of the Window Hodoscope for the new WASA 4pi Detector at CELSIUS*, Diploma thesis, Universität Tübingen, 1999.

[Mie] M. Mielke, *The ABC effect in $d+p \to^3 He+\pi^+ +\pi^-$ at ANKE*, Few-Body 19 Conference .

[Pau] C. Pauly, private communication.

[Pau06] C. Pauly, *Light Meson Production in pp Reactions at CELSIUS/WASA above the eta Threshold*, Dissertation, Universität Hamburg, 2006.

[PDG] Particle Data Group: K. Nakamura, *Review of particle physics*, J. Phys. **G37** (2010)

[Per06] Perez del Rio, E., *The Double Pionic Fusion in the reaction $pd \to {}^3\mathrm{He}\pi\pi$*, Dissertation, Eberhard-Karls-Universität Tübingen, in preparation.

[Per09] Perez del Rio, E., *Upgrade of the Forward Veto Hodoscopes at WASA*, master thesis, Eberhard-Karls-Universität Tübingen, 2009.

[PFW90] F. Plouin, P. Fleury, and Colin Wilkin, *Identification and analysis of the $np \to d\eta$ cross-section near threshold*, Phys. Rev. Lett. **65** (1990), 690–693.

[Phoa] Photonis, XP3112PB data sheet.

[Phob] Photonis, XP2020 data sheet.

[Pil67] H.M. Pilkuhn, *The interactions of hadrons*, North Holland, Amsterdam, 1967.

[Plo78] F. Plouin et al., *Observation of the ABC Effect in the Reaction $np \to d(mm)^0$ with a 1.88-GeV/c Neutron Beam*, Nucl. Phys. **A302** (1978), 413–422.

[Pod09] P. Podkopal, *Performance of the new plastic scintillator barrel detector for wasa-at-cosy*, IKP / COSY Annual Report (2009).

[Pra00] D. Prashun et al., *Electron and stochastic cooling at COSY*, Nucl. Instrum. Methods **A441** (2000), 167–174.

[Red10] C.F. Redmer, *In search of the Box-Anomaly with the WASA facility at COSY* , Dissertation, Universität Wuppertal, 2010.

[Rex] Rexroth, Bosch Group, *Mechanik-Grundelemente*.

[RS73] T. Risser and M. D. Shuster, *Anomalous enhancements in multiple-pion production with deuterons*, Phys. Lett. **B43** (1973), 68–72.

[Seb65] J. Sebastian, *Do you believe in magic*, Do You Believe in Magic, 1965.

[Sim93] D.A. Simon, *Guideit v1.1 users manual*, October 1993.

[Sko09] T.Skorodko et al., *Two-Pion Production in Proton-Proton Collisions – Experimental Total Cross Sections and their Isospin Decomposition*, Phys. Lett. **B679** (2009), 30–35.

[Ste03] E.J. Stephenson et al., *Observation of the charge symmetry breaking $d + d \to^4 He + \pi^0$ reaction near threshold*, Phys. Rev. Lett. **91** (2003), 142302.

[Tei97] S. Teis et al., *Pion-production in heavy-ion collisions at SIS energies*, Z. Phys. **A356** (1997), 421–435.

[Tho83] L. Thornhill, *Technology of Scintillation Counter*, CERN, Tech. report. **144808** (1983)

[Tro95] B. Trostell, *Vacuum injection of hydrogen micro-sphere beams*, Nuclear Instruments and Methods in Physics Research Section A: Accelerators, Spectrometers, Detectors and Associated Equipment **362** (1995), no. 1, 41 – 52, Proceedings of the 17th World Conference of the International Nuclear Target Development Society.

[Yur] L. Yurev, private communication.

[Zwo94] K. Zwoll et al., *Flexible data acquisition system for experiments at cosy*, IEEE Trans. Nucl. Sci. **41** (1994), 37–44.

Acknowledgments

> Oh, I get by with a little help from my friends
> Mm, I get high with a little help from my friends
> Mm, gonna try with a little help from my friends
>
> *With a little help from my friends*, Joe Cocker [Len67]

Well, here we are, finally. The last part to write, the first to read. If you don't plan to read more than this, go at least to pages 106 and 116, the final result - it's worth it.
The years I spend for my thesis were great (well, most of the time), which was, of course, because I could do some great physics. But the most important part on this being great were the people around me. I'd like to thank:

- first of all (I know that's what everybody writes but it's simply true) my advisor Prof. Heinz Clement for his help and support. For the nice group feeling he created, the discussions and coffee breaks. Especially for his tolerance and support after a certain daughter fought for attention with the work on the thesis.

- Mikhail Bashkanov for answering millions of questions and his companionship during our stays in Jülich or wherever.

- Prof. Hinterberger and Prof. Bisplinghoff for the possibility to do the thesis in Tübingen, still holding the connection to Bonn.

- Prof. Wagner for his help especially during the last part of the thesis.

- the CELSIUS/WASA and the WASA-at-COSY Collaboration for keeping the detector alive. To name just a few people: Magnus Wolke (for being everywhere), Volker Hejny (for not hitting my when I came with stupid computer questions), Andrzej Kupcs, Hans Calen, Jozef Zlomanczuk (for their help and advice, which usually meant more work) and Christian Pauly (for answering lots of questions).

- the Pellet group for keeping the pellets falling, the COSY crew for keeping the beam running and Kjell Franson for letting the trigger trigger.

- the (former) WASA-at-COSY and CELSIUS-WASA PhD students for the fantastic atmosphere, for sharing shifts, cookies, bugs and bars.

- the "Jülich people": Well, it's kind of a pity that WASA moved to COSY and not the other way round, since Uppsala is actually a little nicer than Jülich. But to be honest, I always liked being in Jülich, seeing you again and talking

to you - feeling kind of home. Especially I'd like to thank the members of the coffee corner at the 1st floor printer, Gisela Roes for organizing the stays in COSY-Hilton (it's not her fault), Susan Schadmand, Volker Hejny, Christoph Redmer and Christian Pauly and Frank Goldenbaum and their families for their friendship and rescuing me when I was caught in the Forschungszentrum.

- Norbert Paul, for answering all my questions about the technical stuff, for helping me to find the best solution, for his ideas how to fix what, for many tea bags during coffee breaks and especially NOT for a certain song text on a certain occasion.

- the Tübingen workshop, especially Mr. Brodbeck and Mr. Stockmaier for their tolerance when I came, knowing nothing about tolerances and technical drawings. For their help and advice about what can be done and what not, and in particular Mr. Stockmaier for his huge efforts to prepare the lightguides in time. And Michaela Lang, who had the back luck to do her few weeks "praktikum" just in time for polishing lightguides.

- the Jülich workshop for their support when we were wrapping and glueing the detector and especially Mr. Hadamek for convincing us to buy the diamond polisher and for sharing a bit of his enormous knowledge about plexiglass and how to build lightguides ("you need them in summer - next year I assume ?").

- the Tübingen group: Tatjana Skorodko, Evgeni Doroshkevitsch, Florian Kren, Katharina Ehrhardt, Arthur Erhardt (the soul of our computers), Olena Khakimova, Elena Perez del Rio and Mikhail Bashkanov for the nice atmosphere in the group, especially in some bar during our travels. And for your help with the FWC and the FVH manufacturing - there is nothing better than spending a weekend wrapping scintillators.

- the extended 4th floor for the great atmosphere, the cakes and for reminding me that there is actually some physics besides the ABC effect.

- Markus Knapp, Daniel Greiner, Claudia Oßwald, Gerhard Deuter and Markus Röhling for their constant efforts to save the world and fight the darkness.

- Eric Burdon, the Beatles, Joe Cocker, the Lovin' Spoonful, Blind Guardian, Steppenwolf and all the others for their applications of classical mechanics.

- my family and family in law, for daring to ask what I'm doing more than once, knowing very well I would talk for hours about it, and especially for taking care of Eva every now and then in the last couple of months. In particular I'd like to thank my parents - for everything.

- my daughter Eva for her constant reminders about what really matters

- my Sebastian for - actually I think the sentence from last time still fits best - being at my side wherever I was.